INVESTIGATIONS TO IMPROVE PRODUCT CLEANLINESS DURING THE CASTING OF STEEL INGOTS

BY

BRET THOMAS RIETOW

B.S., University of Illinois at Urbana-Champaign, 2003

THESIS

Submitted in partial fulfillment of the requirements
for the degree of Master of Science in Mechanical Engineering
in the Graduate College of the
University of Illinois at Urbana-Champaign, 2007

Urbana, Illinois

ABSTRACT

With advances in research technologies, the quality of cast steel product has vastly improved. Software has allowed researchers to develop models to not only predict such important characteristics as fluid flow and particle movement, but also to investigate why certain phenomena happen. Through a standard K-ε flow model, the fluid flow profile for a funnel mold and its associated nozzle were investigated using Fluent. Using new techniques, mass and momentum losses at the solidifying shell coupled with wall laws have been implemented with success. By performing parametric studies with simulated water models, the effect of these losses at the shell walls was shown to be quite significant in predicting the flow patterns of funnel-mold and thin-mold casters. Water models greatly underestimate the flow velocity and overall pattern in the upper portion of the mold, especially at the top surface (where velocity is critical to steel quality). The Nailboard Method has been developed to actively determine this top surface velocity of operating casters. After inserting a steel nail through the slag layer and into the liquid steel for a prescribed time, the solidified knob formed on the nail allows for determination of top surface velocity given the knob diameter and knob profile. A three-dimensional RANS turbulent K-ε model was created, with the spines method employed to allow free-surface movement. The effect of varying knob diameter and flow velocity was investigated through parametric study. The difference between the highest and lowest points on the knob top surface coupled with knob diameter proved to directly related to flow velocity. Experimental results at Algoma steel confirmed the feasibility of this technique in practice. The cleanliness of bottom-teemed ingot steel was experimentally investigated via SEM. A rigorous polishing process allowed for the location and size of numerous inclusions to be reported. Teeming without inert gas shielding caused the formation and entrapment of numerous macro-scale reoxidation inclusions (46 / 78 total inclusion), some extremely large in size (>> 20 µm). The highest inclusion concentrations were found at the ingot bottom, with no preference regarding trumpet direction. Refractory bricks high in SiO_2 facilitated the formation of many alumina reoxidation inclusions, and it is therefore suggested that high-quality runner lining bricks be used, void of silica.

TABLE OF CONTENTS

LIST OF TABLES

LIST OF FIGURES

NOMENCLATURE

Chapter 2 Nomenclature: Funnel Mold Flow Study

$\Delta Height$	Change in free-surface height from pressure approximation [m]
A	Area [m^2]
C_{1x}	Turbulence theory empirical constant [= 1.44]
C_{2x}	Turbulence theory empirical constant [= 1.92]
C_{μ}	Turbulence theory empirical constant [= 0.09]
E	Empirical wall law constant [= 9.793]
ε	Turbulent dissipation rate [m^2/s^3]
G_K	Generation of turbulent kinetic energy
g	Absolute gravitational acceleration [= 9.81 m/s^2]
$\vec{g}$	N-dimensional gravitational vector [m/s^2]
h	Height in the domain [m]
I	Unit stress tensor
K	Turbulent kinetic energy [m^2/s^2]
κ	von Karman constant [= 0.42]
n	Empirical constant for low-turbulence flow-in-a-pipe simulation
σ_K	Turbulence theory empirical constant [= 1.0]
σ_τ	Turbulence theory empirical constant [= 1.3]
p	Pressure [N/m^2]
p_{ferro}	Ferrostatic pressure [N/m^2]
p_o	Reference pressure [N/m^2]
p_{tot}	Total pressure [N/m^2]
ρ	Density [kg/m^3]
r	Nozzle radius [m]
S_ε	Turbulence dissipation rate source
S_K	Turbulent kinetic energy source
S_m	Mass source
S_{mom}	Momentum source
$\overline{\overline{\tau}}$	Reynolds stress term
τ_ω	Shear force induced at the wall [N/m^2]
$u_{casting}$	Casting speed [m/s]
u_i	Fluid velocity in the *i*-direction [m/s]
u_{ref}	Free-stream nozzle reference speed [m/s]
μ	Dynamic fluid viscosity [Pa-s]

μ_{eff}	Turbulence-adjusted effective fluid viscosity [Pa-s]
μ_o	Laminar fluid viscosity [Pa-s]
μ_t	Turbulent flow component of fluid viscosity [Pa-s]
x_i	Units in the *i*-direction [m]
x_{char}	Characteristic length (chosen to be nozzle radius) [m]
y^*	Unitless wall unit
y_o^*	Transition point from laminar to turbulent flow near the wall [~ 11.225]
y_p	Distance from point *p* to the wall [m]

Chapter 3 Nomenclature: Nailboard Method

$\Delta Height$	Surface height deformation via pressure approximation [m]
Δh_{knob}	Knob height difference [m]
α	Empirical constant [≈ 0.005 for low-shear flow]
B	Buoyancy term [N]
b	Body force term [N]
β_c	Volumetric expansion coefficient associated with the concentration variations [Δm^3/ Molarity]
β_T	Coefficient of volumetric expansion associated with temperature variations [$\Delta m^3/\Delta K$]
C	Constant (Bernoulli Equation)
C_f	Force coefficient (Morison Equation) [= 6 for this study]
C_m	Inertia coefficient [= 1 + k]
C_x	Stiffness matrix incorporating effects of pressure gradients on variable *x* (used in Galerkin FEM logic)
C_x^T	Stiffness matrix incorporating effects of velocity divergence on variable *x* (used in Galerkin FEM logic)
c	Species concentration [Molarity]
c_1	Empirical constants (used in turbulence modeling) [= 1.44]
c_2	Empirical constants (used in turbulence modeling) [= 1.92]
c_3	Empirical constants (used in turbulence modeling) [= 0.09]
c_μ	Empirical constant (relating viscosity to turbulence) [= 0.09]
D	Diameter of immersed cylinder [m]
δ	Distance from the wall (used in wall-law modeling) [m]
δ_{ij}	Kronecker delta [0,1]
ε_{ijk}	Total strain in all directions (of 3-D model) at the surface [m]
E	Empirical constant (depending on wall roughness) [≈ 9.0 for smooth walls]
F	Field in the VOF method
F_{max}	Maximum force exerted on cylinder by fluid (Morison Equation) [N]
f_x	Vectors representing gradient boundary conditions and source/sink terms (used in Galerkin FEM logic)
G	Generation of shear stress
g	Gravitational acceleration [m/s^2]
λ_s	Surface relaxation factor
H	Mean Gaussian curvature of the surface [m]
H_o	Initial wave height (Morison Equation) [m]
H_o'	Unrefracted wave height (Morison Equation) [m]
h	Height (Bernoulli Equation) [m]

$h_{run\text{-}up}$	Run-up along the leading edge of submerged cylinder [m]
K_x	Stiffness matrix incorporating effects of advection and diffusion on variable x (used in Galerkin logic)
k	Ratio of wave crest elevation above still height to the wave height [= 0.78 for this study]
k_s	Solidification constant
κ	Dimensionless parameter (Sloshing in a tank)
κ_o	von Karman constant [≈ 0.41]
κ_m	Mean Gaussian surface curvature (= $1/2R_i$)
L	Depth of nail immersion (Morison Equation) [m]
$n(t)$	Free surface elevation at time t (Sloshing in a tank) [m]
n_o	Initial free surface elevation (Sloshing in a tank) [m]
n^*	Normal vector to the free-surface
n_i	Normal vector in the i-direction [m]
σ_i	Stress in the i-direction
σ_i^x	Stress in the i-direction just away from the surface in fluid x [m/s]
σ_{ij}	Stress tensor across the ij-plane
σ_ε	Prandtl-Schmidt number for dissipation energy [= 1.30]
σ_t	Turbulent Prandtl number
σ_K	Prandtl-Schmidt number for kinetic energy [= 1.00]
ρ	Density (= kg/m^3)
p	Fluid pressure [N/m^2]
p_{air}	Atmospheric pressure above external free surface [N/m^2]
p_{ferro}	Ferrostatic pressure [N/m^2]
$\overline{p_i}$	Averaged pressure component in i-direction [N/m^2]
p_o	Reference fluid pressure [N/m^2]
p_s	Pressure induced upon a surface [N/m^2]
p_{tot}	Total pressure [N/m^2]
R	Radius of curvature at the free surface [m]
R_μ	Ratio between turbulent and laminar viscosity [≈ 10 for low-turbulence flow]
S	Vector incorporating surface parameters (used in Galerkin FEM logic)
S_t	Turbulent Schmidt number
s_{ij}	Strain rate tensor
T	Temperature [k]
t^*	Tangential vector at the free surface
t	Time [s]
t_s	Timestep (Morison Equation) [= 0.030 s for this study]

τ	Stress tensor at free surface
τ_{ij}	Deviatoric stress tensor across the *ij*-plane
τ_w	Stress tensor at wall surface
u^+	Characteristic non-dimensionalized velocity near the wall
$\overline{u_i}$	Average velocity in *i*-direction [m/s]
$\overline{u^{/}_{i,j}}$	Time-averaged velocity in *i*-direction differentiated in the j-direction [m/s^2]
$u_{interface}$	Velocity at the free-surface [m/s]
$\overline{u^x_j}$	Averaged velocity in the *j*-direction just away from the surface in fluid *x* [m/s]
u_N	Normal velocity [m/s]
u_T	Tangential velocity [m/s]
μ_{eff}	Turbulence-adjusted effective fluid viscosity [Pa-s]
μ_o	Laminar fluid viscosity [Pa-s]
μ_t	Turbulent flow component of fluid viscosity [Pa-s]
U	Vector of unknowns containing all variables at discretized points (used in Galerkin logic)
u_w	Velocity along the wall surface [m/s]
V	Fluid velocity (Bernoulli Equation) [m/s]
x_i	Units in the *i*-direction [m]
x_3	Height in the 3rd direction (*z*-direction) [m]
y^+	Characteristic non-dimensionalized distance from the wall
γ	Surface tension [N/m^2]

Chapter 4 Nomenclature: Ingot Cleanliness Investigation

d_p	Inclusion Diameter [m]
n_{2D}	Number of inclusions per mm^2 steel surface area
n_{3D}	Number of inclusions per mm^3 steel volume

UNITLESS TRANSFORMATIONS

V	Fluid velocity [m/s]
ρ	Density [kg/m^3]
H	Fluid height [m]
Δp_c	Characteristic pressure difference [N/m^2]
μ	Fluid viscosity [Pa-s]
ν	Fluid kinematic viscosity [m^2/s]
v_c	Characteristic velocity [m/s]
L_c	Characteristic length [m]

Position:

$$x_i^* = \frac{x_i}{H} \qquad H\partial x_i^* = \partial x_i$$

Velocity:

$$\overline{u^*} = \frac{\overline{u}}{V} \qquad V\partial\overline{u^*} = \partial\overline{u}$$

Pressure:

$$\overline{p^*} = \frac{\overline{p} - p_{ref}}{\Delta p_c} \qquad \Delta p_c \partial\overline{p^*} = \partial\overline{p}$$

Shear Stress:

$$\tau^* = \frac{\tau}{\mu V / H} \qquad \left(\frac{\mu V}{H}\right)\partial\tau^* = \partial\tau$$

Curvature:

$$R_i^* = \frac{R_i}{H} \qquad H\partial R_i^* = \partial R_i$$

CHAPTER 1: INTRODUCTION

Continuous Casting Background

The continuous casting industry is one of the largest industries in the world, producing over 500 million tons of steel, 20 million tons of aluminum, and 1 million tons of copper, nickel and other metals every year. In fact, the continuous casting process is used to produce over 90% of steel in the world today[1)]. Figure 1.1 provides a visual representation of the entire continuous casting process.

Once the proper steel grade is reached, the continuous casting process begins by pouring molten steel into the tundish via ladle. The tundish serves to provide a buffer area such that molten steel continuously flows into the mold, preventing stoppage of molten steel flow between ladles. Many detrimental impurities are removed from the liquid pool when inert gas is bubbled through the steel in the tundish. A submerged entry nozzle (SEN) deposits the molten steel into the mold from the tundish, typically through bifurcated ports. The cold walls of the mold solidify the steel near it, essentially creating a “bottomless” vessel containing molten steel. Oscillations of the mold coupled with mold slag (acting as a lubricant) prevent sticking of the solidified shell with the mold itself. Refer to Figure 1.2 for a close-up schematic of the upper mold and tundish region, including the critical meniscus area (corner region where the mold meets the top liquid steel surface). With the steel shell thickness large enough to support the weight of the inner liquid pool, it is continuously withdrawn from the mold by drive rolls at a prescribed casting speed (dictated by the mass flow rate through the nozzle). Outside of the mold, support rolls retain the desired shape of the steel slab as the inner layers harden. Spray cooling continues to remove heat from the strand, and once the slab becomes fully solidified, a torch cuts the continuous strand into desired lengths.

Continuous Caster Mold/Nozzle Design

Developing an acceptable caster requires optimizing component design specifically to be operated under a prescribed range of conditions. Nozzle port design is critical to ensuring that a constant, predictable stream of superheated steel enters the mold. Most nozzle designs are tailored to specific mold design to ensure that the flow patterns cater to inclusion removal and allow for correct levels of heat transfer to ensure regular shell formation. Steelmaking using incompatible nozzles and molds or operating under extreme conditions increases the likelihood of experiencing casting problems. For example, with excessive nozzle exit velocity or with elevated levels of superheat, thinning of the mold wall near jet impingement may promote breakouts or other detrimental failures[2].

Fluid profiles and velocities within the liquid steel region have direct correlation to serious defects in the final steel product[3]. With increased flow velocities, the upward velocity along the narrowface (corresponding to the upper roll of the internal double-roll steel flow pattern) can result in large standing waves on the top surface. Large disturbances, including standing waves, can prevent slag flux from providing adequate lubrication between the solidified shell and the oscillating mold wall. Even slight variation in slag coverage may result in large thermal gradients (due to irregular cooling) and increased mold friction, yielding breakouts and/or crack propagation[4].

Simulating Mold Flow via Water Models

Improved characterization of the inter-mold flow gives insight into the origin of defects and into the continuous casting process as a whole. Understanding and predicting flow patterns is critical to minimizing undesired circumstances from occurring (inclusion entrapment, breakouts, etc…). However, with so many factors needed to build a complete continuous casting model, mathematical models typically become prohibitively complicated. Parameters such as mold dimensions, gas injection rates, casting speed, and steel composition all can have large influences on final product quality, causing numerical methods to require lengthy simulations and intricate domains to incorporate all phenomena. An alternate method was desired to study fluid flow through a continuous caster; this was solved with the inception of water models.

The testing standard for many innovative caster designs is to perform water model tests in which full-scale transparent molds are produced. Because water has a similar Reynolds number to molten steel, observing the flow of water through transparent walls allows observation of flow patterns without having to endure the harsh environment of an actual caster. Some more elaborate water models even incorporate curvature in the mold walls to simulate shell thickness[2]. However, water models fail mainly because they cannot simulate the mass and momentum loss of steel solidifying to create the shell region. For large-slab casters this may not be a significant problem, however for thin-slab casters (including funnel molds) in which the shell occupies significant percentage of slab cross-section at mold exit, the water model artificially accelerates flow out of the mold. Internal flow patterns (including top surface velocities) are subsequently quite different within the water model than the actual steel caster. One purpose of this study is to simulate funnel-mold flow patterns incorporating mass and momentum losses at the curved shell wall. The results will be compared to a mathematical recreation of a water model to determine their validity in estimating caster flow. Additionally, by incrementing the casting speed in the funnel mold model, variations of flow patterns/velocities of critical areas within the mold can be quantified. Future work will be required to research the effect of other parameters and phenomenon (such as nozzle submersion depth, alternate mold designs, different steel grades, etc…) not discussed in this work.

Simulating Mold Flow via Mathematical Models

Certain assumptions must be made when transforming the real life processes into mathematical models. Assigning boundary conditions, grid refinement levels, and turbulence models are all factors which greatly impact the modeling of fluid flow. Creech *et. al.* has shown that the implementation of wall laws using the standard *K-ε* turbulence theory to model molten steel flow in a 3-D caster yields accurate flow patterns, even at relatively low levels of mesh refinement[5)].

Determining Steel Velocity at the Mold Top Surface

Excessive fluid velocities at the top surface encourage inclusions to become entrapped within the solidified slab. Liquid slag globules may be sheared off and emulsified in the liquid steel pool with sufficiently high velocities[2)]. Previously entrained particles may not have enough time to be captured by the slag layer and removed from the liquid pool. The presence of inclusions in the final product results in many unwanted consequences, such as lower product yield and decreased material properties.

It is desired that the flow velocity be characterized at the liquid top surface, as the velocities found in this region are strong predictors of the internal flow pattern. By knowing the speed of liquid steel past the slag layer in the mold, adjustments can actively be made in the casting process if the velocities were less than ideal. A method for determining molten steel (in particular, the meniscus level) velocity will be examined in this project.

Experimental Inclusion Analysis via Ingot Dissection

While mathematical models allow for prediction of inclusion travel, they rarely can indicate where the particles originated from. Physical examination of cast steel, including sectioning of the ingot, will help to serve two purposes. First, areas of lower quality (characterized by excessive levels of inclusion concentration) within the ingot can be identified. Second, elemental composition analysis of entrapped particles will entertain ideas as to their source. By discovering the likely originations of the most prevalent inclusions, recommendations can be made to the casting process to reduce the occurrence of these detrimental impurities. Additionally, plotting inclusion distribution within the ingot allows for comparison between mathematically predicted inclusion deposition location to actual data. Active comparison such as this allows for models to be either validated or discredited.

Investigations of this Thesis

Through mathematical models and experimental investigation, a greater understanding of casting processes can be gained. This thesis is subdivided into three main components with the central intent of improving steel cleanliness:

- Model turbulent, steady-state flow inside a funnel caster mold and nozzle. Through quantification of the flow patterns and velocities inside the mold, comparisons can be drawn between the actual steel mold and its water model approximation. Using mass and momentum loss subroutines at the solidifying wall front allows more accurate flow pattern to be established as compared to previous models which treat these losses as trivial. By performing a parametric study incrementing the casting speeds and boundary conditions, characterization will be drawn between critical fluid velocities/pressures and actual casting conditions.

- Develop a mathematical model to simulate the Nailboard Method, which estimates liquid steel velocity at the top surface of the mold. Model considerations include 3-D, turbulent, multi-liquid (incorporating both steel and slag layers), and free-surface phenomena. Relations between knob profiles will be quantified by incrementing nail diameter and flow velocity. A rigorous testing procedure for implementing this technique in practice will be also outlined.

- Investigate ingot-cast steel samples to characterize location and frequency of inclusion entrapment. Morphology analysis using 2-D microscopic analysis and 3-D Scanning Electron Microscopy (SEM) methods will assist in classifying the inclusions. Electron Dispersive X-ray Spectroscopy (EDS) methods will reveal inclusion composition, allowing for predictions to be made as to their origin.

By using the models and results covered in this work, a step forward will be taken towards the production of cleaner steel. Discovering flow patterns in funnel-mold casters and how they relate to product quality allows for optimal casting conditions to be quantified, thereby minimizing defects. Creating a method for casting operators to effectively and easily measure realtime top surface velocity allows for better product control. Examination of particle entrapment frequency and composition within ingots leads to identification of areas with lowered product quality as well as identifying casting methods and materials which would improve overall ingot cleanliness. These modeling techniques utilized may serve as a basis for future numerical models of the casting process, and experimental procedures outlined may be used in practice to directly affect casters and their methods.

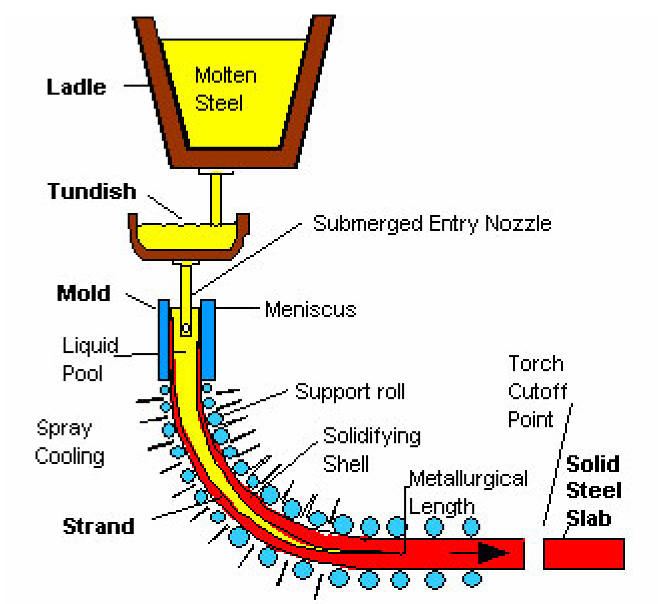

Figure 1.1: Schematic of the complete continuous casting process[1)]

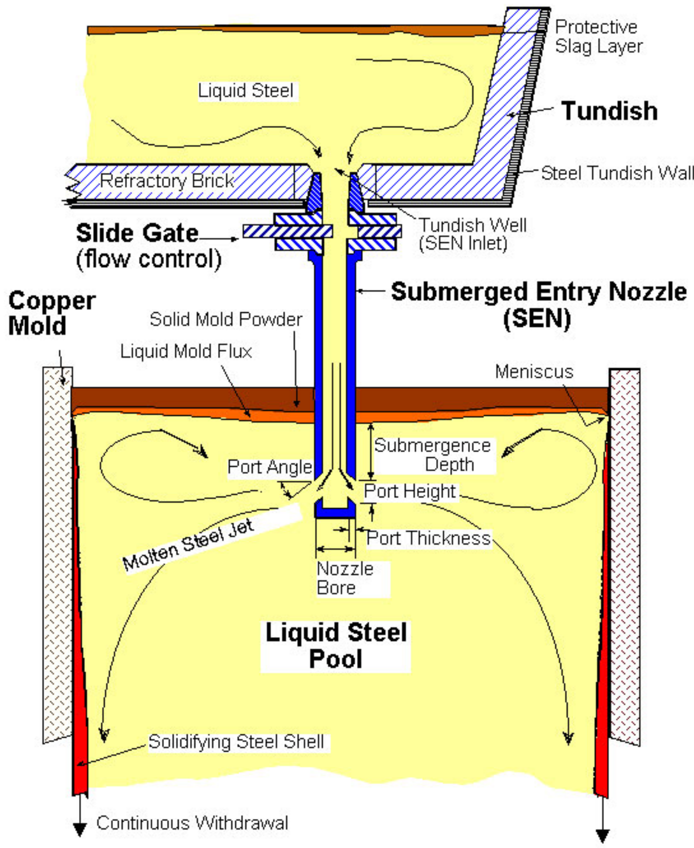

Figure 1.2: Close-up of upper mold and tundish region, showing the meniscus[1)]

CHAPTER 2: FUNNEL MOLD FLOW STUDY

2.1 Introduction

A largely unexplored realm of the continuous casting process involves the study of funnel-mold casters. Funnel molds have recently marked an important trend in the steel industry of casting using near-net-shape molds. By producing steel with slab dimensions more closely resembling the final product, cost and production time have been vastly lowered[6-9]. The goal of the funnel mold design is to use near-net-shape casting principles by producing the thinnest slab possible. In cases of the slabs being machined into rolls, the thinner the slab is, the less deformation flattening processes must be performed to attain the desired sheet thickness. Funnel mold casters typically yield slab widths of 50-100 mm while withdrawing the slab at a rate of 4-6 m/min.

The limiting factor as to how narrow the mold can be made is a product of the nozzle thickness. Proper continuous casting requires the nozzle outlet to be submerged into the liquid steel pool, but when attempting to cast extremely thin slabs, inserting the SEN likely will contact the mold walls. Therefore, a new design was created which incorporates a funnel-like section cut out of the mold, creating room to accommodate the SEN. A schematic of a funnel mold is shown in Figure 2.1. Note that at mold exit, the wide-face walls are nearly flat; the funnel portion of the slab undergoes physical deformation to achieve the proper slab dimensions prior to leaving the mold.

With funnel molds, additional sources for defects are introduced over conventional molds casters. Steel can be produced at a much higher rate in a thin slab caster due to the large reduction in cross-sectional area at mold exit; however, higher casting speeds make the process more vulnerable to break-outs and other shell defects. Compounding shell-related issues is the physical deformation (due to mechanical force) imposed on the shell as it exits the funnel portion of the mold. Also, with a smaller strand volume, small amounts of turbulence in the liquid pool are more likely to propagate throughout the mold and yield increased levels of defects, whether it be from attenuation of surface disturbances, meniscus instability, or altered thermal transfer profiles[10].

With increased dependence on flow patterns and thermal profiles, funnel molds absolutely require the use of compatible nozzle and mold designs when casting. Cramb and Szekeres have justified the importance of fabricating appropriate nozzles/molds combinations and maintaining suitable operating conditions to maximize production and minimize defects[8)]. Unfortunately, little research has been done to quantify flow in funnel molds despite recognizing the need for predicting and understanding intra-mold flow patterns.

For this study, an actual funnel mold and its associated SEN currently employed by Algoma Steel Co. will be modeled. By performing a case study of a production caster, mathematical models and the information deduced from them can be directly correlated to a real-world process. Graciously, Algoma provided blueprints including all relative dimensions for the two domains which will be used as a basis for the creation of the mathematical model. Furthermore, casting parameters including complete composition of the steel have been made available, ensuring the mathematical model will closely mirror the representative casting process.

2.2 Literature Review

2.2.1 Funnel Mold

Due to the relative dimensional complexity and newness of funnel molds, there is a deficiency of published information regarding flow in this type of caster. The majority of previous research employed water model interpretations to generate results. Honeylands *et. al.* created a water model and compared physical simulations to numerical simulations using commercially available fluid flow software[11)]. While good agreement between the two was reached, their simulation consisted of a simple thin parallel-walled mold and cannot be applied to complex geometries such as funnel molds. What can be taken from their work is the notion that mathematical fluid flow models are able to accurately mimic real thin-slab casting processes.

Nam *et. al.* developed a numerical finite volume model for simulating funnel-mold flow, heat transfer, and shell solidification[12)]. Through examination of breakout shells, good agreement was reached between the numerical model and plant observation. While flow patterns inside the mold were quantified, model emphasis was not entirely placed on flow characteristics. Whereas

Nam's model allows for topical discussion of in-mold flow, it is not sufficient to fully quantify the liquid steel flow properties. One key area neglected from his research involves top surface flow past the slag layer, a vital factor in minimizing inclusions and defects.

One major drawback of most continuous casting models (both water and mathematical models) is the neglect of mass/momentum loss at the solidifying shell. In one of the few models to actually consider solidification effects, Yuan incorporated a porous wall boundary condition in his treatment of shell mass loss[13)]. By quantifying tangential and normal angles at the shell boundary, Yuan was able to calculate the mass loss at the solidification front. Simple calculations using this mass loss allowed him to define normal velocities at the shell wall, essentially removing mass from the liquid pool. However, this approach does not directly include momentum loss through the wall, and thus is not completely accurate.

A unique model incorporating mass/momentum loss methodology at shell walls was developed by Creech[14)]. In his work, Creech compared different boundary conditions at the wall and investigated their effect on fluid flow within the mold. While results showed that fluid flow profiles are greatly affected by the losses associated with shell solidification, his model neglected the downward movement of the shell as it is drawn out of the mold (a physically incorrect zero velocity boundary condition was imposed on the shell wall). While his solidification loss model will serve as a basis for this work, incorporating the translational movement of the shell may prove to be an important aspect of the actual process.

2.2.2 Water Models

Water models are used extensively to visualize flow through continuous casting, due to the similar fluid properties of steel and water[13,15-18)]. With kinematic viscosities only ~20% different, water and liquid steel develop relatively similar flow patterns for complex geometries. By constructing a mold, tundish, and nozzle out of clear plastic, water flowing through the mock caster can be followed through visualization techniques of fluid patterns. Outlet ports on the bottom of the mold allow for the water to recirculate back into the tundish, through the nozzle, and subsequently into the mold. Occasionally, the water model mold boundaries are tapered to simulate the solidification front of the steel shell[2].

Due to the simplistic construction and excellent visualization of flow patterns in water models, they are frequently used to validate mathematical models. In cases which require quantification of flow inside the harsh conditions of an actual steel caster, water models offer a valuable alternative to confirm model validity. Thomas *et. al.* produced a full-scale water model to simulate flow through a continuous thin-slab stainless steel caster[19]. By superimposing mathematical model velocity vector data on water model dye-injected flow pattern photos, the water model was shown to qualitatively predict nearly identical flow patterns as the mathematical model.

Gupta *et. al.* developed water models to investigate the asymmetry and transient oscillations of fluid flow inside the mold[17]. Using dye injection, he was able to quantify flow asymmetries within the water model simulation. Through additional work, Gupta performed a parametric study to investigate flow asymmetries in the mold, varying the mold dimensions, casting speed, nozzle submersion and nozzle type[20]. It was concluded that the fixed bottom wall of his water model appeared to affect flow in the lower mold region by suppressing the asymmetries.

2.3 Model Formulation

Numerical models will be used to solve governing equations and to accurately develop fluid flow profiles within the liquid steel region. The SEN domain considered will be the entire nozzle (omitting the stopper rod), while the mold domain extends from the top fluid level to 3.5 m below the top surface. Due to the importance of SEN and mold design in minimizing casting problems, the exact geometry of a funnel-mold and its associated nozzle will be considered without simplification. An in-house 1-D shell thickness program was used to obtain accurate shell dimensions throughout the domain.

The physics of SEN flow will be solved separately from the mold, using nozzle outputs to define inlet boundary conditions for the mold simulation. This method of separating the two domains yields faster convergence while allowing the mesh design to be more flexible. All boundary conditions for both the SEN and mold runs are exactly specified and special treatment of the solidifying shell boundary conditions are given (which incorporate mass/momentum losses).

2.3.1 Governing Equations

Due to complex geometries, direct numerical simulation of the complete transient turbulent Navier-Stokes (NS) fluid flow equations is not possible; an approximate modeling methodology is needed. By transforming the time-dependent NS equations, the Reynolds-averaged Navier-Stokes (RANS) allows for turbulent flow to be accurately predicted without directly simulating the small-scale turbulent fluctuations (thereby allowing coarse meshes to capture turbulent behavior). The use of averaged flow parameters significantly reduces the computational effort required to solve the RANS equations; the time derivatives in the original steady-flow NS equations are eliminated. Refer to the Nomenclature section for a complete description of all the symbols used in the following equations.

The time-averaged RANS mass conservation (continuity) governing equation is defined as:

$$\frac{\partial}{\partial x_i}(\rho u_i) = S_m \tag{2.1}$$

where the velocity term u_i is extended to fluid flow in all directions (i = 1,2,3 for a 3-D domain), and S_m represents a mass creation/destruction term. Using mass sinks to simulate shell solidification makes this term non-trivial to ensure model continuity. The time-averaged RANS momentum transport term is:

$$\frac{\partial}{\partial x_j}(\rho u_i u_j) = -\frac{\partial p}{\partial x_i} + \frac{\partial}{\partial x_j}(\bar{\bar{\tau}}) + \frac{\partial}{\partial x_j}\left(-\rho\overline{u_i u_j}\right) + \rho\vec{g} + S_{mom} \tag{2.2}$$

The momentum source term (S_{mom}) will be used in the creation of “sinks” near the liquid pool boundaries to simulate momentum loss due to solidification. The additional term introduced into the momentum conservation equation ($-\rho\overline{u_i u_j}$) represents the effect of turbulence and is known as the Reynolds stress term, defined by:

$$\overline{\overline{\tau}} = \mu_{eff}\left[\frac{\partial u_i}{\partial x_j} + \frac{\partial u_j}{\partial x_i} - \frac{2}{3}\delta_{ij}\frac{\partial u_i}{\partial x_i}I\right] \tag{2.3}$$

where I represents the unit tensor, and the term incorporating δ_{ij} represents the effect of volume dilation.

Equations 2.1 and 2.2 represent pressure differences due to flow parameters, and does not include the effect of ferrostatic pressure. Because the model includes gravity as a body-force, the pressure for the Equations 2.1 and 2.2 will be calculated via:

$$p = p_{tot} - p_{ferro} = p_{tot} - \rho g h \tag{2.4}$$

Including the effect of turbulence, the effective viscosity is calculated using:

$$\mu_{eff} = \mu_o + \mu_t \tag{2.5}$$

where μ_o is simply the laminar molecular viscosity and μ_t is a the turbulent viscosity term (as discussed in the following section).

2.3.2 *K-ε* Turbulence Model

By artificially increasing the viscosity of a turbulent fluid, it is possible to use a coarser mesh to accurately predict fluid flow profiles. This increased viscosity limits the mesh to only capture relatively large-scale turbulent eddies and neglect eddies that are smaller than mesh elements. Without a turbulence model, the mesh must be sufficiently fine to capture all flow eddies and accurately solve for flow profiles (requiring prohibitively high computational cost and an unnecessarily complicated mesh structure). The turbulence scheme employed in this model is the *K-ε* turbulence model.

Based on a semi-empirical formulation, the standard *K-ε* turbulence model uses model transport equations to solve for the turbulent kinetic energy (K) and its dissipation rate (ε). The following two transport equations are used to solve for K and ε (neglecting buoyancy and compressibility effects):

$$\frac{\partial}{\partial x_i}(\rho K u_i) = \frac{\partial}{\partial x_j}\left[\left(\mu + \frac{\mu_t}{\sigma_K}\right)\frac{\partial K}{\partial x_j}\right] + G_K - \rho\varepsilon + S_K \tag{2.6}$$

$$\frac{\partial}{\partial x_i}(\rho \varepsilon u_i) = \frac{\partial}{\partial x_j}\left[\left(\mu + \frac{\mu_t}{\sigma_\varepsilon}\right)\frac{\partial \varepsilon}{\partial x_j}\right] + C_{1\varepsilon}\frac{\varepsilon}{K}G_k - C_{2\varepsilon}\rho\frac{\varepsilon^2}{K} + S_\varepsilon \tag{2.7}$$

where S_k and S_ε are source terms. The generation of turbulent kinetic energy due to the mean velocity gradients (G_K) is defined by:

$$G_K = -\rho\overline{u_i'u'}_j \frac{\partial u_j}{\partial x_i} \tag{2.8}$$

Knowing the kinetic and dissipation rates, the turbulent viscosity for the fluid can be solved through:

$$\mu_t = \rho C_\mu \frac{K^2}{\varepsilon} \tag{2.9}$$

From experimental tests, the model constants C_{1x}, C_{2x}, C_μ, σ_K, and σ_τ for fundamental turbulent shear flows have been empirically determined to be[21)]:

$$C_{1\varepsilon} = 1.44, \qquad C_{2\varepsilon} = 1.92, \qquad C_\mu = 0.09, \qquad \sigma_K = 1.0, \qquad \sigma_\varepsilon = 1.3 \tag{2.10}$$

2.3.3 Boundary Conditions

In order to fully define the computational domain, special conditions must be assigned at each location on the domain boundary. Each boundary condition employed in the model is defined as follows:

2.3.3.1 Wall Boundary Conditions at Shell Interface and Nozzle Walls

For turbulent flow, areas of high velocity gradients (specifically near no-slip walls) require implementation of additional conditions in defining flow parameters. The turbulent viscosity theory breaks down in these regions due to the predominance of laminar flow in the finite grid boundary layer near a wall. With a highly refined grid near these walls, standard laminar flow models may approach reality. However, in order to utilize a coarser grid and still obtain reasonable results, special equations will be used to describe turbulent flow past a no-slip wall.

A non-dimensionalized distance from the wall will be used, y^* (known as the "wall unit") in the formulation of the mean velocity profile adopted from Launder and Spalding[21]. The wall unit is defined by:

$$y^* = \frac{\rho C_\mu^{1/4} k_P^{1/2} y_P}{\mu} \tag{2.11}$$

Using this wall unit, tangential velocity at a specified normal distance away from the wall can be calculated using:

$$u_P = \begin{cases} \dfrac{\tau_\varpi}{\rho C_\mu^{1/4} k_P^{1/2}} y^* = \dfrac{\tau_\varpi y_P}{\mu} & y^* \le y_o^* \\ \dfrac{\tau_\varpi}{\rho C_\mu^{1/4} k_P^{1/2}} \dfrac{1}{\kappa} \ln\left(E y^*\right) & y^* > y_o^* \end{cases} \tag{2.12}$$

where y_o^* represents the interface between the laminar stress-strain region close to the wall and the logarithmic velocity profile extending past the laminar zone. By setting y_o^* to 11.225, good agreement to experimental near-wall velocity profiles has been established[21,22].

At the wall surface, the boundary condition for the kinetic energy (K) imposed is zero gradient normal to the wall, represented by:

$$\frac{\partial K}{\partial n} = 0 \tag{2.13}$$

Equations 2.6 and 2.7 are used to calculate K and ε in elements away from the wall, however the wall adjacent elements require special treatment for these two parameters. Under the local equilibrium hypothesis, the production of K and corresponding dissipation rate ε are assumed to be equal in these elements. Using this idea, K and ε are computed through (with the subscript p representing a point near the wall)[22]:

$$G_K \approx \tau_\varpi \frac{\tau_\varpi}{\kappa\rho C_\mu^{1/4} K_P^{1/2} y_P} \tag{2.14}$$

$$\varepsilon_P = \tau_\varpi \frac{C_\mu^{3/4} k_P^{3/2}}{\kappa y_P} \tag{2.15}$$

By implementing these wall laws, all parameters of turbulent flow have been explicitly identified. These equations make it possible to capture the laminar flow region close to the wall to a relatively high degree of accuracy without requiring an unnecessarily refined mesh. Wall laws were imposed in the created model at the shell boundaries, SEN walls, and liquid pool top surface.

2.3.3.2 Top Surface Boundary Condition

While it is an unconstrained free surface in the real caster, excessive complexity forces the top surface to be treated as a flat, stationary boundary with zero velocity. McDavid has shown that the top surface shear stress the liquid steel from the slag layer is very large[23)]. High velocity gradients past this boundary dictate the use of wall laws to define flow near the top surface.

2.3.3.3 Nozzle Inlet Boundary Condition

In further attempt to minimize unnecessary complexity, the axisymmetric stopper region at the top of the nozzle was omitted. Rather, it was assumed that fully developed flow has been established prior to entering the SEN domain. Normal flow was specified using the standard flow-in-a-pipe routine with tangential velocities set to zero. Because the nozzle inlet is far from the outlet ports, assigning this inlet velocity boundary condition should have little impact on the downstream profile. The equations defining normal flow-in-a-pipe are as follows:

Using the mass flow rate of the solid slab exiting the caster, the nozzle free stream value (as if the SEN walls imposed no stress upon the fluid) can be calculated via:

$$u_{ref} = \frac{\rho_{steel,solid}}{\rho_{steel,liquid}} * \frac{A_{slab}}{A_{nozzle}} * u_{casting} \tag{2.16}$$

However, the flow in the center of the nozzle must be accelerated to maintain a constant mass flow rate (stemming from the zero-velocity boundary constraint at the nozzle boundaries). The maximum nozzle velocity (found in its center) can be solved using:

$$u_{\max} = \frac{(1+n)*(1+2n)}{2n^2} * u_{ref} \tag{2.17}$$

where the empirical constant n for the low turbulence flow-in-a-pipe simulation is solved via:

$$n = 2.81 * \left(\frac{u_{ref} * \rho * x_{char}}{\mu} \right)^{0.084} \tag{2.18}$$

x_{char} is specified to be the nozzle diameter. Finally, the normal velocity profile for an arbitrary point k on the inlet boundary can be solved using:

$$u_k\left(x_i x_j\right) = x_{\max} * \left(1 - \frac{\left(x_i + x_j\right)^{1/2}}{r} \right)^{1/n} \tag{2.19}$$

The implementation of this subroutine is shown in Appendix D.1.1. Again, all tangential velocities at the nozzle inlet were specified to zero. This flow-in-a-pipe approximation assumes that laminar (or nearly laminar) flow is developed at the inlet. Thus, to maintain consistency between flow velocities and turbulence, the inlet values for K and ε were specified to be very small ($10e^{-6}$ m^2/s^2 and $10e^{-6}$ m^2/s^3). By choosing these small values, the effect of turbulence at the inlet is minimized and thus fully-developed laminar flow is approximated. This allows for no outer disturbances to enter the system, isolating nozzle geometry effects in developing flow through the domain.

2.3.3.4 Mold Inlet Boundary Condition

By creating two separate domains (one for the nozzle, another for the mold), the nozzle outlet parameters must correspond with the mold inlet parameters. This is achieved by first obtaining the steady-state solution for the nozzle, then importing the velocity, turbulent kinetic energy, and dissipation profiles at the corresponding location of the mold domain. Interpolation at locations between nodes generated a continuous flow profile, allowing different grid spacing to be used at the nozzle outlet and the mold inlet.

2.3.3.5 Nozzle/Mold Outlet Boundary Conditions

Through previous work from Bai *et. al.*, specifying pressure values rather than mass flow rates allows for more accurate, less constrained flow profiles at outlet boundaries[24]. Constant pressure boundaries allows the flow to remain unconfined, thereby allowing recirculation zones to extend past the boundary (with flow both into and out of the same boundary; especially important in nozzle simulations). For these reasons, the pressure was set to zero (which is an arbitrary value) for both the nozzle and the mold outlet boundaries. The assignment of pressure value at the domain outlet also creates a pressure reference for the entire domain. Similar to the inlet boundaries, the kinetic and dissipation energy terms were specified to be very small values ($= 10 \times 10^{-6}$). Previous work from Zhang suggests better convergence and increased accuracy are achieved when turbulence is minimized at the outlets[25]. All other variables maintain a zero gradient condition across outlet boundaries.

2.3.3.6 Symmetry Boundary Conditions

At all symmetry boundaries in the domain, the normal velocity is specified to be zero. Furthermore, all gradients at these boundaries are assigned a value of zero to maintain continuity across the symmetrical faces. Because a long-term averaged flow simulation is being performed, the symmetric assumption in this model is valid. Had a transient simulation been performed, symmetry boundaries could not be used; they cannot capture asymmetries associated with short-term disturbances.

2.3.3.7 Mass and Momentum Sink Terms at Shell Front Boundaries

In the continuous casting process, the steel solidifies near the mold due to the local removal of heat via mold cooling. This solidified shell holds the liquid pool inside the slab once removed from the confines of the mold. In most conventional mold cases, the amount of steel that solidifies at mold exit is small compared to the amount of steel in the liquid pool; the presence of a shell has only a small effect on the flow patterns and velocities inside the liquid region. However, the amount of volume that the shell region occupies in a slab drawn from a thin-slab caster is non-negligible. Moreover, the mass/momentum loss from the liquid pool into the solidification front is significant (which will be proved in subsequent sections). These reasons justified the placement of special mass and momentum sink elements at the shell boundaries in the created model.

Consider a small region near the shell wall inside the mold. From a Lagrangian point-of-view, the shell thickness grows as it is being withdrawn from the mold. Alternatively, a Eularian reference frame focuses on a stationary location in the domain in which the shell thickness and curvature remain constant over time. Eularian principles were deemed most appropriate for this model.

In effort to maintain a local mass balance, the amount of mass drawn from each stationary boundary cell due to shell withdrawal must equal the amount of mass passing through the solidification face. Once the normal velocity is solved, momentum loss can calculated simply as a function of steel density and this velocity through the solidification face.

In the model, shell walls are treated as solid boundaries and solidification effects are incorporated through the placement of thin sink elements (0.1 mm thick) directly adjacent to the solid wall. Choosing the smallest possible thickness (which allows for solution convergence) ensures that the effect of the sink elements in affecting inner liquid pool flow patterns is minimized. Because the thickness of the shell at every distance from the top surface is known (predicted through CON1D), shell curvature can be used to estimate the amount of mass to remove from the system. The effect of solidification is simulated through sinks by extracting mass and momentum from the liquid pool without using heat transfer/solidification equations. A detailed record of the mass and momentum sink term calculations is outlined in Appendix A.

2.3.4 Solution Procedure

It may be appropriate to label this project as a case-study of an existing funnel mold and its associated nozzle. Algoma Steel Co. supplied blueprint and casting condition data, while solution techniques mirrored previous Continuous Casting Consortium methods for investigating mold/nozzle fluid flow problems. The novel aspect of this project involves the mass/momentum loss associated with the solidifying boundary and the extremely complex geometry associated with a funnel mold and solidification fronts.

2.3.4.1 Software Methodology and Usage

Utilizing the steel grade and casting conditions supplied by Algoma, the shell thickness as a function of distance from the top of the mold was supplied by the in-house code CON1D, as seen in Figure 2.2. Developed by Thomas *et. al.*, CON1D has been validated as an accurate shell thickness predictor through comparison with break-out shell samples[26)]. Shell thickness data was added to the mold dimensions to define the liquid boundary domain.

A completely structured numerical grid was created for both the nozzle and mold complex domain geometries using the commercial software Gambit by Fluent, Inc. By outputting the mesh the Computational Fluid Dynamics (CFD) solver Fluent, the governing equations were discretized for the mesh and solved.

Fluent utilizes a segregated solution method to solve the flow governing equations. Owing to the inherent segregated nature of the governing equations and fluid properties, the segregated solver requires each property be first solved independently at an inner iteration level. By creating a system of linear equations with one equation for each cell in the domain, a series of equations are generated in which only one parameter is unknown. Fluent utilizes a point implicit (Gauss-Seidel) linear equation solver coupled with an algebraic multigrid (AMG) method to solve the resultant scalar system of equations for the dependent variable in each cell[27)]. All cells are considered in the solution of each single variable field, then Fluent moves onto the solution of the next variable in a similar fashion.

The fluid properties are solved in the following order: momentum (u, v, then w), pressure-correction (continuity equation), energy, species, turbulence, and finally user-defined scalar equations. Using the initial velocity conditions (if solving for first iteration) or the previous iteration's converged parameters, the momentum equations are solved and the velocity profile is updated. While the velocities solved in this step may satisfy the momentum equations, the local continuity equation may not be satisfied. In this case, a "Poisson-type" equation (derived from the continuity and linearized momentum equations) makes necessary corrections to pressure and velocities fields/fluxes such that the continuity equation is exactly solved. The mass and momentum sink terms are used to establish proper face flux values within this step.

With a proper velocity profile established, the turbulence equations are solved at all locations in the domain using the discretized cell volumes. User defined scalar functions would be implemented at this point, however, none are used in this model. Finally, residual values are compared with the convergence criteria to determine if the model has been solved to a correct degree of accuracy. If the residuals are not small enough, another iteration is performed using the previously solved values as input criteria for the new iteration. A step-by-step schematic displaying the solution procedure for this segregated solver is shown in Figure 2.3[27)].

2.3.4.2 Mesh Creation/Refinement

One main obstacle of this simulation was to mathematically recreate the complex geometry of a funnel mold coupled with the associated solidified steel shell. Once accurate domain boundaries were generated, the real domain was broken up into logical space and a fully structured mesh was created. Levels of high mesh refinement were limited to the areas near the walls (for both the nozzle and mold) and areas encompassing the recirculation zones where there exist high velocity gradients (for the mold). By only specifying the mesh to be refined where necessary, the mesh was able to be relatively coarse in other areas of lesser velocity gradients minimizing computational cost. Using these ideas, the nozzle and mold meshes included 100,000 and 500,000 elements, respectively.

2.3.4.3 Relaxation Parameters

As discussed by Hershey and Thomas, turbulent flow is plagued by divergence problems related to the cross-diffusion terms in the K and ε turbulence equations[28)]. In the equations which include both the kinetic and dissipation terms (Equations 2.6 and 2.7), small disturbances in either propagate quickly and lead to rapid divergence of flow parameters. One way to remedy this is through application of relaxation schemes to the turbulence terms. By taking a high percentage of the previous iteration's solution for K and ε, the advancement of these terms is slowed, resulting in a higher level of system stability over successive substitution methods. Convergence to solution is typically slowed by using significant levels of relaxation, but due to the nature of relaxation coefficients, solution accuracy is not affected.

The presence of irregular boundary conditions at the shell fronts in the mold simulation forced relatively high levels of turbulence relaxation to be used in effort to maintain steady convergence. The CFD software allows the user to have greater control over model simulation and convergence by modifying the dedicated relaxation factor for each solution variable. The relaxation parameters for this model ranged from 0.3 to 0.5 for velocity, pressure, and turbulence values (with u-relax = 1 implying 100% of the new solution is applied through successive substitution).

2.3.4.4 Model Simulation

Solution Methodology

Convergence difficulties and mesh refinement restrictions forced the nozzle and the mold to be solved for independently. First, the flow profile through and out of the nozzle was solved. Fluent allows for parameter profile outputs of one run to be saved and used as a profile input for a separate domain. Thus, with the velocity and turbulence characteristics at the output of the nozzle completely solved, the inlet conditions of the mold could be explicitly defined.

Convergence Statistics

The flow simulations were considered to be completely converged when all residuals were less than 1e-5 (residuals are defined as percentage change from the previous iteration solution, with 1e-5 corresponding to 0.001% change). Flow solution convergence was reached after approximately 500 iterations for the nozzle and 2400 to 4000 iterations mold (with the water models converging quicker, as they lack user-defined source terms due to solidification effects at the boundaries). In addition, computational times for the nozzle and mold were typically 0.5

hours and 10 hours (0.5 and 2.5 hours per 1000 iterations), respectively. All computation was performed on a single Intel processor PC with a computational power of 3.06 GHz. Convergence histories for a typical nozzle solution and mold solution are shown in Figures 2.4 and 2.5 respectively. These runs correspond to the water model with a casting speed of 3.6 m/min.

2.4 Model Validation

To ensure complete model accuracy, comparison was made with a previously examined thin-slab mold and its associated nozzle. In his work, Yuan developed a Large Eddy Simulation (LES) mathematical model to predict turbulent flow in a thin-slab mold caster[13)]. Through comparison with water models, Yuan was able to prove the accuracy of his model. His work will serve as a basis for determining the current model's accuracy.

The stainless steel composition used in the model matches steel produced by Nucor Steel, and is displayed in Table 2.1[29)]. The domain of the thin-slab caster to be analyzed is displayed in Figure 2.6, while the dimensions and the operating conditions are presented in Table 2.2. A trifurcated SEN was coupled with the mold for this simulation, which is also shown in Figure 2.6. As previously discussed, the mold simulation and nozzle simulation were run separately, with the mold entry boundary mirroring the flow parameters at the nozzle outlet boundary.

By comparing the current model with Yuan's model, results agree favorably. On a purely qualitative level, both models predict a traditional double-roll flow pattern along the wideface centerplane within the mold. However, it is necessary to quantify certain flow characteristics to further confirm model validity.

Figure 2.7 compares the time-averaged stream-wise velocity (V_z) out of the center jet between the current model and Yuan's mode (for this analysis, the RMS velocity plots will be neglected). While the maximum velocity is not shown, the current model predicts the downward velocity immediately past the SEN to be ~20 % higher than Quan's model (1.22 versus 1.02 m/s). Yuan's model incorporates transient swirling effects propagating from the stopper rod, causing the flow at the output port to be non-uniform. So even though the plot axis remains identical in both models, they pass through different regions of the converged flow pattern; the plot axis intersects the created steady-state model where velocity is highest, while the swirling of Quan's model causes maximum velocity to occur elsewhere in the nozzle. In any case, acceptable agreement is reached between the two models once the distance below the nozzle becomes sufficiently large (> 0.5 m), as the difference in nozzle flow becomes a factor of diminishing importance away from the nozzle.

Figure 2.8 compares wideface centerline velocities at the top surface. Examining Yuan's mean-velocity results for the "2-S Left" case, good agreement to the created model is reached. Note that both plots predict a maximum velocity of approximately 0.24 m/s occurring at the same distance from the narrow-face centerplane (0.29 m). The current model predicts slightly higher velocities near the SEN and the narrowface than Yuan's model, which can be attributed to Yuan's LES simulation capturing small turbulent eddies (while the coarser grid of the current model cannot resolve them). With a finer grid in these locations, the Fluent finite-difference turbulence simulation most likely will predict these small recirculation zones. Still, capturing small fluctuations such as these would only marginally increase macro-level simulation accuracy at an excessive computational expense.

The downward velocity for the wideface centerline at a distance of 0.5 m below the top surface is plotted in Figure 2.9. The presence of the trifurcated nozzle is apparent in the strong downward velocities present near the mold center and near the walls. Again, strong agreement between Yuan's model and the current model is established. The downward velocities are accurately predicted in the current model, indicative by similar roll patterns and velocity magnitudes within the rolls. Only slightly higher downward velocity is predicted at the mold center, which again is a product of different nozzle outlet flow patterns. The Fluent turbulence model predicts smaller velocity gradients near the narrowface than the LES simulation, most likely due to the increased flow detail captured by LES.

Yuan's LES model has been proven correct in his report; Good agreement with his LES model indicates the current Fluent model is also accurate in predicting flow patterns and velocities within an actual mold. Results generated by the Fluent model for this investigation will be assumed to be correct and valid in solving nozzle/mold simulations.

2.5 Typical Flow Results

For all of the funnel mold cases considered, similar macro-scale flow patterns emerged in the nozzle and the mold. Flow in both domains for a characteristic case (3.6 m/min steel case) will be examined in detail. Fluid properties and composition percentages for the steel (as cast by Algoma Steel) can be found in Table 2.1[30)]. Note that in all figures within this chapter, the zero value along the z-axis corresponds to the bottom of the nozzle (at the SEN submergence depth, 265 mm below the mold top surface).

2.5.1 Flow in the Submerged Entry Nozzle

Mesh Description

A realistic bifurcated nozzle was modeled to generate accurate steady-state inlet flow parameters for the funnel mold domain. Dimensions and operating conditions for the Algoma SEN modeled are presented in Table 2.2. The mesh generator Gambit was employed to discretized the domain into a fully structured mesh containing approximately 100,000 elements, shown in Figure 2.10.

Velocity Solution Plots

The velocity solution for the nozzle simulation is shown in Figures 2.11 through 2.13. The flow pattern along the nozzle centerplane (Figure 2.11) shows smooth, predictable flow from the upper nozzle through the outlet ports. Note there is relatively little turbulence throughout the entire nozzle, which is important in minimizing the probability of inclusion formation and clogging[31)]. The smoothly shaped nozzle expansion region facilitates near-laminar flow, as identified via postprocess streamlines.

By focusing on the velocity vector plot of lower nozzle (Figure 2.12a), a small amount of recirculation across the upper outlet is observed. Notice the high nozzle wall curvature just prior to the outlet. The pressure void formed in this region causes liquid from the mold to be slightly drawn back into the nozzle across the upper port. While this recirculation zone is quite small, its effect may introduce an initiation point for clogging within the nozzle. It is the author's recommendation that this sharply curved section immediately preceding both outlets be smoothed or eliminated to reduce the risk of defects associated with nozzle flow.

Figures 2.12b and 2.12c show velocity contours in the x and y-directions for the lower nozzle. Very regular near-laminar flow is developed throughout most of this region, evident by the smooth velocity contours seen in the plots. The only region of high velocity gradient is near the walls, where the zero-velocity boundary conditions result in the formation of high u_z gradients extending into the domain (Figure 2.12c). Flow segregation at the bottom of the nozzle (sharply branching the fluid into the two ports) can be visualized in the u_x plot (2.12b). Also note how u_z is nearly zero for the regions at the top of the outlet ports. Extremely low velocity in these regions encourage nozzle outlet recirculation, especially in the real-world unsteady case (again propagating the formation of clogs).

Because of the time-averaged nature of the simulation, both outlets had very similar velocity profiles. It is expected that during actual casting, this symmetry will not be present; instabilities resulting in transient oscillations between flow of the two outlets will cause outlet preference according to time.

Turbulent Energy Plot

With the free stream being sharply diverted into the nozzle ports and severe wall-induced u_z gradients, the highest level of turbulent kinetic energy was found near the lower nozzle obstruction (Figure 2.12d). Excessive turbulence is a concern, as nozzle erosion (which is prevalent in turbulent regions) leads to deposition of unwanted inclusions in the cast ingot.

Outlet Velocity Vector Plots

Time-averaged velocity vector plots at the 2-D outlet boundaries are shown in Figure 2.13. As expected with the straight-through nozzle design, outflow velocity is proportional to outlet height (with the highest exit velocity occurring at the bottom of the outlet). The slight recirculation near the upper outlet can be further observed in this plot. While for the steady-state case the problem of flow back into the nozzle may seem insignificant, high levels of nozzle recirculation are very likely to occur in the transient atmosphere of real-world casting.

The transport of impurities is greatly influenced by the outlet jet downward angle, which in this simulation approximated as 15.6° (with 0° corresponding to the vertical axis). Steeper inlet jet angles cause inclusions to travel deeper into the liquid pool, greatly increasing their probability of becoming entrapped in the final product. Moreover, inter-mold velocity along the top surface is directly related to the inlet jet angle. With a more horizontal trajectory out of the nozzle, flow is generally more likely to be directed into the upper mold recirculation zone, increasing the velocities and shear forces along the top surface. As discussed, excessive steel velocity past the steel-slag interface can yield slag entrainment problems. The strong downward flow out of the nozzle examined indicates a high flow rate can be tolerated while maintaining acceptable top surface velocities. Still, clean steel techniques must be employed as inclusions will have only a small chance of being removed from the slab once entering the mold via nozzle.

2.5.2 Flow in the Funnel Mold

Mesh Description

The funnel mold modeled in this investigation is a case study of an actual caster currently in operation by Algoma Steel. The overall schematic, dimensions, and operating conditions for the Algoma funnel mold can be seen in Figure 2.1 and Table 2.2. As with the nozzle, Gambit was used in the mesh-generation step. The discretized mold domain of approximately 500,000 elements is outlined in Figures 2.14 through 2.16. Again, a fully structured mesh was created, yielding minimum computational time and a high degree of computational efficiency over an unstructured mesh. The tapering effect of the funnel as well as the solidification front can be observed and quantified in the mesh figures.

Velocity Vector Plots

A characteristic double roll flow pattern emerged, as shown in the wideface centerplane velocity vector and streamline plots of Figure 2.17. This double roll pattern is formed from the splitting up of the nozzle jet after it contacts the narrowface wall (which in this case is located at approximately -0.565 m; see Figure 2.17b). At this location, flow is diverted both upward and downward, resulting in two large recirculation zones. The upper roll carries flow upward along the narrowface wall, toward the SEN along the top surface, and then back downward toward the incoming jet. A high pressure region is formed at the meniscus, resulting in the formation of a standing wave along the top surface. The lower recirculation zone does not have any pronounced lower boundary, so it typically encompasses a much larger area than the upper recirculation zone. Instead, shell formation (with its associative mass loss and reduction of liquid cross sectional area) shortens the distance required for near-uniform flow to develop. When the shell is sufficiently thick, the flow is greatly restricted and the lower zone dissipates, resulting in near-uniform downward flow equivalent to the casting speed.

The complete velocity solution (vector plots at 2 mm inside the top surface, 2 mm inside the narrowface, the wideface centerplane, and at 2 mm inside the wideface) is shown in Figure 2.18. The vector plots shown represent *parallel* planes at 2 mm offset from the irregular domain walls rather than *flat* 2-D cutting surfaces. A few key findings are observed: Just below the top surface (Figure 2.18a), the upper recirculation zone retains enough strength to have substantial velocity when contacting the wall of the SEN. Separation between the upper and lower recirculation zones is quite apparent near the narrowface (Figure 2.18b), and the effect of the funnel region on redirecting fluid flow can be visualized just inside the wideface (Figure 2.18d).

Velocity Slice Plots

The dissipative effect of the inlet jet moving through the liquid domain can be seen in the u_x and u_z velocity slice plots of Figures 2.19 and 2.20. The jet is initially highly concentrated at the nozzle outlet. As the jet propagates further into the mold, it widens out by entraining more fluid into its path (from all directions) until it reaches the narrowface. This entraining effect can also be observed in the velocity vector plot of Figure 2.17; observe how the velocity gradient between the upper and lower recirculation zones soften as the incoming stream approaches the narrowface wall.

The u_x and the u_z velocity slice plots reiterate the strong formation of the double roll flow pattern. The maximum horizontal (u_x) velocity is found just below the top surface, indicative of strong recirculation toward the nozzle. At its peak, the velocity just below the top surface is approximately 0.479 m/s. Remember that excessive velocity at this slag-steel interface can promote slag entrainment and be the source of numerous final product defects. Consequently it is important to quantify this parameter in the funnel-mold model. In the u_z slice plot (Figure 2.20), the recirculation zones are also quite distinct. The separation of flow along the narrowface wall with flow diverted into the upper and lower rolls is quite pronounced. The highest upward (u_z) velocity of 0.463 m/s occurs just above the impingement location at the narrowface. The maximum downward velocity (not surprisingly) occurs just below the incoming jet, with a maximum value of -1.36 m/s.

Pressure Contour Plot

Pressure contour slices along 2-D planes throughout the domain can be seen in Figure 2.21. The absolute maximum pressure occurs directly below the nozzle inlet jet, located where the quickly-moving steel first enters the liquid pool. While initially concentrated as high pressure, the jet entrainment of the surrounding fluid dissipates the pressure, resulting in overall lower pressures/velocities as the distance from the nozzle increases.

Even though the model treats the top surface as a fixed boundary, the surface height profile can be estimated from the calculated surface pressure distribution (which will be further discussed in Section 2.6)[32]. Remember the slag-steel interface slope at the shell walls is critical in ensuring proper slag lubrication and preventing shell breakouts. The upward flow along the narrowface (due to the upper recirculation zone) causes the top surface pressure to be highest at the meniscus, with subsequent decreasing pressure closer to the SEN. The implications of this pressure distribution would be a standing wave forming along the top surface; the highest point of the wave located at the meniscus with a smooth, decreasing wave height profile forming toward the SEN (evident by the gradually decreasing pressure along this top surface). Note how the pressure is lower along the wideface boundaries than along the centerline at the top surface. Because the no-slip boundary conditions yield slow velocities at the shell walls, low pressure forms in these regions. Higher pressure near the wideface centerline would yield a convex-upward or “bubble” shaped top surface (from wideface to wideface), with the profile sloped down toward the steel shell along both boundaries.

Turbulent Energy Plot

Kinetic energy contours throughout the domain are shown in Figure 2.22. In lieu of being repetitious, the effect of jet entrainment can be further visualized. Initially concentrated to a narrow region near the nozzle outlet, the kinetic energy expands out to encompass a larger volume of fluid as the distance from the nozzle increases. Because turbulent energy is highest in regions of sharp velocity gradients, it is expected that the highest amount of turbulent energy in the model should occur just below the nozzle inlet, which is confirmed in the *KE* solution figure.

Note the relatively high kinetic energy in two key regions: where the dispersed inlet jet reaches the wideface and along the narrowface of the upper recirculation zone. While the shell walls require a no-slip velocity boundary condition (at the casting speed), the flow just into the liquid pool is comparatively high. Thus sharp velocity gradients emerge in these areas, resulting in rather high levels of kinetic energy. As kinetic energy is directly proportional to shear forces, excessive levels of *KE* at the liquid steel boundaries can promote formation of breakouts or other shell defects.

Disproportionate amounts of *KE* at the top surface propagate into surface level fluctuations, further causing improper slag lubrication or slag entrainment. By treating the top surface as a no-slip fixed entity, the amounts of *KE* calculated are quite conservative in predicting the worst-case scenario. Even though only moderate levels of *KE* were observed at the top surface in this model, there remains the necessity to monitor slag-steel interface *KE* to ensure fluctuations remain within acceptable parameters during actual casting.

2.6 Steel/Water Model Investigation

Water models provide a convenient method for estimating fluid flow within a steel caster. One fundamental assumption of water models is that water and steel have identical fluid properties. With kinetic viscosities only ~20% different, water has been shown to generate similar flow patterns to the liquid steel it is simulating.[19)]. In any case, this assumption will be tested using mathematical models.

Water models rarely consider shell growth in defining the liquid pool domain and never accommodate loss of mass/momentum through the boundaries. Remember that the shell comprises a much higher percentage of the slab domain in a thin-slab caster relative to a conventional caster. A water model with its walls curved to match the shell fronts is less accurate in predicting inter-mold fluid flow, as it exaggerates velocities due to a larger amount of non-solidified fluid in the shell-reduced domain.

Whereas the steel caster has no fixed bottom (the liquid pool tapers off with the steel solidification front until a solid slab is formed), the water model has a bottom plate which diverts fluid into recirculation channels. Though the presence of this unnatural bottom causes disruptions in fluid flow, its effect may be limited to the lower regions of the model. Hypothetically it is possible to have a water model with a tall enough domain such that the effect of this bottom plate is nearly negligible at the top surface. Because of the ability to modify testing procedure around this problem, it is not considered a fundamental difference between water models and steel casters. The water model will use an identical domain (san solidification front for the water model) to the steel model; that is, the physical bottom plate will be omitted. Standard pressure outlet boundary conditions will be used to define flow leaving both domains.

As with water models, most mathematical models neglect the effect of shell solidification due to simplicity. The CFD model developed for this analysis incorporates mass and momentum losses into the shell front. One main objective of this investigation is to consider the effects and consequences of neglecting solidification in obtaining accurate flow parameters.

In this investigation, the fundamental differences (dissimilar fluid properties and solidification effects) between the water model and the caster it represents will be investigated. Through this research, the validity of using thin slab water models to simulate caster flow will be challenged.

2.6.1 Model Cases

Two separate domains will be compared: a mathematical representation of a water model and the steel caster it represents.

2.6.1.1 Water Model Case

A water model simulation was created to model flow through an actual water model. The domain does *not* include the contribution of solidified shell to altering the domain walls. Previous work from Creech suggests that water models which neglect shell thickness in their domains more closely approximate actual casters with solidification fronts and mass loss at the boundaries[14)]. The domain for the water model simulation simply consists of the unmodified mold dimensions and the exiting slab dimensions. Because there is no solidification in the water model, there is no mass or momentum removed at the domain boundaries. Fluid properties were specified to water values.

2.6.1.2 Steel Model Case

In the steel model case, the domain is modified to incorporate the solidification front into the liquid pool dimensions (via CON1D shell thickness predictions, smoothed to neglect the effect of oscillation marks and surface irregularities). Therefore, a slightly different domain with curved sides and a sloping inner liquid cavity was used for the steel case. The effects of solidification are implemented in this case through the placement of thin mass/momentum sink elements at the shell front. Model fluid properties were set to liquid steel values.

2.6.2 Solution Methodology

Using the simulation parameters displayed in Table 2.2, a typical water model run reached steady-state (converged to maximum residuals of 1E-5) in approximately 2400 iterations, while the steel model converged in approximately 4000 iterations. In both cases, the fluids were given an initial downward velocity equivalent to the casting speed (3.6 m/min downward), which sped up convergence. The disparity in convergence iterations between the two cases can be attributed to the addition of mass and momentum sink elements near the shell boundaries in the steel case. Convergence took approximately 6 hours and 10 hours for the water model and steel model, respectively, on a single Intel processor PC with a computational power of 3.06 GHz. With very similar liquid pool dimensions, mesh refinement was nearly identical for the two models (only slightly more elements were needed in the steel model to incorporate the effect of solidification near the walls).

2.6.3 Results

Macro-scale Velocity Solution

Both the water model and steel cases exhibit similar, characteristic double-roll flow patterns with the nozzle jet impinging on the narrowface wall. Velocity vector/streamline plots for the wideface centerplanes of both cases are shown in Figure 2.23a and 2.23b. Note how the water model predicts a straighter jet trajectory as it passes through the domain, yielding a lower jet impingement location and elongated rolls (in the *z*-direction) over the steel model. Further velocity plots confirm this phenomenon and will give rise to possible explanations in ensuing paragraphs.

2-D Velocity Line Plots along Horizontal Axes on Wideface Centerplane

Velocity profiles along various 2-D lines in the domain are shown in Figures 2.24 through 2.35. In Figure 2.24, the wideface centerline 10 mm below the top surface, the velocity magnitude for the two cases are compared. While both predict a maximum velocity at about 0.38 m from the center of the SEN, the fluid speed at this location is greatly underestimated by the water model (approximately 32% lower than the steel case, 0.324 m/s versus 0.478 m/s). The tapering of the shell and subsequent reduction in fluid cross-sectional area provides resistance for fluid leaving the domain. The higher resistance to downward flow in the steel case facilitates more fluid being "pushed" into the upper recirculation zone, yielding higher velocities at the top surface. Note the lack of turbulent eddy formation near the meniscus in the water model, evident by the smooth velocity profile in this region. Different turbulent fluid properties between steel and water coupled with overall slower upper recirculation zone velocities explain this inconsistency between the two cases.

At a distance of 1 m below the surface (0.735 m below SEN, Figure 2.25), the downward velocity versus distance from the mold center along the wideface centerline is quantified. The highest downward velocity occurs approximately 0.42 m from the centerline in the water model, a full 0.14 m earlier than the steel case. Without the shell to restrict the flow, the fluid exiting the nozzle in the water model maintains a straighter trajectory along the nozzle exit angle. Observe how the velocity decreases at a much faster rate toward the narrowface in the water model. With a lower jet impingement location for the water model, the plotting line is much closer to the separation point where the jet forms the upper and lower recirculation zones, yielding much slower velocities near the narrowface. In contrast, the steel model is already well into the lower recirculation zone at 1 m below the surface, resulting in much higher downward velocities.

At a distance of 2 m below the top surface (1.735 m below SEN, Figure 2.26), the velocity profiles for the steel and water case are reasonably close. However, at 3 m from the meniscus (Figure 2.27), the downward velocities have extremely different profiles. Nowhere else in the domain is the effect of shell omission in the water model so apparent. The lower roll in the water model flow profile extends through the domain outlet, including a large recirculation effect through the pressure outlet boundary condition. The steel case maintains near uniform downward velocity at approximately the casting speed, owing to the reduced liquid steel cross sectional area.

Another interesting issue is the average velocity along this wideface centerline 3 m from the top surface. Assuming that velocities along this axis are directly proportional to flow through the horizontal plane it lays on, the average downward velocity is about 0.0062 m/s greater for the water model over the steel case. The disparity observed in velocity is most likely due to the differences in solid and liquid steel densities (7800 kg/m^3 versus 7000 kg/m^3 for solid, liquid steel respectively); 11% more mass must be removed from the liquid steel pool to yield an equivalent volume of solid steel. At this height, shell growth has shrunken the liquid domain in the narrowface and wideface directions by 2.79% and 48.22%, respectively (corresponding to ~49.66% reduction of the original liquid domain). Even though the water model domain has identical dimensions to the outer shell in the steel model, the 11% extra steel removed from the steel model to form the shell translates into a reduced amount of steel flowing through its liquid domain. This phenomenon is confirmed by the lower average velocity of the steel plot in Figure 2.27.

2-D Velocity Line Plots along Horizontal Axes parallel to Narrowface Centerplane

Switching point-of-view, Figures 2.28 through 2.30 show downward velocity profiles for horizontal 2-D lines, parallel to and 0.6 m from the narrowface centerplane at prescribed distances from the top surface. The amount of liquid domain reduction due to solidification is easily seen in these figures. Notice as the length from the top surface increases, the downward velocity for the water model progressively increases (relative to the steel plots). Remember that in the water model, the lower roll flow pattern extends well past the outlet boundary; the strong downward velocity along the plotted plane maintains strength through the entire height of the domain. In the steel cases, solidification effects have a dissipative effect on flow in regard to velocity. It promotes more uniform flow patterns with velocities homogeneously approaching casting speeds as the distance to the top surface increases.

While steel and water have similar fluid properties, differences between the laminar and turbulent flow regimes are readily apparent, especially in Figure 2.28. Note the average velocity for the two cases is dissimilar simply because this line represents differences in the flow pattern. Qualitatively though, it can be seen that the steel fluid has a smaller boundary layer than water. While this may be slightly due to different fluid properties, it is the author's contention that the boundary layer is much thinner for the steel case because the solidification draws fluid from the liquid pool immediately adjacent to the shell front. A fully developed boundary layer cannot be formed, and the higher velocity flow replaces the removed fluid closer to the shell. By underestimating the boundary layer flow velocity profiles, the water model may not give an adequate velocity approximation near walls. In areas sensitive to flow velocity (for example, near the jet impingement region or at the slag-steel interface), the water model may indicate lower, acceptable velocities when in fact the opposite exists in the steel caster.

On a micro scale, shell solidification drawing liquid to the wall relaxes the eddies and recirculation zones that form along these boundaries. This effect is apparent at the shell boundaries (especially at the meniscus level, where there is relatively slow flow and high solidification rates); solidification imposes a calming effect on fluid flow turbulence near the shell front Many small eddies (possibly creating casting problems) which form near the walls will be suppressed as the steel solidifies.

2-D Velocity Line Plots along Vertical Axes on Wideface Centerplane

Switching point-of-view again, Figures 2.31 through 2.35 represent vertical 2-D lines, along the wideface centerplanes at set distances from the center of the caster. Along the caster centerplane (Figure 2.31), the water model has a stronger upward velocity directly below the SEN due its longer, more pronounced lower roll flow pattern. Without the mass loss and dissipative effects of the shell, flow in the water model has a stronger tendency to recirculate than the steel models. The lack of shell presence and restriction associated with it promotes a lower narrowface jet impingement location for the water case, which is seen in Figures 2.32 through 2.35. The point at which there is zero downward velocity in the figures is interpreted as the parting between the upper and lower roll. It can be seen that the roll separation height is consistently lower for the water case over the steel case.

In the 2-D downward velocity plot along the wideface centerline close to the narrowface shell wall (Figure 2.35), the water model predicts a lower impingement location by approximately 0.13 m (-0.566 m for the steel case, -0.695 m for the water model). A false lower jet impingement location implies that the shell has a greater thickness and will be less affected by variations in superheated flow from the nozzle. The difference in shell thickness from the predicted impingement locations is nearly 1 mm (9.33 mm for steel case, 10.25 mm for the water model). The deeper location of the water impingement location may give false confidence as to breakout prevention when in reality a serious problem exists.

On a macro scale, the vertical velocity line plots for the water case exhibit a smoother, more consistent profile than the steel model. Without the shell to restrict flow, the fluid is allowed to travel a greater distance before being suppressed, yielding softened velocity gradients than the steel case. Because regions of high turbulence are minimized with weakened gradients, the water model may also under-predict turbulent characteristics in the steel caster.

2.7 Casting Speed Parametric Study

Because the funnel mold is relatively unexamined via mathematical models, little information is known about how different operating parameters will affect flow within the mold. As discussed in Chapter 1, many serious defects are caused by excessive fluid flow parameters along boundaries of the fluid domain (i.e. slag entrainment at the top surface, breakout or crack formation along the narrowface, etc…). Simulation parameters for all cases can be found in Table 2.2.

A parametric study was performed to study the effect of varying casting rates on aspects important to slab quality. With higher casting velocities, two factors augment the potential for catastrophic casting failure (i.e. breakout):

1. The flow velocities within the mold will be higher with increased casting speed, as more fluid must flow into the mold to accommodate the higher mass of steel extracted.
2. With the slab being extracted at a higher rate of speed, the mold has less time to cool the shell. The thinner the shell when removed from the mold, the more unstable the slab is as the lessened shell thickness may not be strong enough to support the inner liquid pool.

Coupling thin shells with high fluid velocities increases the probability of casting failure exponentially. Care must be taken to quantify flow characteristics and shell thicknesses in effort to prevent casting problems. The following investigation focuses on how varying casting speed affects flow parameters within a funnel mold.

Due to the upper roll of the double-roll flow pattern inside most molds, standing waves typically develop on the top surface. The highest point of the wave usually occurs near the meniscus, where the strong upwards flow along the narrowface wall reaches the top surface. Higher casting velocities typically yield higher wave elevations, sometimes to a level which prevents slag from lubricating the gap between the shell and the mold. Due to model complexity, this wave was not allowed the freedom to deform the mesh. Rather, by treating it as a fixed surface, the increase in pressure along this surface allows for an estimation of the free surface deformation using energy conservation laws. The following equation will be employed to estimate free surface deformation along this top surface:

$$\Delta Height = \frac{p - p_o}{g\left(\rho_{steel} - \rho_{slag}\right)} \tag{2.20}$$

Panaras *et. al.* used a simplified, single phase flow model to test the accuracy of the height approximation with actual top surface deformation[32)]. By neglecting the slag layer and treating the top surface as fixed, he found reasonable agreement between the pressure estimation equation and mathematically computed surface waves. Results were subsequently collected using a water model, which also agreed favorably.

2.7.1 Model Cases

Three cases will be considered in this investigation, with the intent of encompassing a typical operating range of actual casters. The liquid domain dimensions were modified independently for each case to include the solid shell dimensions (via CON1D shell thickness predictions). Shell thicknesses for the three casting speeds can be found in Figure 2.2. As in the water model comparison, solidification effects are incorporated through the placement of thin mass and momentum sink elements directly adjacent to the solid wall. Due to the different casting rates, shell thicknesses and mass sink terms will be unique for each of the three cases, requiring the use of three separate domains for the analysis.

2.7.2 Solution Methodology

Using the simulation parameters displayed in Table 2.2, all mold models converged in approximately 4000 iterations. While the domain dimensions for each case were slightly different, the method by which the domain was broken up for meshing and the number of elements used in the domain remained constant. Using the solid slab dimensions and the casting speed, proper velocities were calculated and inputted at the nozzle entry. The nozzle model was solved first, and the nozzle output flow properties were subsequently used in the mold model as the inlet conditions. In all cases, the fluids were given an initial downward velocity equivalent to the casting speed. Convergence took approximately 1 hour and 10 hours for the nozzle and mold, respectively, on a single Intel processor PC with a computational power of 3.06 GHz. By keeping all other aspects of the models consistent, the effect of varying casting speeds was explored.

2.7.3 Results

Quantification of flow characteristics allows for recommendations to be made with intent of minimizing casting defects. Using the created model, critical parameters which are directly related to product quality (i.e. top surface velocity) can be predicted. In Section 2.6, the accuracy of water models in predicting thin-slab caster flow was shown to be relatively poor. Knowing this, mathematical models may be the only precise way of quantifying flow in funnel mold caster.

Macro-scale Velocity Solution

Velocity vector plots along the wideface centerplane for all steel cases can be seen in Figure 2.23. Each plot depicts a characteristic double roll flow pattern, as explained in Section 2.5.2. Notice that the flow patterns are generally quite similar for all cases. Higher velocity cases yield a more pronounced and elongated lower recirculation zone. The increased kinetic energy input associated with higher casting velocities translates into more inter-mold steel motion, yielding the observed larger recirculation zones. The downward velocity plots along the wideface centerline (at 1 m and 2 m below the top surface) of Figures 2.25 and 2.26 support this theory; the higher the casting speed, the larger absolute velocity at all locations along this axis. Stronger, more pronounced recirculation zones may facilitate higher levels of inclusion entrapment, as the particles might not have enough time to reach the slag layer and be removed from the liquid pool.

Jet Impingement

Another critical area within the mold involves the jet impingement location on the narrowface. In looking at the downward velocity along the wideface centerline near the narrowface (Figure 2.35), the zero-velocity point corresponds to the jet impingement location. Note that all of the steel cases have nearly the same impingement height (~0.57 m in the graph; 0.835 m below the top surface). In reality, however, the impingement is not expected to be the same. The model assumes an isothermal condition, resulting in no buoyancy force terms added to the flow calculations. Assuming constant superheat levels for each case, the effect of buoyancy forces will have less of an impact on the higher speed flow; buoyancy would have a shorter time to deflect the flow toward the top surface before the steel contacts the narrowface. It is expected that if buoyancy was considered, the higher jet momentum possessed of the higher casting speed cases will cause the impingement location to be slightly lower than that for slower casting cases. Recall that the jet impingement location is critical in preventing breakouts as shell thinning occurs in this location (due to the inlet jet superheat).

The likelihood of breakouts forming at the impingement location is vastly increased with higher casting speeds. Assuming that the isothermal assumption is correct, the jet impingement locations are essentially identical for all cases tested. At this location along the narrowface, the shell thickness is 9.7% and 17.8% thinner for the 4.2 m/min and 4.8 m/min (respectively) than the 3.6 m/min casting speed case (8.44 mm, 7.66 mm versus 9.35 mm). With larger amounts of superheated steel reaching the narrowface, solidification will be slowed and higher levels of remelting will further erode the shell wall. These two effects work in unison, exponentially decreasing shell thickness at the impingement location with faster casting. Extreme care must be taken when casting at high speeds to ensure acceptable shell thickness, thereby preventing detrimental shell breakouts.

Flow Parameters at the Top Surface

Recall the model defines a zero-velocity boundary condition at the top surface boundary; thus, velocity profile data was collected along the wideface centerline just below this surface (plotted in Figure 2.24). A critical aspect of flow within the mold involves velocities past the slag-steel interface, as excessive flow contains enough emulsion energy to shear off slag globules and entrain them into the steel pool. The higher the velocity past this interface, the more likely unwanted slag inclusions will be present in the final steel product. It is fairly intuitive that higher casting velocities (with their higher inlet jet speeds) would yield higher steel velocities past the slag-steel interface, which is confirmed in Figure 2.24. Note that the maximum speed occurs at about 0.39 m from the narrowface centerline in all cases, with the 4.8 m/min casting speed having the highest velocity at this point (0.569 m/s, compared to 0.511 m/s and 0.478 m/s for the 4.2 and 3.6 m/min casting speeds, respectively). While high, it is unclear if this velocity is sufficient to propagate into a high level of slag emulsion.

Because the velocity profile along the top surface is quite dependent on the casting speed, it has been proposed that if this velocity can be measured, other critical steel flow values can be approximated *during* the casting process. In Chapter 3, a novel method for measuring high temperature flow has been created for this exact purpose.

Even though the top boundary is fixed in the model, the free surface level was approximated using the pressure distribution (Equation 2.20). Figure 2.36 plots this approximation along the wideface centerline at the top surface. Predictably, the higher the casting speeds, the more distinctive the top surface wave. The high point of the wave occurs near the meniscus (where the upper recirculation zone contacts the top surface), and a steadily decreasing wave profile extends to the SEN. Note how the maximum and minimum wave height values increase exponentially as the casting speed increases. Even with only three steel cases studied, the wave gets dramatically more pronounced for the 4.8 m/min casting speed case over the slower cases.

One major phenomenon that the approximation neglects is the effect of surface tension on surface deformation. Had surface tension been considered, the surface height gradients would be reduced especially near the narrowface and the SEN. It is expected that the peaks of the wave would be slightly more bubble-shaped, similar to the water model approximation. A close examination of the pressure/wave height approximation for a separate model is discussed in Section 3.8.3.4.

2.8 Summary

Through computational models, fluid flow through a funnel mold, its associated nozzle, and through a water model approximation has been analyzed. A standard K-ε turbulence model (created using the CFD program Fluent) was verified to be accurate by comparison to previously published work by Yuan. By developing a mass and momentum loss strategy to treat shell solidification at wall boundaries, a water model was compared to its associated steel caster for model validity. Additionally, the effect of casting speed on critical mold flow parameters was researched. Qualitative examination of flow patterns coupled with quantitative analysis of critical parameters (velocities, pressures, etc…) have yielded the following important results:

Steel/Water Model Investigation

1. While both cases generate similar double roll flow patterns, the water model greatly underestimates flow velocities within the mold region. The resistance to flow provided by the shell in the steel case "pushes" more fluid to the surface than the water model, generating the higher recirculation velocities.

2. The critical velocity just below the steel slag interface is greatly underestimated by the water model (32% lower, 0.344 m/s versus 0.478 m/s). Minimizing flow at this surface reduces the number of inclusions trapped via slag entrainment and also gives inclusions more time to "float" out of the liquid pool.

3. The nozzle jet trajectory for the steel case is markedly different than for the water model case due to shell tapering effects restricting downward flow. The critical jet impingement location is predicted to be lower (~0.13 m lower) in the water case, corresponding to ~0.92 mm difference in shell thickness. Inclusions deposited into the mold via nozzle will have a much greater change of becoming entrained with steeper jet trajectories (as in the water model).

4. Far from the top surface, the steel case predicts near uniform downward flow (at the casting speed), while the water model maintains an extended recirculation zone far into the strand. This effect in the steel case is due to the ~49.66% reduction in cross sectional area, which smoothes out flow disturbances.

5. The effect of solidification drawing fluid into the shell coupled with slightly different flow properties dictates a much smaller boundary layer thickness for the steel case as opposed to the water model. Flow velocities near walls have large implication on steel quality (slag entrainment, shell solidification, etc…), with lower velocities preferred to cast high quality steel.

6. Many small eddies observed in the water model (especially in regions of low velocity and high solidification; for example, the meniscus) are not found in the steel case. Because the steel is being drawn into the shell and removed from the eddy regions, they are effectively suppressed from the flow.

7. Internal velocity gradients are lessened in the water case, as the restrictive shell forcing the fluid into the upper recirculation zone is not present. Highly turbulent regions are underestimated, which has large implications on inclusion entrapment.

Casting Speed Parametric Study

1. All velocity cases of the isothermal steel model exhibited very similar, double roll flow patterns. Higher velocities were seen within the recirculation zones with faster casting speeds. As velocity increased, the lower recirculation extended further into the strand.

2. Jet impingement was nearly identical for each case (-0.835 m below the top surface). In non-isothermal reality, jet impingement is predicted to be slightly lower in the mold for higher casting speeds cases, as the buoyancy force has a lessened effect on higher speed flow (resulting in a straighter jet trajectory).

3. The shell thicknesses at jet impingement are 9.7% and 17.8% thinner for the 4.2 m/min and 4.8 m/min (respectively) over the 3.6 m/min casting speed case (8.44 mm, 7.66 mm versus 9.35 mm), assuming the model predicts the correct jet impingement location for each case.

4. Maximum velocity along the slag/steel interface at the top surface is higher for increased casting speeds, with the 4.2 m/min and 4.8 m/min casting speeds having 6.9% and 19.0% higher velocity than the 3.6 m/min case (0.511 m/s, 0.569 m/s versus 0.478 m/s).

5. With stronger upper recirculation velocity, increased casting speeds produce *exponentially* larger top surface waves (in regard to min/max heights and overall profile). The highest point of the wave occurs near the meniscus and slopes downward to the SEN.

Table 2.1: Composition of steel used in the Validation and Algoma Funnel Mold Models[29,30]

Element	Validation Case Steel[29]	Algoma Funnel Mold Steel[30]
C	0.047%	0.030%
Mn	0.480%	0.170%
S	0.001%	0.005%
P	0.026%	0.007%
Si	0.039%	0.030%
Cr	16.710%	0.000%
Ni	0.200%	0.000%
Cu	0.100%	0.000%
Mo	1.000%	0.000%
Ti	0.000%	0.000%
Al	0.003%	0.000%
V	0.026%	0.000%
N	0.056%	0.000%
Nb	0.010%	0.000%
Sn	0.008%	0.000%
Co	0.020%	0.000%

Table 2.2: Model simulation parameters (unlisted values carry-over from left)

	Parameter/Property	Validation Case	Water Case	Steel Cases			
Simulation Parameters	Casting Speed	25.4 (1.524)	60 (3.6)	60 (3.6)	70 (4.2)	80 (4.6)	[mm/s] ([m/min])
	Fluid Density	---	1000	7000			[kg/m^3]
	Fluid Laminar Viscosity	---	0.001	0.006			[kg/m-s]
	Fluid Kinematic Viscosity	7.98 x 10^{-7}	1.00 x 10^{-6}	8.57 x 10^{-7}			[m^2/s]
	Gravitational Acceleration	9.81	9.81				[m/s^2]
	Mass/Momentum Sinks at Shell	Yes	No	Yes			
SEN	Bore Inner Diameter	*70*	80				[mm]
	Submergence Depth (top surface to bottom of nozzle)	127	265				[mm]
	Vertical Port Angle	72.5	9.8				° down
	Side Ports (H x W x T, inner bore)	75 x 0 x 32	141 x 127.16 x 28				[mm x mm]
	Bottom Port Diameter	32	N/A				[mm]
	Domain Modeled	1/1	1/1				SEN
Mold	Mold Width	984	1450				[mm]
	Mold Thickness	132	90, 170				[mm]
	Mold Length	1200	1200				[mm]
	Domain Width — Top	984	1450				[mm]
	Domain Width — Bottom	934.04	1450	1405.2	1409.49	1412.87	[mm]
	Domain Thickness — Top	132	90, 162.88				[mm]
	Domain Thickness — Bottom	79.48	90	42.44	46.89	50.46	[mm]
	Domain Length	2400	3500				[mm]
	Domain Modeled	1/1	1/2				Mold

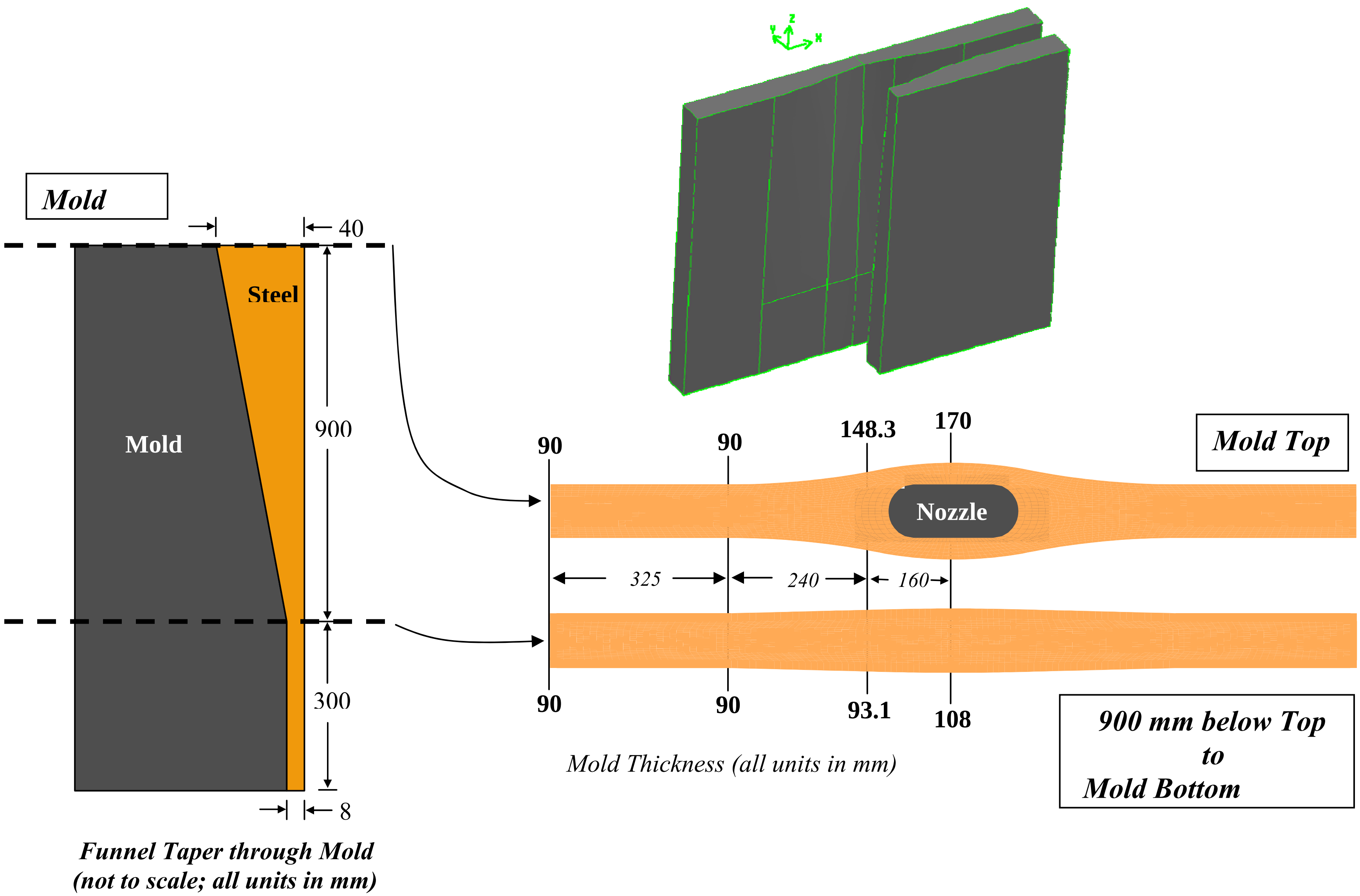

Figure 2.1: Schematic depicting Algoma Steel funnel mold studied with relative dimensions

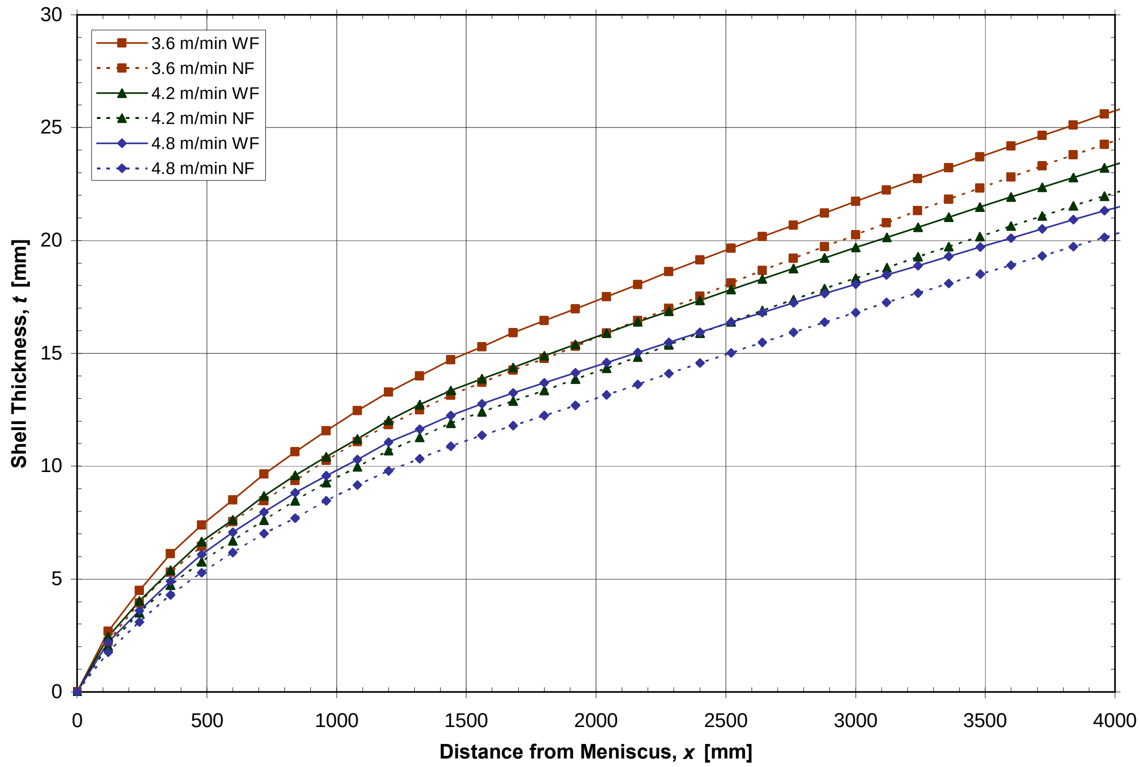

Figure 2.2: Shell thickness comparison (from CON1D[26])

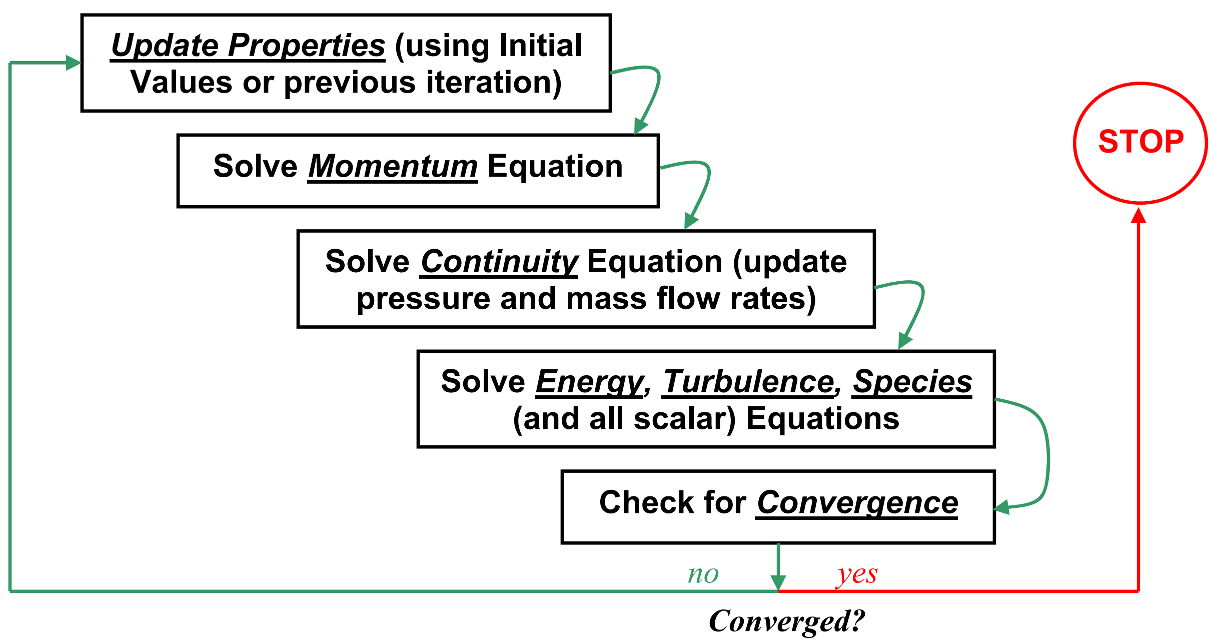

Figure 2.3: Solution procedure and convergence progression for the Fluent segregated solver[33]

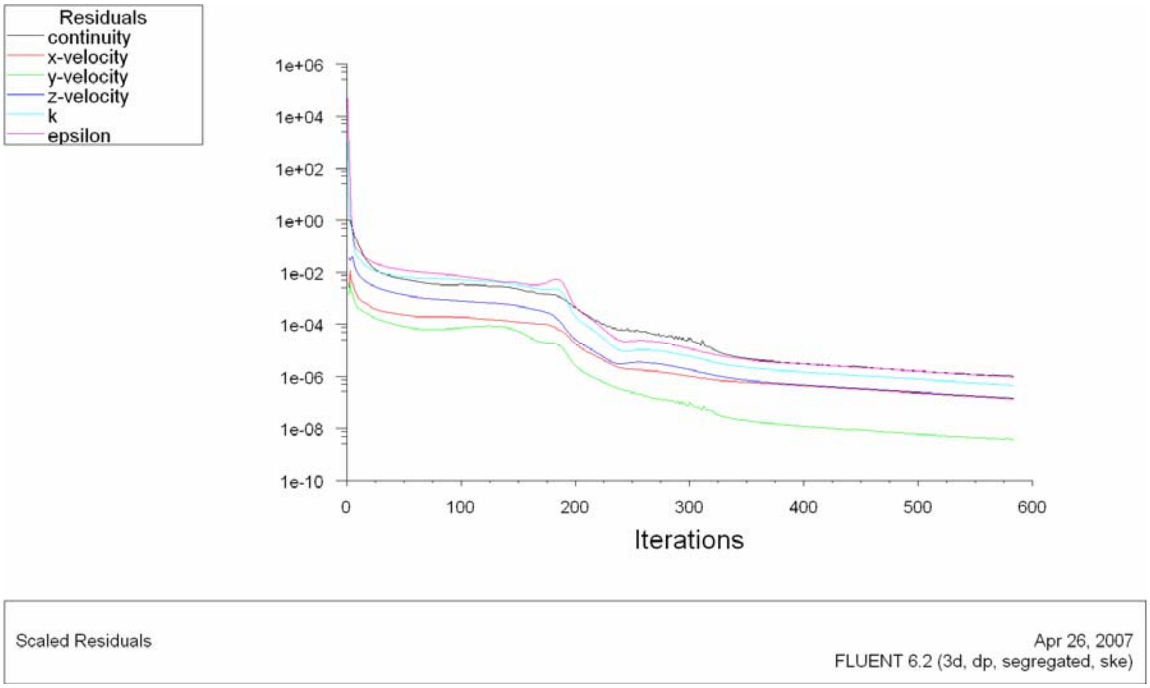

Figure 2.4: Convergence history for nozzle solution (3.6 m/min water model)

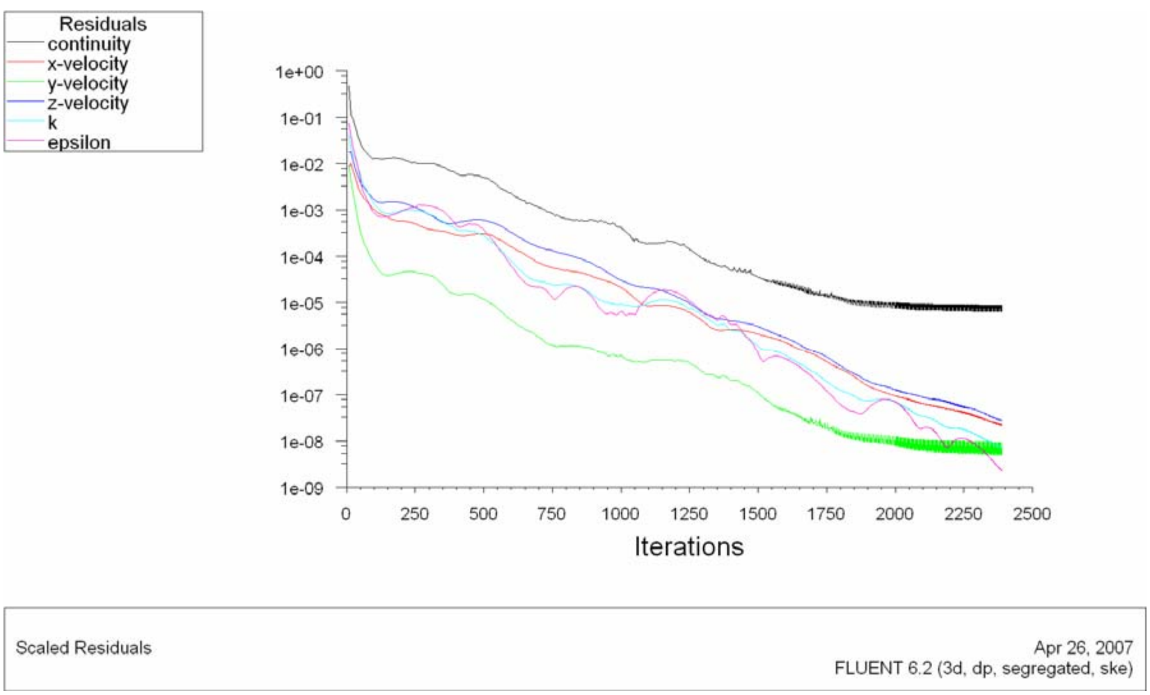

Figure 2.5: Convergence history for typical mold solution (3.6 m/min water model)

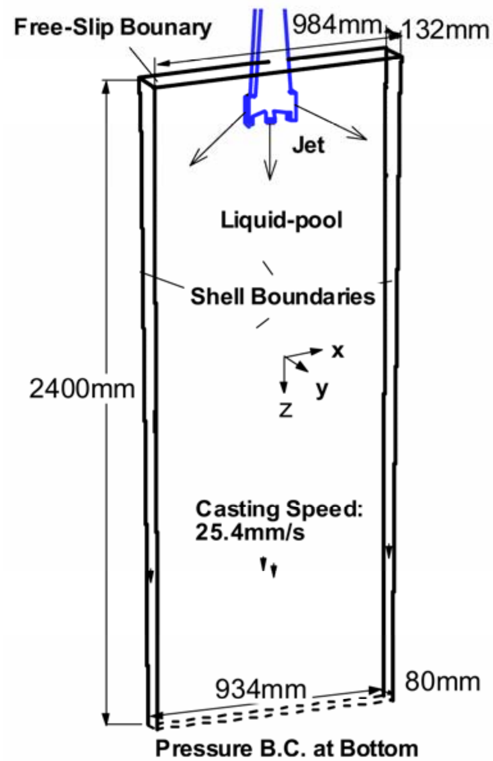

Figure 2.6: Schematic of thin-slab computational domain used for model validation[13)]

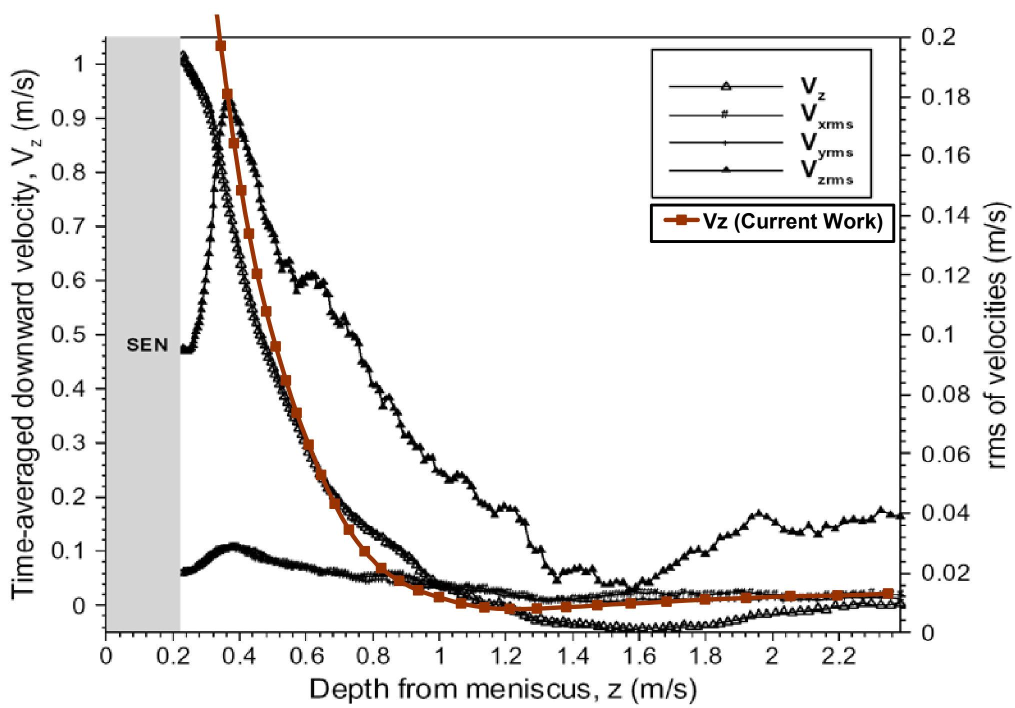

Figure 2.7: Validation of time-averaged velocity along the lower jet centerline axis[13)]

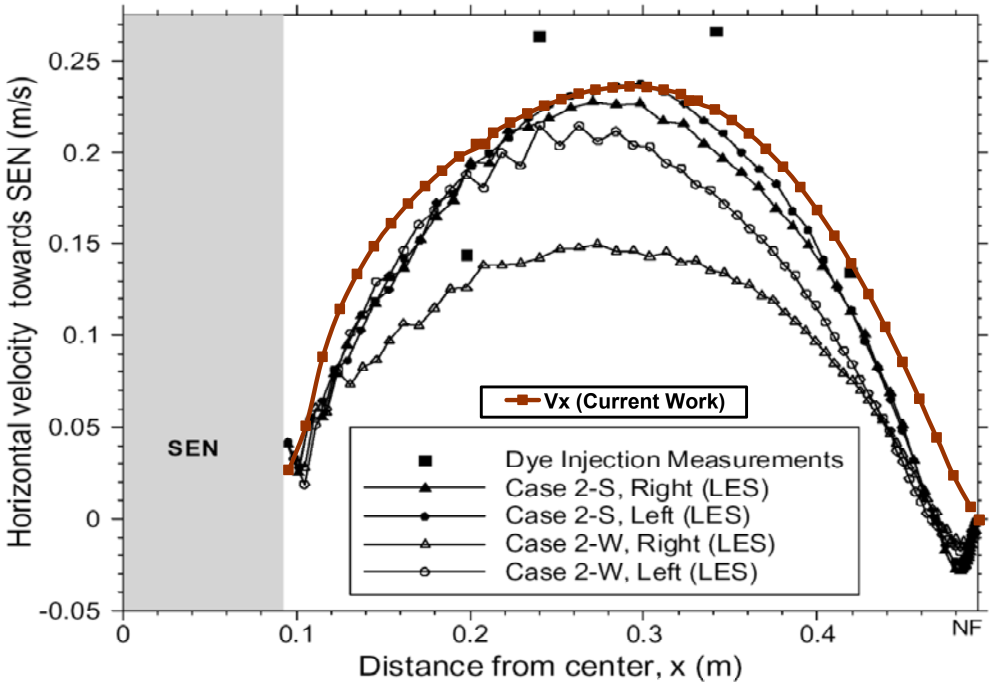

Figure 2.8: Validation of time-averaged horizontal velocity towards SEN along wideface centerline at the top surface[13)]

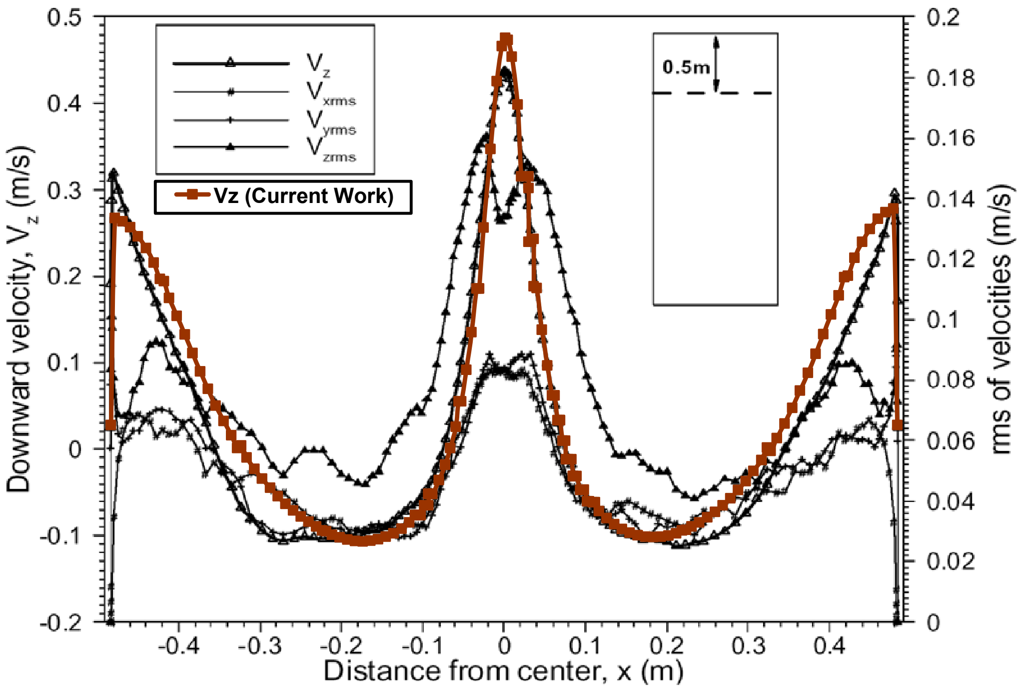

Figure 2.9: Validation of time-averaged velocity along horizontal wideface centerline, 0.5 m below the meniscus[13)]

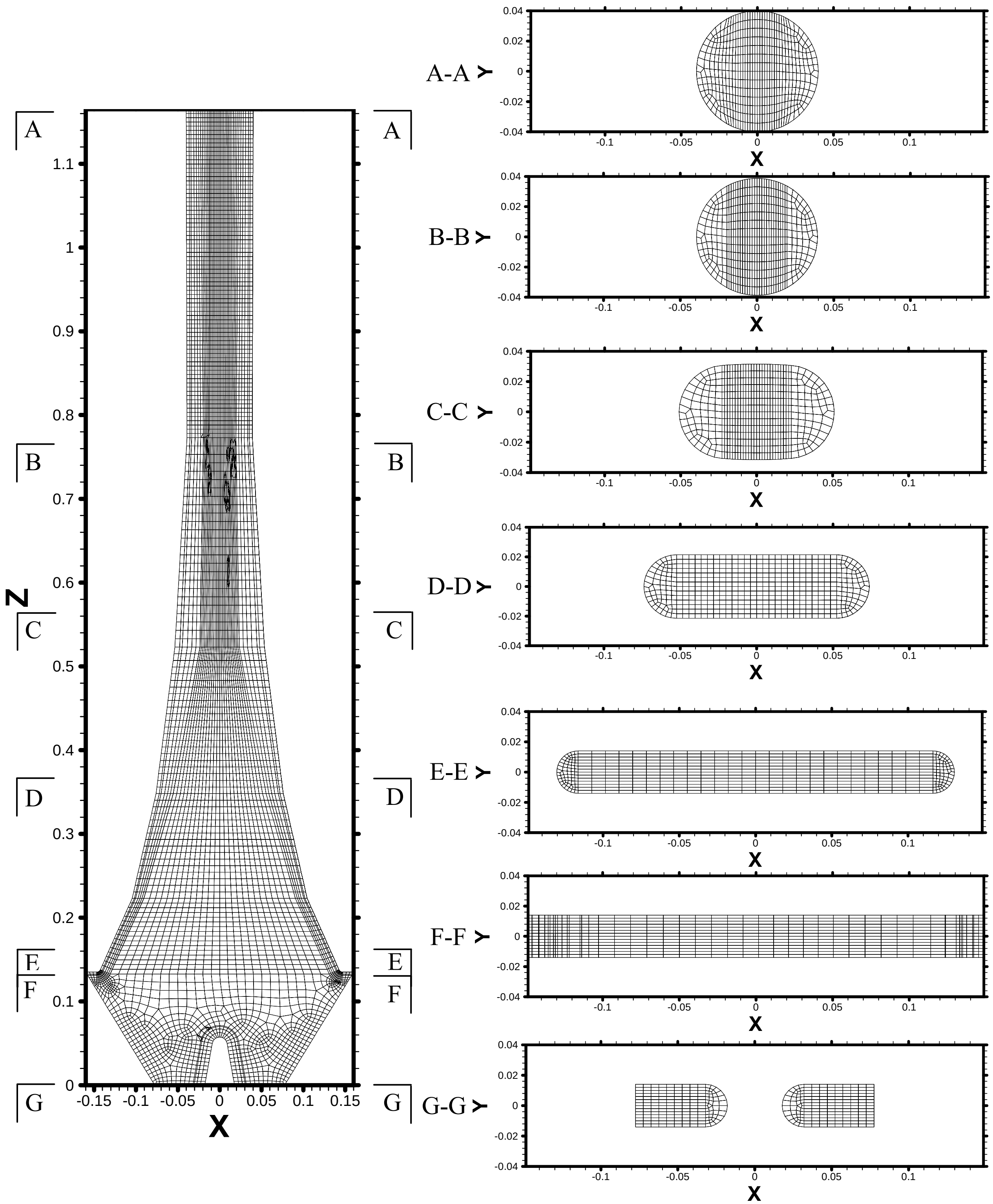

Figure 2.10: Bifurcated nozzle schematic including mesh; grid units in [m]

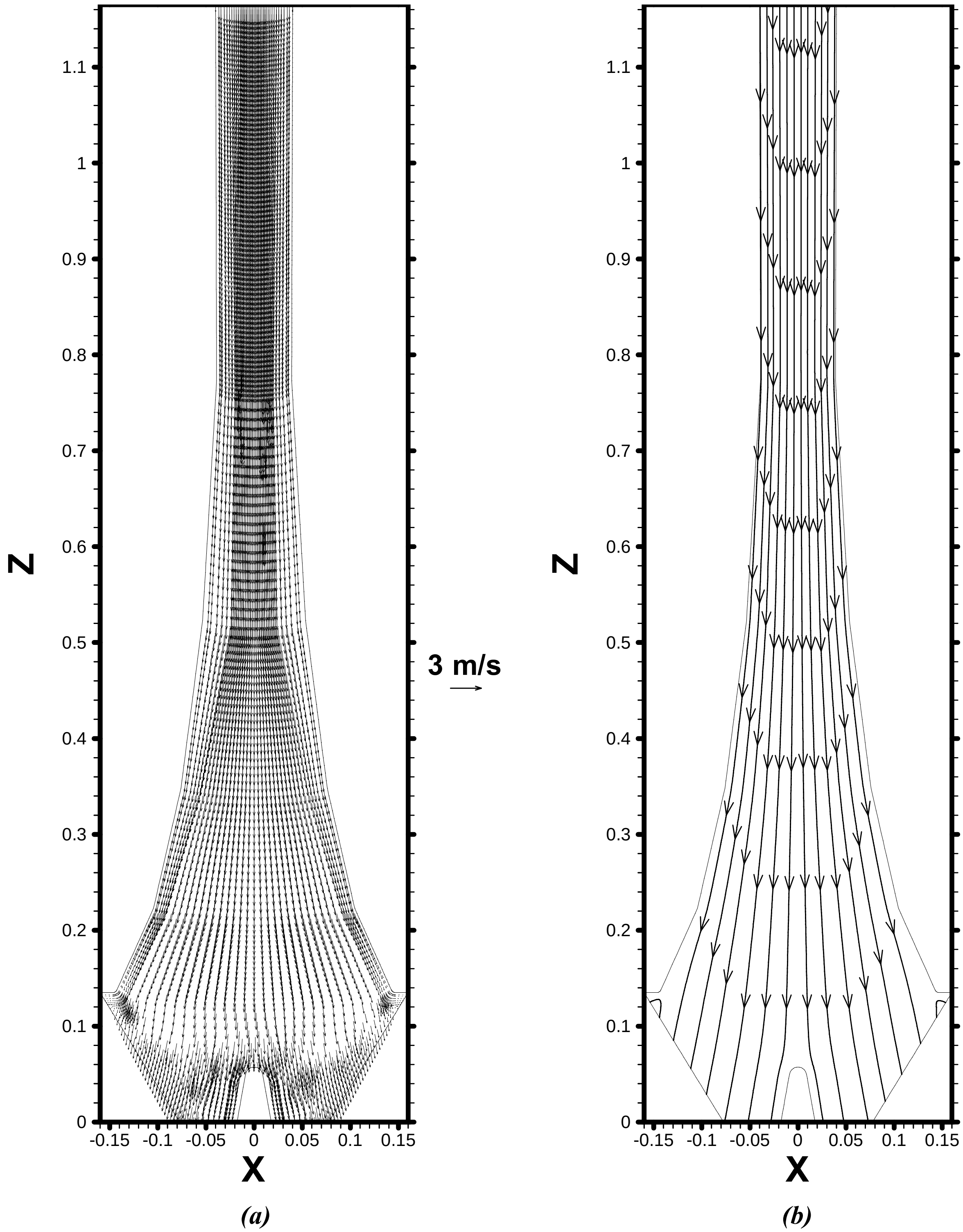

Figure 2.11: Velocity vector **(a)** and streamline plot **(b)** along the nozzle wideface centerline (3.6 m/min case); grid units in [m]

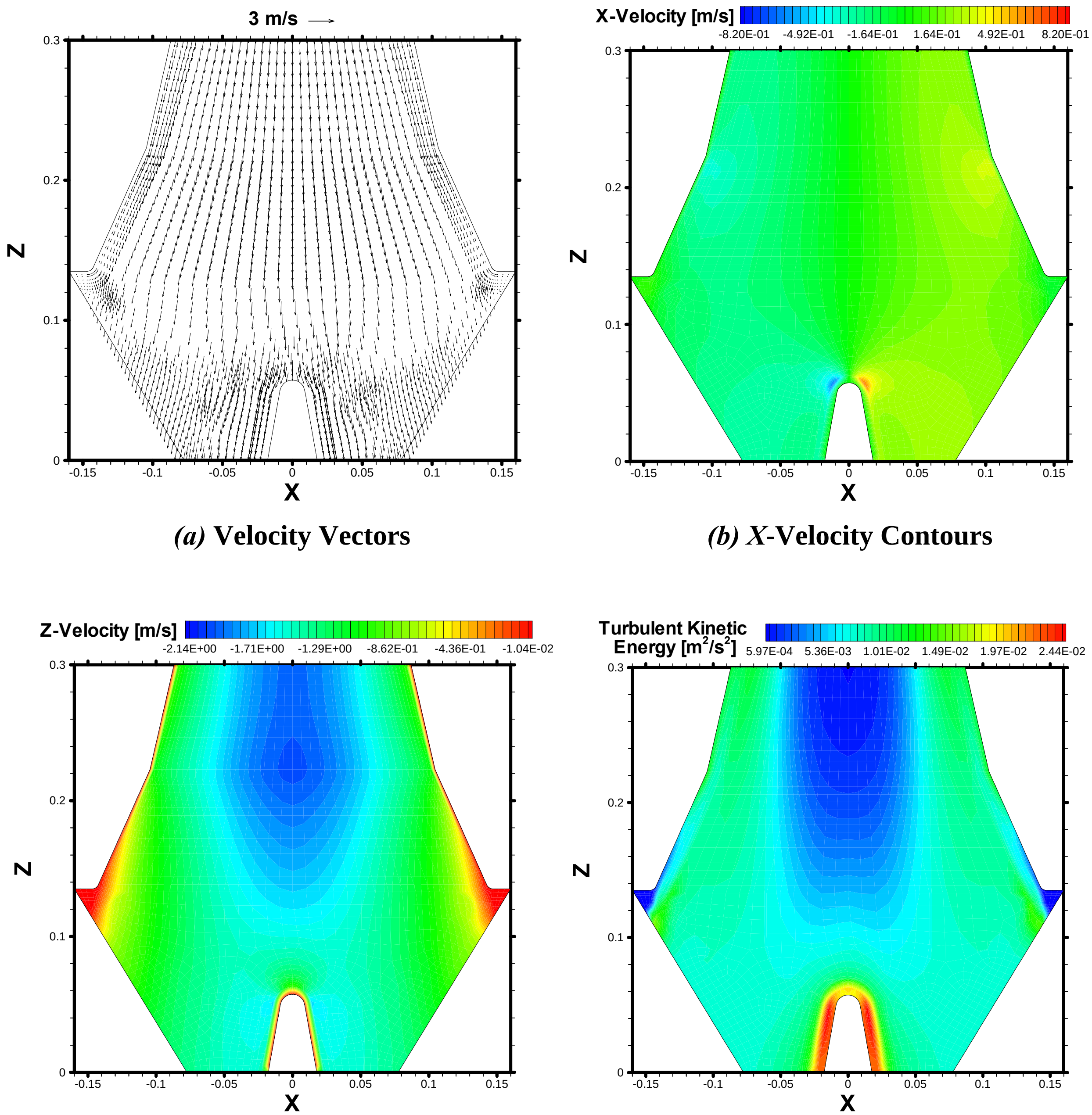

***(a)* Velocity Vectors** ***(b) X*-Velocity Contours**

***(c) Z*-Velocity Contours** ***(d)* Turbulent Kinetic Energy Contours**

Figure 2.12: Velocity and turbulence plots for the lower nozzle centerplane (3.6 m/min steel); grid units in [m]

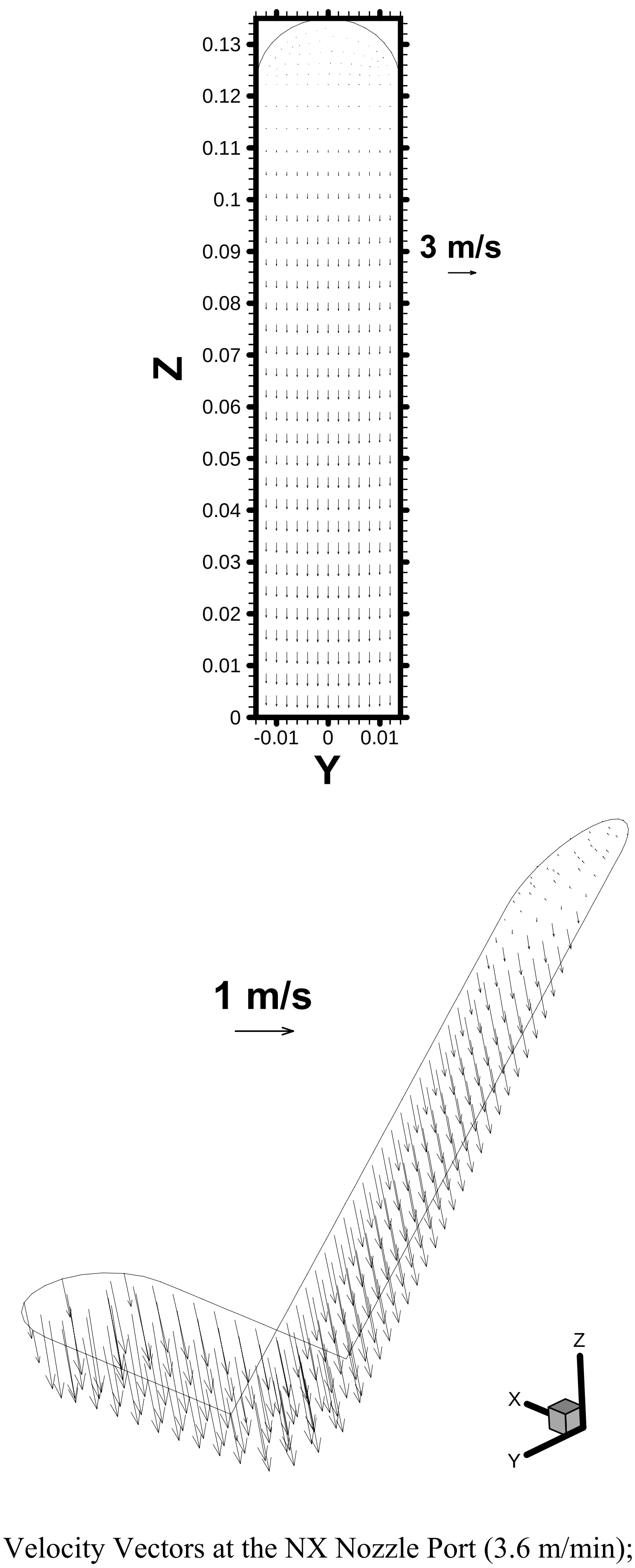

Figure 2.13: Velocity Vectors at the NX Nozzle Port (3.6 m/min); grid units in [m]

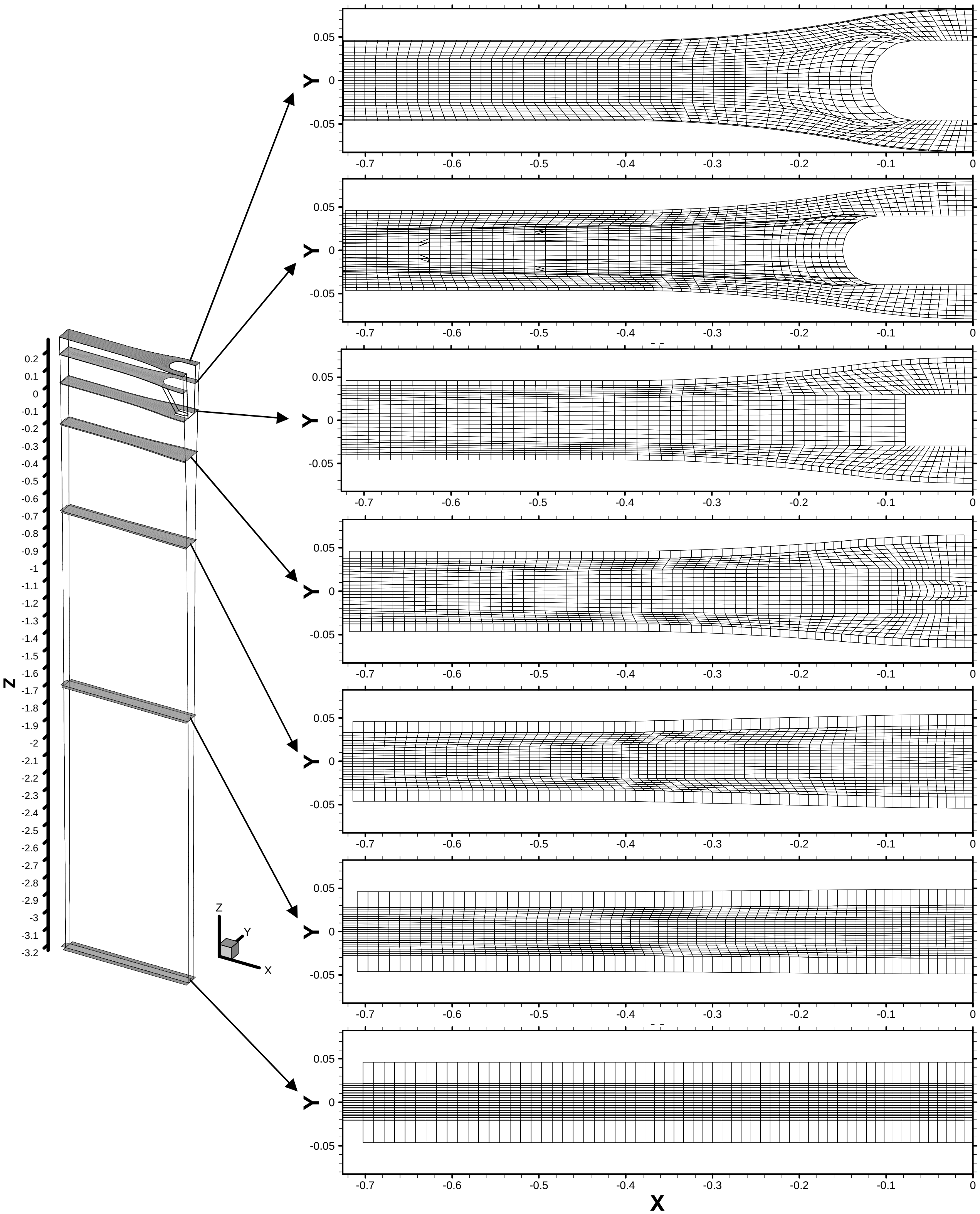

Figure 2.14: Funnel mold schematic including mesh; grid units in [m]

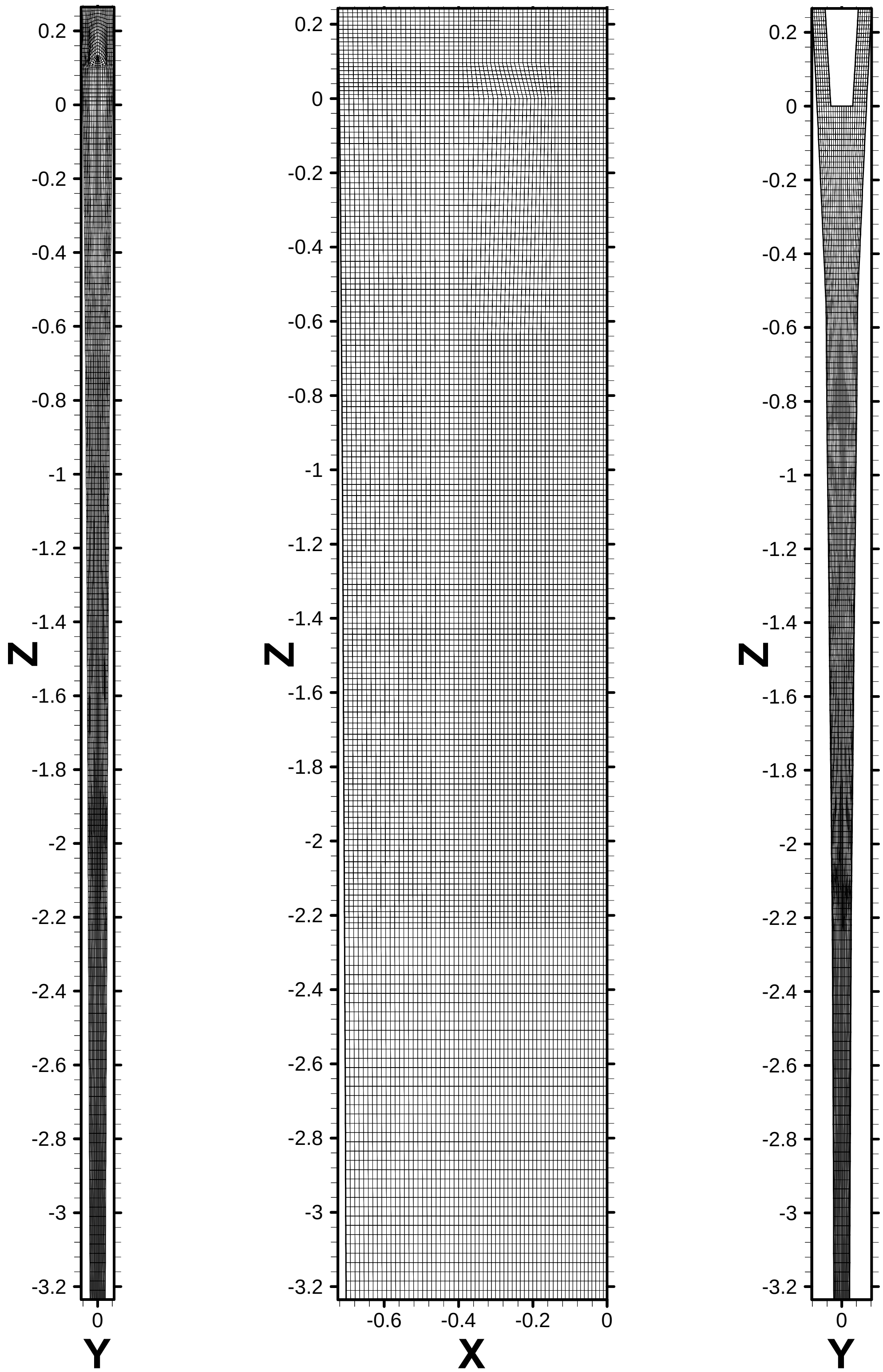

(a) *(b)* *(c)*

Figure 2.15: Funnel mold mesh at **(a)** narrowface, **(b)** wideface, and **(c)** narrowface centerplane; grid units in [m]

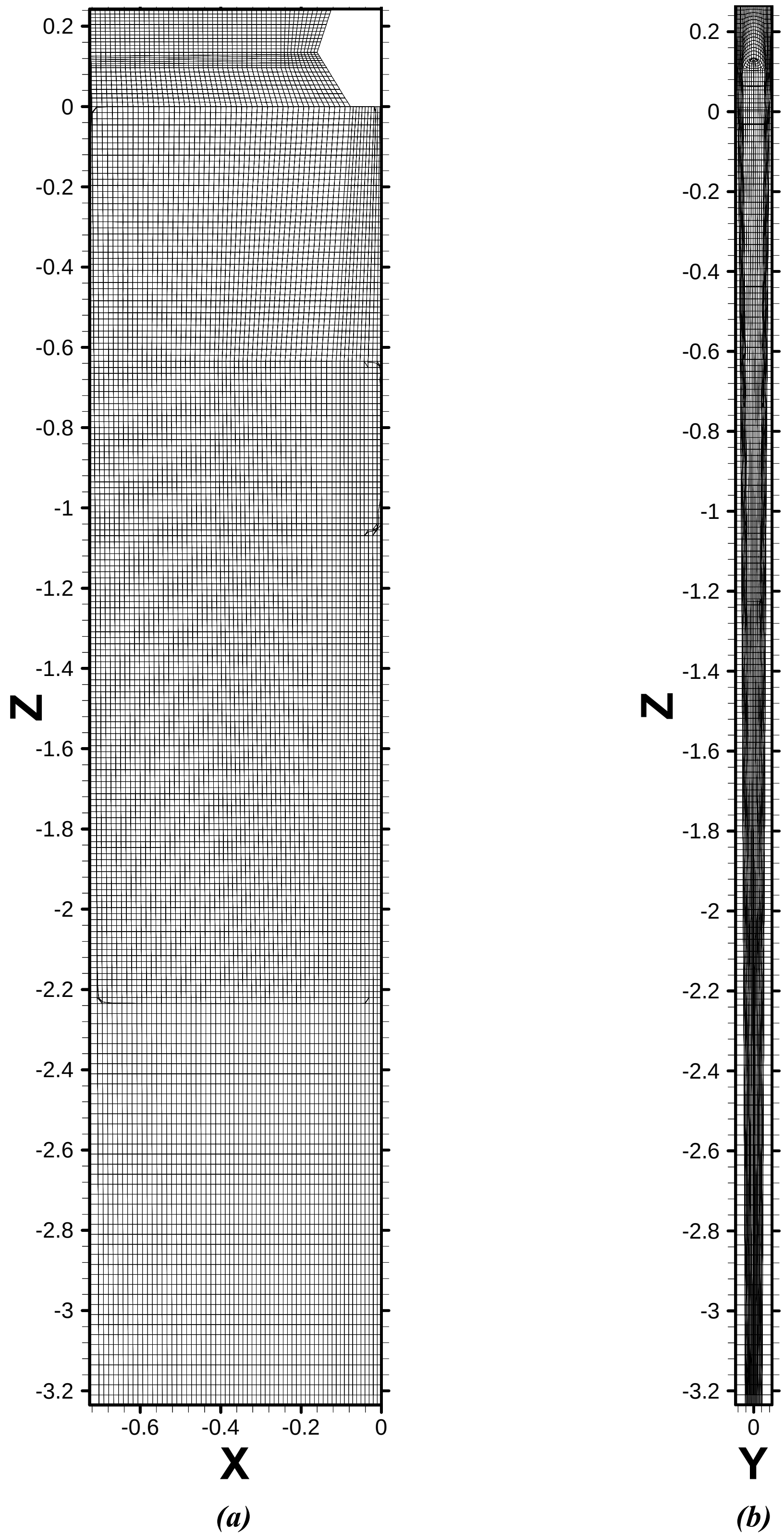

Figure 2.16: Funnel mold mesh at **(a)** wideface centerplane and **(b)** cross section 0.4 m from narrowface centerplane; grid units in [m]

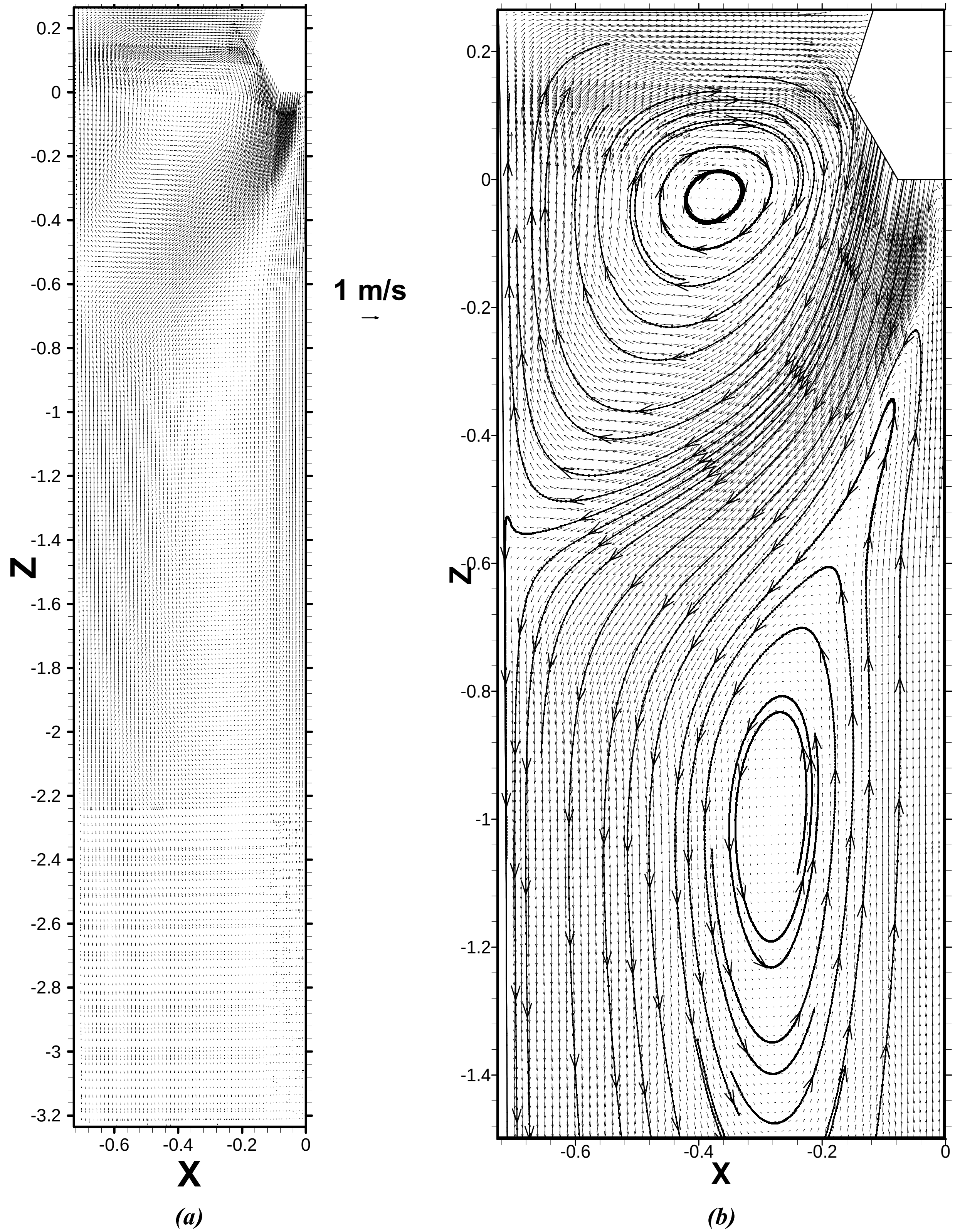

Figure 2.17: Velocity vector **(a)** and streamline plot **(b)** for the wideface centerplane (3.6 m/min steel case); grid units in [m]

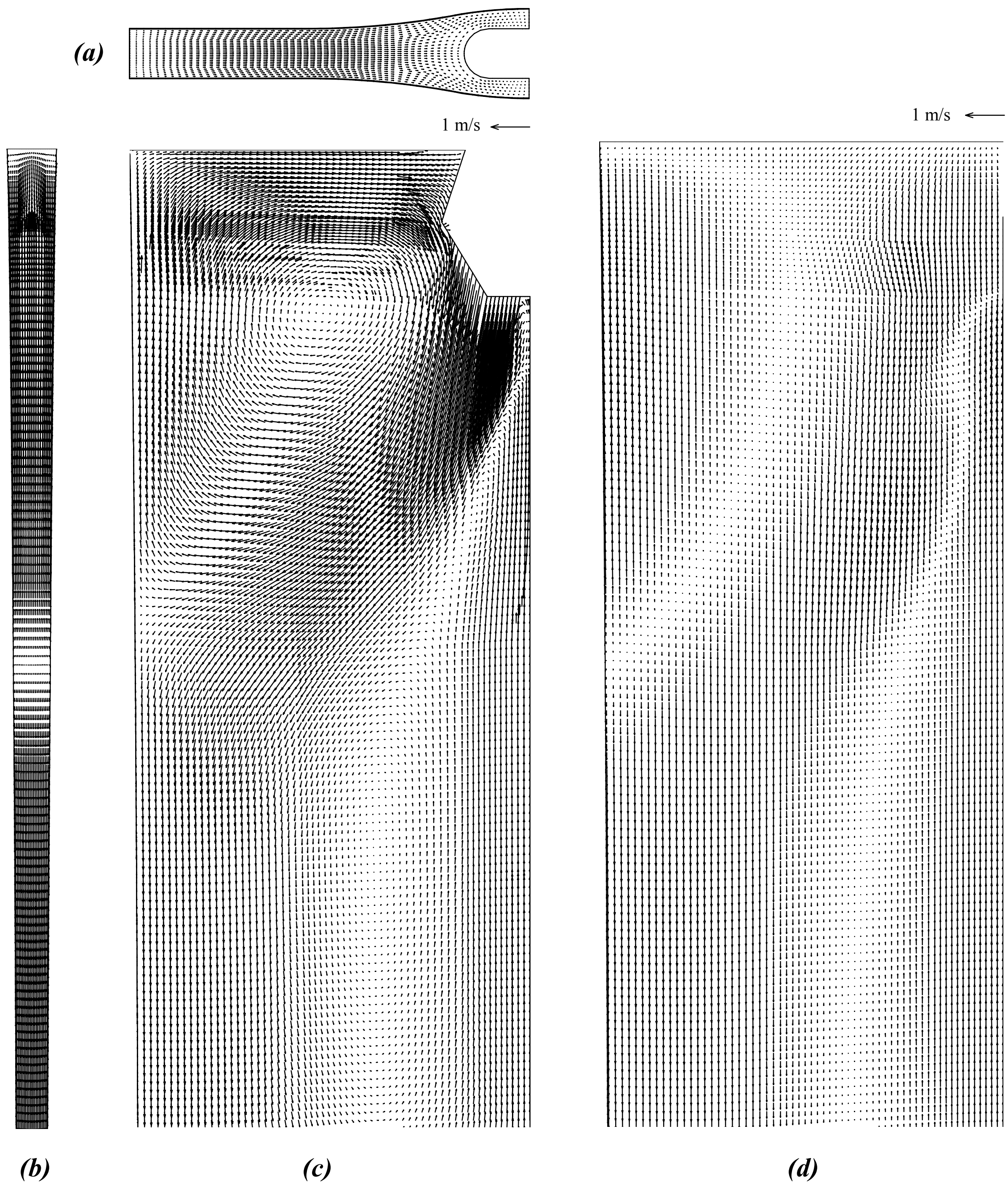

Figure 2.18: Velocity vectors along the 2-D planes **(a)** 2 mm below the top surface, **(b)** 2 mm from narrowface, **(c)** wideface centerplane, and **(d)** 2 mm from wideface (3.6 m/min Steel Case)

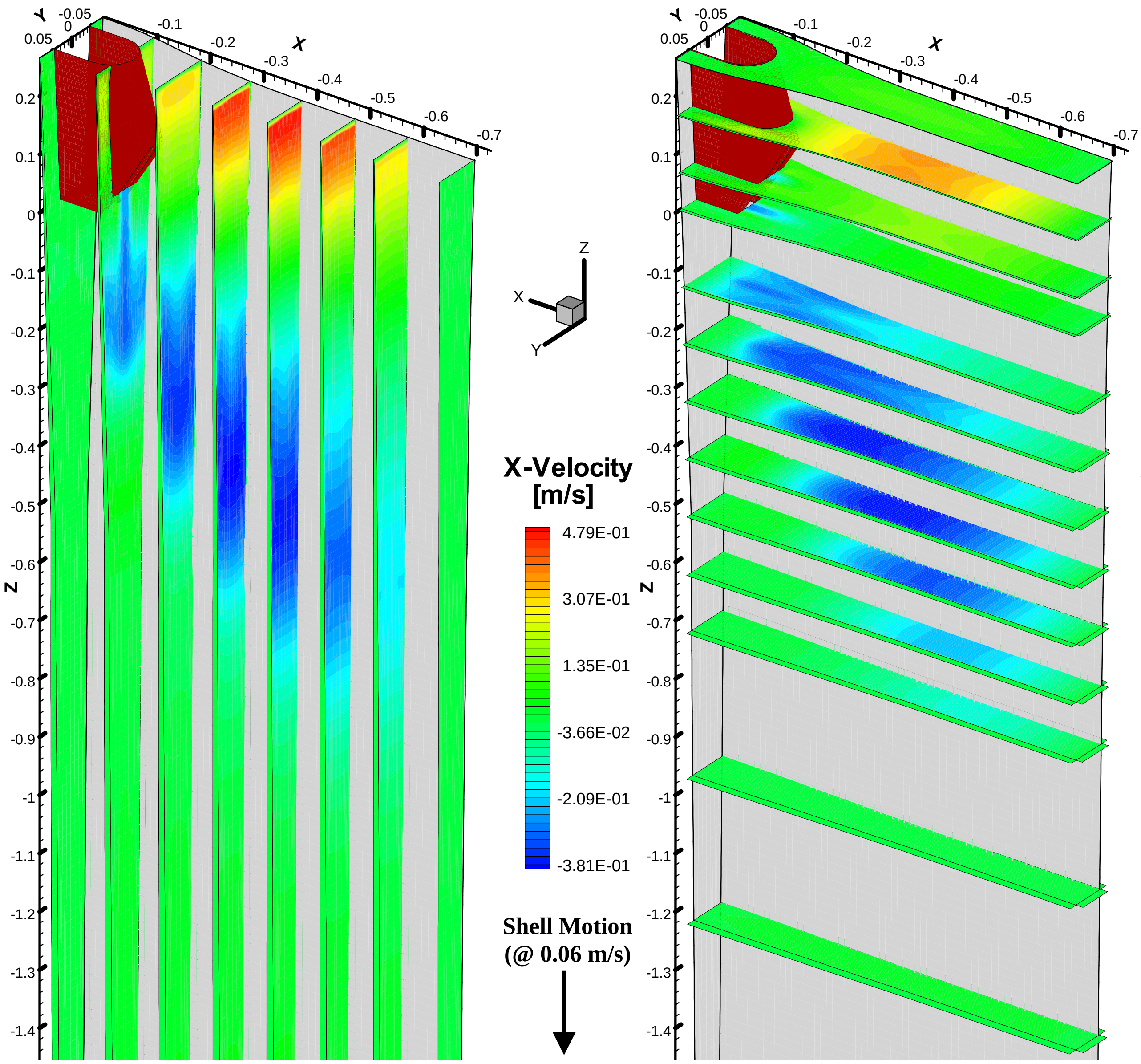

Figure 2.19: U_x contour slices (3.6 m/min Steel Case); grid units in [m]

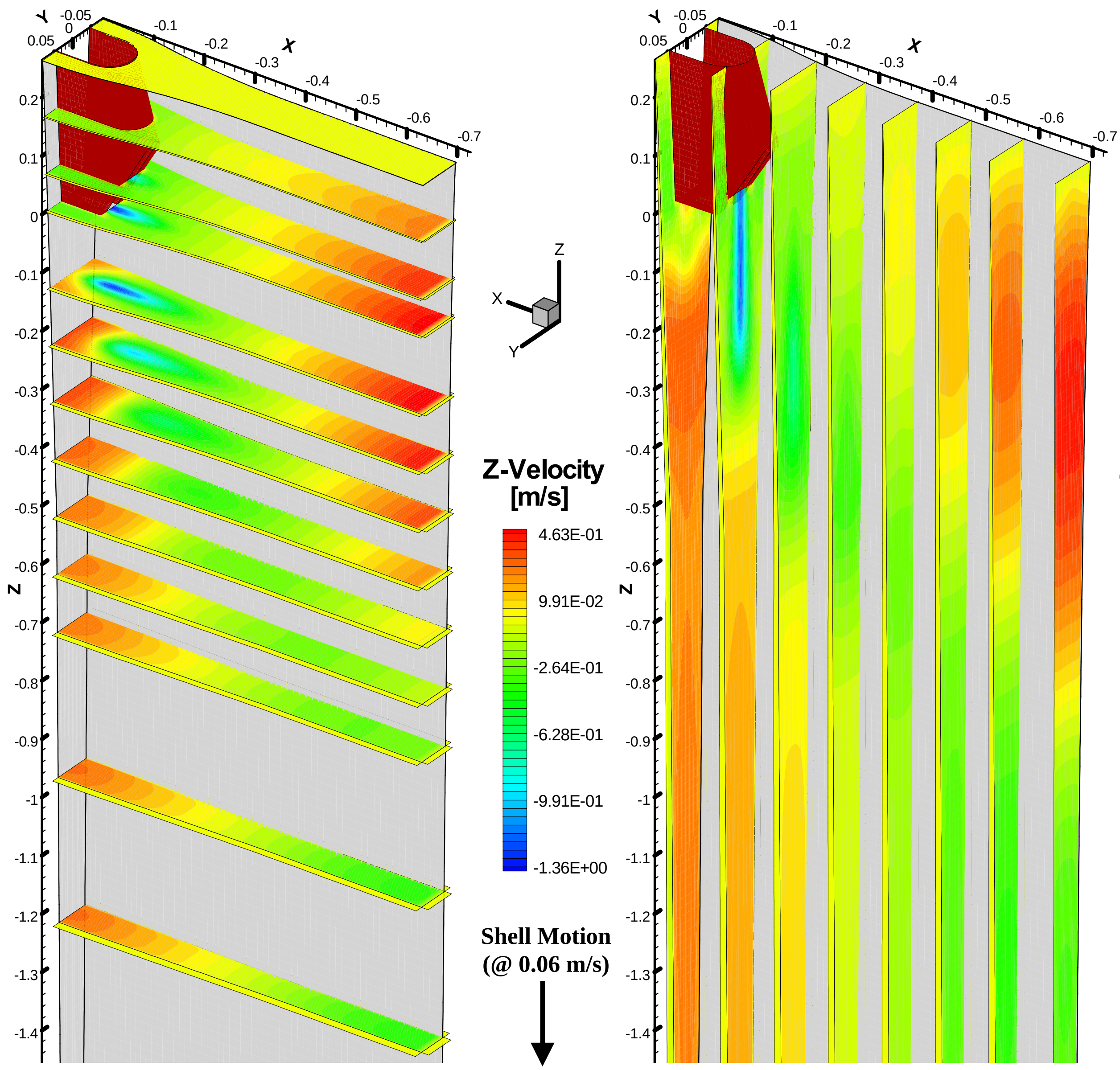

Figure 2.20: U_z contour slices (3.6 m/min Steel Case); grid units in [m]

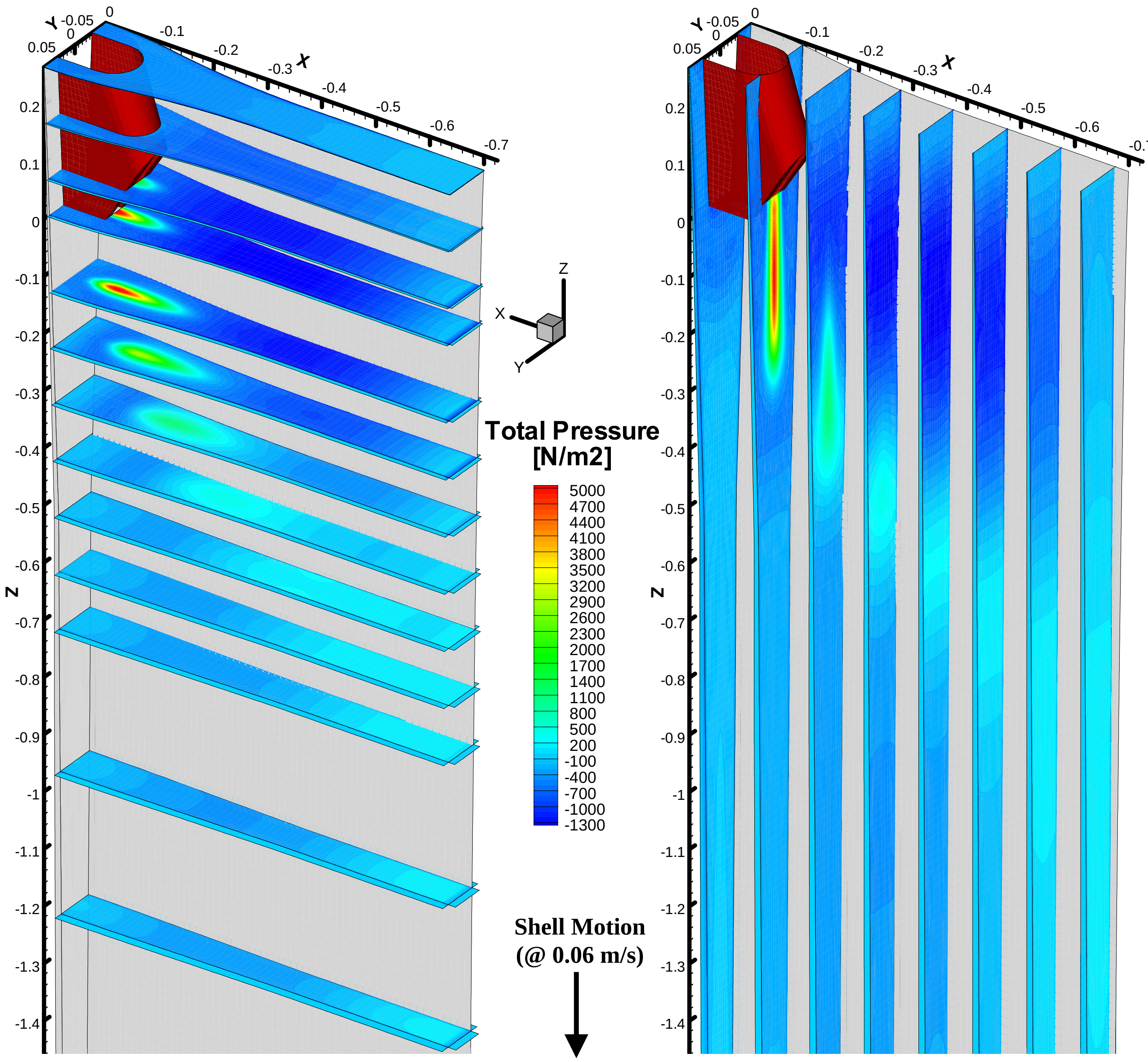

Figure 2.21: Pressure contour slices (3.6 m/min Steel Case); grid units in [m]

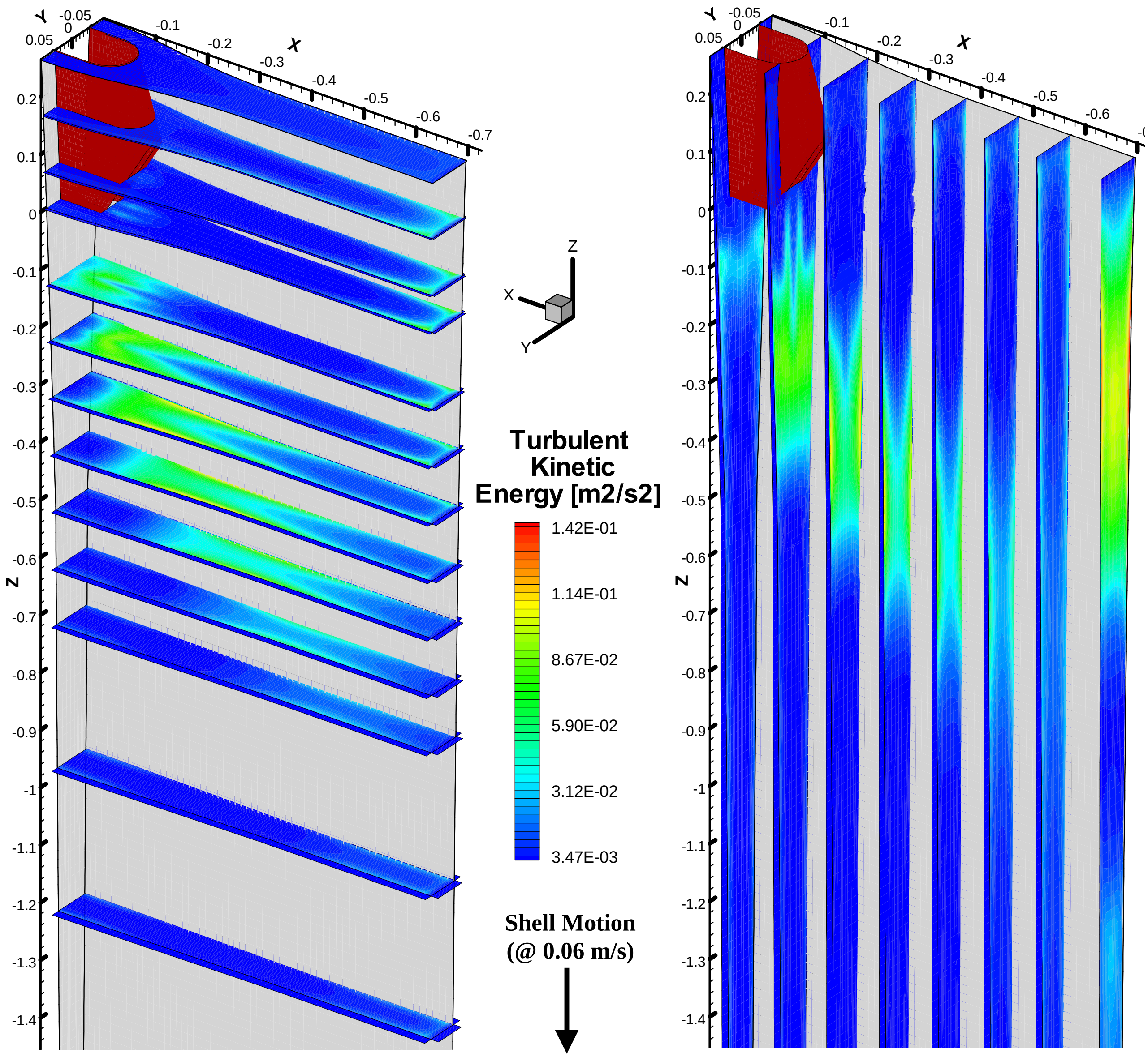

Figure 2.22: Turbulent kinetic energy contour slices (3.6 m/min Steel Case); grid units in [m]

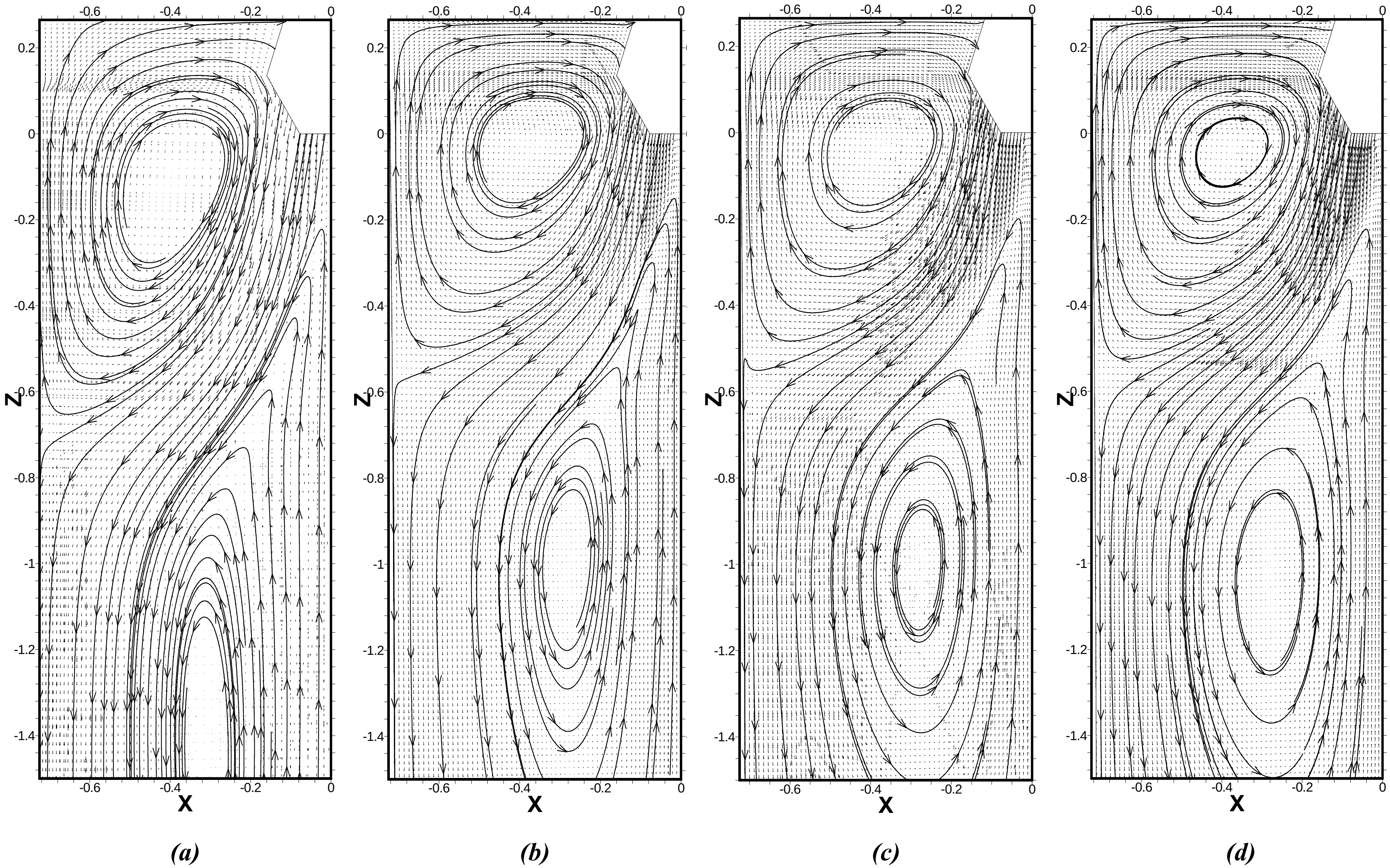

Figure 2.23: Velocity vector plots (with streamlines) along the wideface centerplane for **(a)** 3.6 m/min Water Model, **(b)** 3.6 m/min Steel Case, **(c)** 4.2 m/min Steel Case, and (d) 4.8 m/min Steel Case; grid units in [m]

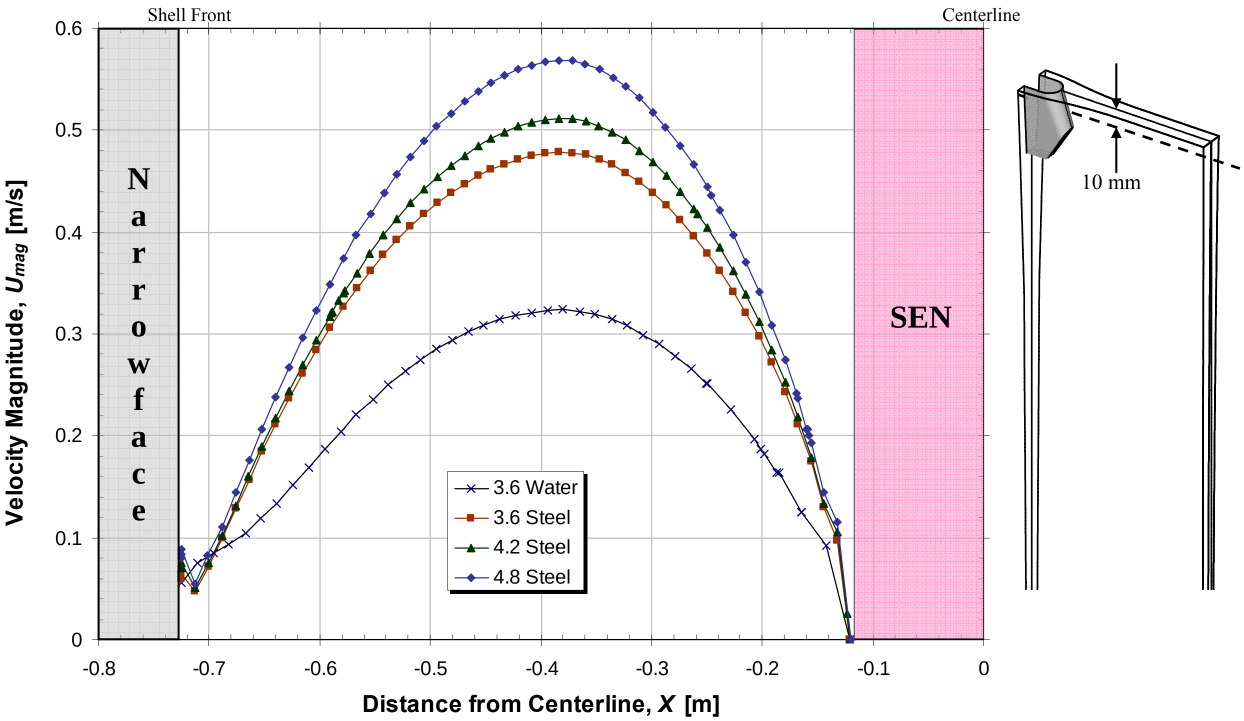

Figure 2.24: Velocity magnitude comparison along the wideface centerline @ 10 mm below the top surface.

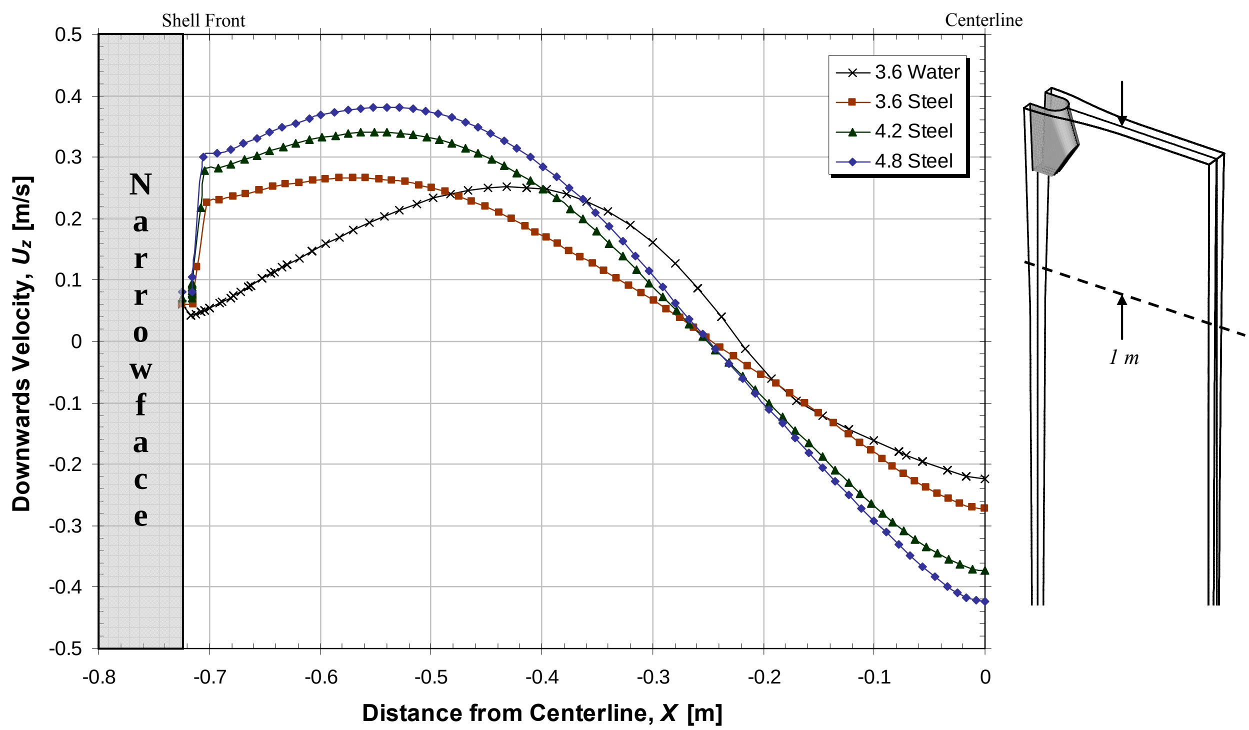

Figure 2.25: Downward velocity comparison along the wideface centerline @ 1 m below the top surface.

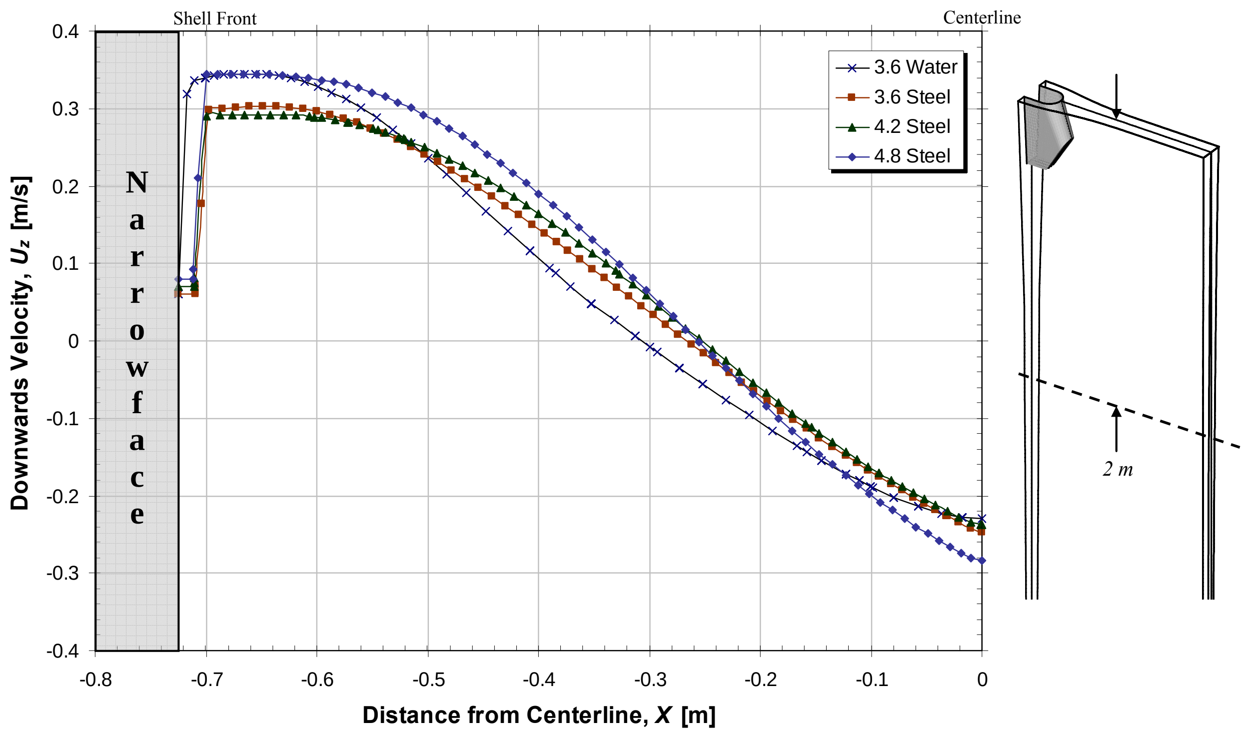

Figure 2.26: Downward velocity comparison along the wideface centerline @ 2 m below the top surface.

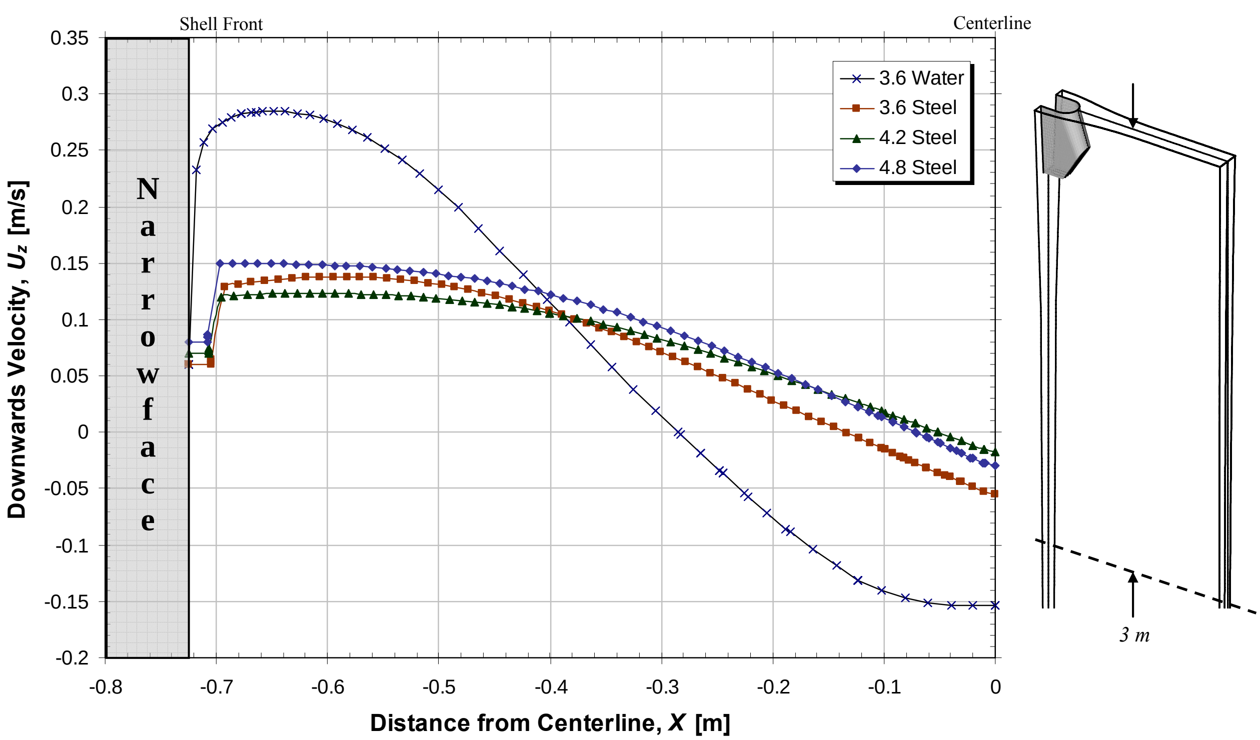

Figure 2.27: Downward velocity comparison along the wideface centerline @ 3 m below the top surface.

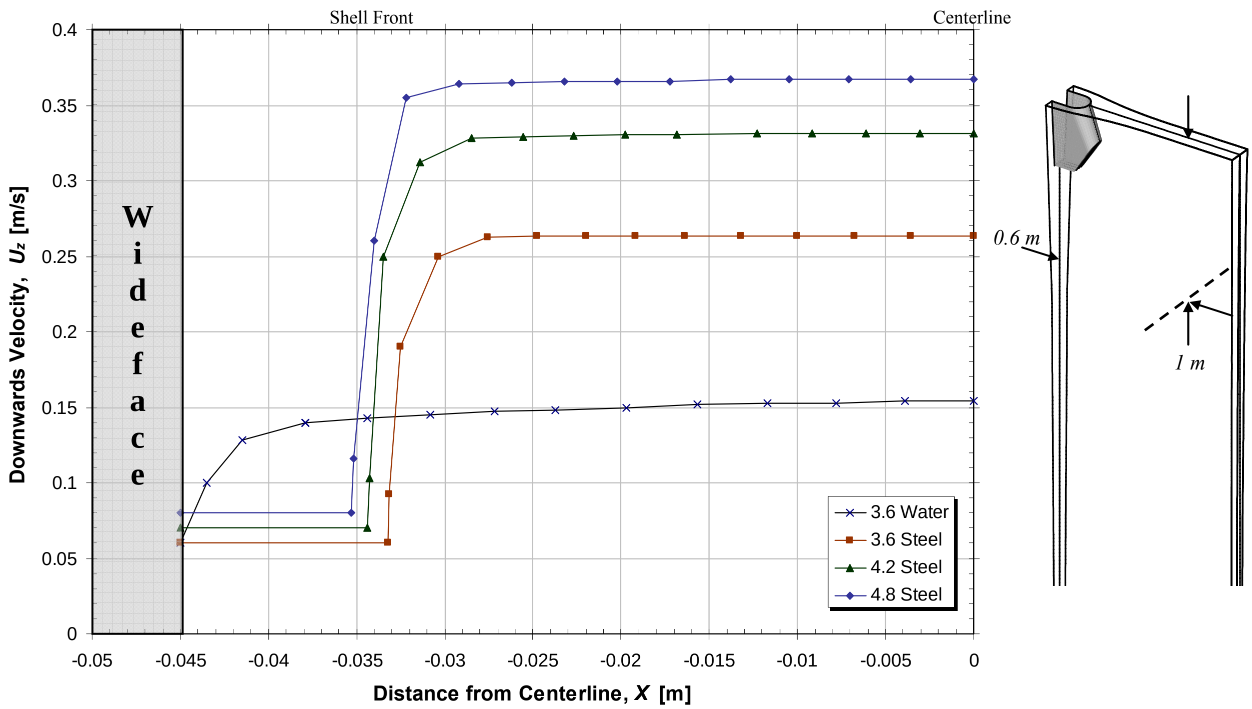

Figure 2.28: Downward velocity comparison @ 0.6 m from narrowface centerline, 1 m below top surface

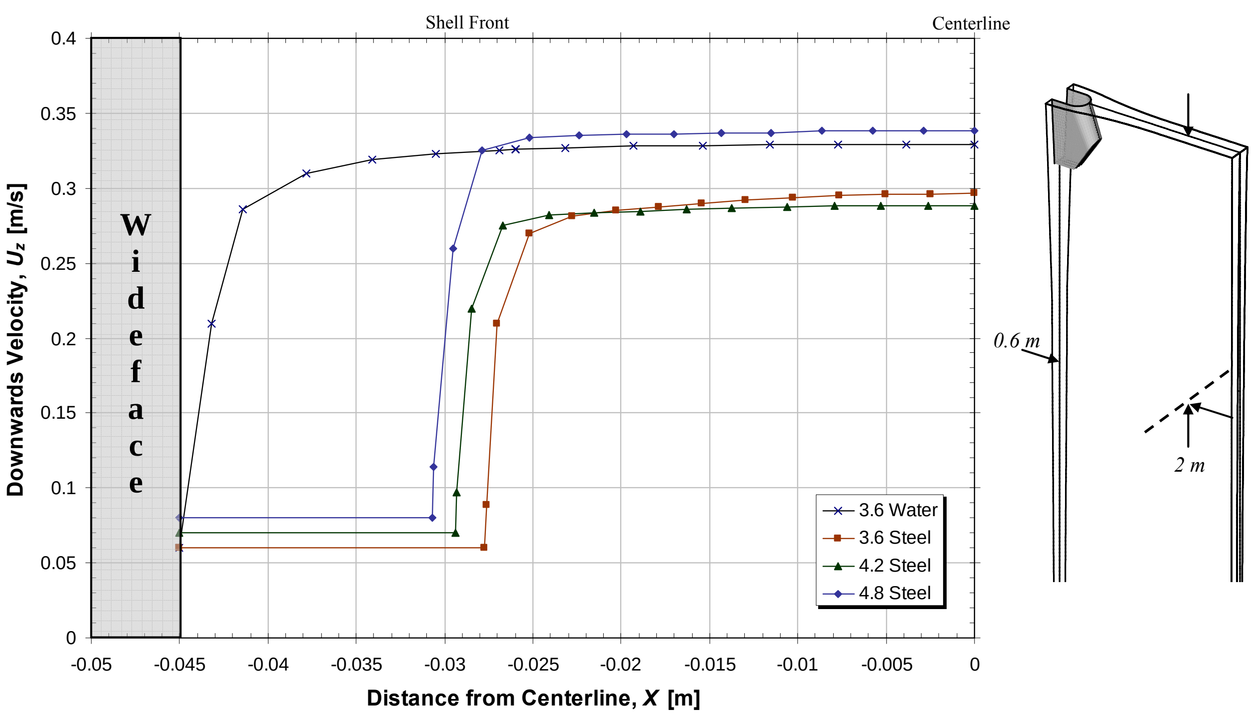

Figure 2.29: Downward velocity comparison @ 0.6 m from narrowface centerline, 2 m below top surface

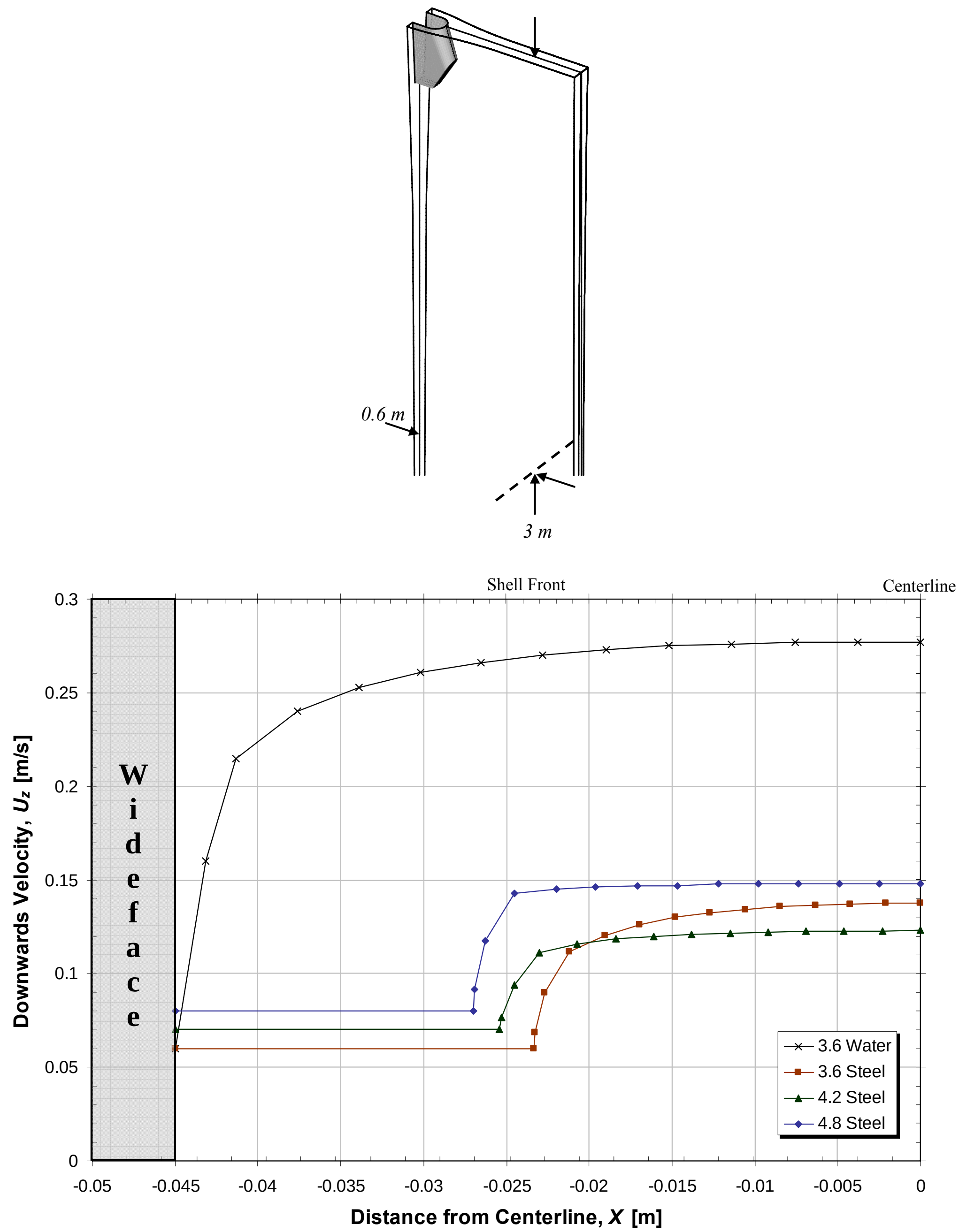

Figure 2.30: Downward velocity comparison @ 0.6 m from narrowface centerline, 3 m below top surface

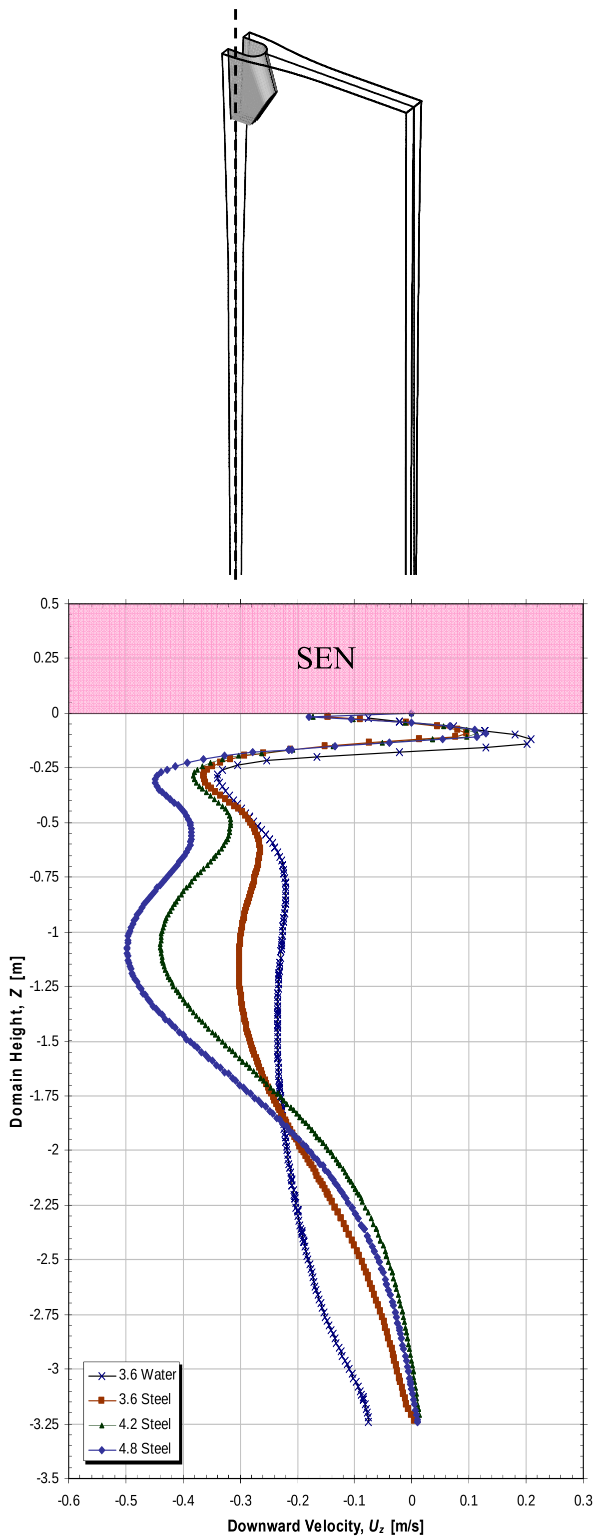

Figure 2.31: Downward velocity comparison along wideface and narrowface centerplane intersection

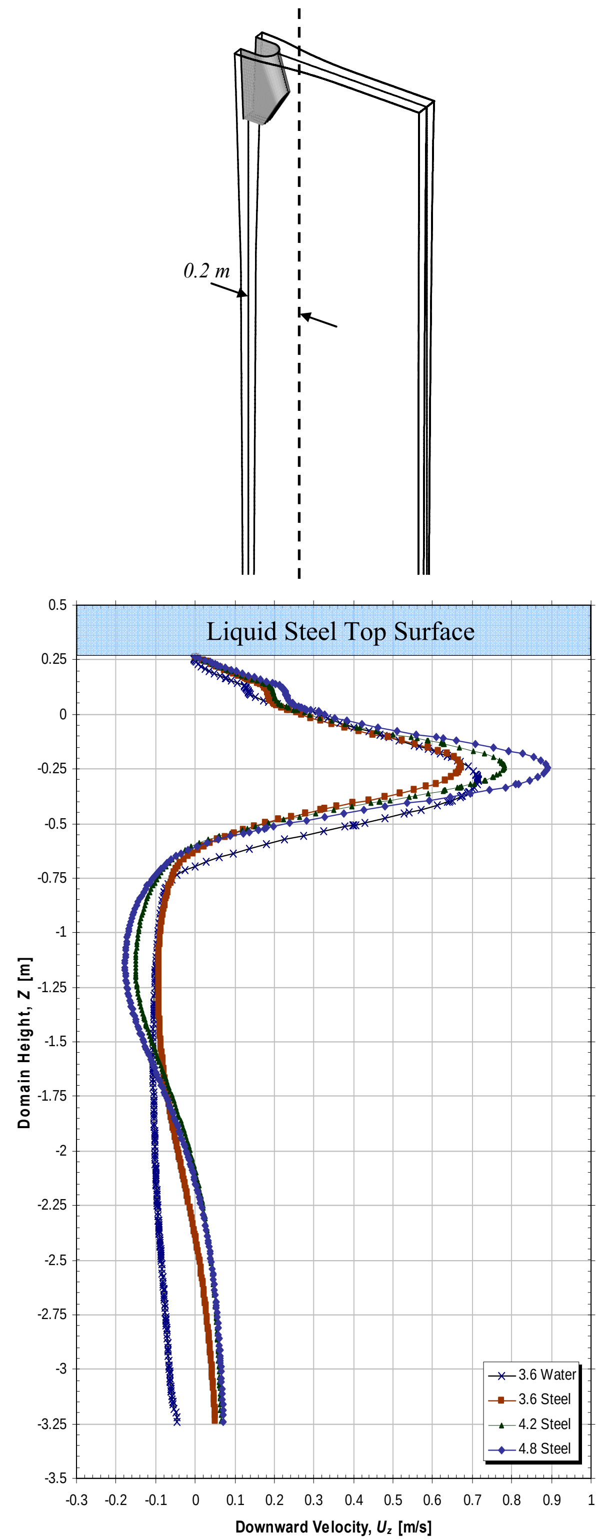

Figure 2.32: Downward velocity comparison along wideface centerplane, 0.2 m from narrowface

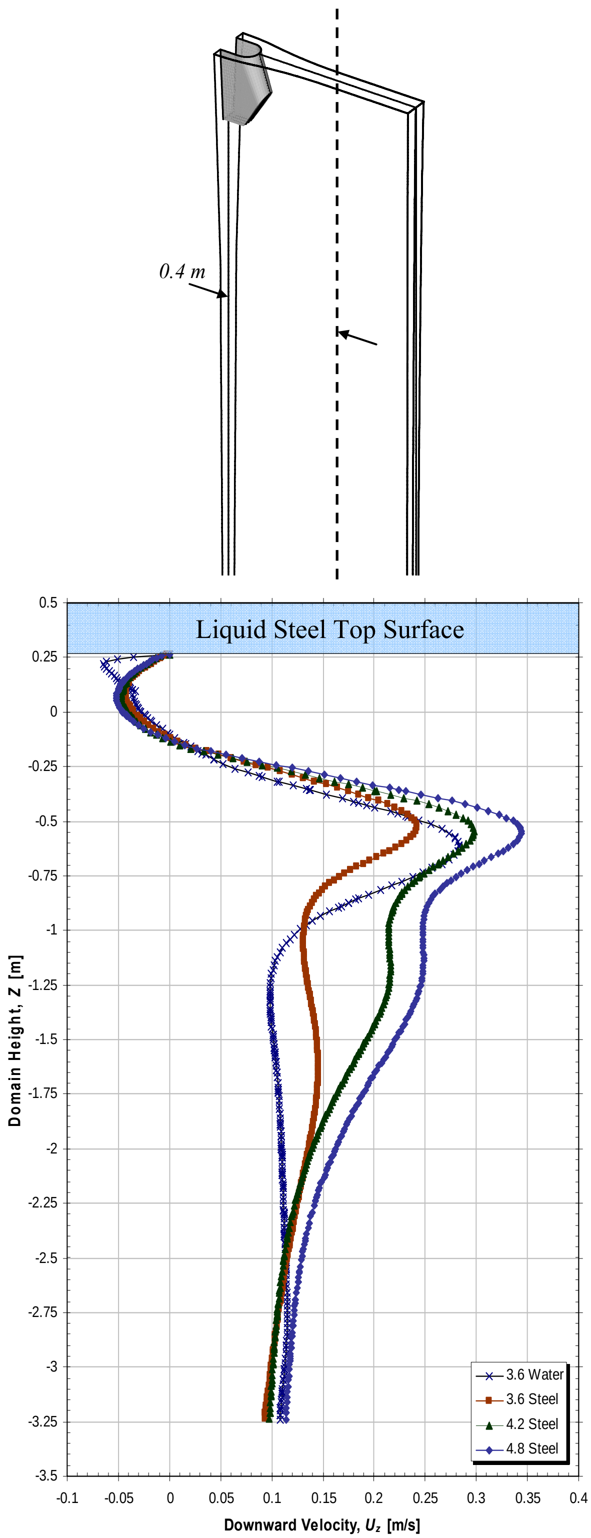

Figure 2.33: Downward velocity comparison along wideface centerplane, 0.4 m from narrowface centerplane

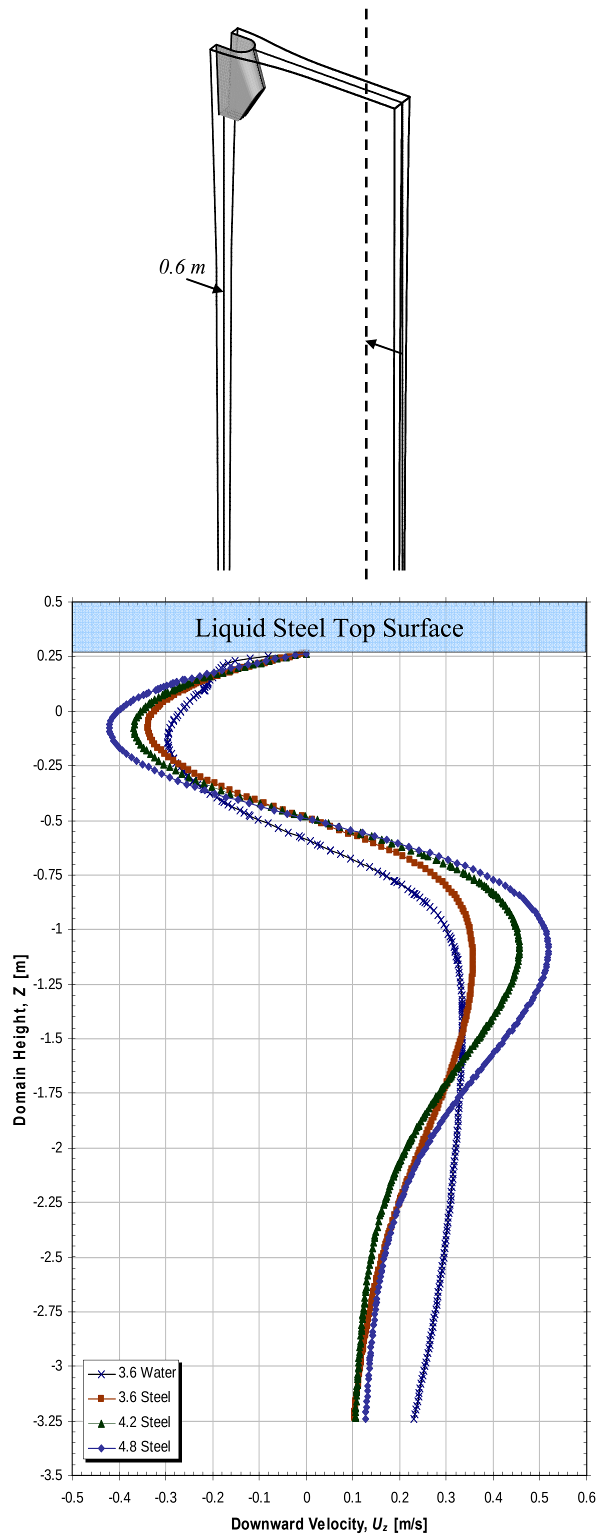

Figure 2.34: Downward velocity comparison along wideface centerplane, 0.6 m from narrowface centerplane

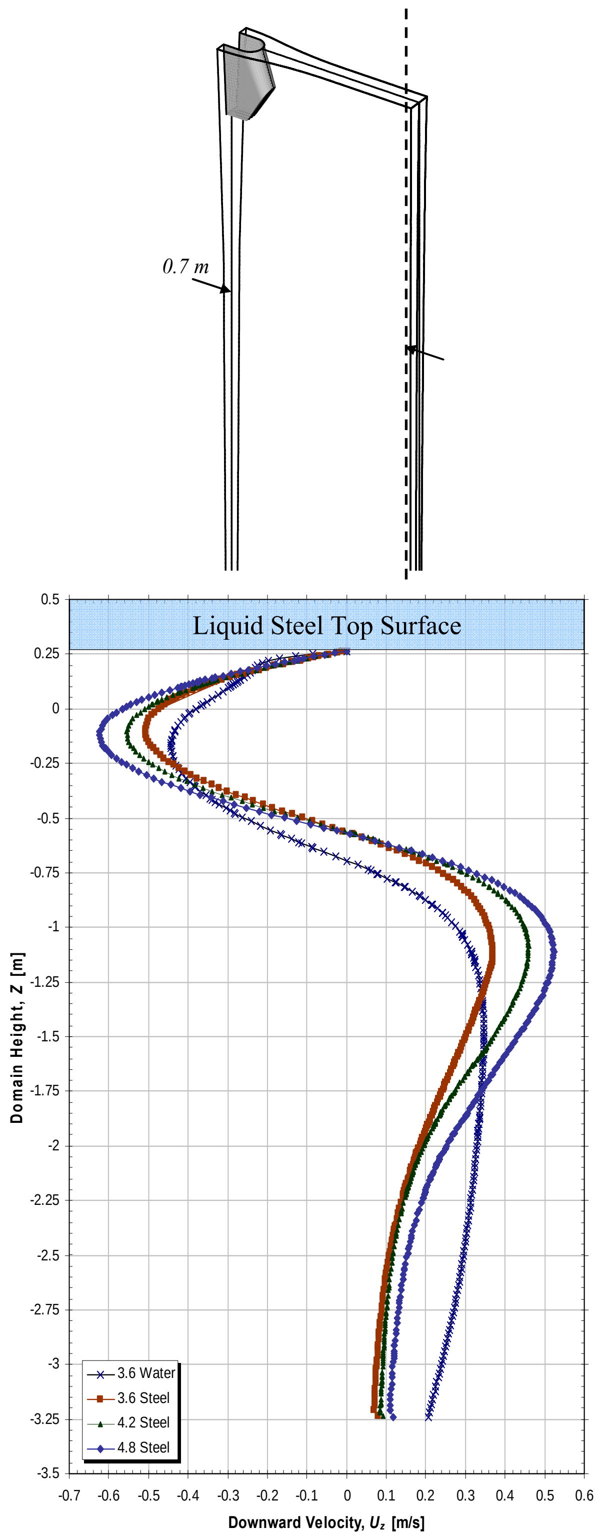

Figure 2.35: Downward velocity comparison along wideface centerplane, 0.7 m from narrowface centerplane

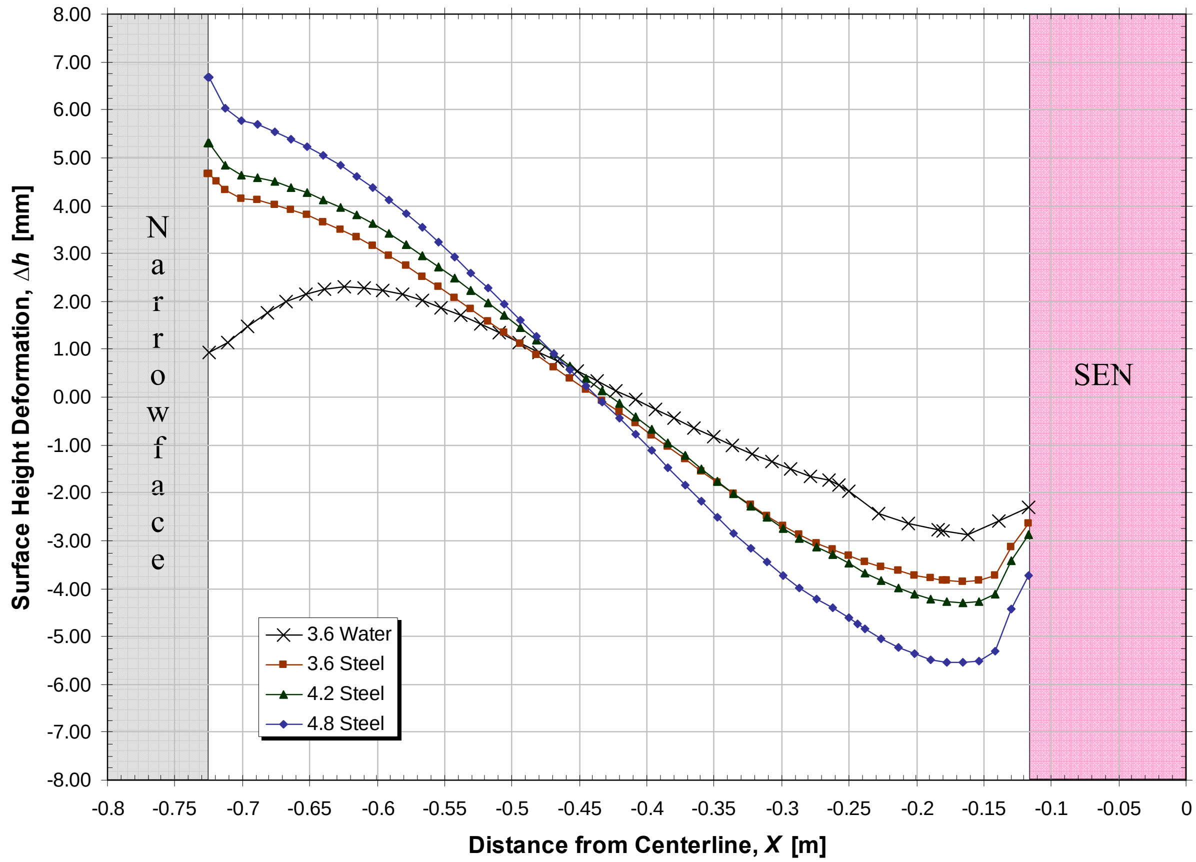

Figure 2.36: Top surface height approximation along wideface centerline using fixed surface pressures

CHAPTER 3: NAILBOARD METHOD

3.1 Introduction

In regard to the surface quality, meniscus-level velocity has been shown to have a large impact on the quality of the final steel product[34]. Through this, the need to monitor the velocity at the meniscus is apparent. With a simple, effective way to determine this critical velocity, off-line models can be created which allow for more rigorous control over the entire continuous casting process. The result of this control will be a tighter grip on quality and thus a more consistent final product.

The method to determine meniscus velocity which will be investigated in this model is termed the "Nailboard" Method. In this procedure, one or more nails are inserted into a wooden board and subsequently dipped into the molten steel at the top surface for about 3-5 seconds. Care is taken not to hold the nails submerged in the molten steel for longer to prevent complete melting of the nail, which would yield no results. A simple schematic of this procedure is outlined in Figure 3.1. Once removed from the fluid, the nails will have a "knob" of solidified steel on the previously submerged end. The top surface of this knob has a characteristic profile in relation to the nail axis, which is used to estimate steel velocity at the test location.

The Nailboard Method is not an entirely new procedure. In previous studies, McDavid has performed a variation of this process, albeit to achieve a different goal. Steel rods with aluminum wires affixed to them were submerged into the liquid steel pool at the top of the mold[35]. Exploiting the lower melting temperature of aluminum than steel, a solidified knob was formed on the steel rod while the aluminum wires were melted off by the steel and slag layers. McDavid was able to experimentally determine the height of the steel top surface as well as the liquid slag layer thickness through his tests. Unfortunately, he did not use the knob to generate any steel velocity estimations.

Assuming that the nails are inserted exactly perpendicular to the top surface, Thomas proposed that this profile could be used to determine the meniscus-level fluid velocity[4]. A similar technique is commonly used in the continuous casting industry to determine the flow direction, as the higher end of the knob shows the direction in which the flow approached the nail. However, a model has not yet been developed to provide a relation between fluid velocity and the exact shape of the knob of solidified steel. Practical implementation will be in terms of simple reference charts relating the knob profile and diameter to flow velocity. Ideally, casting engineers will be able to quickly and accurately determine velocity at any point along the top surface using this technique. Researchers or scholars interested in estimating high-temperature flow may also benefit from the model in terms of their own particular models.

The main objectives of this project are as follows:

- Develop and validate a model simulating 3-D steel/slag flow around a stationary nail.
- Using the model, create a simple empirical relation relating knob profile and diameter to flow velocity which can be implemented by continuous casting engineers in the field. Once the diameter of the solidified knob is found, reference charts will be provided to compare the profile of the knob with computationally solved profiles for that specific diameter and a range of velocities.

The goal of this research was to provide an inexpensive, non-intrusive, quick, and quantitative method to determine top surface velocity. The Nailboard Method represents all of these characteristics. The cost for implementing this procedure is negligible; no expensive equipment must be purchased (only steel nails and a wood board). Furthermore, it is not necessary to mount a fixed apparatus to the mold which can interfere with the casting process. With the testing duration of mere seconds, the quickness requirement is satisfied. Although there are a number of methods currently available to measure high temperature fluid flow, various reasons prevent these methods from being utilized to detect meniscus flow (as discussed in Section 3.2.1).

3.2 Literature Review

Prior to developing the model, critical information regarding the continuous casting process, high temperature flow measurement techniques, and free surface phenomena were researched. The relevant outcomes of this research will be discussed in the following sections.

3.2.1 High Temperature Flow Measurements

The problem with measuring the flow speed of high temperature fluids is that most conventional methods cannot tolerate the hostile environment and high temperatures of a steel caster. Still, there have been alternative techniques developed for measuring this high temperature flow. In his report, Mikrovas identifies a number of measurement techniques for liquid metals, and identifies situations in which each excels, along with each technique's limitations[35]. Two techniques stand out as the most feasible methods for use in the steel caster; however they have been excluded for use in a steel caster for the following reasons: flow visualization techniques are unable to "see through" the slag layer above the molten steel, and probes (reaction and electromagnetic) cannot be inserted into fluid with a melting temperature beyond 720°C[35].

Von Karman vortex shedding techniques have recently been developed to measure fluid flow velocity[34]. Unfortunately, the requirement of a fixed base and electrically sensitive equipment positioned above an oscillating mold reduces the practicality of this method in this situation. Tracer techniques provide an alternative way to measure high temperature flow by tracking the trajectory of injected particles through the fluid. Fluid velocity is estimated by dividing the particle distance traveled over the sampling time. Alas, tracer particles are unlikely to work in a caster because of the following: flow through a continuous casting mold is not uniform from location to location (due to transient effects), visual techniques cannot transmit images through the non-transparent slag layer, and there is not a robust meniscus injection point (the only feasible injection point would be the nozzle)[16,34,36].

Mikrovas developed a new technique for estimating velocity in liquid steel. By immersing steel spheres into the fluid, the mass transfer of these spheres melting into the fluid can be detected. He proved that the sphere melting time is directly related to the flow velocity and fluid temperature[35]. Note that the spheres must be chemically identical to that of the fluid to maintain the integrity of the steel composition. As with previous methods described, the lack of a robust visualization method prevents this approach from being implemented.

3.2.2 Free Surface Flow

In the modeling of free surface flow, four main approaches can be taken: the Volume of Fluid method (VOF), pressure/potential energy relations, movable grid methods, and the spine/local perturbation method.

Volume of Fluid Method (VOF)

The volume of fluid method requires the definition of a value (F) for each element in the domain. F ranges from 0 → 1 continuously, with 1 representing a grid unit solely containing fluid, 0 for grid units containing no fluid, and a fractional amount for grid units partially containing fluid. The evolution of the F field is governed by the time dependent equation:

$$\frac{\partial F}{\partial t} + u_{T1}\frac{\partial F}{\partial x_{T1}} + u_{T2}\frac{\partial F}{\partial x_{T2}} = 0 \tag{3.1}$$

The VOF method can be either implemented using an Eulerian or a Lagrangian frame of reference. A particular regime using the volume of fluid method is termed the Marker and Cell Method, as developed by Harlow and Welch[37)]. In this scheme, the primary dependent variables are pressure and velocity. Requiring minimum storage requirements, this method is applicable to three-dimensional computations in which conserving stored information is highly advantageous[38)]. However, the volume of fluid method may not effectively model the surface tension at the free surface boundary.

Pressure/Potential Energy Relations

In the pressure/potential energy regime, the free surface boundary is treated as a fixed wall using standard finite volume techniques. Solving for the pressures at the free surface, standard conservation of energy equations relate free surface height to the known pressures. Meniscus heights have been accurately predicted using this method[39)]. An ideal case for the use of pressure/potential energy relations are cases in which surface tension effects (which are not considered in the equations) are minimal. Should there be large fluctuations in free-surface height in which surface tension restricts boundary movement, the accuracy of this method decreases[40)].

Movable Grid Methods

A movable staggered mesh accurately solves free surface flow problems using interface tracking rather than interface capturing. Interface tracking techniques have been implemented in a few ways, mainly using an Arbitrary Lagrangian Eulerian approach[41-44)] or a deformable-spatial-domain/stabilized space-time technique[45)]. Adopting from the ALE formulation, Rabier and Medale have developed a Lagrangian-Eulerian kinematic method to effectively model free-surface sloshing in a 2-D rectangular tank[46,47)]. Furthermore, work by Perot and Nallapati with this method have allowed them to simulate sloshing in a tank, droplet oscillation, and flow over a hump with an extremely high degree of accuracy[48)]. Staggered mesh methods possess several attractive properties in free surface modeling, including local conservation of mass, momentum, kinetic energy, and vorticity[48)]. A key feature of this method is the discretization of pressure at the cell center and velocity at the cell faces, which aids in solving the governing equations. Because the mesh is unstructured and not based on a control volume, the main drawback of this method is that correctly implementing the moving mesh is a non-trivial problem[48)].

Spine/Local Perturbation Method

The final method considered to model free-surface flow is the spine/local perturbation method. From the initial structured grid, spines (a set of straight generator lines which guide the free surface movement) are drawn from the free surface to some fixed reference within the mesh. Examples of both external and internal spines are shown in Figure 3.2. The aspect ratio between nodes along a spine is conserved, from the initial undeformed mesh to the final deformed interface. With the spines constructed and the mesh generated, the free surface nodes are allowed to move along the direction which the spine points. Remeshing is performed at each iteration update, insuring that the newly derived node locations are preserved for the subsequent iteration. In one case, turbulent free-surface flow over a cylindrical obstruction was modeled and simulated using the spines method. Excellent agreement between the mathematical results and experimental measurements from Forbes was reached[49,50)].

3.2.3 Flow Past a Cylinder

Only a small amount of effort to model flow past a vertical cylinder was found in previous research, presumably due to the specificity of this topic to very few research problems. One interesting research experiment involved dragging a cylinder through a pool of stationary water by Chaplin[51)]. While the main intent of the investigation was to analyze the drag coefficients of the 0.21 m cylinder traveling at different velocities, he also recorded data such as the run-up on the leading edge of the cylinder. Diagrams showing the leading edge node in relation to the domain are shown in Figure 3.3. Typical flow past a cylinder produces a continuous free surface profile as represented by the solid line in the figure. Two cases tested by Chaplin *et. al.* with similar velocity magnitudes to those experienced at the mold top surface (0.96 and 1.36 m/s) will be used to experimentally validate the Nailboard model.

At high velocities (orders of magnitude faster meniscus-level intra-mold flow), excessive turbulence causes the free surface to break up around the cylinder. The higher speed fluid provides enough energy to overcome surface tension forces and disrupt flow. With the flow upset in this manner, the free surface profile will not follow a continuous slope down around the cylinder; the separation of the run-up flow and the wake flow yields a staggered free surface (displayed as the dashed profile in Figure 3.3a). Luckily, the relatively slow velocities at the Nailboard testing locations will likely be insufficient to produce this surface disruption. Thus, this effect is neglected and the model in this work assumes a continuous free surface profile. It is important to recognize that the model is not valid at very high velocities, when this non-regular flow pattern is present.

3.3 Model Formulation

Frame of Reference

Prior to developing the numerical model, the proper frame of reference was determined. Choosing an Eularian reference frame would involve observing a static section of the domain and neglecting the motions of the individual particles in the domain. The main advantage to this method is that the cells can undergo large amounts of distortion while maintaining a high level of accuracy[52)].

Alternatively, the Lagrangian method follows the trajectory of the individual particles rather than focusing on a fixed domain location. In essence, this procedure involves using a moving grid as it travels through the domain. The attractiveness of the Lagrangian approach is that it allows for material interfaces, free surfaces, and other complex boundary conditions to be easily implemented[52)]. Because of its individual particle approach, the continuity equation is not needed to yield a solution, thereby simplifying the governing equations. One drawback is that as the amount of mesh deformation increases, the accuracy of the solution decreases. Furthermore, looking at individual particles makes consideration of surface tension effects very difficult.

Free Surface Model

The VOF method can be used in either a Lagrangian or Eularian reference frame, however it lacks enough knowledge of the free surface profile to allow for accurate presence of surface tension effects (without an immensely fine mesh). As previously stated, the pressure/potential energy formulation method loses accuracy as the free surface profile becomes more distorted (due to neglecting surface tension), and thus this method will not be used. The ALE method has been shown to be quite accurate, utilizing the best characteristics of both the Eularian and Lagrangian approaches. In spite of this, the relative mathematical complexity and the lack of a robust, available code using this method prevents its use. The spines/local perturbation method possesses many attractive characteristics with no immediate drawbacks. Its accuracy, availability in a commercial CFD code, and robustness are the reasons why the spines method was used as the mathematical basis for this investigation.

Model Creation

Analysis begins with the creation of a simplified 3-D domain neglecting the slag layer (termed the No-Slag Model). A schematic with dimensions (relative to the diameter, D) is shown in Figure 3.3b. The model consists of a single fluid layer with a free surface boundary at the top of the domain. Domain height is set as a constant 0.03 m for each case (similar to actual nail insertion depths). Even though this model neglects the important influence of the slag layer, it does accomplish several tasks; it allows for comparison to experimental results (for model validation), it allows for a baseline to be set with which to compare the full mathematical representation (Slag Model), and it enables the inherent differences between water models and the actual metal casting process to be quantified.

The second analysis involves the creation of a 3-D domain including two fluid layers- a molten steel lower layer and a slag upper layer. The addition of an internal free surface between the two fluid layers proved to make this Slag Model much more complicated than the previous single-layer model. An external free surface is maintained at the top of the domain. The 3-D Slag Model domain can be seen in Figure 3.3c. Note the different relative dimensions of the two model domains. The increase in number of elements caused by the addition of the slag layer forced the domain to be slightly smaller in the x and y-directions (to reduce computational intensity). In subsequent sections, the width and length of the Slag Model domain is shown to be acceptable. Additionally, flow gradients stemming from the top zero-velocity boundary condition require a larger insertion depth to accurately generate boundary layer flow, causing the height of the steel layer domain to be an extended 0.06 m. Results obtained from this model will provide a better approximation of the actual Nailboard process than the single fluid layer model. Note that symmetry has been utilized in both models (only $^1/_2$ of the actual domain will be considered).

Simulation Phenomena

In this study, free surface flow is the main phenomenon to be considered. Consequently, surface tension effects must be incorporated. Phenomena which will be neglected in this model include incompressible flow, von Karman vortices, and heat/mass transfer (including solidification). The latter phenomena were judged not to have a significant effect on the accuracy of the model prediction of interface shape.

3.3.1 Model Assumptions

The main assumptions of the model are:

- Inlet flow has only x and z-components of velocity, both of which are parallel to the symmetry plane. Due to the axisymmetric nature of the nail, this assumption is accurate-steady flow will always intersect the axis of the nail.

- Heat transfer does not play a role in the simulation. While in the real world there is mass transfer from the molten steel to the nail via solidification, incorporating heat transfer phenomenon into the model adds unnecessary complexity.
- The diameter growth rate of the solidifying knob is much smaller than the velocity of the fluid. The knob is assumed to have a constant diameter for each simulation (logically equal to the final diameter of the solidified knob). This assumption will be proved valid in Section 3.5.3.
- Newtonian fluid with constant μ and ρ (incompressible flow).
- The domain is large enough that each vertical wall has virtually zero velocity gradients across its boundary (Far-Field assumption). The domain size was chosen via trial and error simulations.
- Wall law conditions are accurate near the nail surface and along the steel/slag interface (Slag Model).
- The air above the upper free-surface has negligible viscosity and pressure.
- No capillary effects pull the steel up the nail.
- Fluid diverted under the nail has no impact on the steel free surface flow. The boundary condition of no normal flow at the bottom surface is acceptable in maintaining fluid continuity within the model.

3.3.2 Governing Equations

Direct numerical simulation is not appropriate for this problem (due to high Reynolds number turbulent flow in complex geometries); instead the standard Reynolds-averaged Navier-Stokes equations for viscous, single-phase fluids are implemented to solve for turbulent flow profiles. The Nailboard model utilizes both steady-state and transient simulations, so the governing equations include time-dependent variables. For a full definition of the variables in the following equations, please refer to the Nomenclature page.

In this mathematical model, turbulent behavior is expressed using mean values. Because the mesh size is not infinitely small, turbulent eddies smaller than the elements will not be captured in the model. Their influence in developing the global flow patter, however, will be realized through averaging of the solution parameters within each element. Coarser meshes (reducing computational expense) will produce accurate results using this averaged approach. Note that the overbars in the following equations represent these averaged quantities.

The mass conservation governing equation is defined as follows (neglecting external mass sources, simplified for constant density fluids):

$$\frac{\partial}{\partial x_i}\left(\overline{u_i}\right) = 0 \tag{3.2}$$

where the velocity term u is extended to fluid flow in all directions (i = 1,2,3 for a 3-D domain). The conservation of linear momentum equation (assuming constant density and constant viscosity) is:

$$\rho\left(\frac{\partial \overline{u_i}}{\partial t} + \frac{\partial}{\partial x_j}\left(\overline{u_i u_j} + \overline{u_i' u_j'}\right)\right) = \frac{\partial}{\partial x_j}\sigma_{ij} + \rho b \tag{3.3}$$

with the stress tensor term defined by:

$$\sigma_{ij} = -p\delta_{ij} + \tau_{ij} \tag{3.4}$$

For viscous, incompressible fluids, the deviatoric stress tensor and the subsequent strain rate tensor are described by:

$$\tau_{ij} = 2\mu_{eff} s_{ij} \tag{3.5}$$

$$s_{ij} = \frac{1}{2}\left(\frac{\partial}{\partial x_j}\overline{u_i} + \frac{\partial}{\partial x_i}\overline{u_j}\right) \tag{3.6}$$

Inserting Equations 3.4, 3.5, and 3.6 into Equation 3.3, the stress divergence arrangement of the momentum equation is formed. The resulting Navier Stokes momentum equation is simplified and defined as:

$$\rho\left(\frac{\partial \overline{u_i}}{\partial t} + \frac{\partial}{\partial x_j}\left(\overline{u_i u_j} + \overline{u_i' u_j'}\right)\right) = -\overline{p_i} + \mu_{eff}\frac{\partial}{\partial x_j}\left(\frac{\partial \overline{u_i}}{\partial x_j}\right) + \rho b \tag{3.7}$$

The pressure terms in Equations 3.3, 3.4, and 3.7 represent pressure differences due to flow parameters and do not include the effects of ferrostatic pressure and pressures induced at the free surface. Because the model includes gravity and surface tension effects as body forces, the pressure in the above equations will be calculated as:

$$p = p_{tot} - \left(p_{ferro} + p_{steel,surface}\right) = p_{tot} - \left(\rho g x_3 + p_{steel,surface}\right) \tag{3.8}$$

Due to the presence of turbulence, the effective viscosity is calculated using:

$$\mu_{eff} = \mu_o + \mu_t \tag{3.9}$$

where μ_o is simply the laminar molecular viscosity and μ_t is the turbulent viscosity term (which will be discussed in the subsequent section).

3.3.3 *K-ε* Turbulence Model

The standard *K-ε* turbulence model is employed. In this methodology, the turbulence field is characterized in terms of two variables- the turbulent kinetic energy (*K*) and the turbulent energy dissipation rate (*ε*). Through implementation of these two additional parameters, the viscosity term in the fluid conservation equations is modified to incorporate the effect of turbulence. The additional turbulence parameters are defined as:

$$K = \frac{1}{2}\overline{u_i' u_i'} \tag{3.10}$$

$$\varepsilon = \left(\frac{\mu_o}{\rho}\right)\overline{\frac{\partial u_i'}{\partial x_j}\frac{\partial u_i'}{\partial x_j}} \tag{3.11}$$

The contribution of turbulence to the fluid viscosity in Equation 3.9 is then expressed through:

$$\mu_t = c_\mu \rho \frac{K^2}{\varepsilon} \tag{3.12}$$

where c_μ is an empirical constant of value 0.09. To find the spatial distribution of *K* and *ε*, the following two semi-empirical transport equations are solved:

$$\rho\frac{\partial K}{\partial t} + \rho u_j \frac{\partial K}{\partial x_j} = \frac{\partial}{\partial x_j}\left(\mu_o + \frac{\mu_t}{\sigma_K}\frac{\partial K}{\partial x_j}\right) + G + B - \rho\varepsilon \tag{3.13}$$

$$\rho \frac{\partial \varepsilon}{\partial t} + \rho u_j \frac{\partial \varepsilon}{\partial x_j} = \frac{\partial}{\partial x_j}\left(\mu_o + \frac{\mu_t}{\sigma_\varepsilon} \frac{\partial \varepsilon}{\partial x_j} \right) + c_1 \frac{\varepsilon}{K} G + c_1 (1 - c_3) \frac{\varepsilon}{K} B - c_2 \rho \frac{\varepsilon^2}{K} \tag{3.14}$$

where c_1, c_2, c_3 represent empirical coefficients and σ_K, σ_ε are the turbulent Prandtl-Schmidt numbers for the kinetic energy and turbulent dissipation rate. These equalities are derived directly from the instantaneous flow patterns using the standard Navier Stokes momentum equation (Equation 3.7). Optimizing the empirical constants for isothermal fundamental turbulent shear flow with no mass transfer, the simulation values used are[21)]:

$$c_1 = 1.44 \quad c_2 = 1.92 \quad c_3 = 0.09 \quad \sigma_k = 1.00 \quad \sigma_\varepsilon = 1.30 \tag{3.15}$$

Included in Equations 3.13 and 3.14 are shear generation and buoyancy terms (G and B, respectively). Using the Boussinesq approximation for constant density fluids, these parameters are defined as:

$$G \approx \mu_t \left(\frac{\partial \overline{u_i}}{\partial x_j} + \frac{\partial \overline{u_j}}{\partial x_i} \right) \frac{\partial \overline{u_i}}{\partial x_j} \tag{3.16}$$

$$B = g_i \left(\frac{\mu_t}{\sigma_t} \beta_T \frac{\partial T}{\partial x_i} + \frac{\mu_t}{S_t} \beta_c \frac{\partial c}{\partial x_i} \right) = 0 \quad \text{(for isothermal fluids)} \tag{3.17}$$

The previous equations allow for full characterization of turbulent viscosity at all locations in the domain. Using this effective viscosity, the standard fluid flow conservation equations are now able to estimate turbulence effects within the macro-scale grid.

3.3.4 Boundary Conditions

Special conditions were assigned at each location on the domain boundary. Each boundary condition and its attributes will be fully described in the following sections.

3.3.4.1 Free Surface Conditions

Arguably the most important (and complicated) aspect of the model is the implementation of free surfaces within the domain. As previously discussed, the spines method will be invoked to solve for the free surface deformation profiles. The following equations describe spine motion within the model.

Interface Between Two Liquids

A free surface interface separating two liquids represents the most generic surface formulation. An additional unknown (the surface deformation along the spines direction) is introduced into the governing equations and must be solved as part of the flow solution. The Van der Waals molecular forces at the surface (creating surface tension) must be included in the calculations.

By definition, the surface always remains an interface throughout the simulation. Known as the kinematic condition, the mathematical representation is (with superscripts 1 and 2 denoting the two fluid regions above and below the interface) [49]:

$$S(x,t) = \frac{\partial S}{\partial t} + \overline{u^1_j}\frac{\partial S}{\partial x_j} = \frac{\partial S}{\partial t} + \overline{u^1_j}\frac{\partial S}{\partial x_j} = 0 \tag{3.18}$$

$$\sigma^1_i - \sigma^2_i = 2\gamma H n_i - \frac{\partial \gamma}{\partial x_i} \text{ (on the surface)} \tag{3.19}$$

where σ_i represents the stress at the surface in the *i*-direction. In addition, a no-slip boundary condition at the interface is required:

$$\varepsilon_{ijk} n_j \left(\overline{u^1_k} - \overline{u^2_k}\right) = 0 \tag{3.20}$$

The dynamic boundary condition (resulting from a force balance at the surface) is expressed by[53]:

$$(p_{steel,surface} - p_{air})n - n \cdot \tau = -2\kappa_m \gamma n - \nabla_{surf}(\gamma) \tag{3.21}$$

Because the transient simulation involves a moving boundary, the normal velocity at the free-surface is the velocity of the interface:

$$u_{interface} = (u \cdot n)n \tag{3.22}$$

Interface Between Liquid and Gas

The most popular implementation of the spines method occurs at the surface formed when a liquid surface meets a gaseous region. The gas is effectively treated as a vacuum, contributing no density or viscosity which would influence free surface flow and deformation. Therefore, the terms in the free surface calculations representing the upper fluid can be neglected from the formulation. While the kinematic condition remains the same as in Equation 3.18, the continuous stress condition (Equation 3.19) simplifies into:

$$\sigma_i = \sigma_{ij} n_j = (2\gamma H - p_s) n_i - \frac{\partial \gamma}{\partial x_i} \quad \text{(on the surface)} \tag{3.23}$$

3.3.4.2 Wall Boundary Conditions at Nail Boundary and Slag/Steel Interface (Slag Model)

Special treatment must be given to regions of high velocity gradients, especially near no-slip boundaries. The *K*-*ε* turbulence model typically produces poor flow results in regions with low Reynolds numbers; the predominance of laminar flow in the finite grid boundary layer near the wall causes the turbulent viscosity theory to break down. Rather than increasing the refinement of the mesh in these areas (which may allow standard laminar flow models to solve accurate flow profiles), wall laws are applied to describe flow in regions with high velocity gradients. Specifically, two regions exist in the Nailboard model where this is necessary:

- Near the surface of the zero-velocity nail
- At the steel/slag interface (extending into the steel region within the Slag Model).

The following equations assist in solving for the boundary-layer flow.

The derivation of a universal near-wall flow profile begins by developing a characteristic non-dimensionalized distance from the wall (y^+, known as the "wall unit"). This parameter will be used in the formulation of the mean velocity profile. The wall unit is defined by:

$$y^+ = \frac{(\rho \tau_w)^{1/2} \delta}{\mu} \tag{3.24}$$

Wall laws are implemented by modifying the fluid viscosity term, μ, near the wall boundary. Because a non-dimensional wall unit is used in the following equations, a non-dimensional velocity term must also be formed:

$$u^{+} = (u - u_w)\left(\frac{\rho}{\tau_w}\right)^{1/2} \tag{3.25}$$

Flow past a wall can be broken into three distinct regions of flow. The first flow zone (termed the viscous sublayer) spans from the surface of the wall to $y^{+} = 5$ from the wall. In this region, the well-known linear velocity wall law is formed, and is described by:

$$u^{+} = y^{+} \qquad y^{+} < 5 \tag{3.26}$$

Far from the wall, the fully turbulent region emerges (at $y^{+} > 30$). This region is described by the relation:

$$u^{+} = \frac{1}{\kappa_o}\ln\left(Ey^{+}\right) \qquad y^{+} > 30 \tag{3.27}$$

where κ is the Von Karman constant (≈ 0.41), and E is an empirical constant dependant on the roughness of the wall (≈ 9.0 for smooth walls, as are assumed in this model). It is in the "buffer zone" or transition region between the viscous sublayer and the fully turbulent region ($5 < y^{+} < 30$) in which the velocity calculation is not so simple. Flow within this region combines the linear profile of the viscous sublayer and the logarithmic profile of the turbulent region. Rather than using separate models to define flow in each region, continuous empirical equations have been developed to approximate flow at *all* distances within the wall law profile. One such equation developed by Reichardt is described by[52)]:

$$u^{+} = \frac{1}{\kappa_o}\ln\left(1 + \kappa_o y^{+}\right) + 7.8\left[1 - \exp\left(-\frac{y^{+}}{11}\right) - \frac{y^{+}}{11}\exp\left(-0.33y^{+}\right)\right] \tag{3.28}$$

Equation 3.28 is only used to develop fluid flow within the wall boundary layer. Once the distance from the wall becomes sufficiently high ($y^{+}>30$), the full governing equations and turbulence model are used to solve for flow parameters.

In regard to turbulence parameters, special treatment must only be given to the elements adjacent to the wall boundary (all other elements in the domain follow the standard *K-ε* Turbulence model as described in Section 3.3.3). Two special equations associated with these layer wall-adjacent elements are:

$$\frac{\partial K}{\partial n} = 0 \qquad \text{(Neumann Condition[55])} \tag{3.29}$$

$$\varepsilon = \frac{\left(c_\mu^{1/2} K\right)^{3/2}}{\kappa_o \delta} \tag{3.30}$$

Through these equations, all parameters of turbulent flow near wall boundaries can been explicitly solved.

3.3.4.3 Steel/Slag Inlet Boundary Conditions

No-Slag Model

The inlet boundary condition for the No-Slag domain is relatively simple. Without the presence of a slag region, there is nothing restricting the flow through the steel layer (other than the nail). Thus the steel inlet velocity profile was set to a constant normal velocity at all locations on the boundary (with a value that is case-specific). The tangential velocities at the inlet were set to zero to ensure constant, 1-D flow into the domain. Being a turbulent simulation, the kinetic and dissipation energies must be clearly defined at the inlet boundary. Developing a reasonable estimate for K in unconfined flow as a function of free-stream velocity meant using the equation:

$$K = \alpha u_c^2 \tag{3.31}$$

where α is an empirical constant taken to be 0.005 (appropriate for low-shear flows). The turbulent dissipation energy at the inlet follows the formula:

$$\varepsilon = \rho\alpha \frac{K^2}{R_\mu \mu} \tag{3.32}$$

where R_μ is the ratio between the turbulent and laminar viscosities. While only an approximation, $R_\mu = 10$ was used in Equation 3.32. This value is consistent typical low-turbulence flow, which properly describes the constant velocity flow of the inlet.

Slag Model

Unlike the No-Slag Model, normal flow across the steel and slag layer inlet boundaries could not be represented by constant values. The zero tangential velocity boundary condition imposed at the slag top surface resulted in a nearly stationary slag layer culminating at the slag/steel interface. Wall laws imposed at this slowly-moving interface generated a logarithmic flow profile extending into the steel layer. The result was a non-regular velocity gradient forming through the domain height, from the top slag surface to the bottom steel boundary. Research indicated that even parabolic inputs could not be manipulated to produce accurate inlet velocity and turbulence profiles. Thus the Slag Model required *explicit definition* for normal velocity and kinetic/dissipative energies *at each nodal location* along the inlet boundary. Tangential velocities at the boundary inlet are set to zero to ensure 1-D inlet flow (similar to the No-Slag Model).

3.3.4.4 Steel/Slag Outlet and Far-field Boundary Conditions

The Neumann boundary condition (zero-gradient, zero-flux) is imposed on the fluid at the outlet boundary. By leaving all parameters unknown, the fluid flows naturally with no artificial constraints. The mathematical representation of the Neumann Condition is as follows:

$$\frac{\partial u_N}{\partial x_i} = 0 \qquad \frac{\partial u_{T1}}{\partial x_i} = 0 \qquad \frac{\partial u_{T2}}{\partial x_i} = 0 \qquad \frac{\partial p}{\partial x_i} = 0 \qquad \frac{\partial K}{\partial x_i} = 0 \qquad \frac{\partial \varepsilon}{\partial x_i} = 0 \qquad (3.33)$$

Using the Neumann Condition, the proper flow pattern evolves as if a “slice” had been taken through the extended real-world domain. It is important that the outlet is placed far away from any large flow perturbations. Should there be high velocity gradients or large recirculation zones extending into the outlet, the Neumann boundary condition (and its gradient-driven formulation) will basically suppress the flow patterns, causing an improper velocity profile to emerge. While designing the model, care was taken to make the computational domains large enough such that flow was nearly uniform at the domain exit.

3.3.4.5 Symmetry Boundary Conditions

At the symmetrical boundary in the domain (vertical plane intersecting the nail), the normal velocity was specified to be zero. In addition, all tangential velocity and turbulence gradients were fixed to be zero via the Neumann boundary condition (Equation 3.33) to maintain continuity. Implementation of these symmetrical faces allows the domain size to be reduced without loss of steady-state solution accuracy.

3.3.5 Solution Procedure

The uniqueness of this model involves incorporating numerous phenomena working simultaneously to develop flow patterns. Important aspects considered in the model include:

- 3-Dimensional domain
- Internal free surface separating steel and slag regions using Spines methodology (for the slag model)
- Upper free surface using Spines methodology
- Turbulent flow with wall law considerations at internal free surface and nail boundary
- Transient flow calculations

3.3.5.1 Solution Methodology and Program Selection

The high level of complexity within the Nailboard model required optimization of the mathematical approach in effort to minimize computational cost. Finite element methods were chosen over a standard finite difference approach due to their high efficiency in generating accurate solutions. The following section reveals the guts of the Finite Element Method (FEM).

Galerkin FEM Governing Equation Solution

As the first step in the standard Galerkin FEM formulation, the continuum flow equations are converted into global discretized matrices of the form:

$$K(U)U = F \tag{3.34}$$

Due to extreme complexity, the entire global system of matrices was not formed using Equation 3.34 directly. Instead, decoupled sub-matrix systems for the three-dimensional components of the continuity, momentum, and surface equations were formed, given by (neglecting the temperature equation for the isothermal model):

$$C_1^T u_1 + C_2^T u_2 + C_3^T u_3 = 0 \tag{3.35}$$

$$K_1 u_1 - C_2 p - C_3 p = f_1 \tag{3.36}$$

$$K_2 u_2 - C_1 p - C_3 p = f_2 \tag{3.37}$$

$$K_3 u_3 - C_1 p - C_2 p = f_3 \tag{3.38}$$

$$K_S S = f_S \tag{3.39}$$

where K_i includes advection, diffusion, and temporal terms in a stiffness matrix; C_i represents the pressure gradient matrix while its transpose incorporate velocity divergence operators; f_i represent the combined effects of gradient boundary conditions, source/sink presence, and contributions from the previous time step; and S represents movement normal to the free surface. A standard segregated solver was employed to solve the series of matrix equations. This method uses an inner iterative procedure to arrive at convergence; a single iteration is outlined next.

Fixed Surface Segregated Solver

The fixed surface segregated solver begins by algebraically manipulating the continuity and momentum equations (Equations 3.35 through 3.38) such that the pressure distribution can be directly solved. With four equations and four unknowns (the three components of velocity plus the pressure term), a single equation isolating the pressure term was formed via pressure projection method. This pressure equation is solved using *initial guess* parameters for the other three unknowns (the first part of the iteration), then the result is modified according to the user-defined relaxation coefficient. In the second part of the iteration, manipulation of the momentum equations allows the velocity components to be solved using the pressure solution. Once the change in pressure/velocity from the previous iteration is determined, the mass flow rates are adjusted to satisfy the continuity equation.

Free Surface Segregated Solver

The free surface segregated algorithm incorporates a slightly different methodology to achieve iteration convergence, including the addition of Equation 3.39. Additional equations are required to define unconstrained surface movement in the free surface model. Each free surface segregated iteration is solved in two steps. First, the free surface is rigidly constrained and the standard segregated methodology (as previously discussed) is performed. As a requirement, either a kinematic condition or a normal stress balance must be satisfied at the surface during this step. In the second step, the remaining equation (kinematic or normal stress balance) is used to define Equation 3.39, and the free surface movement required to satisfy the current flow solution is computed. These two steps constitute one iteration. Once the free surface position change between iterations decays to values smaller than specified convergence limits, the simulation is considered to be solved and iterations are ceased.

If the normal stress balance is used in the first step and the free surface movement is described through the kinematic condition, solution is reached through what is called the *kinematic iteration*. Conversely, should the kinematic condition be used in the initial flow solution (leaving the normal stress balance to define Equation 3.39 in the second step), the solution method is termed the *normal stress iteration*. For brevity, only the method used (the normal stress iteration) will be outlined.

Normal Stress Iteration

For small Capillary flows (Ca < 1, as in this model), the kinematic condition is utilized first and the normal stress equation is used to define free surface movement. The algorithmic solution procedure for the normal stress iteration model is summarized by (with superscripts representing the iteration number):

1. Update the free surface level:

$$S^i = \lambda_s * S^i + (1-\lambda_s)S^i \tag{3.40}$$

2. Solve flow parameters using fixed surface segregated solution algorithm with pressure projection methods. Additional equation are necessary at the free surface, which are:

$$(n\sigma)\cdot t^* = -t^* \cdot \nabla\gamma \qquad \text{(tangential stress balance)} \tag{3.41}$$

$$u^i \cdot n^{\bullet} = 0 \qquad \text{(kinematic condition)} \qquad (3.42)$$

3. Allow for free surface deformation, and solve for updated surface profile (S_i):

$$(n\sigma) \cdot n = p_s + 2\gamma H \qquad \text{(normal stress balance)} \qquad (3.43)$$

This concludes a single iteration update using the standard, fixed surface segregated solver. Again, iterations are ceased when the change from one iteration to the next for all unknown parameters are smaller than the simulation convergence criteria. By using an inner iteration (to reach convergence at a single time step) and an outer iteration (to reach transient simulation solution) routines, divergence and the propagation of divergence was minimized.

Commercial CFD Package

With many commercial packages on the market, care was taken to choose the proper program which incorporated FEM modeling and had the capability to include the features required for this model (3-D flow, interfacial free surfaces using spines methodology, K-ε turbulence modeling, wall laws, etc…). The program best suited to model this project is Fidap. Fidap exploits the finite element approach which generates solutions to a high degree of efficiency in regards to computational cost over finite difference methods. This Fluent Inc. commercial package also utilizes the spines routine to model free surfaces, which through research proven to be quite accurate[49)].

One convenient feature of Fidap is the presence of an internal mesh generator. A completely structured numerical grid was created for all Fidap simulations using this meshing tool, and the governing equations were discretized and solved. Fidap utilizes a specialized segregated free-surface algorithm very similar to the approach previously outlined to solve such problems. The reader will be directed to the Fidap Theory Manual for a more comprehensive look at the solution procedures offered by the software[49)].

3.3.5.2 Mesh Creation/Refinement

While the actual domain is not overly complicated in shape, the structured mesh required intuitiveness in its creation. In using Fidap's internal mesh generator (termed FiMesh), nodal coordinate inputs for element endpoints along with node information (number of nodes, node spacing ratio along lines, etc…) must be specified.

High levels of mesh refinement were limited to the area directly around the nail and close to the slag/steel interface (in the Slag Model). By only specifying the mesh to be refined where necessary, the mesh was able to be relatively coarse in other areas of lesser velocity gradients, thereby minimizing computational cost.

Using these ideas, the entire domain for the No-Slag Model contained 4088 elements. Typical computational times to reach residuals of 1e-3 with this mesh sizes for the first steady-state run took approximately 0.1 hours. In the second transient run, computational time was approximately 8 hours to go through 10,000 time steps (dt = 0.0003s) to achieve residual errors of 1e-3 (residual errors are defined as the percentage change of converged parameter values from one time step to the next; a full description can be found in the text Modeling in Materials by Dantzig and Tucker[53)]). The entire domain for the Slag Model was composed of 5760 elements. Typical computational times to reach residuals of 1e-3 with this mesh size for the first steady-state run took approximately 0.2 hours. In the second transient run, computational time was approximately 12 hours to simulate 10,000 time steps with a residual convergence of 1e-3. All computations for both models was performed using an IBM POWER4 p690 processor with a computational power of 1.3 GHz.

3.3.5.3 Relaxation Parameters

While the Galerkin FEM can solve fluid flow problems with high accuracy, it also has a tendency to become unstable during simulations. Instability occurs in regions of high flow variable gradients with a poorly refined mesh. In these areas, fluid convection dominates diffusion, and a situation in which two adjacent nodes tend to overshoot and undershoot (respectively) the correct flow parameters emerges. The flow profile becomes choppy, resembling teeth of a saw. Termed "wiggles", it is desired to relax the flow parameters from iteration to iteration to smooth out these over/undershoots.

Compounding the problem of solution divergence, turbulent flow typically becomes unstable due to the cross-diffusion terms in the K and ε turbulence equations. Hershey and Thomas discovered that in the equations including both kinetic and dissipation terms (Equations 3.13 and 3.14), small disturbances in either term quickly propagate, leading to rapid divergence of the residuals[28)]. This problem can be remedied by applying relaxation techniques to the turbulence terms. Through relaxation, only a portion of the new flow solution parameters (with the remaining portion carried over from the previous iteration) will be used as the initial solution in the subsequent iteration. A higher level of system stability emerges over successive substitution methods because the advancement of the turbulence terms is slowed. Convergence to solution is typically slower using significant levels of relaxation, but due to the nature of relaxation coefficients, accuracy of solution utilizing relaxation methods is not affected.

Fidap allows the user to have greater control over model simulation and convergence by modifying the dedicated relaxation factor for each solution variable. The relaxation values were carefully chosen to ensure proper convergence. Because the models for the first steady-state run and the second transient simulation were identical, the relaxation parameters remained constant for both runs. The simplified No-Slag Model reached convergence within each time step with relative ease; the relaxation parameters approached successive substitution with values ranging from 0.3 to 0.5 for each velocity, pressure, and turbulence value (with u-relax = 0 implying 100% of the new solution is carried-over through successive substitution). The inherent instability caused by the internal interface of the Slag Model meant higher relaxation parameters than the No-Slag Model, typically in the 0.7 to 0.9 range for all components.

3.3.5.4 Model Simulation

Inlet Flow Solution

Constant values for velocity and turbulence were specified at all heights of the No-Slag Model domain inlet, as specified in Section 3.3.4.3. For the Slag Model, the irregular flow profile at the inlet necessitated an alternate way to define flow at the inlet boundary. For this purpose, a simple 2-D velocity profile test case was created. Starting with a constant velocity in the slag and the steel (equivalent to the simulation velocity), a transient run allowed the flow pattern to evolve using a successive substitution methodology. The simulation end time was determined as a function of flow velocity and distance (taken to be 0.35 m, the distance from the meniscus to the approximate sampling location at the top surface). Once completed, velocity and turbulence for all heights along the 3-D model inlet could be explicitly defined using the 2-D profile test case data. At this point, all boundary conditions have been specified.

Solution Methodology

For simulations involving large free surface displacements, computational code has difficulty reaching the final deformed solution in one step. Small, intermediate steps must be taken in the form of a transient time stepping routine to achieve steady-state solution. Using these principles, model simulation was broken up into two runs: an initial Steady-State (SS) run and a subsequent transient run. The first SS run serves only one purpose; solve flow profiles throughout the domain to be used as initial conditions for the transient simulation. The free surfaces were treated as fixed boundaries for the SS simulation. Fluid velocity and turbulence initial conditions throughout the domain mirrored their respective inlet boundary values. Residual convergence to only 1e-3 was considered appropriate for this simulation, as only a coarse approximation is needed to generate the transient model initial condition. Flow solution convergence typically was reached in 100 and 300 iterations for the No-Slag and Slag Models, respectively. The convergence history plot for the 0.010 m diameter, 0.3 m/s inlet velocity Slag Model is shown in Figure 3.4.

In the second, transient run, the free surfaces were allowed to deform. Initial flow values were set to converged SS simulation values, thereby minimizing free surface overshoots and oscillations. The edges formed at the free surface/inlet boundary intersections were specified to be zero-displacement references for the deforming surfaces. Global solution convergence occurred when mesh movement essentially ceased from one time step to the next. While somewhat user subjective, steady-state could be visualized when the history plots of free surface node locations leveled out at a constant height. The z-height history plot for a random free surface node is plotted in Figure 3.5. Note how at past 2.20 s, the nodal height remains nearly constant. When numerous free surface nodes at all areas of the domain exhibited similar behavior, it was determined that the transient model has reached its steady-state approximation.

Free surface position data for this case (No-Slag Model, 0.010 m diameter, 0.3 m/s inlet velocity) was subsequently collected from the deformed mesh at 2.70 s for analysis. A typical simulation required about 3 seconds of simulation time, using approximately 10,000 time steps of 0.0003s increments. However, simulations using large diameter nails and higher velocities required slightly more simulation time to reach steady-state. Inner-routine residual convergence to 1e-3 was specified.

3.4 Pre-Simulation Analytics

3.4.1 Estimation

An estimation routine was performed to identify important simulation phenomena. For this project, the main governing equations to be used are the incompressible continuity equation given in Equation 3.2 and the Navier-Stokes momentum equation given in Equation 3.7 Note that the continuity equation contains only velocity parameters. Because the velocities remain unknowns at this stage, no conclusive evidence of negligible terms exists for this equation. However, due to the inclusion of diffusive, pressure, and transport phenomenon, an estimation routine was performed on the momentum equation.

For this analysis, the body force terms in the governing equations are neglected. Being a free-surface problem, it is already known that the gravitational force has a large impact on the final shape of the free surface profile, qualifying its omission from the estimation routine. Inputting the non-dimensional values found in the Nomenclature section into the momentum equation, the steady-state version of Equation 3.7 (minus the body force term) becomes:

$$\rho\left(\frac{\partial \overline{u_i}}{\partial t}+\frac{\partial}{\partial x_j}\left(\overline{u_i u_j}+\overline{u_i' u_j'}\right)\right)=-\overline{p_i}+\mu_{eff}\frac{\partial}{\partial x_j}\left(\frac{\partial \overline{u_i}}{\partial x_j}\right)+\rho b \tag{3.7}$$

$$\left[\frac{\rho V^2}{H}\right]\left(\overline{u_i^*}\frac{\partial \overline{u_j^*}}{\partial x_i^*}\right)=-\left[\frac{\Delta p_c}{H}\right]\frac{\partial \overline{p^*}}{\partial x^*_{,i}}+\left[\frac{\mu V}{H^2}\right]\left(\frac{\partial^2 \overline{u_j^*}}{\partial x_i^{*2}}\right) \tag{3.44}$$

Dividing Equation 3.44 by $\rho V^2/H$:

$$\left(\overline{u_i^*}\frac{\partial \overline{u_j^*}}{\partial x_i^*}\right) = -\left[\frac{\Delta p_c}{\rho V^2}\right]\frac{\partial \overline{p^*}}{\partial x^*_{\,i}} + \left[\frac{\mu}{HV\rho}\right]\left(\frac{\partial^2 \overline{u_j^*}}{\partial x_i^{*2}}\right) = -\left[\frac{\Delta p_c}{\rho V^2}\right]\frac{\partial \overline{p^*}}{\partial x^*_{\,i}} + \left[\frac{1}{\mathrm{Re}}\right]\left(\frac{\partial^2 \overline{u_j^*}}{\partial x_i^{*2}}\right) \tag{3.45}$$

In this case, a characteristic pressure difference (Δp_c) is difficult to directly specify. To properly estimate this value, the coefficient for the pressure variation in Equation 3.45 will be forced to 1. Now, the characteristic pressure difference equals:

$$\Delta p_c = \rho V^2 \tag{3.46}$$

With the pressure gradient coefficient forced to 1, the fully scaled momentum equation becomes (substituting the Reynolds number for the diffusion coefficient):

$$\left(\overline{u_i^*}\frac{\partial \overline{u_j^*}}{\partial x_i^*}\right) = -\frac{\partial \overline{p^*}}{\partial x^*_{\,i}} + \left[\frac{1}{\mathrm{Re}}\right]\left(\frac{\partial^2 \overline{u_j^*}}{\partial x_i^{*2}}\right) \tag{3.47}$$

The Reynolds number for this simulation can be approximated by:

$$\mathrm{Re}^{-1} = \left(\frac{v_c * L_c}{\nu}\right)^{-1} = \left(\frac{0.25\frac{m}{s} * 0.015m}{8.1\times10^{-7}\frac{m^2}{s}}\right)^{-1} = 2.2\times10^{-4} \tag{3.48}$$

Due to its small coefficient (= 2.2 x 10^{-4}) compared to the other coefficients (= 1) in the final scaled equation, the viscosity term (the rightmost term in Equation 3.47) plays a minor role in the fluid flow; the fluid inertia and pressure terms dominate the flow.

In addition to the two governing equations, a scaling estimation performed on the pressure term is necessary to determine whether surface tension will play a large role in this simulation. Equation 3.21 (the dynamic boundary condition at the free surface) can be scaled into the form (only considering surface curvature in one direction):

$$(p_{steel,surface} - p_{air})n - n\cdot\tau = -2\kappa_m \gamma n - \nabla_{surf}(\gamma) \tag{3.21}$$

$$\left[\rho V^2\right]\overline{p^*} \cdot n - \left[\frac{\mu V}{H}\right] n \cdot \tau^* = -\left[\frac{\gamma}{H}\right]\frac{1}{R^*} \cdot n \qquad (3.49)$$

Dividing by $\rho V^2 L/H$, Equation 3.49 becomes:

$$\left[\frac{\mu}{\rho H V}\right]\overline{p^*} \cdot n - \left[\frac{\mu}{\rho V L}\right] n \cdot \tau^* = -\left[\frac{\gamma}{\rho V^2 L}\right]\frac{1}{R^*} \cdot n \qquad (3.50)$$

Substituting non-dimensional values into Equation 3.50:

$$\left[\frac{1}{\mathrm{Re}}\right]\overline{p^*} \cdot n - \left[\frac{1}{\mathrm{Re}}\right] n \cdot \tau^* = -\left[\frac{1}{2 * We}\right]\frac{1}{R^*} \cdot n \qquad (3.51)$$

For cases in which the inertial forces are more dominant than the viscous forces (as in this case), the Weber number is used to relate the inertial forces to the surface tension forces. The Weber number has a value of:

$$We = \left[\frac{7400\frac{kg}{m^3} * \left(0.25\frac{m}{s}\right)^2 * 0.015m}{2 * 1.6\frac{N}{m}}\right] = 2.168 \qquad (3.52)$$

Because the Weber number is on the same order as 1, the surface tension forces will be nearly as important as the inertial forces. In fact, a very erroneous solution would be formed if surface tension was neglected. Because the spines method was chosen to quantify free surface deformation, surface tension will be considered.

3.4.2 Analytical Solution

Several analytical solutions have been researched. These solutions provide fundamental trends which should be present in the final solution as well as providing a crude reference as to the accuracy of the end result. In the following subsections, two analytical solutions will be described.

3.4.2.1 Bernoulli Relations

The Bernoulli Equation is derived from a basic conservation of energy balance within the fluid. It has been proved by Bernoulli that:

$$p + \frac{1}{2}\rho V^2 + \rho g h = C \tag{3.53}$$

In fact, the same principles were used to develop both the Bernoulli Equation and the Navier Stokes conservation of momentum equation (Equation 3.7). However, the derivation of the Bernoulli Equation required the following fluid assumptions: constant density, inviscid, steady flow with no heat transfer. For this analysis, a fluid molecule on the free surface of the liquid in the No-Slag Model is considered. Estimating the free-surface run up in the Slag Model is fruitless due to the unknown slag/steel interface velocity. It will be established that this molecule (with initial velocity equal to the free-stream velocity) follows a single streamline towards the surface-piercing nail. Once reaching the nail, it impinges on the nail surface pointing directly upstream (represented by the leading edge location of Figure 3.3). Simply put, the kinetic energy of the molecule in the free-stream is completely converted into potential energy, given by a change in height at the surface of the nail. From the Bernoulli Equation, the change in height of this molecule after contacting the nail is:

$$\Delta h = \frac{1}{2g} V^2 \tag{3.54}$$

The run-up estimation will be used as a baseline with which to compare free surface height changes at the leading edge of the nail. Because the Bernoulli Equation assumes perfect transfer of energy, it represents the maximum amount of run-up possible for any given case. A sample calculation estimates that for a free-stream velocity of 0.25 m/s contacting a nail of any diameter, the leading edge run-up is estimated as 3.19 mm. The turbulent, non-regular flow which is prevalent downstream of the nail prevented Bernoulli relations from estimating run-down height along the nail trailing edge.

3.4.2.2 Fluid Dynamics and Morison Equation

The second analytical approach involves utilizing an unrefracted wave approach. This method was previously derived by Shaver[56)], and his work is summarized in the following paragraphs.

The first step to approximating free surface flow past a submerged nail is to develop the relation between the unrefracted wave height (measured as the distance between the high point and the low point on the steel knob, $H_o^{'}$) and the initial wave height (H_o).

$$H_o = k * H_o^{'} \tag{3.55}$$

Weigel and Beebe empirically determined that the ratio between unrefracted and initial wave heights (k) is approximately 0.78[57]. Shaver then approximated the leading edge run-up height to approximately half of the unrefracted wave height, represented by[56]:

$$h_{run-up} = 0.507 H_o^{'} \tag{3.56}$$

With the wave height nomenclature defined, the maximum force of the moving steel flowing past the nail was calculated. Known as the Morison Equation, this force is related to the unrefracted wave height by:

$$F_{\max} = \frac{\pi^2 \rho H_o' L D^2 k^2 C_m}{8 t_s^2} \tag{3.57}$$

In his work, the maximum frequency (wave period) detectable was 0.030 seconds. The velocity can now be deduced from the maximum force equation through[58]:

$$V = \left(\frac{2F_{\max}}{L \rho C_f D} \right)^{1/2} = \left(\frac{\pi^2 H_o' D k^2 C_m}{C_f 4 t_s^2} \right)^{1/2} \tag{3.58}$$

Rearranging to solve for the unrefracted wave height, Equation 3.58 becomes:

$$H_o' = \frac{4 t_s^2 V^2 C_f}{\pi^2 D k^2 C_m} \tag{3.59}$$

Using the rearranged Morison Equation to estimate the 0.25 m/s free stream, 15 mm nail diameter case, the unrefracted wave height and the run-up height are approximated as 8.42 and 4.27 mm, respectively.

3.4.3 Pre-Simulation Conclusions

Estimation

Through the estimation routine previously outlined, the following conclusions have been reached:

- The diffusion term is negligible compared to the inertia term in the momentum equation.
- Shear stress effects are negligible compared to surface tension and pressure effects in driving the flow.
- Surface tension effects cannot be neglected.

Analytical Solution

Analytical solutions of the Bernoulli and Morison equations are applied to relate fluid velocity to the steel knob profile. Both methods predict that as velocity increases, knob run-up increases quadratically. The Morison Equation further provides a relation between the nail diameter and knob profile; as diameter increases, the unrefracted wave height decreases.

Even though there is a higher degree of inclusiveness with the Morison analysis over the Bernoulli approach, its accuracy is questionable. Because the Bernoulli Equation describes a perfect transfer of energy to change in surface height, it is quite suspicious that the Morison Equation predicts greater run-up values. Discrepancies between both analysis further necessitate the creation of a model solely dedicated to solving the Nailboard problem. All is not lost however; the Bernoulli Equation will be included in all run-up data plots representing the upper run-up bound, and the Morison wave prediction provides a basis for the knob profile analysis.

3.5 Validation

3.5.1 Program Validation

In his study "The Effect of Viscosity on the Transient Free-Surface Waves in a Two-Dimensional Tank.", Wu finds an analytical equation for wave height at any point on the free surface[59)]:

$$\frac{\eta(t)}{\eta_0} = 1 - 2\kappa \operatorname{Re} \sum_{i=1}^{2} \frac{A_i \left\{ -\gamma_i e^{(-1+\gamma_i^2)\nu k_2^2 t} \left[1 + erf(\gamma_i k_2 \sqrt{\nu t}) \right] + \gamma_i + erf(k_2 \sqrt{\nu t}) \right\}}{1-\gamma_i^2} \tag{3.60}$$

Most of the variables in the above equation are omitted from the Nomenclature section, as many are empirical solutions to real and imaginary equations. The reader will be referred to the published text for more information regarding the derivation of this analytical solution.

The simulation consisted of a 2-D container filled with fluid exhibiting only laminar behavior. Simulation parameters are shown in Table 3.1, while the 2-D mesh is shown in Figure 3.6. Note the initial free surface elevation is higher on the right side of the domain. The initial wave coupled with gravity causes a periodic wave to form in the transient simulation, either favoring the right or left domain side over time. Termed "sloshing", this motion (in particular, nodal free surface height) is exactly solved via Equation 3.60.

The Fidap output for wave height compares remarkably well to the analytical solution (Figure 3.7). Although the analytical solution interprets the wave profile as a sine wave, it was unnecessarily complicated to develop an initial mesh with a non-constant free surface slope. Because the initial conditions (specifically the free surface profile) were not identical to the analytical case, an overshoot in the Fidap model occurs at the second oscillation peak. Once the flow is "developed", then the Fidap output mirrors the analytical solution. Through this analysis, it can be concluded that Fidap's use of the spines method for transient simulations are accurate. A copy of the analytical validation input file can be found in Appendix C.2.1.

3.5.2 Model Validation

Prior to simulation of the Nailboard measurement process, the model was applied and compared to experimental results to confirm model validity. J.R. Chaplin *et. al.* performed experiments involving dragging a vertical cylinder through still water, as demonstrated in Figure 3.8[51)]. By transforming Chaplin's physical experiment setup into a mathematical model (with the model parameters shown in Table 3.1), the run-up on the leading edge was computationally solved using Fidap. Diagrams of the location of the leading edge node within the domain are shown in Figure 3.3. The dimensions of the domain were consistent with the values displayed in Figure 3.3b for a 0.21 m diameter cylinder.

Only two of Chaplin's experimental velocities were tested using Fidap (0.96 m/s and 1.36 m/s). The highest velocity to be considered in the molten steel will be 0.6 m/s. Thus, comparing the molten steel model with this water experimental model for velocities much higher than 0.6 m/s is unnecessary.

Figure 3.9 compares the Fidap outputs for run-up at the cylinder's leading edge to Chaplin's experimental results. The Bernoulli line was also plotted in this figure (as the upper bound reference; refer to Section 3.4.2.1). Close agreement between the experimental results and the Fidap outputs was reached, with both mirroring the Bernoulli line. It is concluded through this comparison that the model is accurate using water properties. Moving forward, it is assumed that the model is valid in modeling the Nailboard models.

3.5.3 Testing the Solidification Assumption

Although this Fidap model was proven accurate when compared to Chaplin's water experiments, there is one key difference between the two simulations- the molten steel solidifies to the nail (thus creating the knob) whereas the experimental water model has no mass transfer. The model assumes that nail growth due to solidification is unimportant.

Data was collected from actual Nailboard tests conducted at Nucor Steel in Decatur, AL. Nails were dipped for various submersion times ranging from 2 to 10 seconds. Figure 3.10 shows a photograph of a sample solidified knob along with the locations at which knob diameters data was taken. The experimental data is plotted in Figure 3.11. Treating the axisymmetric solidifying knobs as 1-D shell growth, the solidification front thickness and the rate at which solidification occurs are approximated by:

$$s = k_s t^{1/2} \tag{3.61}$$

$$\frac{ds}{dt} = \frac{1}{2} k_s t^{-1/2} \tag{3.62}$$

The solidification constant, k_s, was unknown for this model; by varying its value until Equation 3.61 best fit the data (designated by the solid line in Figure 3.11), it was empirically determined that $k_s \approx 21\ ^{\mathrm{mm}}/_{\mathrm{min}^{\wedge}.5}$. Knowing k_s, the rate of solidification (Equation 3.62) can be directly computed. At a time of 2 seconds (the absolute minimum submersion time required to develop a substantial knob), $^{ds}/_{dt} \approx 9.6\text{x}10^{-4}$ $^{m}/_{s}$. Even the largest observed solidification rate is over two orders of magnitude lower than the slowest inlet velocity simulated (0.2 $^{m}/_{s}$). Thus, the fluid flow field will evolve much faster than the solidification rate, and therefore the solidification of the knob can be ignored; the knob diameters are considered to be explicit, discrete values.

During the first few seconds of submersion, there is pure solidification of molten steel onto all locations of the nail. As the submersion time increases, the knob growth slows because of the lessened temperature gradient between the fluid and the knob. In fact, as the knob temperature continues to increase to the steel superheat level, it begins to remelt into the liquid pool (as the knob surface temperature exceeds the solidus temperature of the steel). The solidification equation assumes that there will be pure solidification, thus for submersion times large enough to include knob remelting, Equation 3.61 is not accurate.

Note that the diameters at the top of the nail are consistently larger than the rest of the nail (especially at higher submersion times). At the surface of the molten steel, there is a relatively high amount of heat transfer with the environment. With a path for heat to escape, knob diameter will continue to grow throughout submersion. Whereas the diameter of the knob levels off at all diameters below the knob surface, the diameter keeps increasing at the surface. A sample exhibiting this "mushrooming" behavior at the top of the knob can be seen in Figure 3.12. In any case, the solidification equation does represent the regions of pure solidification fairly well (at low submersion times, favoring the top diameter measurement).

3.6 Typical Flow Results

For all of the cases considered (all combinations of inlet velocity and nail diameter), similar macro-scale flow patterns emerged. Flow in both the No-Slag and the Slag Model domains are examined in detail for a characteristic case (0.3 m/min inlet velocity, 0.010 m nail diameter). Typical results for each step in the solution procedure of the characteristic case are given in Figures 3.14-3.29.

3.6.1 Flow in the No-Slag Model

As previously discussed, a No-Slag Model was created for several reasons. Sample Fidap input files for the No-Slag model (including both the first steady-state, fixed free surface run and the second transient free surface run) can be found in Appendices C.2.2 and C.2.3.

Mesh Description

The overall dimensions and operating conditions for the No-Slag model can be seen in Figure 3.3a and Table 3.1. A domain was discretized via FiMesh and contained 4088 elements. The generated mesh can be seen in Figure 3.13a. A fully structured mesh was created (as required for spine generation), yielding minimum computational time and a high degree of computational efficiency over an unstructured mesh. Note the increase in mesh refinement around the nail, the region expected to generate the highest flow gradients.

3.6.1.1 Steady-State Simulation

In order to generate appropriate fluid initial conditions for the second-step transient free-surface run, an initial steady-state simulation is performed. In this simulation, the free surface was not allowed to deform, and constant values (velocity, kinetic and dissipation energies) were used at the domain inlet boundary. The following section discusses the results of a typical steady-state analysis.

Velocity Vector Plots

The velocity vector solution for this initial, fixed surface, steady-state run can be seen in Figure 3.15. The flow enters the domain with constant velocity and is diverted around the stationary nail. Intuitively, the velocity in the z-direction for the fixed free surface run should be positive directly in front of the nail, indicating the fluid wants to "climb" up the front of the nail. To maintain a constant mass flow rate, the reduced fluid area (due to the presence of the nail) causes fluid acceleration in the regions directly adjacent to the nail. Once past the nail, the gravitational bodyforce imposed on the steel coupled with the pressure drop in the nail wake causes downward flow (which translates into a decrease in free surface elevation in the subsequent free surface run). While small flow gradients still exist at the outlet boundary, they are not significant enough to discredit the implementation of the boundary conditions at this surface (as explained in Section 3.3.4.4).

It is important to note that the flow remains uniform on the far-field wall opposite from the nail. Because the flow there was not disturbed, it can be assumed that this wall is far enough away that it does not influence flow patterns near the nail (per the far-field assumption).

Pressure Contour Plot

In Section 3.4.1, it was determined that the pressure was an important factor in driving flow profiles. Looking at the pressure solution plots (Figure 3.17), similar trends confirm ideas deduced from the velocity vector plots. A high pressure region is formed directly in front of the nail, indicating that the fluid level will rise in this region once the free surface is unconstrained. In contrast, the area directly behind the nail has lessened pressure in relation to the unconstrained flow, allowing the fluid height to lower. Away from the nail, relatively no pressure gradients are found (indicating constant velocity and constant direction flow).

Turbulent Kinetic and Dissipation Energy Contour Plots

Turbulent kinetic energy and dissipation energy contour plots can be seen in Figures 3.19a and 3.20a, respectively. Understandably, the highest levels of turbulence are found in the region directly behind the nail. A large wake region, or recirculation zone is expected to form as a result of flow past the nail. With increasing velocity gradients and the entrainment of surrounding fluid, fluid turbulence increases (as conveyed through higher energy regions). Because there is no slag layer in this model, higher levels of turbulence should not have a large impact on the simulation (it is unlikely that air above the free surface interface will become entrained with this magnitude of turbulence). Even in the unlikely situation where air does become entrained and multiphase flow emerges, the turbulent region is downstream of the nail and thus should have little bearing on the flow in the region of interest near the nail.

Notice that there is virtually no gradient for either kinetic or dissipation energy with increasing distance from the inlet boundary. This confirms that all of the inlet boundary conditions are reasonable, including the assumption of $\mu_t \approx 10*\mu_o$ in specifying inlet turbulence. In addition, previous work by Zhang *et. al.* determined comparable values of dissipation energy near the mold top surface when considering similar values of inlet velocity[16)].

3.6.1.2 Transient Simulation

The converged solution of the steady-state flow problem becomes the initial condition for the second step, which is a transient simulation with a free top surface. All boundary conditions remained constant between the two models, except for allowing the free surface to deform. The following section discusses the results of the converged transient simulation.

Mesh Deformation Plots

The initial, undeformed mesh and the final deformed converged mesh are outlined in Figure 3.21a (including a zoomed view of the nail region). On a purely qualitative level, the simulation produces results which match the hypothesis reached from the initial steady-state fixed-surface simulation. The free surface rises at a very slight gradient as the flow enters the domain, then accelerates upward immediately in front of the nail. A nearly constant $^{dx}/_{dz}$ free surface slope is established as the flow passes the nail. As also seen in the steady-state problem, a pressure drop is formed downstream causing a recessed region behind the nail (due to the wake effect). The free surface deformation is limited to the area directly around the nail. However, with increased fluid velocities, the free surface deformation extends further into the domain. Waves can be seen propagating away from the nail in the downstream region. At no point does the deformation reach any vertical walls (with the exception of the outlet boundary), which indicates that the domain is properly sized to simulate this process.

Velocity Vector; Pressure, Turbulent Kinetic and Dissipation Energy Contour Plots

Recall that the only major difference between the steady-state simulation and the transient simulation was the release of the fixed top surface constraint. Because of this, the macro-scale fluid trends for the transient run are expected to be similar to those found in the steady-state simulation. This is confirmed by examining Figures 3.24, 3.26, 3.28a, and 3.29a, and comparing them to their respective steady-state run equivalent. For this reason, the reader is directed to the previous section (Section 3.6.1.1) for a discussion of the flow trends in the No-Slag transient simulation.

3.6.2 Flow in the Slag Model

With a baseline set via the completed No-Slag Model, simulations incorporating the slag into the mathematical domain were carried out The Slag Model incorporates all of the phenomena important to the molten-steel process in its formulation. Sample Fidap input files for an entire Slag model run (including the inlet velocity simulation, the first-step steady-state fixed surface run, and the second-step transient free surface run) can be found in Appendices C.2.4, C.2.5, and C.2.6.

Mesh Description

The overall dimensions and operating conditions for the Slag model can be seen in Figure 3.3c and Table 3.1. FiMesh was used to discretize the domain into 5760 elements, which can be visualized in Figure 3.13b. Spine generation requires structured meshes, which was satisfied in the mesh generation step. Besides being required for this particular free surface simulation, structured meshes generate results with higher accuracy and less computational cost than unstructured meshes. The mesh was refined in two regions: around the nail (similar to the No-Slag Model) and near the internal free surface. The velocity and pressure gradients (both the slag and steel) are expected to be highest at these locations, necessitating the higher number of nodes via mesh refinement.

3.6.2.1 Inlet Velocity Simulation

Adding the slag layer introduces a top-surface zero tangential velocity boundary condition and an internal free surface (in addition to the second fluid region) to the model. Due to this complexity, the proper steel and slag inlet boundary velocities could not be determined a-priori as in the No-Slag Model. Instead, a simple 2-D transient simulation was created with no nail to generate accurate far-field flow parameters to use as the inlet boundary conditions for the Slag Model. Identical node heights were used in the Inlet Velocity Simulation as in the Slag Model, allowing for direct transfer of nodal values between models. The inlet and outlet boundaries of the Inlet Velocity Simulation were given Neumann boundary conditions to ensure that nothing prevented the flow from establishing a natural boundary layer gradient. Beginning with initial steel velocities dictated by the particular run (i.e. 0.3 m/s steel inlet velocity), the transient run progressed to a specific simulation time dictated by the steel velocity and a constant value (in this case, the distance from the meniscus to the approximate sampling location) using a successive substitution algorithm. The following section includes the findings of this Inlet Velocity Simulation.

Velocity Vector Plot

The velocity vector solution is shown in Figure 3.14a. Immediately after the transient simulation began, the high viscosity of the slag layer slowed the velocity of the internal interface, causing the steel near this interface to slow. Because no explicit velocities were imposed on the inlet and outlet boundaries, the gradients were able to propagate freely throughout the entire domain. Implementation of wall laws at the internal interface generated high gradients propagating into the steel layer. The nodal velocities from this simulation were manually collected and inputted at the inlet boundary of the Slag Model.

Pressure Contour Plot

As seen in the pressure contour plot (Figure 3.14b), a quantifiable pressure gradient is formed as a function of height. Because there are no explicit flow boundary conditions for this Inlet Velocity simulation, external pressure forces are not driving the flow. The observed pressure distribution is almost solely hydrostatic, due to gravity "pulling" down on the fluids. Consequently, it was not required to define the fluid pressure at each node in the Slag Model domain inlet; the static pressure distributions generated automatically by the gravitational bodyforce were sufficient.

Turbulent Kinetic and Dissipation Energy Contour Plots

The highest levels of turbulence were found near the internal interface (Figures 3.14c and 3.14d). Large velocity gradients in the steel layer due to wall laws at the interface generate high levels of shear stress, which tend to generate high levels of turbulence. Very similar turbulence patterns are expected to be formed throughout the 3-D Slag Model domain at the internal interface.

Nodal kinetic and dissipation energies (K and ε) were extracted from this model and used to define equivalent values at the Slag Model inlet boundary nodes.

3.6.2.2 Steady-State Simulation

Transient simulation accuracy is extremely dependent on accurate initial conditions. For this reason, a steady-state simulation (using the Slag Model) was performed with the intent of using the converged simulation as the initial condition for the transient run. Both the upper and internal interfacial free surfaces were not allowed to deform, and the inlet boundary flow parameters were assigned values corresponding to the Inlet Velocity Solution output. The following section summarizes the findings of the converged steady-state analysis.

Velocity Vector Plots

The velocity vector solution for the Slag Model steady-state simulation is shown in Figure 3.16. Many of the same trends are observed here as in the No-Slag steady-state simulation. The flow enters the domain according to the specified inlet profile and gets diverted around the stationary nail. Steel is directed upward in front of the nail, while a pressure drop gives rise to downward flow immediately past the nail.

As visualized in Figure 3.16, flow through the slag layer is severely restricted (due to high viscosity and the zero horizontal velocity boundary condition enforced at the upper surface). The result of the nearly stagnant slag is a steel/slag interface with extremely slow velocities. Note how the upward flow strength directly in front of the nail in the Slag model pales in comparison to that in the No-Slag Model. Using energy balance logic, slower flow with less energy has a smaller tendency to distort the free surface.

Remember that the fluid density difference is much less for the steel-slag interface than the steel-air interface of the No-Slag Model. Essentially, smaller interfacial density differentials require less energy to deform the surface a given amount. So even though flow normal to the interface is much less than that of the No-Slag Model, the presence of the slag layer indicates less energy is required to deform the surface. At this point, these opposing effects make free surface deformation predictions between the two models nearly impossible.

Pressure Contour Plot

Through the estimation routine outlined in Section 3.4.1, pressure differences were found to be an important factor in driving the flow and establishing flow patterns. Pressure contours for the Steady-state Slag Model run are shown in Figure 3.18. Very similar pressure gradients are formed in both the Slag and No-Slag Models, indicating that the extra pressure due to the slag layer is not likely to affect flow in the steel layer. The characteristic high pressure region in front of the nail and low pressure region after the nail are formed.

Slight pressure disturbances are found in the steel layer near the inlet boundaries along the steel/slag interface. One major difficulty of the Slag Model was treatment of the inlet boundary flow profile. While close to being exact, irregular pressure disturbances near the inlet indicate the boundary conditions at this surface were not completely correct. It is expected that these pressure variations will cause the interfacial free surface to slightly distort once it becomes unconstrained. Further explanation of the inlet boundary velocity definition problem and its subsequent handling can be found in Appendix B.

Turbulent Kinetic and Dissipation Energy Contour Plots

Turbulent kinetic and dissipation energy contour plots for the Slag Model steady-state simulation are shown in Figures 3.19b and 3.20b, respectively. A small amount of turbulence is found in the steel layer near the internal free surface throughout the domain (due to large steel velocity gradients). Turbulence also arises when the flow initially contacts the stationary, no-slip nail surface. However, the highest turbulence is generated within the large recirculation zone of the wake region past the nail. It is known that level fluctuations are directly related to the amount of turbulence near the free surface[60)]. Because this highly-turbulent region is located downstream of the nail, however, level fluctuations are not expected to have a significant impact on surface profiles along the nail.

3.6.2.3 Transient Simulation

Upon convergence of the steady-state simulation, the solution flow parameters are inputted as the initial conditions for the second-step, transient simulation. The free surfaces were now allowed to deform; all other boundary conditions for the transient simulation remained identical to that of the steady-state simulation. The following section discusses the results of the Slag Model transient simulation.

Mesh Deformation Plots

Figure 3.21b shows the final deformed mesh superimposed with the initial, undeformed mesh. Very similar trends to the No-Slag Model emerge; the interface surface is accelerated up the front of the nail, as the fluid pressure increases with the liquid steel impacting the leading edge of the nail. The low-pressure region created in the liquid steel downstream of the nail (as observed in the steady-state simulation) causes the interfacial level to drop, extending from the downstream-facing nail edge into the wake region. The interfacial deformation area increased with faster inlet velocities. For instance, the wake in high velocity, large nail diameter cases extended nearly to the outlet boundary. Despite this, the domain size was determined to be appropriate for the simulations; the domain boundaries were far enough from the critical nail region to have no noticeable effect on flow in that area.

An interesting trend occurs at the free surface of the slag layer near the nail. Whereas the steel interface rises as the flow approaches the nail (from the upstream direction), the slag free surface level actually *drops* close to the nail. It was expected that the incoming slag flow should yield a run-up approaching the nail, not a run-down. An explanation for this behavior is found by examining the velocity solution.

The interfacial free-surface shape along the far-field boundary opposite to the nail is plotted in Figure 3.22. Because the nail influence is negligible in determining flow at this far-field boundary, the interfacial deformation seen in this plot confirms the expectation that the fluid inlet profiles were not perfectly defined. This edge was subsequently used as a reference edge in ensuing knob profile postprocessing sections. The assumption made is that the same minor deformation due to erroneous boundary conditions occurs at ALL locations in the domain (as a function of distance from the inlet), and this deformation is accurately represented by the far-field reference edge. By this logic, subtracting the control axis edge deformation from the knob axis profile will solve for the “filtered” deformation caused ONLY by the nail presence, which is the objective of this project.

Note the relatively small amount of deformation along the far-field (reference) wall of Figure 3.22, indicative of reasonably-accurate inlet velocities. Also represented in the graph are the unfiltered and filtered surface deformations of the symmetry interface boundary (along which the nail lies). Logically, the immediate increase in surface elevation of the unfiltered plot near the inlet seems to be wrong. By subtracting the control edge, the resulting filtered plot has a much more gradual surface rise leading up to the nail, which is more physically correct. Thus for subsequent analyses, only filtered surface deformation lines are considered.

Velocity Vector

From the perspective of Figure 3.23, a counter-clockwise recirculation zone is formed in the steel layer while clockwise recirculation occurs in the slag layer. Interestingly, both fluids along the interface actually travel *upstream* close to the nail. It appears that once the steel layer pushes the interface level high enough (and a large enough interface slope is developed), the very slow initial velocities at the interface allow the fluid to change direction and travel down the slope. Albeit extremely small velocities, clockwise recirculation causes the slag to flow down the front of the nail, causing a drop in slag top surface elevation near the nail. With higher velocities, the amount of recirculation increases, enhancing both free surface deformation effects.

The complete velocity vector solution for the transient Slag Model solution can be seen in Figure 3.24. Very similar flow patterns throughout carried over from the steady-state simulation. Refer to Section 3.6.2.2 for a complete analysis of the velocity flow patterns established in the transient simulation.

Pressure Contour, Turbulent Kinetic and Dissipation Energy Contour Plots

Allowing the free surfaces to deform in the transient simulation did not change macro-scale fluid trends from the steady-state runs for these flow parameters. This is confirmed through examination of Figures 3.27, 3.28b, and 3.29b, and comparing them to their steady-state run equivalents. To prevent repetitiveness, the reader is directed to the steady-state run description (Section 3.6.2.2) for discussion of overall pressure and turbulence results.

3.7 No-Slag Model Investigation

Prior to the complete Nailboard method investigation, a simplified domain was created using only the steel layer. Results generated from this No-Slag Model agreed favorably to an experimental simulation in which a cylinder is dragged through a pool of stationary water (Section 3.5.2). The hypothesis that water models may accurately simulate the Nailboard technique and the interchangeability of these methods will be tested. Furthermore, the No-Slag Model allows for general trends to be made regarding single layer flow past a nail; trends which are also expected to be present in the full Slag Model. Through the No-Slag Model, a concrete basis for the complete steel/slag domain will be formed.

3.7.1 Model Cases

In this study, free surface deformation near the critical nail region are investigated using the single layer fluid model. Simulation cases were chosen to encompass the typical range of meniscus-level velocities. By observing the free surface profile established at the nail surface, trends relating nail diameter and velocity past the nail were developed. The overall domain dimensions (length, height, and depth) were held constant, the nail diameter within the mold was altered for each simulation case. Refer to Figure 3.3a for a visual representation of the No-Slag Model domain. Nearly identical meshes were utilized in all cases, containing 5445 nodes and 4088 elements.

3.7.1.1 Steel No-Slag Model

The primary focus of the overall No-Slag Model is to examine single-layer steel flow through the domain. Inlet velocities were varied from 0.2 to 0.6 m/s (via 0.1 m/s increments) and the nail diameter was varied from 0.005 m to 0.015 m (via 0.005 m increments), yielding fifteen total cases. Fluid properties were set to liquid steel values for this analysis.

3.7.1.2 Water No-Slag Model

A water model case was developed for comparison to the steel model. Identical meshes and simulation parameters were used in both models; fluid properties will be solely responsible for generation of result differences. The particular simulation which will be compared is the 0.005 m nail diameter, 0.3 m/s inlet velocity case. The experimental validation model represents a test case of the water model, but because that simulation has already been solved and proved accurate, it will be omitted from this study.

3.7.2 Solution Methodology

Using the simulation parameters displayed in Table 3.1, both the steel and water model steady-state runs converged in about 100 iterations, while the transient runs were completed after approximately 10,000 time steps (converging in 3 iterations at each time step, with Δt = 0.003 s). In the transient simulation, the larger diameter and higher velocity transient runs required slightly more time steps to reach "steady-state" as the free surface deformation was more pronounced. Convergence took approximately 30 minutes and 10 hours for the first-step, steady-state run and the second-step, transient run (respectively) on a IBM POWER4 p690 processor with a computational power of 1.3 GHz. By keeping all other aspects of the models consistent, the effects of the inlet velocity, nail diameter, and fluid properties in deforming the free surface were studied.

3.7.3 Results

3.7.3.1 Leading Edge Run-up (Steel Model)

One of the key regions of interest of the deformed free surface is the run-up on the leading edge of the nail (in which the normal points directly upstream). Being the first part of the nail which the fluid contacts, the run-up has a direct relation to the fluid velocity. The particular node at which the following measurements were taken can be visualized in Figure 3.3b. Leading-edge run-up values for all converged simulations are plotted in Figure 3.30a.

It was estimated through the Bernoulli Equation that the run-up height is proportional to the inlet velocity squared. This trend is observed in the figure; as velocity increases, the run-up increases exponentially. Each set of data is fitted with a second order polynomial curve, which is also seen in the figure. High degrees of correlation (evident by R^2 values of nearly 1) were established for the best fit curves, indicating the data strongly follows the Bernoulli approximation.

Given perfect transfer of kinetic energy into potential energy, the Bernoulli Equation represents this upper run-up limit. As the nail diameter increases, the fluid is more inclined to push up the free surface upstream of the nail rather than be diverted around it. Recall that in the experimental comparison, the cylinder diameter was 0.21 m (considerably larger than the diameters this simulation runs). For those cases, the leading edge run up was extremely close to the Bernoulli prediction. The intuitive conclusion is that for larger diameters, the Bernoulli approximation becomes better in predicting leading edge run-up.

If the leading edge run-up and the nail diameter are known, a fairly good approximation of the fluid velocity can be made through Figure 3.30a. However, the undisturbed free surface level prior to testing is typically unknown, rendering the run-up parameter indeterminate. The complete knob profile is needed to generate the fluid velocity estimation.

3.7.3.2 Knob Profiles (Steel Model)

It was originally expected that the knob profile (including knob diameter) would be sufficient to determine the inlet (far-field) flow velocity of the liquid steel. The converged free surface elevation profiles (only considering the nodes along the nail) for the three nail diameters (0.005, 0.010, and 0.015 m) are plotted in Figures 3.31a, 3.32a, and 3.33a, respectively. Each inlet velocity is given its own curve, and free surface height is plotted as a function of *x*-distance along the nail (see Figure 3.3b for coordinate reference).

Analysis of the converged solution reveals very distinctive knob surface profiles for each inlet velocity. Whereas the knob profile has nearly a linear slope for slow velocities, the profile becomes less linear as the inlet fluid velocity increases. Higher velocities produce a higher leading-edge run-up (as confirmed in Section 3.7.3.1), but also the knob profile remains at this increased height for a greater distance before trailing off near the end of the knob. For example, the 0.005 m diameter nail case with 0.6 m/s inlet velocity has a knob height that remains above the initial free surface along the entire nail section ($\Delta h > 0$ for all x-values; Figure 3.31a). Only past the nail into the wake region does the free surface decrease lower than the initial surface height. With higher velocities, the increased momentum of the fluid and the increased run-up height allow the fluid to be carried further along the nail before gravitational effects can pull it down. If a knob with a sharp drop at the trailing edge is produced during testing, the flow past the top surface likely is traveling at a very high velocity.

As the nail diameter increases, an interesting finding occurs. Because of the extra width (x-distance) of large diameter cases, the flow cannot maintain an elevated free surface level through to the end of the knob. In these situations, the wake region is formed *prior* to the knob end, causing the free-surface level to actually rise before the flow is completely past the knob. A "lip" is formed at the downstream side of the knob, as evident in the 0.015 m diameter plot (Figure 3.33a). It is predicted that this "lip" should be visible on large-diameter test samples taken from actual casters.

In plots for all three diameters, it is important to recognize the different knob surface shapes formed by varying the inlet velocities. It should be possible to accurately solve for steel velocity knowing the entire knob profile shape and diameter, but it is difficult to compare the entire profiles quantitatively. An alternative, simpler method is desired to accurately estimate flow velocity.

3.7.3.3 Knob Profile Height Difference (Steel Model)

The knob height difference is calculated as the leading edge run-up height minus the trailing edge run-down height, as shown in Figure 3.3a. Height difference data for all velocities and diameters simulated by the No-Slag Model are plotted in Figure 3.34a. One benefit of this measurement is that the initial free surface level is irrelevant to the calculation. All that is required are two discrete, easily measured values: the knob diameter and the knob height difference along the nail axis.

This parameter can be thought of as a balance between surface tension, boundary layer flow velocity, gravitational forces, and leading edge run-up. Three regions are identified in the plot: the Undeveloped Profile (UP), the Developing Profile (DP) and the Overdeveloped Profile (OP) regions. From basic boundary layer flow theory, fluid velocity is directly influenced by the length of the no-slip (nail) surface and free-stream velocity. This idea will help explain flow patterns in the following investigation.

At slow velocities (≤ 0.2 m/s), the height difference is described by the UP region in which the knob height difference is too small to measure. Slow boundary layer velocity (yielding low fluid energy) causes gravitational forces and surface tension to dominate the flow, however small run-up heights prevent this theory from being visualized. A very small knob height difference results, as seen in the figure. Fortunately, most defects develop as a result of excessive flow, thereby rendering undeveloped knob profiles acceptable.

Increasing velocity causes the knob profile to enter the DP region in which height difference increases linearly with increasing velocity. Remember that higher fluid velocity yields increased run-up heights, promoting more free surface deformation around the nail. Increased boundary-layer velocity/momentum become prominent in developing the flow past the nail.

Once the velocity becomes sufficiently large, the OP region emerges. Boundary layer velocity/momentum dominates gravitational and surface tension forces in generating flow past the nail. Note that the OD region emerges quicker for the small diameter case; the shortened *x*-distance along the nail causes boundary layer flow to remain high across the entire nail, allowing for smaller velocities to become more important than gravity. Further increased velocities actually causes the knob height difference to decrease- gravitational force becomes negligible compared to boundary layer flow in developing the knob profile, allowing the flow to maintain a more horizontal trajectory past the nail (as seen in the gray dotted line of Figure 3.3a). The straightening knob surface causes surface tension forces (which are proportional to curvature) to become negligible, further promoting a lower knob height difference.

The increased DP region of the large diameter knob case indicates testing should be performed with the largest diameter possible. For the 0.015 m diameter case, the DP region spans the range of typical top surface velocities of a thin-slab caster (0.3-0.5 m/s). Test speeds within the actual caster should never be over 0.6 m/s (which generates more ambiguous, lower height difference values, as described by the OP region). In any case, the linear increase of the height difference curves with increasing velocity indicates this is a very simple, accurate, and convenient way to estimate flow velocity using the Nailboard method.

3.7.3.4 Water/Steel Model Comparison

In the modeling of high temperature fluid flows, water models generally provide an accurate way to observe flow without enduring the severe environment of the real process. After all, water and molten steel flow have very similar Reynolds numbers. The question arises: Is simulating flow through water models appropriate to quantify Nailboard Method of velocity measurements?

Unfortunately, the surface tension of water and steel are quite different, which causes major discrepancies between steel and water in free surface problems. Whereas the density of steel is about 7x larger than the density of water (the same ratio applies to their viscosities), the surface tension of steel is about 22x larger than that of water. With a large relative surface tension, the sharp variations in free surface elevation present in the water model are greatly smoothed in the steel model. As an example, a 0.005 m diameter was modeled with a inlet velocity of 0.3 m/s using both molten steel and water properties. The free surface profiles along the nail axis are compared for the two cases in Figure 3.35.

The shape of the free surfaces for both fluids looks nearly identical in regions of low surface curvature. Near the nail (designated by the two vertical lines in the figure) where the curvature is high, however, the steel model has a much less distorted free surface profile than the water. Again, this is due to the high surface tension of the molten steel; the changes in fluid elevation and sharp surface gradients are more restricted with a higher surface tension. For this reason, a physical water model cannot be used to model free surface behavior in molten steel.

3.8 Slag Model Investigation

Before this current investigation, very little was known about how different velocities and nail diameters affect knob surface profile parameters in the Nailboard Method. As discussed in Chapter 1, many serious defects can result from excessive fluid velocities along the boundaries of the mold domain, particularly across the top surface (through slag entrainment into the steel pool, for instance). By monitoring top surface velocities in realtime, casting conditions can be adjusted accordingly, vastly improving steel quality.

In Section 3.7, the No-Slag Model was created to predict free-surface shape around the nail in the absence of a slag layer. The Slag Model was created as an extension to the previous model, motivated by the necessity for slag layer model presence to solve most real-world molten-metal flow profiles. It is expected that the same general trends (i.e. parabolic run-up height, more pronounced knob profile, and increasing height difference as a function of inlet velocity and knob diameter) should be found in both the domain including the slag layer and the single layer fluid model. A parametric study was performed with the Slag Model to study the effect of varying steel inlet velocities and nail diameters on the final converged steel/slag interface deformation (specifically at the nail). Simulation parameters for all cases can be found in Table 3.1.

Within complex models (as in the Funnel Mold simulation of Chapter 2), an alternate simple method of estimating free surface profiles was desired. By treating free surfaces as fixed and generating the flow solution, the pressure distribution along these surfaces allow for an estimation of the free surface deformation using energy conservation laws.

$$\Delta Height = \frac{p - p_o}{g\left(\rho_{steel} - \rho_{slag}\right)} \tag{3.63}$$

Panaras et. al. used a single-phase steady-state flow model to test the accuracy of the height approximation in Equation 3.63 with the actual top surface deformation[32)]. By neglecting the slag layer and treating the top surface as fixed, he found reasonable agreement between this pressure estimation equation and actual surface waves. Previous work by Anagnostopoulos modeling interfacial surface with water models further confirmed the accuracy of this pressure approximation[61)]. With two independent confirmations, the validity of this approximation appears promising. The simple method was also evaluated in the current work for the prediction of free-surface shape around the nail, using Equation 3.63 with the pressure results from the top fixed surface of the steady-state run

3.8.1 Model Cases

In this study, a steel/slag model was developed to observe deformation of the free surface near the critical nail region of the Nailboard method. For each velocity case, the external domain dimensions (length, height, and depth) were held constant while the nail diameters were altered. Because the wake region and the extent of the free surface deformation is largely related to the size of the obstruction, the model domain dimensions had to be extended to accommodate nails of larger diameters. Figure 3.3c provides a visual representation of the Slag Model domain, while the mesh containing 6851 nodes and 5760 elements can be seen in Figure 3.13b.

Inlet velocities were varied to encompass the typical range of velocities observed at a caster top surface from 0.2 to 0.6 m/s (in 0.1 m/s increments) and the nail diameter was varied from 0.005 m to 0.015 m (in 0.005 m increments), thereby yielding 15 test cases. Liquid steel values dictated the fluid properties used in this model. Water models were proven inaccurate for simulating steel free-surface deformation (Section 3.7.3.4). Consequently, water simulations with the Slag Model were not performed.

3.8.2 Solution Methodology

Using the simulation parameters in Table 3.1, the initial steady-state runs converged in about 300 iterations, while the transient runs completed after approximately 10,000 time steps (converging in 3 iterations at each time step, with $\Delta t = 0.003$ s). Convergence for each steady-state simulation remained relatively constant despite varying domain/mesh sizing and inlet velocities. Model simulations involving higher nail diameters and increased inlet velocities required slightly longer transient simulation time to reach "steady-state" approximation, as the free surface deformation was higher for these cases. Convergence took approximately 2 hours and 48 hours for the steady-state run and the transient run, respectively, on a IBM POWER4 p690 processor with a computational power of 1.3 GHz. By keeping all other aspects of the models consistent, the effects of the inlet velocity and the nail diameter in deforming the free surface were studied.

3.8.3 Results

3.8.3.1 Leading Edge Run-Up

It was shown in the No-Slag model that the nail leading edge run-up (the first part of the nail to contact the incoming fluid at the steel/slag interface, shown in Figure 3.3c) is a good indicator of free-stream fluid velocity. This is no exception in the Slag Model; leading edge run-up height for all cases can be seen in Figure 3.30b.

Note that similar run-up trends emerge from the results of both models:

1. The run-up height is described by a quadratic function of fluid velocity.
2. As nail diameter increases, the Bernoulli approximation (representing the maximum run-up for a given velocity) is approached.

A more detailed description of these trends is given in the No-Slag Model run-up results (Section 3.7.3.1). Unfortunately, the run-up height is very difficult to calculate; determining the nail submersion depth (represented as the undisturbed steel/slag interface height) is a non-trivial problem. Alas, the feasibility of using run-up measurements to estimate fluid velocity is quite low.

3.8.3.2 Knob Profiles

Prior to simulation, it was expected that the knob profile would be sufficient to predict steel velocity. The deformed slag-steel interface profiles (focused on the knob region) for the 0.005, 0.010, and 0.015 m diameter models are plotted in Figures 3.31b, 3.32b, and 3.33b, respectively. Each curve represents a particular far-field and inlet fluid velocity, and the interface height is plotted as a function of x-distance along the nail (see Figure 3.3b for coordinate reference).

Analysis of the converged solutions reveals interesting results; nearly every case generates an almost-linear interface profile! For instance, the knob profiles for 0.4, 0.5, and 0.6 m/s velocity cases of the 0.005 m diameter case are all linear with a characteristic slope ($\Delta \approx -0.78$; see Figure 3.31b). The knob profile begins to lose its linear nature only in simulations with large diameters. Even in these cases, the interface maintains the characteristic linear slope through the first ~70% of the knob; subsequently the knob profile begins a parabolic drop in height. Examination of these profiles reveals that the nail perimeter is so long that the fluid cannot sustain enough momentum to continue along its initial linear path. The no-slip nail surface slows the flow enough such that the gravitational bodyforce causes a freefall of the interface level extending to the nail trailing edge. Note that for higher velocities, this "freefall" occurs close to the nail trailing edge. Should a similar profile be observed during testing in the steel plant, it is likely indicative of very high velocities past the steel/slag interface. Flow past the nail surface in the 0.005 and 0.010 m diameter cases does not slow enough for gravity to have a substantial effect on interface height (thereby maintaining the linear profile across the entire nail). Further explanation of this phenomenon will be offered in Section 3.8.3.4.

In nearly all cases tested (except the 0.005 m diameter, 0.6 m/s inlet velocity case) the wake region forms prior to the end of the nail, indicated by the run-down along the nail's trailing edge. With higher diameters and lower velocity, the wake region forms earlier along the knob. The location along the knob indicating the transition where the final profile crosses through the initial surface height appears to be highly related to fluid velocity. Unfortunately, the initial surface height remains very difficult to determine. It seems unlikely that velocity can be estimated from the knob profile *shape*, given that nearly all velocity cases produce a similar pattern (simply offset by the run-up height).

3.8.3.3 Knob Profile Height Difference

The knob height difference is calculated as the leading edge run-up height minus the trailing edge run-down height, as shown in Figure 3.3a. Height difference data for all velocities and diameter simulated by the Slag Model are plotted in Figure 3.34b. Three distinct regions are observed in the plot: the Undeveloped Profile (UP), the Developing Profile (DP) and the Overdeveloped Profile (OP) regions. Very small knob height differences are seen in the UP region. As velocity increases, the height difference increases linearly in the DP region, culminating with slightly decreasing height differences in the OP region. Please refer to Section 3.7.3.3 for explanation regarding the formation of each region.

Unlike in the No-Slag Model, the three regions for all diameters have similar start/end velocities (with region separation at 0.2 and 0.5 m/s); there exists no explicit diameter preference for testing at any specific fluid velocity. However, notice the increased range of height differences in the 0.015 m diameter line (height differences range from 0.003 m to 0.0177 m within the DP region). Changes in flow velocity for this large diameter case produce greater height differences than for small diameter cases. Testing should be performed using the largest diameter possible, as there will be less uncertainty of fluid velocity from the knob height estimation. In any case, the linear nature of the height difference curves within the revealing DP region indicates this is the most appropriate way to estimate flow using the Nailboard Method.

3.8.3.4 Slag Model/No-Slag Model Investigation

No-Slag Model was created to use as a simplified basis for the complete mathematical interpretation, the Slag Model. Global trends (regarding knob parameters) were predicted to be similar for both models. The current section contains a robust analysis of that hypothesis.

The presence of the slag layer introduces two main differences in generating the knob profile. The first involves the steel velocity at the deforming surface. Remember that the Slag Model was constrained to have zero horizontal velocity at the top surface of the slag layer. The high viscosity of the slag layer constrains the steel/slag interface to have very slow velocities. As a result, steel flow near the top of the steel layer is severely restricted. This is quite different from the No-Slag Model in which velocities at *all* locations in the steel domain are unconstrained. Lower kinetic energies (stemming from lower velocities) in the Slag Model causes steel surface deformation to be less than that for similar No-Slag Model cases.

Second, the slag itself introduces a non-zero density fluid region above the steel layer in the Slag Model. Displacing slag and filling the region with steel requires less potential energy input than when the steel must displace zero-density air. For this reason, similar surface pressure tends to result in more pronounced, larger free surface deformations in the Slag Model than in the No-Slag Model.

These two factors are essentially counteractive in deforming the free surface bounding the steel layer. Nevertheless, distinct differences arise between the free surface profiles established with the Slag and the No-Slag Models, as discussed in the following sections.

Leading Edge Run-Up

Leading edge run-up heights for all cases of both models are given in Table 3.4. Two general trends are observed; The No-Slag Model *overestimates* run-up for:

1. Decreasing nail diameters. The average No-Slag Model run-up is 58.19%, 18.98%, and 0.46% higher than the Slag Model for nail diameters of 0.005 m, 0.010 m, and 0.015 m respectively.
2. Decreasing inlet velocities. The average run-up overshoot for the No-Slag Model is 41.20%, 54.30%, 15.63%, 12.68%, and 5.59% for the 0.2, 0.3, 0.4, 0.5, and 0.6 m/s cases.

Both trends can be explained through examination of flow patterns close to the nail. Flow is more likely to be redirected *around* small diameter nails rather than be pushed upwards to the surface. Additionally, flow deep into the domain of low velocity simulations does not possess enough kinetic energy to travel against gravity up the front edge of the nail. In both cases, the nearly stagnant slag layer stifles flow, and consequently deformation, at the interface.

In cases of larger diameter and/or higher inlet velocity, fluid from lower in the domain begins to influence free surface deformation by being directed up the front of the nail. The boundary layer thickness becomes relatively small compared to the depth of steel influencing free surface flow. With the low-energy boundary layer region less influential to flow development, the Slag Model more closely mimics the No-Slag Model. Near convergence of run-up predictions between the models emerges under these circumstances.

Knob Profile

The difference in free surface profiles around the nail for the two models is substantial, beginning with different run-up heights. With the unconstrained surface flow in the No-Slag Model, the flow uses its increased momentum to maintain a high profile for most of the nail, only causing a decrease in surface height once the non-slip wall boundary of the nail dissipates enough speed to let gravity take over. The No-Slag profile has a nearly-horizontal initial knob region, eventually decreasing exponentially until the end of the nail. Once past the leading edge, the impact of the slow-moving steel/slag interface is seen in the subsequent Slag Model knob profiles. With very slow velocity at the surface *before* the flow reaches the nail in the Slag Model, there is not sufficient momentum to carry the flow at an increased level as it travels past the nail; the free surface level decreases linearly immediately when past the leading edge. Once the flow has become nearly stagnant due to high shear at the nail (about 2/3^{rds} of the way past the nail), gravity takes over and pulls the free surface down at an exponential rate. These different profiles can be easily visualized by comparing Figures 3.33b and 3.34b. From this analysis, it appears that the No-Slag Model is not valid in estimating actual knob profiles.

Knob Height Difference

Knob height differences for all cases of both models can be seen in Table 3.4. As was the case in the run-up investigation, the No-Slag Model increasingly *overestimates* height differences as the nail diameter decreases. The average No-Slag Model height difference is 56.56%, 10.79%, and -13.91% higher than the Slag Model for nail diameters of 0.005 m, 0.010 m, and 0.015 m respectively.

Observe how the No-Slag Model actually under-predicts knob height difference for the 0.015 m diameter case. Despite having reasonably close run-up values, distinctly different surface profiles are formed with the two models- the free surface height decreases immediately past the leading edge in the Slag Model while the surface initially maintains a nearly horizontal trajectory in the No-Slag Model. Because of this flow pattern, run-down at the trailing edge subsequently is lower in the Slag Model. Additionally, the "lip" formed at the trailing edge in the 0.015 m No-Slag simulations (as discussed in Section 3.7.3.2) further lowers the relative height differences. Both these ideas are confirmed through comparison of Figures 3.33a and 3.33b, and both support the observed No-Slag Model height difference under-prediction.

Unfortunately, the effect of inlet velocities on height difference is more complicated; the data is too noisy to identify a clear explanation with certainty. The influence of boundary layer flow compared to flow inertial effects decreases with higher velocity flow. Consequently, higher inlet velocities cases should generate increased height differences for the Slag Model (as it did in the run-up comparison). There seems to be some inclination toward this theory, however more data points must be collected in order to identify conclusive trends. In any case, the effectiveness of No-Slag Models in generating Slag Model predictions is quite low.

3.8.3.5 Comparison to pressure/height approximation

In the world of computational modeling, computational cost often dictates the complexity of phenomena included in the simulation. Typically, approximations are made to obtain useable data in situations where some aspects are neglected from the model. One such approximation involves estimating free surface deformation from the pressure distribution at a fixed boundary. As in the funnel mold simulation of Chapter 2, the top surface was treated as a fixed no-slip wall and surface profile shape was estimated using the pressure of the fluid at the surface of this fixed boundary. Using Equation 3.63, Panaras found reasonable agreement between the approximation and experimental results[32)]. Due to the conducive nature of the Nailboard examination (with a fixed surface run followed by a free surface simulation), the accuracy of Equation 3.63 can be easily tested via mathematical models.

Figure 3.35 contains free-surface-model deformation plots as well as their free-surface pressure approximations. Both single-layer flow and double-layer flow problems were examined through a case study comparing water-model and slag-model simulations. For the sake of comparison, these simulations were all carried out using nail diameter of 0.005 m and an inlet velocity of 0.3 m/s.

A high degree of inaccuracy is seen for the pressure approximations. Although the general trends from Equation 3.63 vaguely approximate the actual deformation, the water and the slag model approximations overestimate the leading edge run-up by 56% and 47%, respectively, while the lowest surface elevation along the nail is under predicted by 92% and 88%, respectively. Observe how the pressure approximation curves predict the knob will have its lowest height *prior* to the trailing edge. Once the nail surface begins to curve away from the incoming fluid (at 50% past the nail; x = 0.04 m in the figure), a low-pressure region forms, causing this extreme drop in predicted height. Similar behavior was seen in actual deformation plots of the No-Slag Model (refer to Figure 3.33a), however it was not seen in the actual deformation plots of this particular case.

The pressure approximation equation assumes complete transfer of energy from pressure to elevation change, but the equation does *not* factor in the energy required by surface tension to deform the surface. Essentially, surface tension smoothes the surface, as sharp surface curvature requires much more energy to overcome tension forces. Thus sharp, high-curvature peaks are allowed in the pressure approximation whereas surface tension prevents such peaks from reaching fruition. While Equation 3.63 is may be relevant in simulating free surface deformation for zero surface tension fluids, it is highly inaccurate in estimating free surface deformation of fluids with non-negligible surface tension forces (i.e. steel and water cases) involving large deformation. At any rate, the approximation should be accurate for predicting gradual surface profiles and provides an upper limit to the surface deformation; Equation 3.63 represents the perfect transfer of energy from pressure to elevation change, so the free surface likely cannot deform more than the approximation dictates.

3.9 Nailboard Method Application

In addition to mathematical simulation, physical testing to obtain real-world results was also performed. Sample nail-board tests were collected from the Nucor Steel plant in Decatur, Alabama on November 7th, 2004. Using their thin-slab continuous caster, 0.008 m initial diameter spikes were dipped into the molten steel for various lengths of time, using identical casting conditions. The following section summarizes the findings from these tests.

3.9.1 Experimental Testing Procedure

Through the development of a rigorous, structured testing routine, repeatability and accuracy of tests can be optimized. Unfortunately, developing a complete testing method is a trial and error problem as different casting conditions require different testing circumstances. For instance, submersion time depends on the grade of steel and the level of superheat; both will affect knob solidification times.

In this test, standard, hardware-grade mild steel spikes (0.008 m diameter, 0.2 m length) were used for the tests. To maintain a constant cylindrical cross section, the flattened ends of the spikes were cut off. Once submerged in the steel, the nail surface is immediately shrouded by solidifying caster steel. The nail material never melts into the liquid, thereby making the steel spike composition irrelevant. A standard holder used to measure top surface profiles was modified to accept a 2" x 2" x 12" piece of wood with a single spike nailed into it. Care was taken to ensure the nail was exactly perpendicular to the top of the mold (otherwise, the mathematical model would be invalidated). Also, the nail was positioned such that the level of submersion would be sufficient to generate an accurate knob (> 6 cm submergence, as was used in the mathematical model). This apparatus was subsequently used for all of the experimental testing.

The nail was dipped at approximately the midpoint between the narrowface and the SEN. During testing, the nail was inserted straight into and straight out of the liquid pool. Sampling proved to be tricky- insertion had to occur fast enough to minimize knob solidification before completely immersed, without disturbing the steel/slag environment. After a specified period of time (2-8 seconds, depending on the test case), the nail was removed and cooled. The optimum submersion time was that which yielded the largest knob size without allowing remelting.

3.9.2 Experimental Findings

Testing Nail Diameter

Various diameter nails (ranging from 3 mm to 8 mm) were tested during the Nucor plant trip. Nails with large diameters overall generated the best results, as testing using small diameter nails produced inconsistent, "lumpy" knobs. The reduced steel volume of the small diameter nails limits the amount of heat it can absorb from the liquid pool. In these cases, knob formation is more highly influenced by variations in localized flow superheat. Lumpy knobs are formed as the knob undergoes non-uniform solidification. With large diameter nails, submersion time can be increased due to increased heat transfer from the fluid to the nail. Knob formation occurs over a longer period of time and thus is less influenced by local temporal variations in flow pattern or superheat. More uniform knobs are formed, with cross-sections nearly identical at all locations along the knob axis. It is recommended that nails with large diameters (≥ 8 mm) be used for testing, however, the knob boundaries must be *at least* 5 cm away from both wideface walls. By maintaining acceptable distance from the wideface, knob formation is not influenced by boundary layer flow near the mold boundary.

Knob Characteristics

As mentioned in Section 3.5.3, the main body of the knob remelts during excessive nail submergence times. At the knob top surface, however, high levels of heat transfer out through the slag layer permit liquid steel to continue solidifying to the knob (creating a "mushroom" knob shape). One example of a nail exhibiting this "mushrooming" effect is shown in Figure 3.12. Care must be taken when performing these experiments to ensure that neither the knob remelting process nor the mushroom solidification effect occurs. Because the Fidap simulations assume constant knob diameter, mathematical results will be inaccurate for these cases. Through experimentation, the optimal submersion time is defined as the time it takes to produce a well-defined knob with little to no remelting. The conditions for each caster are different (the level of superheat, casting speed, etc…), thereby requiring a trial-and-error process to determine the optimum submersion time.

Testing Conditions

During testing at Nucor Steel, electromagnetic brakes (EMBRs) remained on throughout testing. EMBRs employ the use of strong magnetic forces induced in the flowing steel between the externally-mounted brakes to prevent natural steel flow patterns from developing. As a result, molten steel velocity at the top surface tends to be very slow and irregular. The knob shape in Figure 3.10 is consistent with the predictions of this work, and its 6mm knob height difference corresponds with a surface velocity of ~ 0.3m/s. Unfortunately in most cases, the test knobs showed relatively no run-up or upper surface profile; the EMBRs slowed flow at the surface so much that no discernable knob shape could be identified. One of the assumptions of this model is that 1-D, non-fluctuating fluid flows past the nail. In order to maintain this condition, flow-altering devices such as EMBRs which externally manipulate the fluid must be turned off during Nailboard testing.

3.10 Summary

A novel way to determine the flow direction of molten steel is by inserting a nail into the moving fluid, piercing its surface, and observing the physical characteristics of the knob of solidified steel frozen on the end of the nail. It has been proposed that the profile which the top surface of the knob forms with relation to the nail's axis, along with the knob diameter, may be used to determine the molten steel velocity at the top surface of the continuous casting process. By having an accurate, quick way to determine steel velocity at the critical top surface, insight into the complete casting process can be gained in effort to minimize final product defects..

Through the assistance of the finite element CFD package Fidap, simulations incorporating a simplified No-Slag and complete Slag Models have been run. A standard K-ε turbulence model was created which utilized the spines free surface algorithm at fluid boundaries within the 3-D domain. The model was verified accurate by comparison to an analytical sloshing in a tank problem as well as to previously published work on water flow past vertical cylinders by Chaplin. Qualitative examination of flow patterns and quantitative analysis of critical parameters (velocities, nodal elevation changes, turbulence, etc…) have generated important conclusions.

Initially, a simplified No-Slag Model (single layer steel flow, one upper free surface) was created to provide model validation and to provide a basis for the full Slag Model to be build upon. Comparison with a water approximation test case discredited the use of water models to estimate knob profiles generated in a steel environment. The complete Slag Model (both steel and slag layers, with an internal free surface separating the fluids and an external free surface at the top of the slag layer) represented the complete mathematical interpretation. Wall laws were specified at the internal interface to maintain accurate flow profiles extending into the steel region. For both models, the effect of steel velocity and knob diameter on critical knob parameters was quantified. The uniqueness of the Slag Model can be seen in the successful implementation of many complex modeling phenomena: a 3-D transient simulation incorporating turbulence, two free surfaces (one internal, one external) with non-trivial surface tension effects, wall laws, and gravitational body force. More importantly, the models were applied to achieve the following findings:

1. The leading edge run-up on the knob increases in proportion to the square of the inlet velocity. Increasing knob diameters yield leading edge run-ups close to the upper energy-balance limit of the Bernoulli relation. In both the No-Slag and the Slag Models, the leading edge height provides a clear indication of velocity, especially for high velocity (> 0.3 m/s), large diameter (> 0.010 m) cases.
2. Distinct knob profiles for each case are formed in the No-Slag Model. The shape and curvature along the knob free surface provide a unique "stamp" of each velocity/diameter case, making it useful in estimating fluid velocity.
3. In the Slag Model, the presence of the slag layer and the small velocity associated with the steel/slag interface results in nearly linear, gravity-driven free surface profiles at the knob surface ($^{dz}/_{dx}$ = -0.78). Because the knob profile is nearly identical for each case, the shape alone cannot be used to indicate velocity.
4. The knob height difference (measured as the leading edge run-up height minus the trailing edge run-down height) produces a unique indication of velocity, linearly increasing within the Developing Profile region (in which the inlet velocity ranges from 0.2 to 0.5 m/s). Within this region, knob height differences coupled with knob diameter

can be used to accurately determine free-stream velocity values for the real-world interpretation, the Slag Model.

5. Water models were invalidated in approximating steel Nailboard tests; water models produce very different free surface profiles than steel (for identical cases) due to the great disparity in surface tension between the two fluids.
6. Pressure/height approximations proved to be inaccurate for both a Slag Model case as well as a water No-Slag Model case. Because the relation neglects surface tension, it overestimates free surface deformations (at times by an order of magnitude) from the actual case.
7. Optimum nail submersion time varies for different diameter nails used (the smaller nail diameter, the shorter optimum submersion time). "Mushrooming" at the top of the knob is indicative of lower knob remelting, and shorter submersion times are necessary to obtain useable data (as the model assumes constant diameter).
8. Electromagnetic brakes and all other external flow-altering devices must be turned off during Nailboard testing. Data collected from a caster using electromagnetic braking forces proved useless, as the irregular flow and interaction with the magnetic nails generated indistinct knobs.

Table 3.1: Validation, Experimental, and Simulation Model Parameters[62)]

	Parameter/Property	Validation Case	Experimental Case	No-Slag Model	Slag Model	
Simulation Parameters	Flow Type	Laminar	Turbulent	Turbulent	Turbulent	
	Gravitational Acceleration	9.81	9.81	9.81	9.81	[m/s^2]
	Inlet Velocity	---	0.96, 1.36	0.2 - 0.6 [0.1]	0.2 - 0.6 [0.1]	[m/s]
	Fluid Density	1000	1000	7400	7400	[kg/m^3]
	Fluid Laminar Viscosity	0.001	0.001	0.006	0.006	[kg/m-s]
	Fluid Kinematic Viscosity	1.00×10^{-6}	1.00×10^{-6}	8.11×10^{-7}	8.11×10^{-7}	[m^2/s]
	Fluid Surface Tension	0	0.0728	1.6	1.6	[J/m^2]
	Slag Density	---	---	---	3000	[kg/m^3]
	Slag Laminar Viscosity	---	---	---	1.000	[kg/m^3]
	Slag Kinematic Viscosity	---	---	---	3.33×10^{-4}	[m^2/s]
	Slag Surface Tension	---	---	---	0.65	[J/m^2]
Domain	Dimensionality	2-D	3-D	3-D	3-D	
	Nail Diameter (d)	---	0.21	0.005, 0.010, 0.015	0.005, 0.010, 0.015	[m]
	Length (x)	2	30 x d	30 x d	25 x d	
	Width (y)	---	~26 x d	~26 x d	~18.5 x d	
	Height (z)	1.02 (right)	0.5 (water)	0.03 (steel)	0.06 (steel)	[m]
		0.98 (left)			0.01 (slag)	[m]
	Domain Modeled	1/1	1/2	1/2	1/2	Domain

Table 3.2: Run-up height and knob height difference comparison for the No-Slag and Slag Models

RUN-UP HEIGHT DIFFERENCE

Diameter	0.005 m				0.01 m				0.015 m				Averages	
Velocity	**No-Slag**	**Slag**	Δ	Δ%	**No-Slag**	**Slag**	Δ	Δ%	**No-Slag**	**Slag**	Δ	Δ%	Δ	Δ%
0.2	0.349	0.200	0.149	74.46%	0.787	0.570	0.217	38.05%	1.433	1.290	0.143	11.07%	***0.170***	***41.20%***
0.3	1.810	0.832	0.978	117.63%	2.723	1.969	0.754	38.28%	3.081	2.880	0.201	6.98%	***0.644***	***54.30%***
0.4	3.755	2.385	1.370	57.42%	4.739	4.695	0.044	0.94%	5.570	6.293	-0.722	-11.48%	***0.230***	***15.63%***
0.5	4.876	3.909	0.968	24.76%	8.099	7.300	0.799	10.95%	9.458	9.241	0.217	2.35%	***0.661***	***12.68%***
0.6	5.556	4.761	0.795	16.70%	9.830	9.214	0.616	6.69%	12.708	13.608	-0.899	-6.61%	***0.171***	***5.59%***
Averages			***0.852***	***58.19%***			***0.486***	***18.98%***			***-0.212***	***0.46%***		

KNOB HEIGHT DIFFERENCE

Diameter	0.005 m				0.01 m				0.015 m				Averages	
Velocity	**No-Slag**	**Slag**	Δ	Δ%	**No-Slag**	**Slag**	Δ	Δ%	**No-Slag**	**Slag**	Δ	Δ%	Δ	Δ%
0.2	0.936	0.728	0.208	28.56%	1.619	1.724	-0.105	-6.10%	2.066	2.996	-0.930	-31.03%	***-0.276***	***-2.86%***
0.3	4.221	2.152	2.069	96.17%	5.105	5.038	0.067	1.33%	5.774	6.949	-1.175	-16.91%	***0.321***	***26.87%***
0.4	6.730	3.859	2.871	74.41%	10.854	8.926	1.927	21.59%	11.330	13.943	-2.613	-18.74%	***0.728***	***25.75%***
0.5	5.893	3.963	1.930	48.71%	12.538	10.921	1.617	14.80%	16.718	17.695	-0.977	-5.52%	***0.857***	***19.33%***
0.6	5.273	3.908	1.365	34.93%	12.018	9.826	2.192	22.31%	17.490	17.041	0.449	2.63%	***1.335***	***19.96%***
Averages			***1.689***	***56.56%***			***1.140***	***10.79%***			***-1.049***	***-13.91%***		

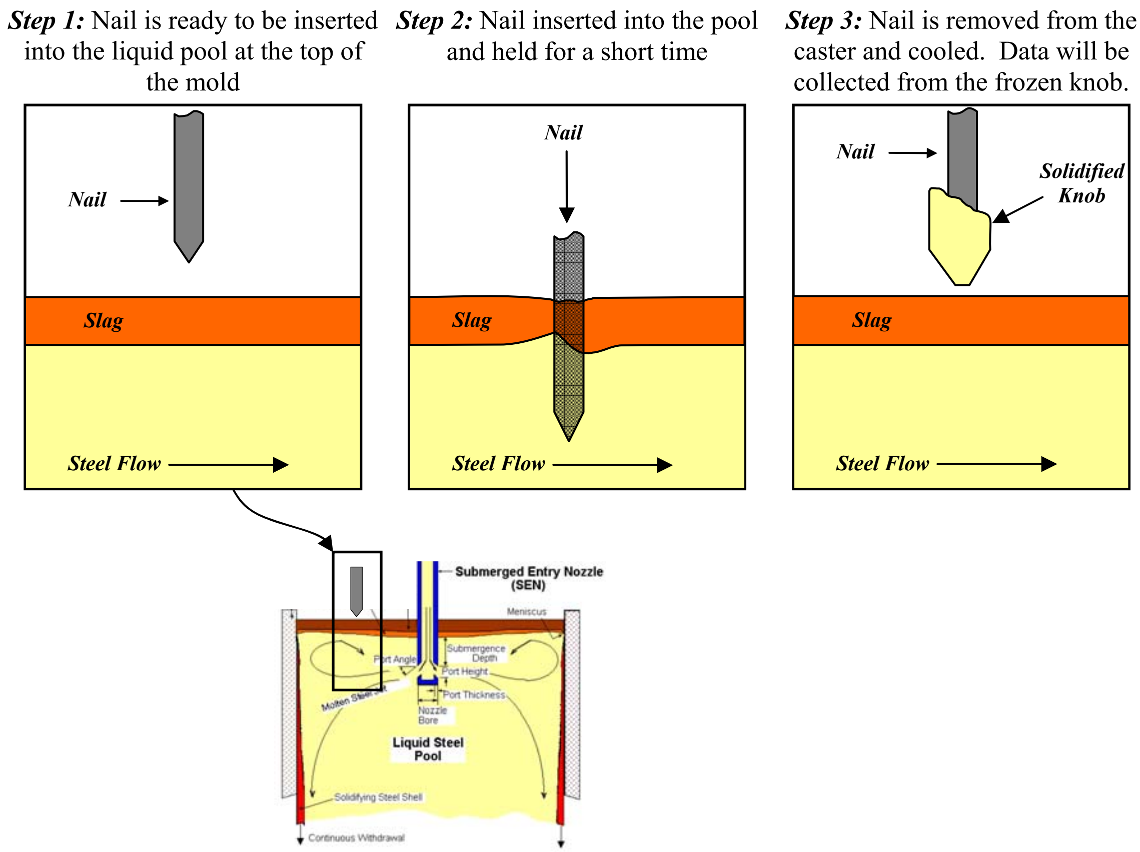

Figure 3.1: Schematic of Nailboard Method

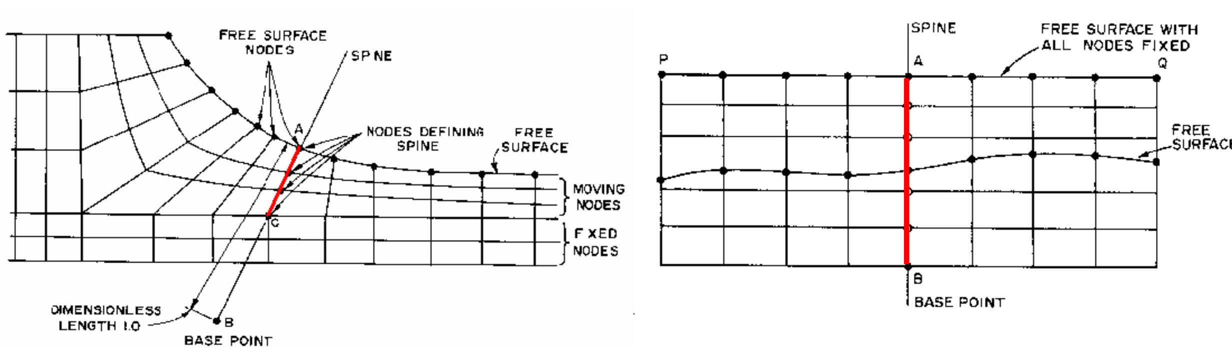

(a) *(b)*

Figure 3.2: Spines mathematical definition for external **(a)** and internal **(b)** free surfaces[25)]

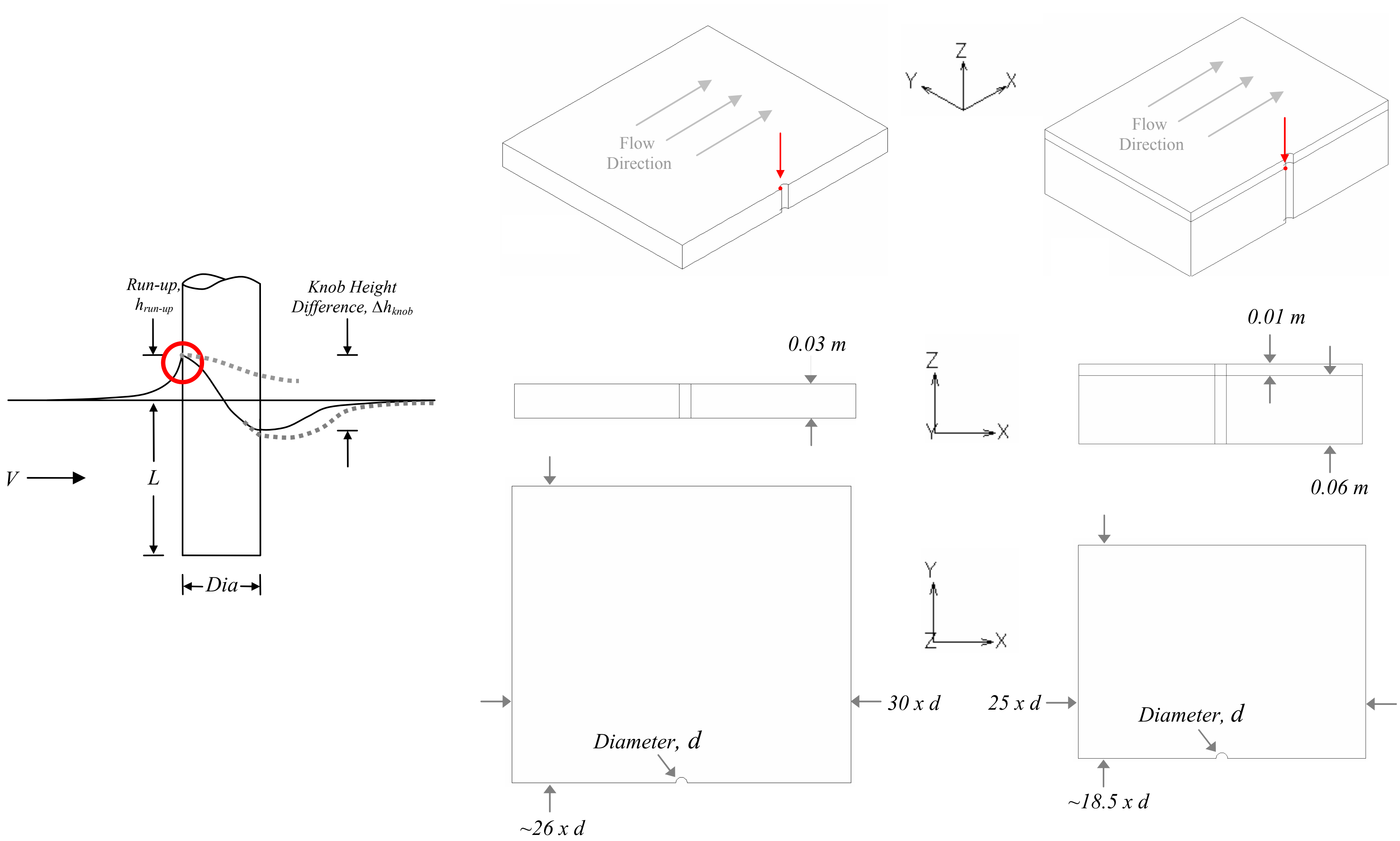

(a) *(b)* *(c)*

Figure 3.3: No-Slag and Slag Model domains. Displayed are **(a)** the node corresponding to the leading edge of the cylinder and its corresponding location in the gridless **(b)** No-Slag and **(c)** Slag Model domains

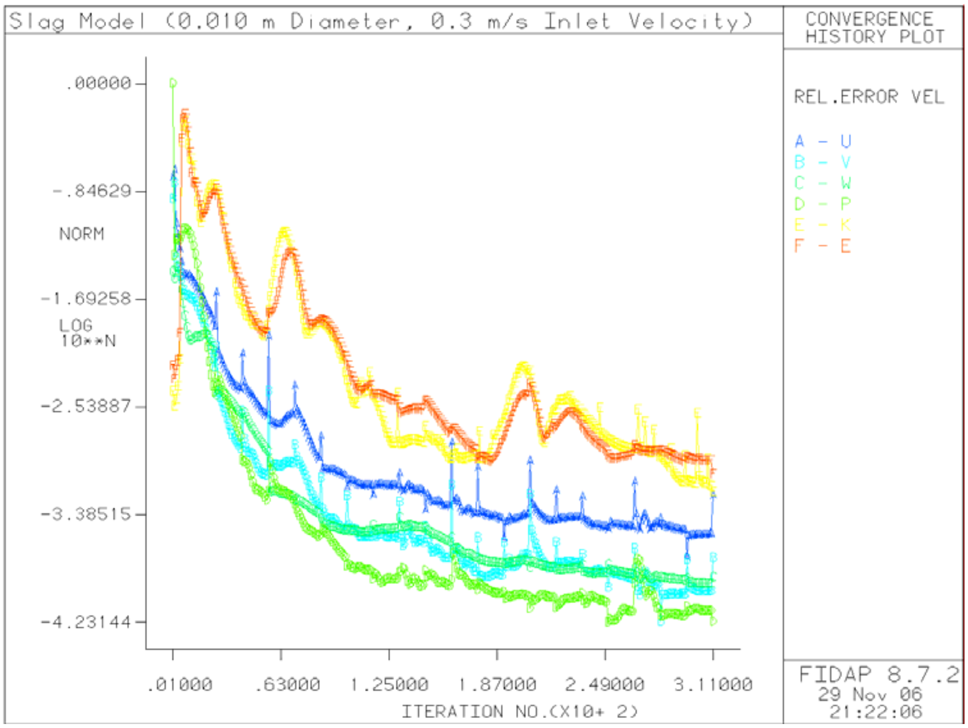

Figure 3.4: Sample flow parameter convergence history for initial, steady-state run (Slag Model, 0.010 m diameter, 0.3 m/s inlet velocity case)

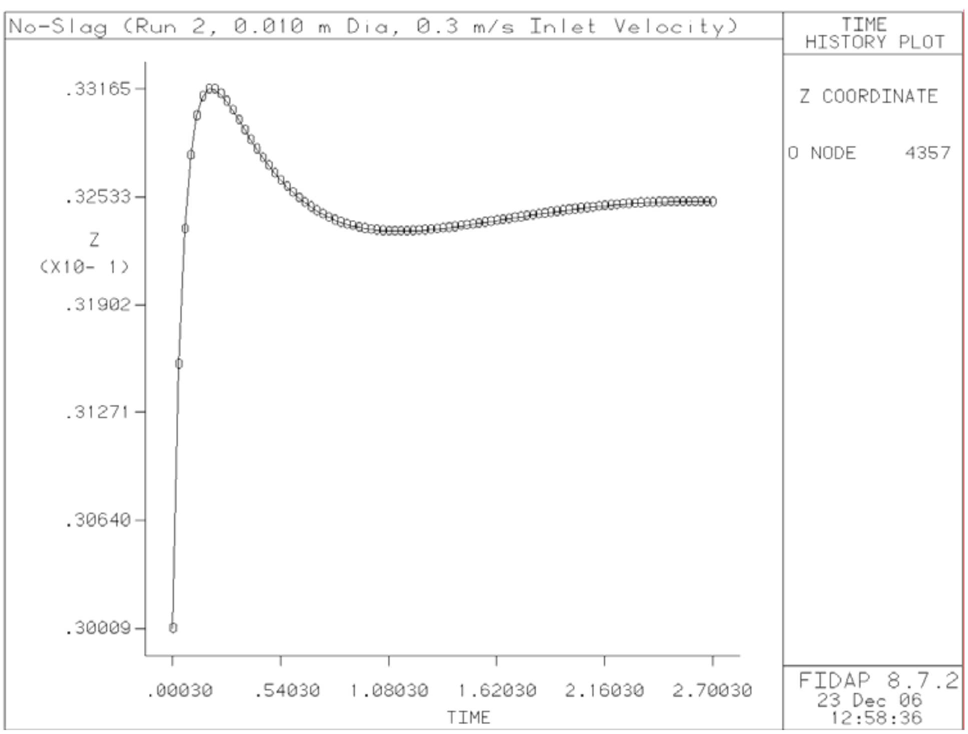

Figure 3.5: Sample *z*-height history plot for a random free-surface node for the second, transient run (No-Slag Model, 0.010 m diameter, 0.3 m/s inlet velocity case)

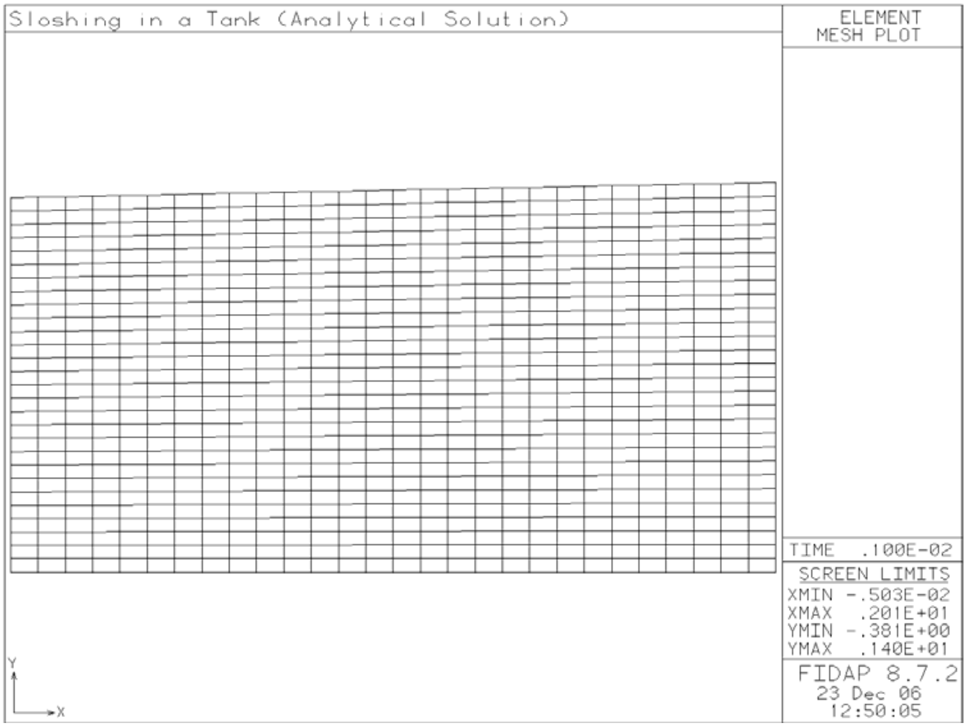

Figure 3.6: Mesh used for the Analytical Solution Simulation (2-D sloshing-in-a-tank problem)

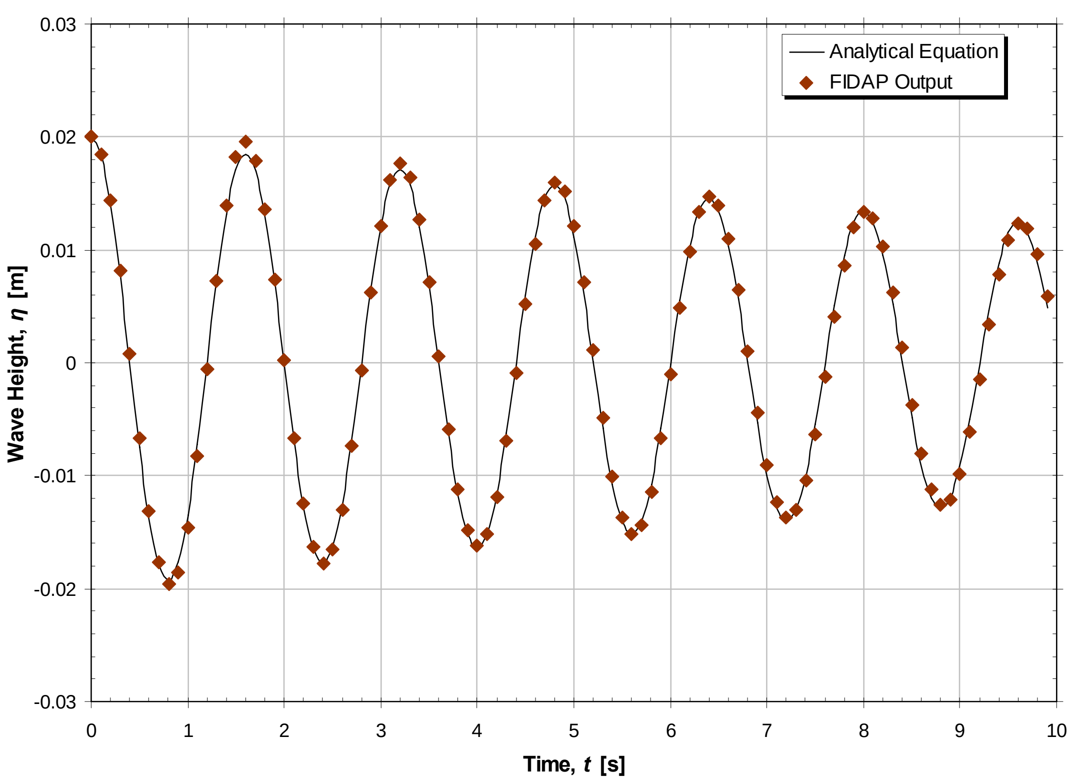

Figure 3.7: Fidap/Analytical equation comparison

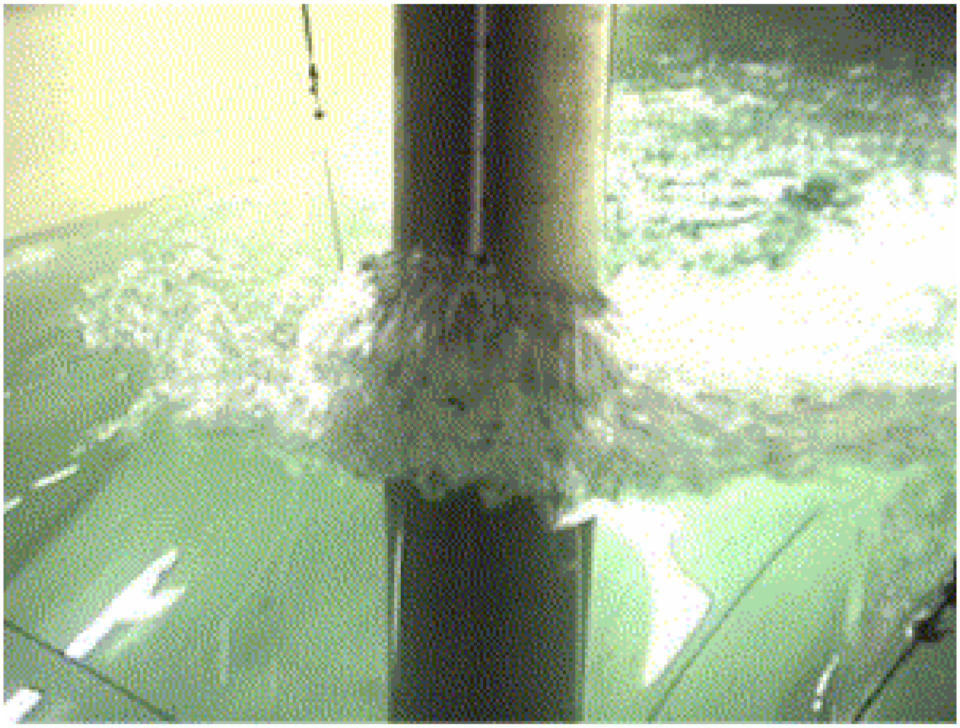

Figure 3.8: Chaplin's experimental test dragging a cylinder through water[51)]

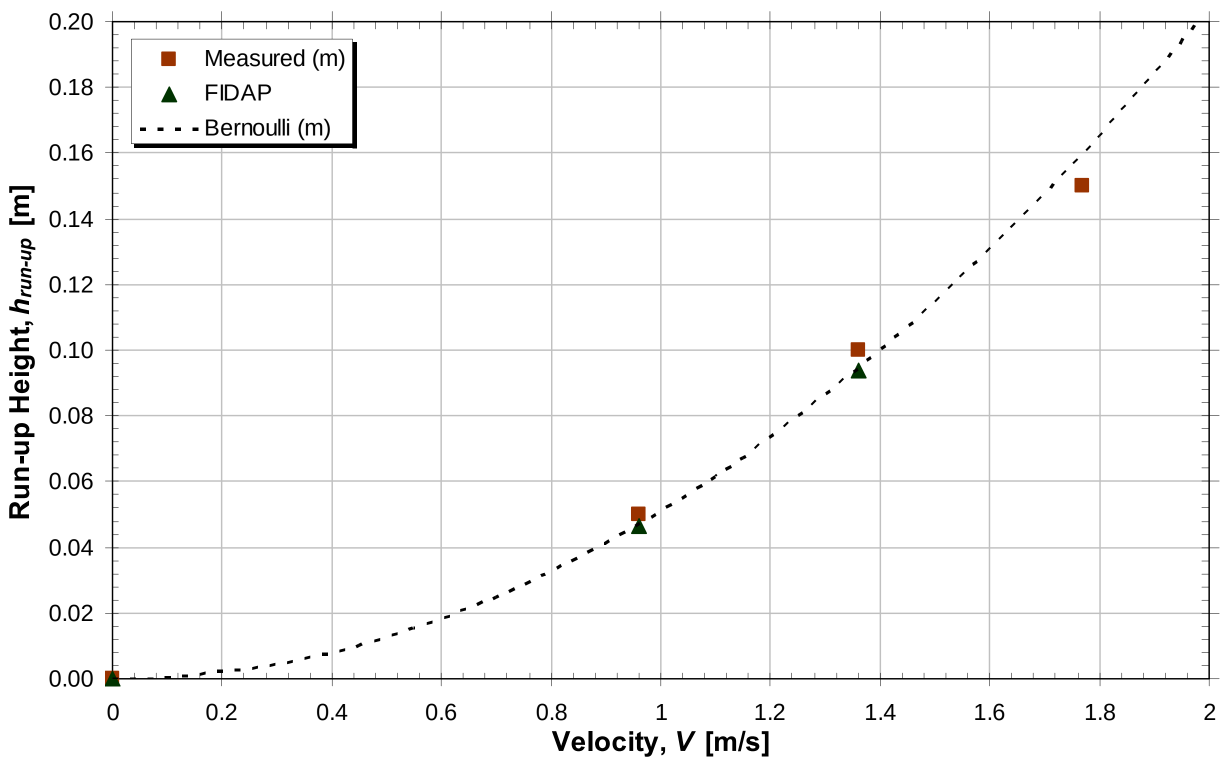

Figure 3.9: Model validation with analytical and experimental test case data

Figure 3.10: Solidified knob produced during experimental testing (including diameter sampling locations)

Figure 3.12: Experimental knob exhibiting a “mushroom” top and a high degree of remelting along the lower 80%

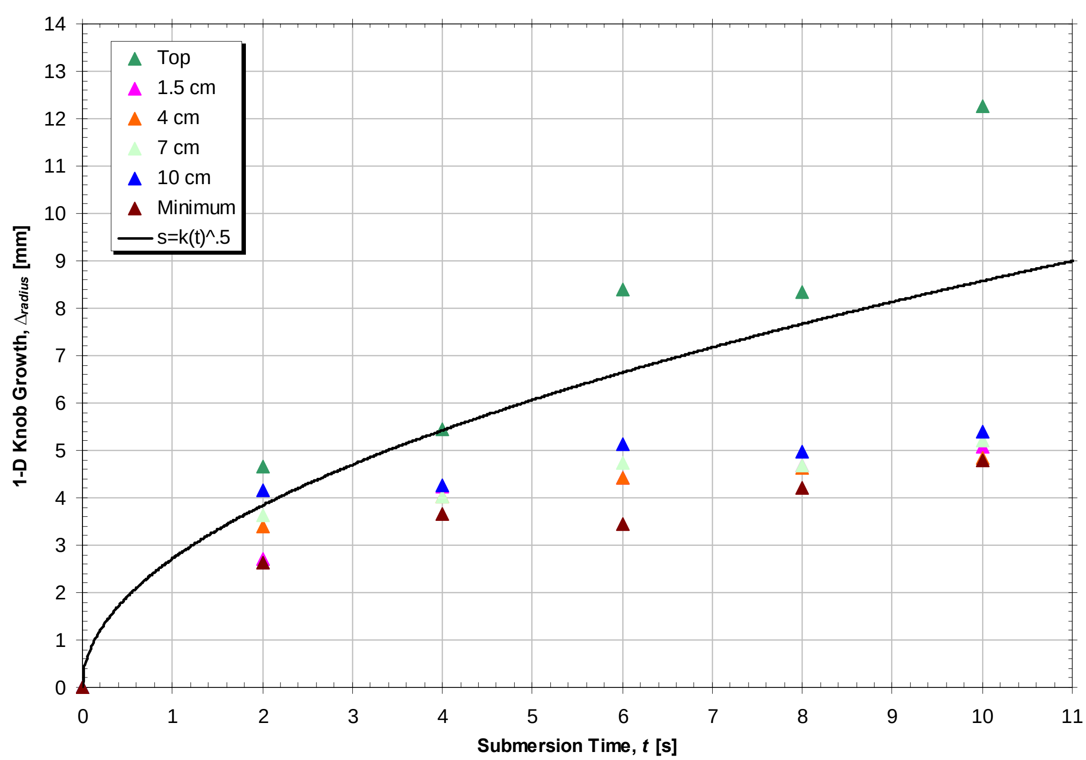

Figure 3.11: Solidified knob growth versus time at prescribed distances from the knob top surface

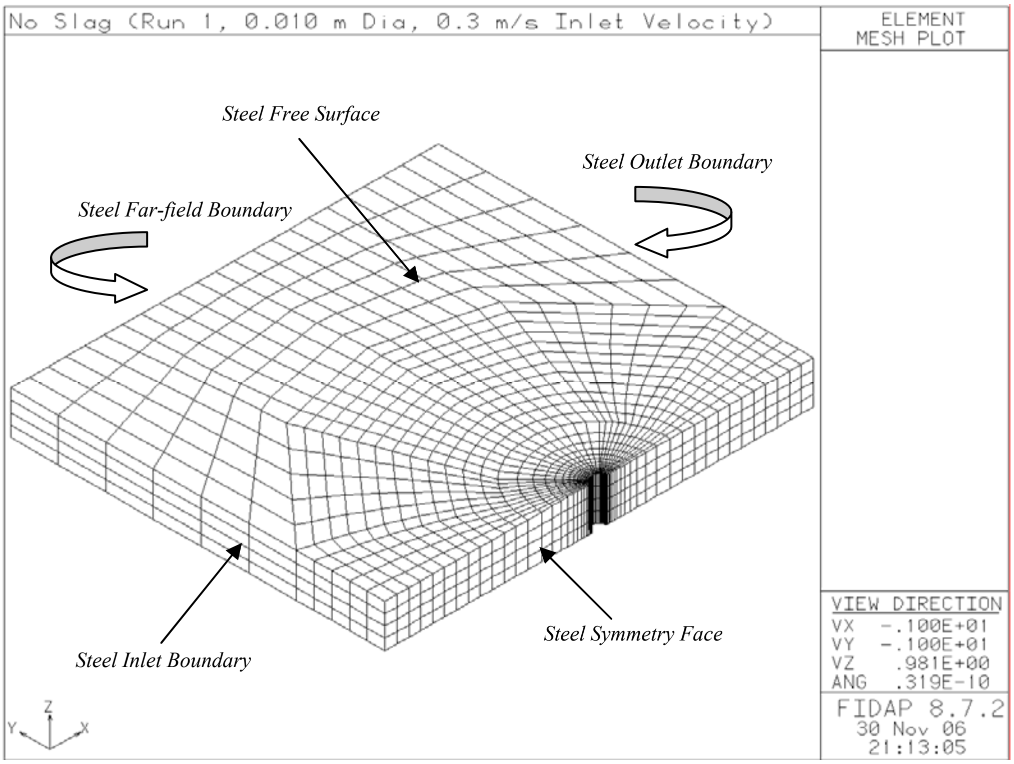

(a)

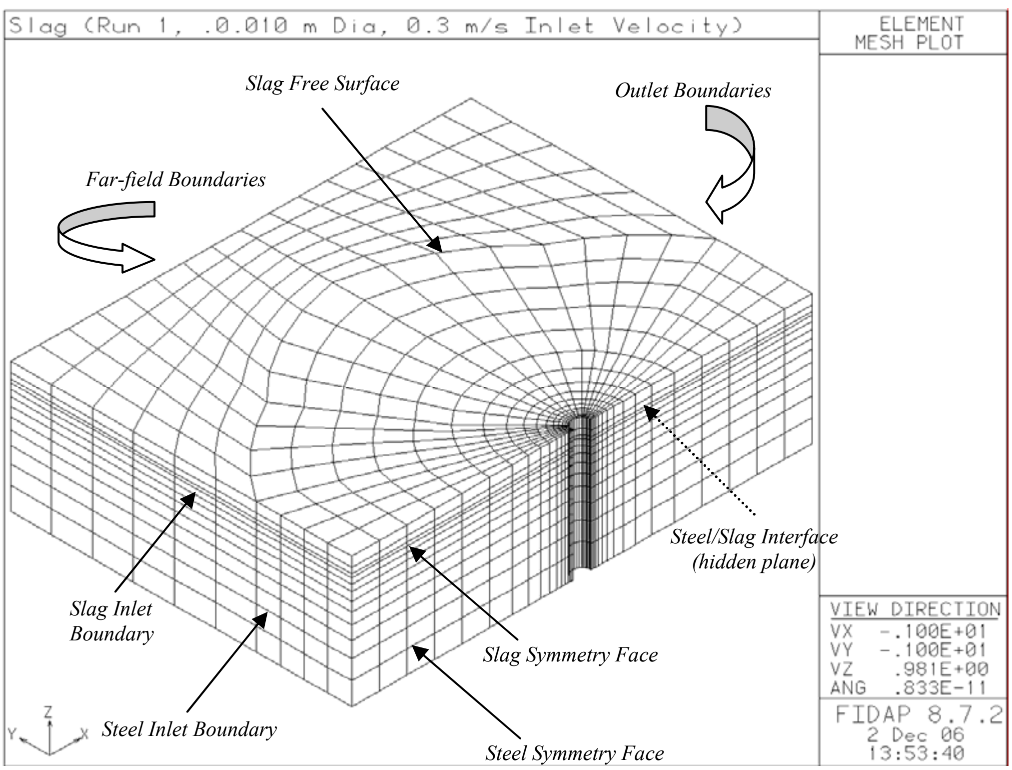

(b)

Figure 3.13: Undeformed mesh created for the **(a)** No-Slag and **(b)** Slag Models

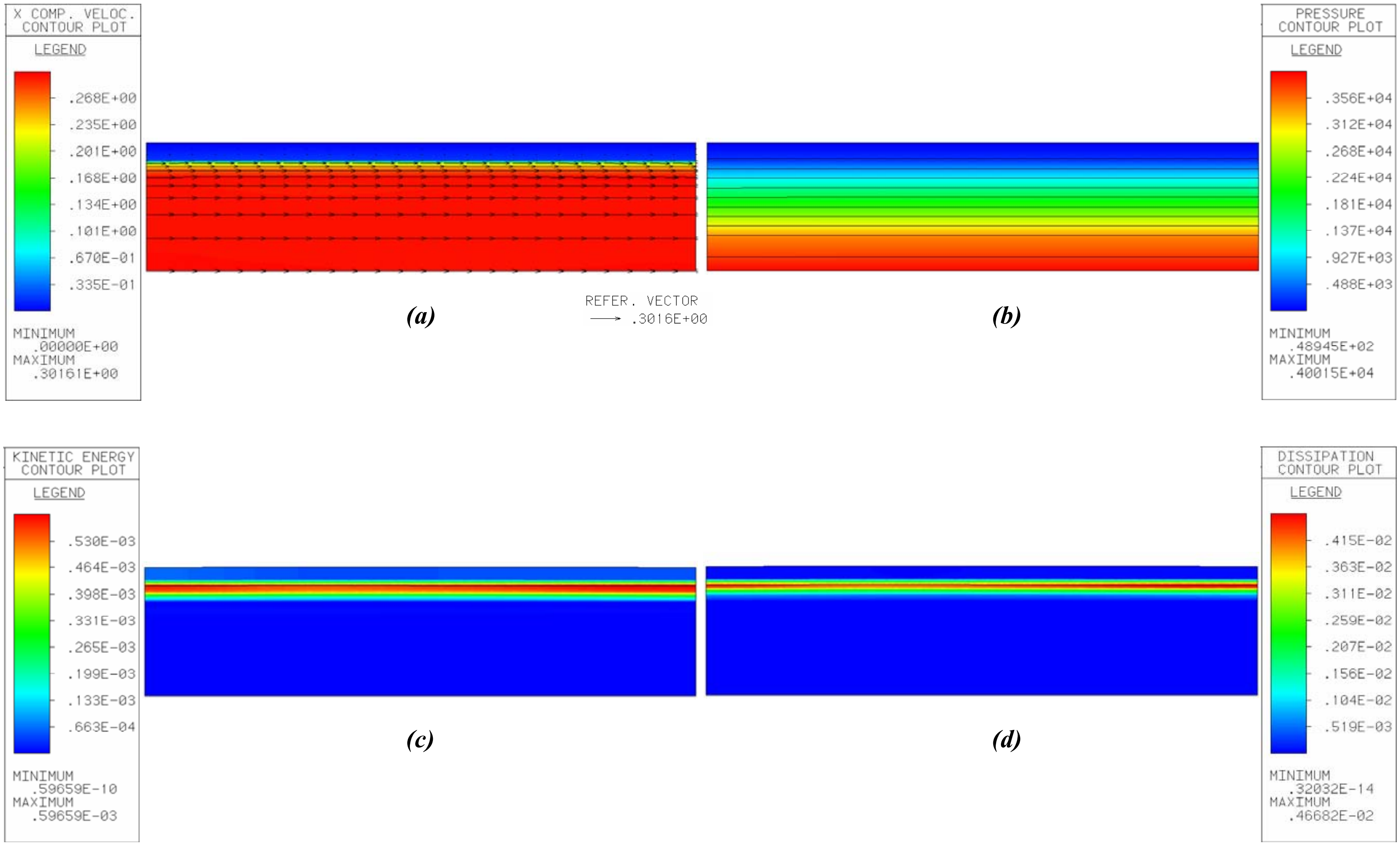

Figure 3.14: Inlet Velocity Simulation converged solution (0.3 m/s steel inlet velocity): **(a)** Velocity Vectors, **(b)** Pressure Contours, **(c)** Kinetic Energy, and **(d)** Dissipation Energy plots

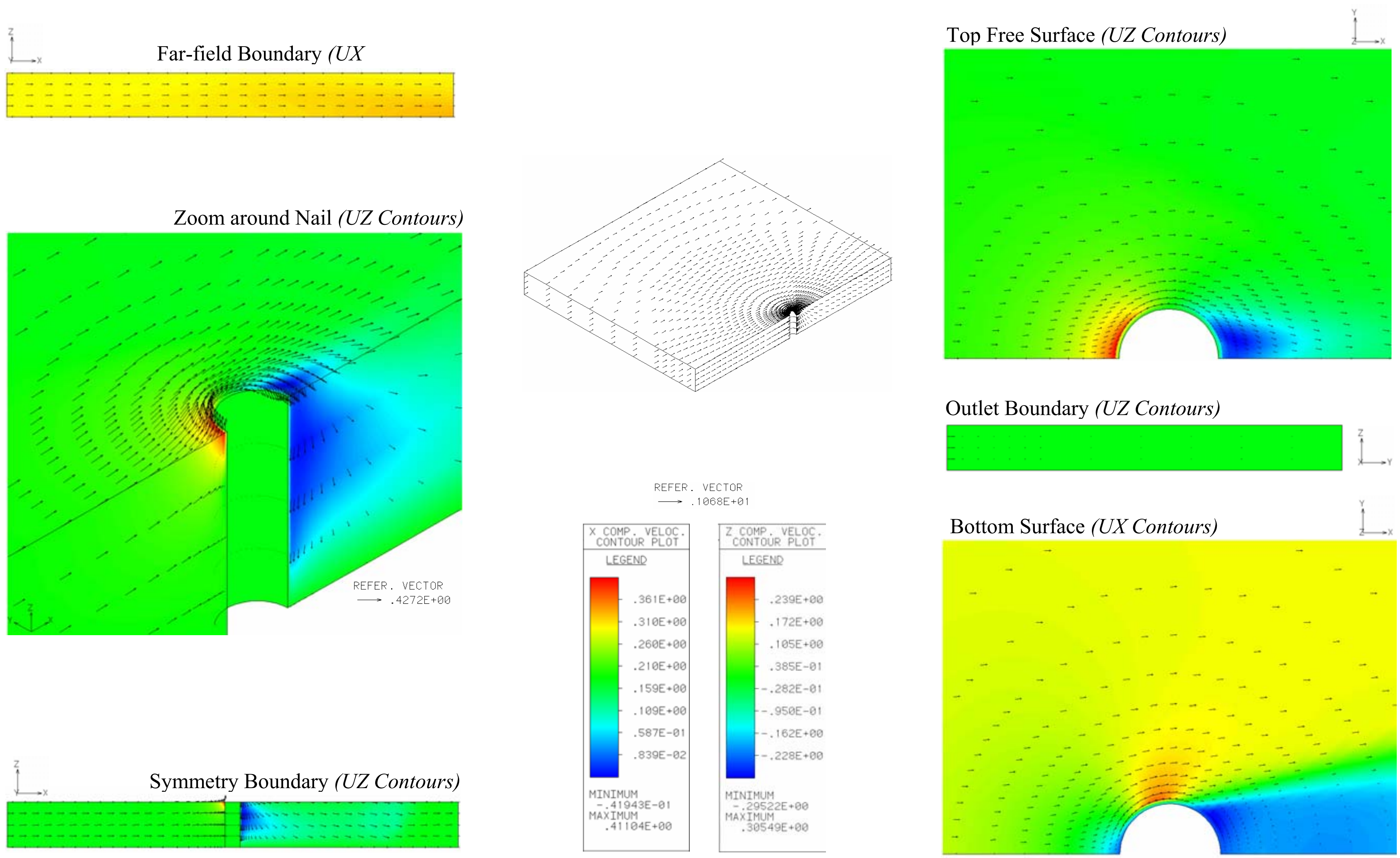

Figure 3.15: Velocity solution for the initial, S.S simulation in the No-Slag Model (0.010 diameter, 0.3 m/s inlet velocity case). Reference vector and contour legends apply to all figures unless otherwise labeled

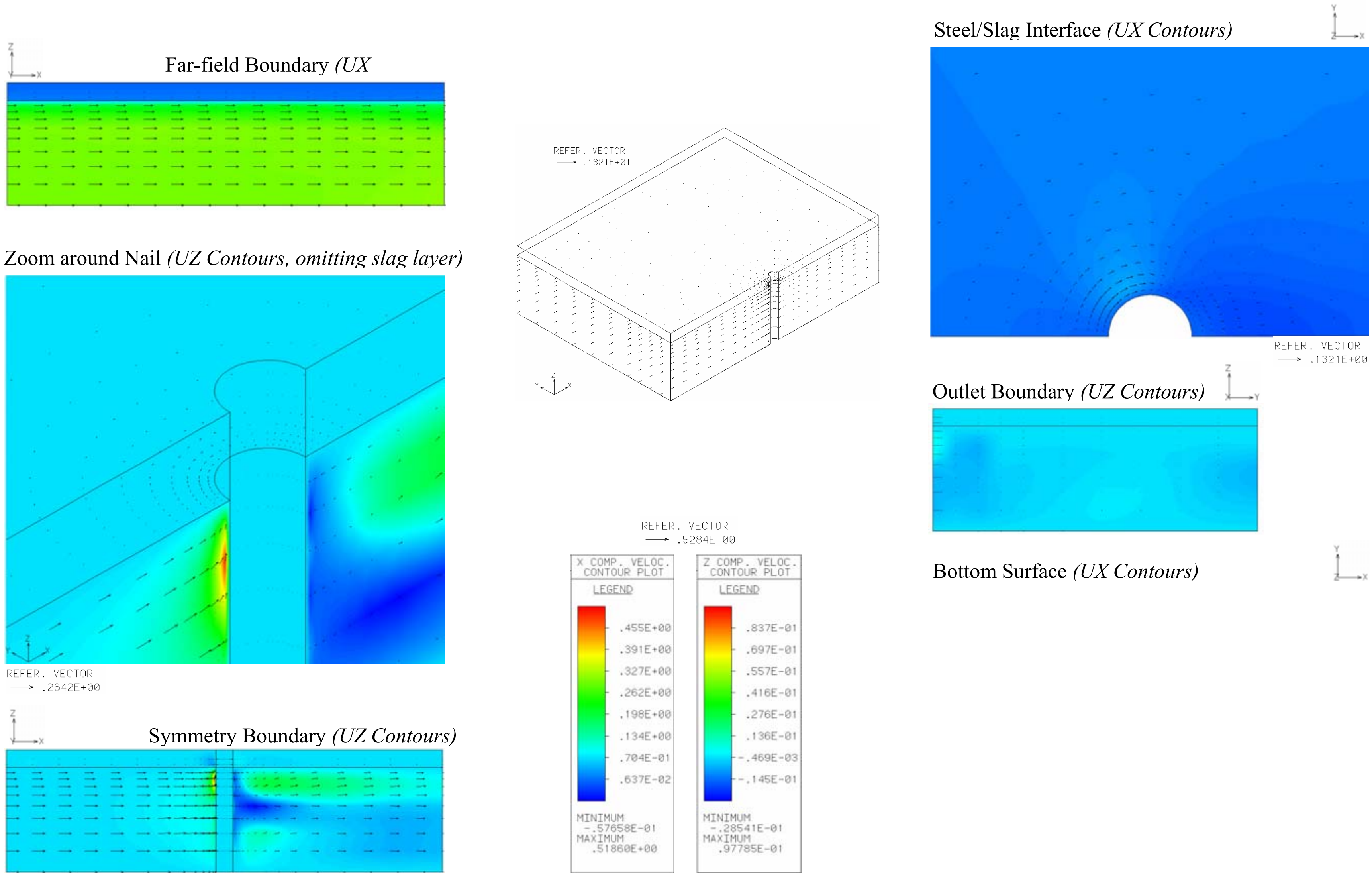

Figure 3.16: Velocity solution for the initial, S.S simulation in the Slag Model (0.010 m diameter, 0.3 m/s inlet velocity case). Reference vector and contour legends apply to all figures unless otherwise labeled

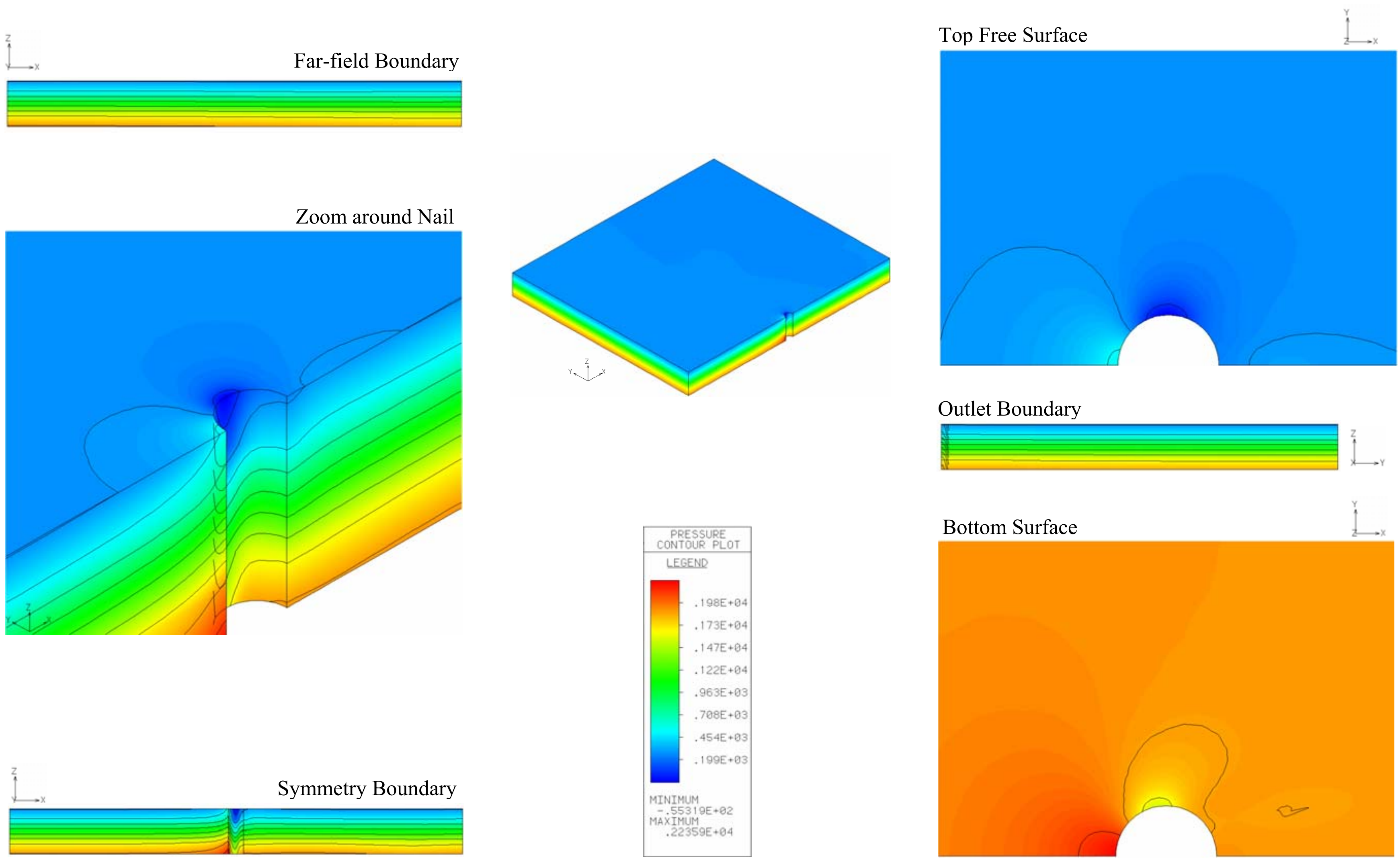

Figure 3.17: Pressure solution for the initial, S.S simulation in the No-Slag Model (0.010 m diameter, 0.3 m/s inlet velocity case)

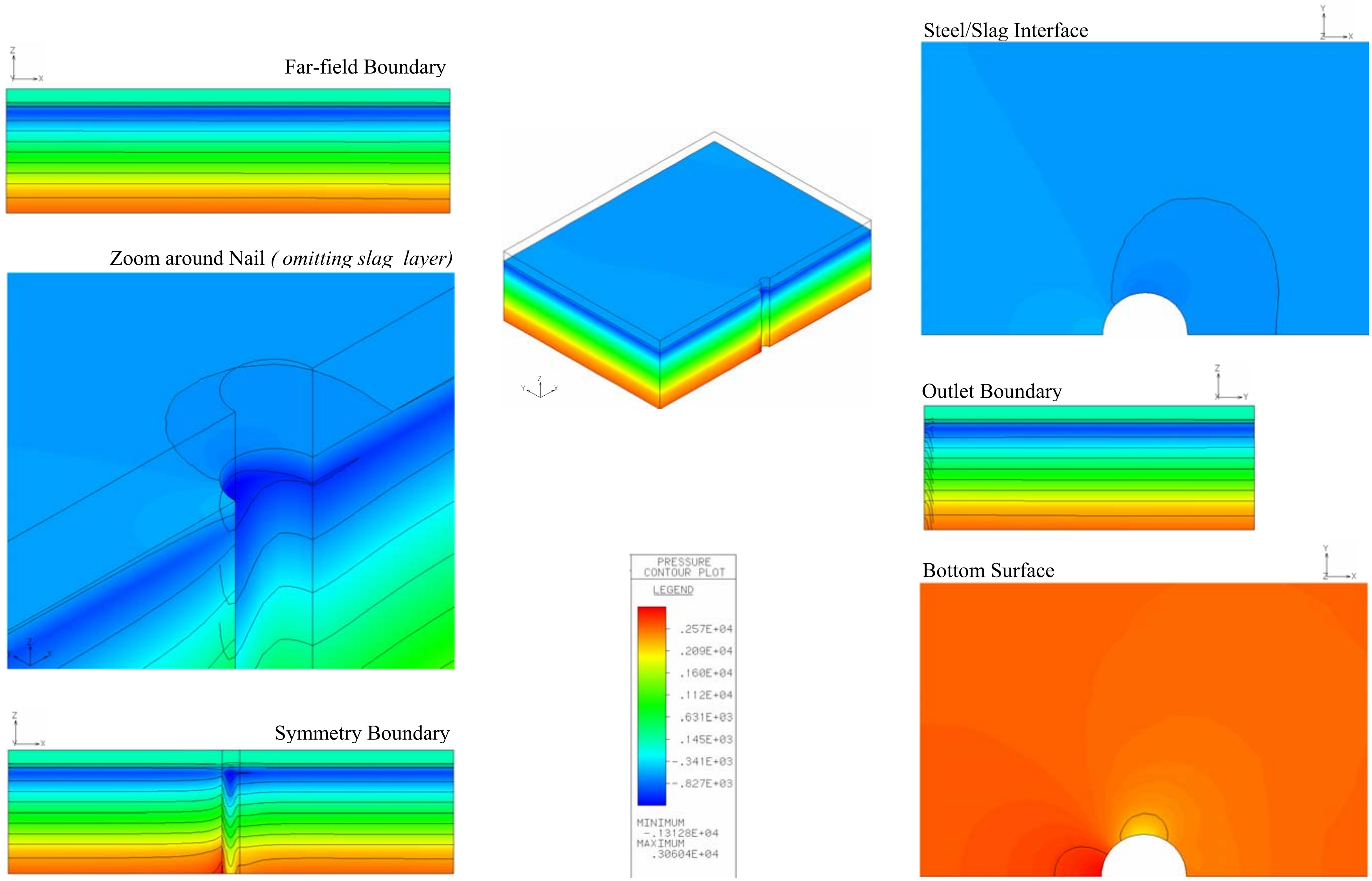

Figure 3.18: Pressure solution for the initial, S.S simulation in the Slag Model (0.010 m diameter, 0.3 m/s inlet velocity case)

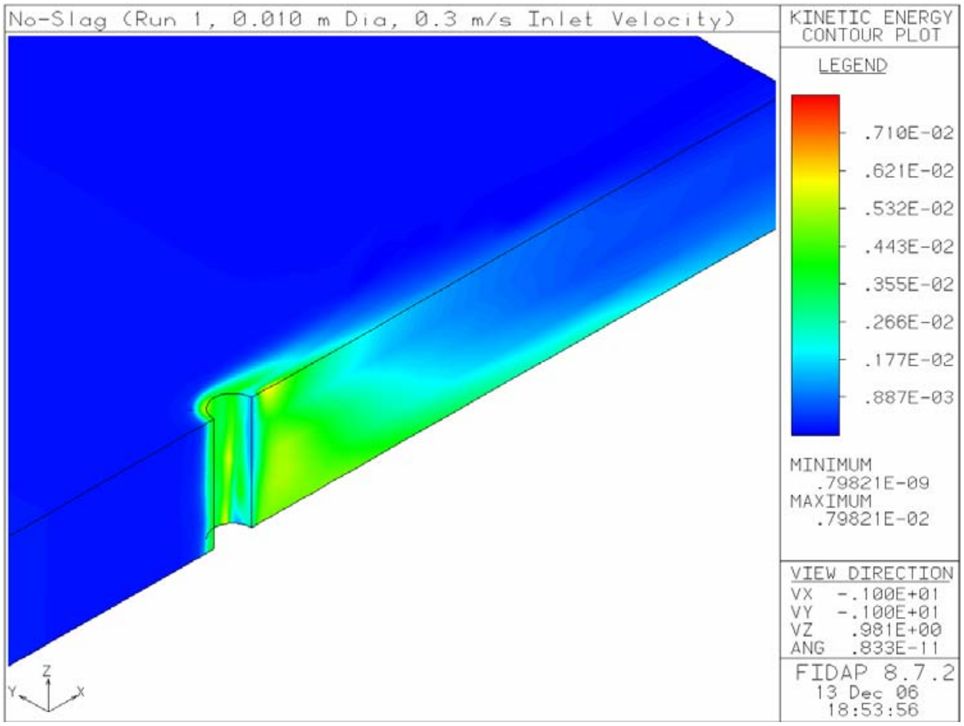

(a)

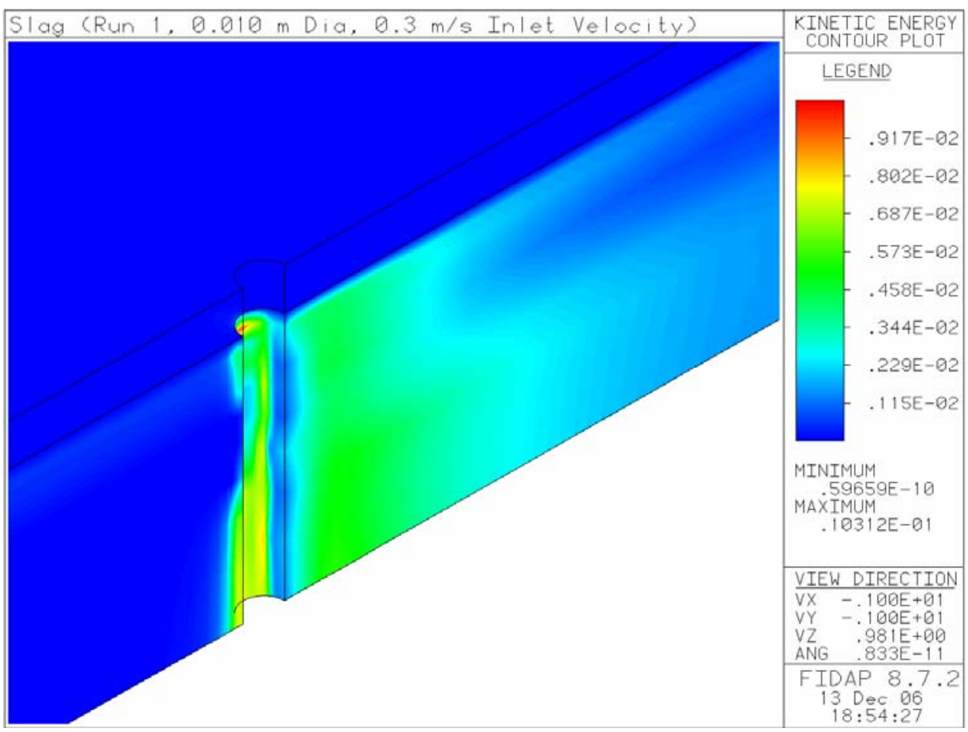

(b)

Figure 3.19: Kinetic energy solution for initial S.S. simulation in the **(a)** No-Slag and **(b)** Slag Models (only steel layer; 0.010 m diameter, 0.3 m/s inlet velocity)

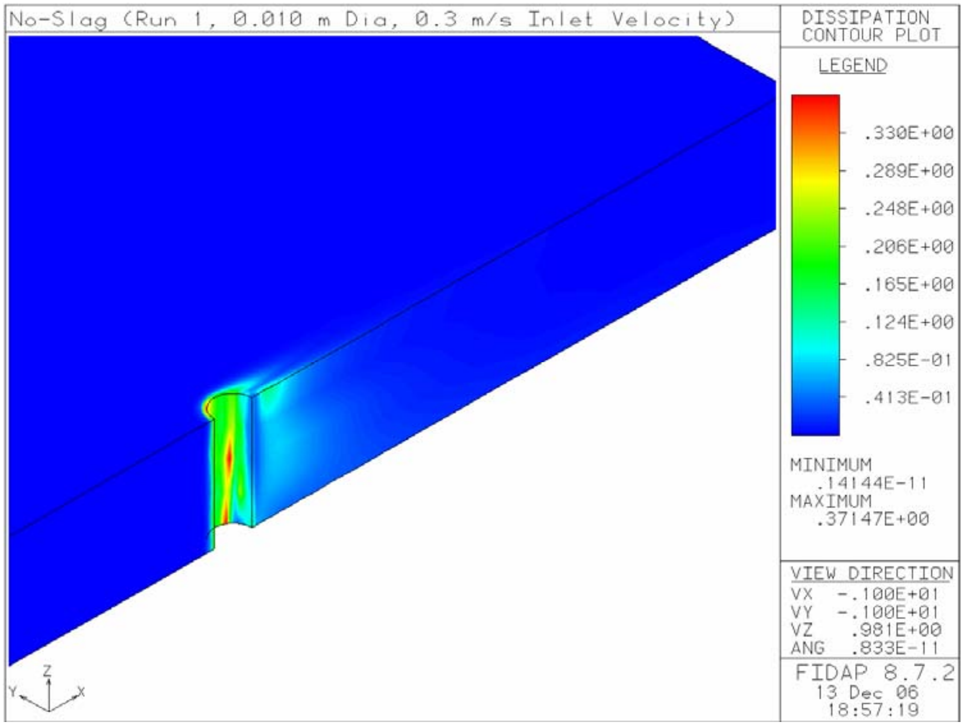

(a)

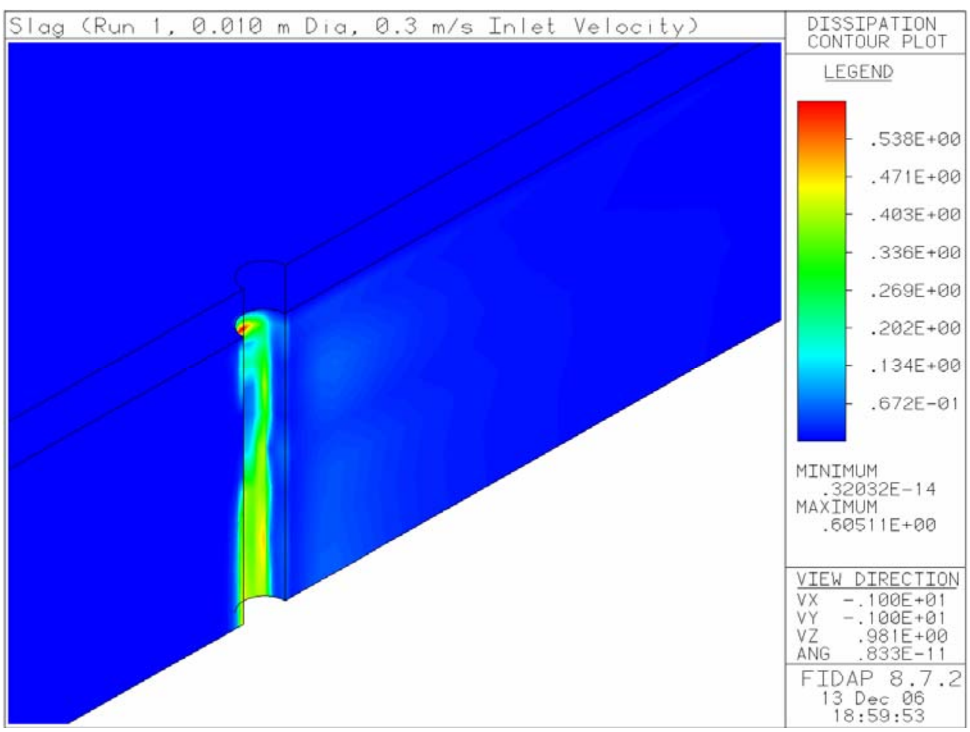

(b)

Figure 3.20: Dissipation energy solution for initial S.S. simulation in the **(a)** No-Slag and **(b)** Slag Models (only steel layer; 0.010 m diameter, 0.3 m/s inlet velocity)

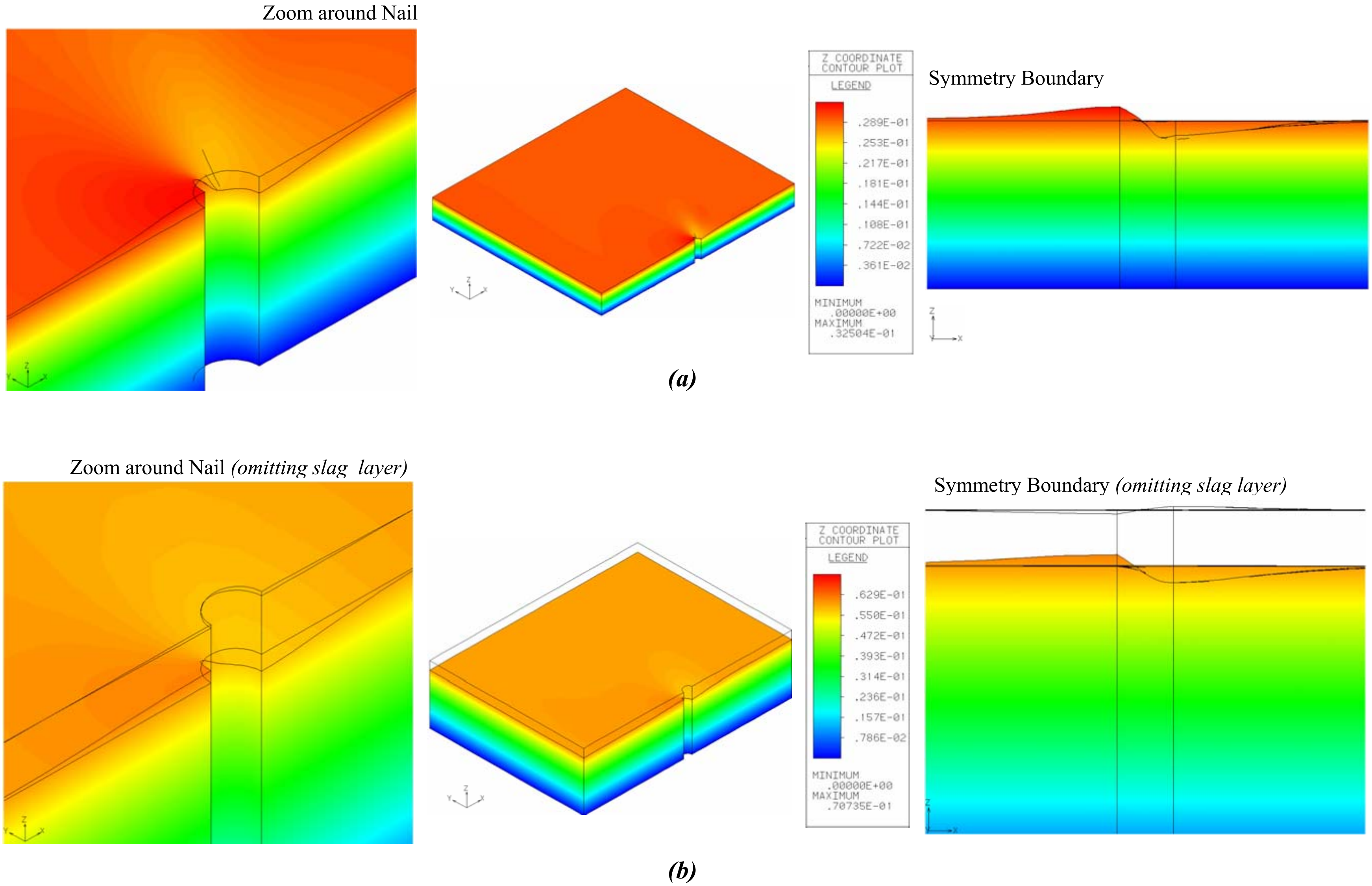

Figure 3.21: Final surface deformation in the **(a)** No-Slag and **(b)** Slag Models (0.010 m diameter, 0.3 m/s inlet velocity)

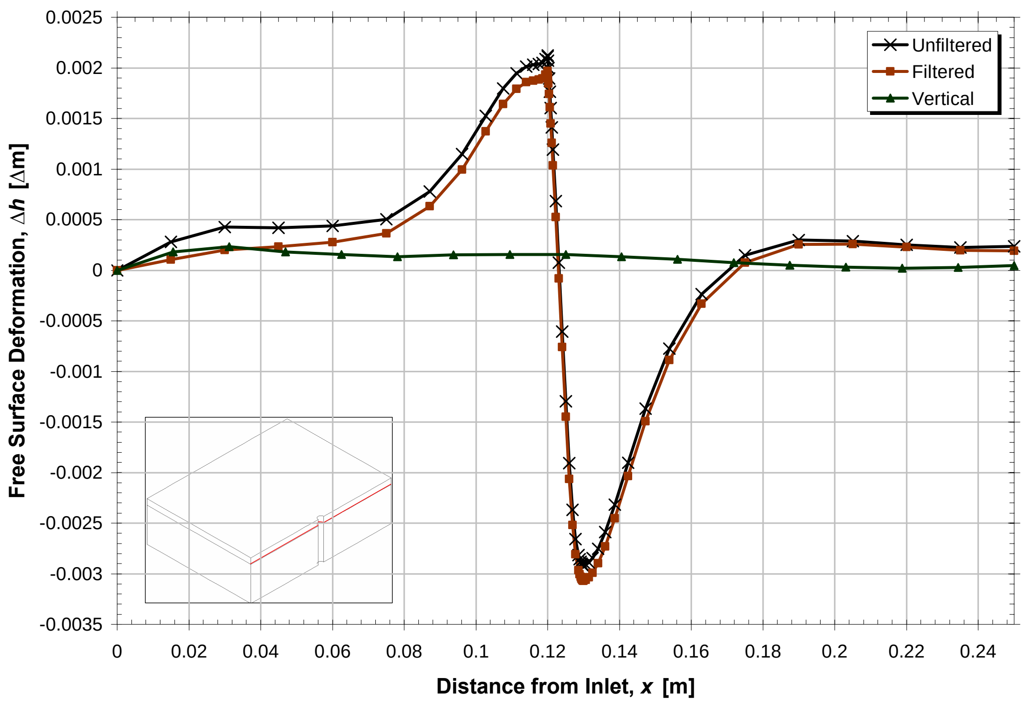

Figure 3.22: Free surface mesh deformation for symmetric and far-field boundaries (Slag Model, 0.010 m diameter, 0.3 m/s inlet velocity)

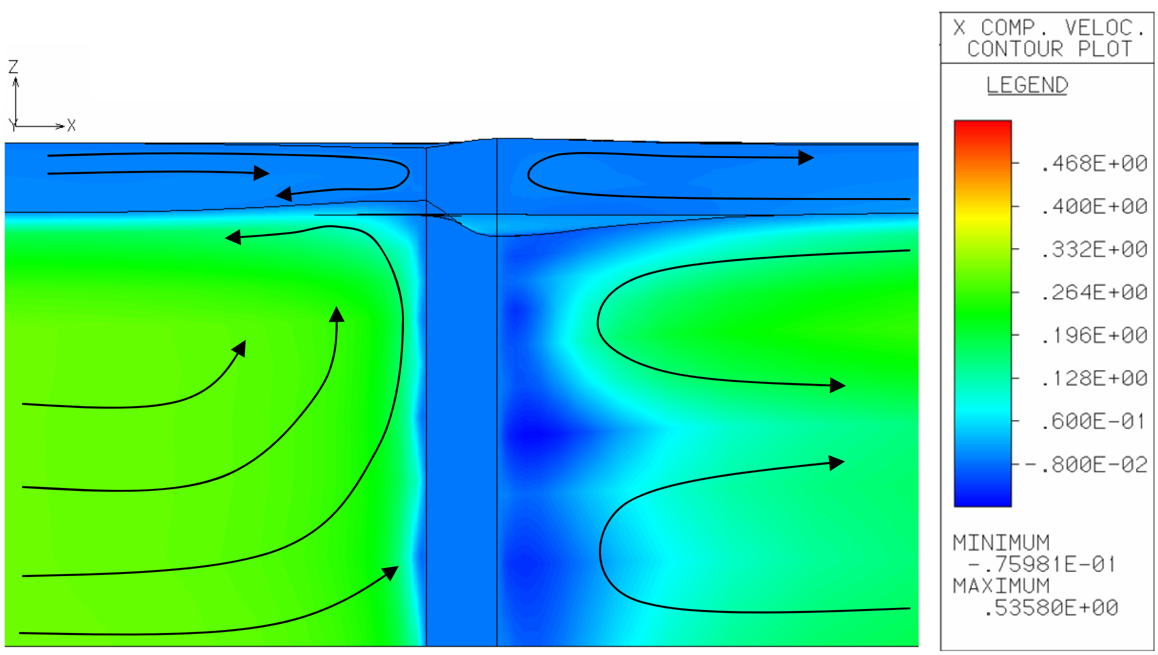

Figure 3.23: Recirculation zones along the symmetry boundary (Slag Model, 0.010 m diameter, 0.3 m/s inlet velocity). Schematic vectors exaggerate vertical velocity in the steel and overall speed in the slag layers for clarity

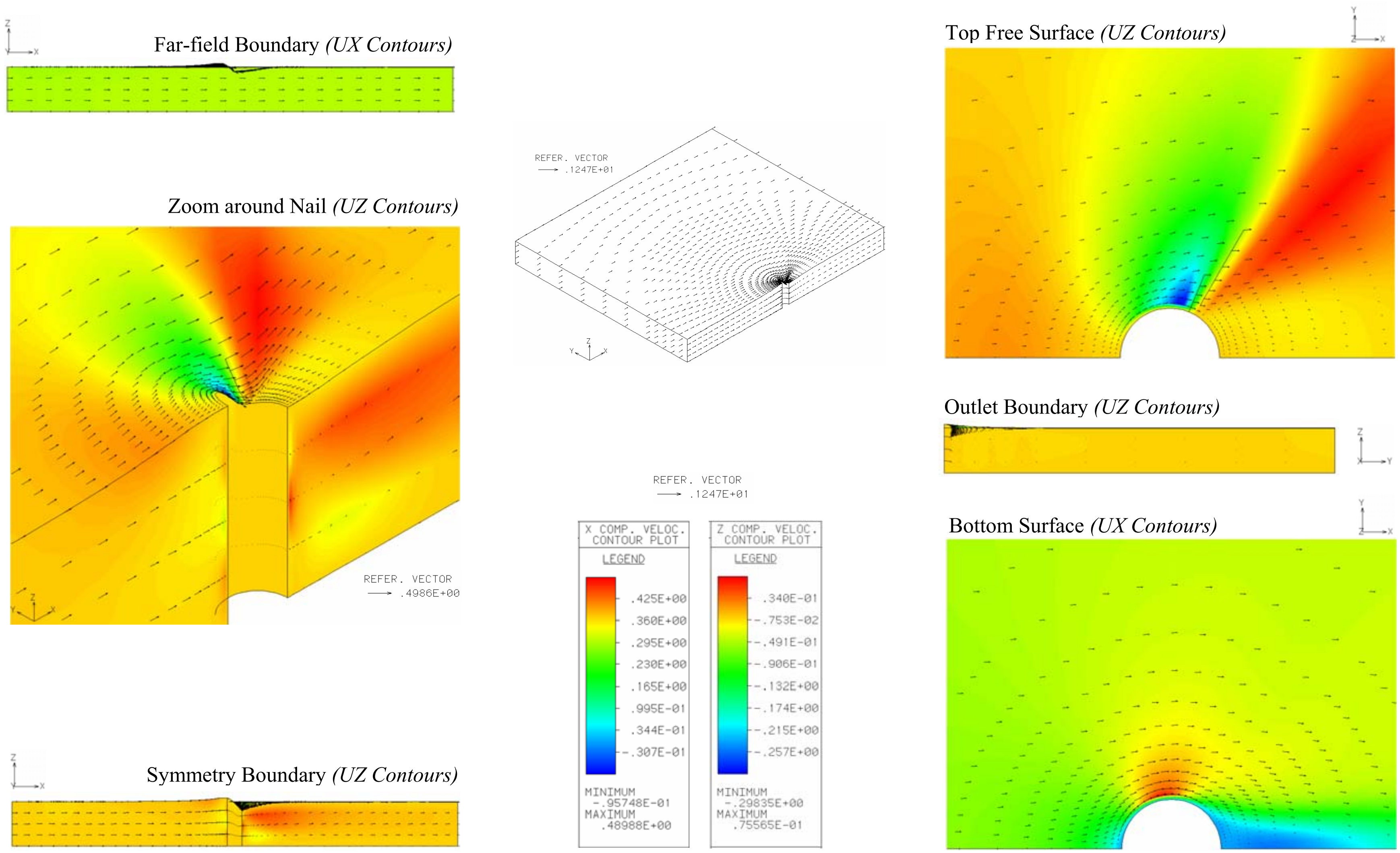

Figure 3.24: Velocity solution for the second, transient simulation in the No-Slag Model (0.010 m diameter, 0.3 m/s inlet velocity case). Reference vector and contour legends apply to all figures unless otherwise labeled

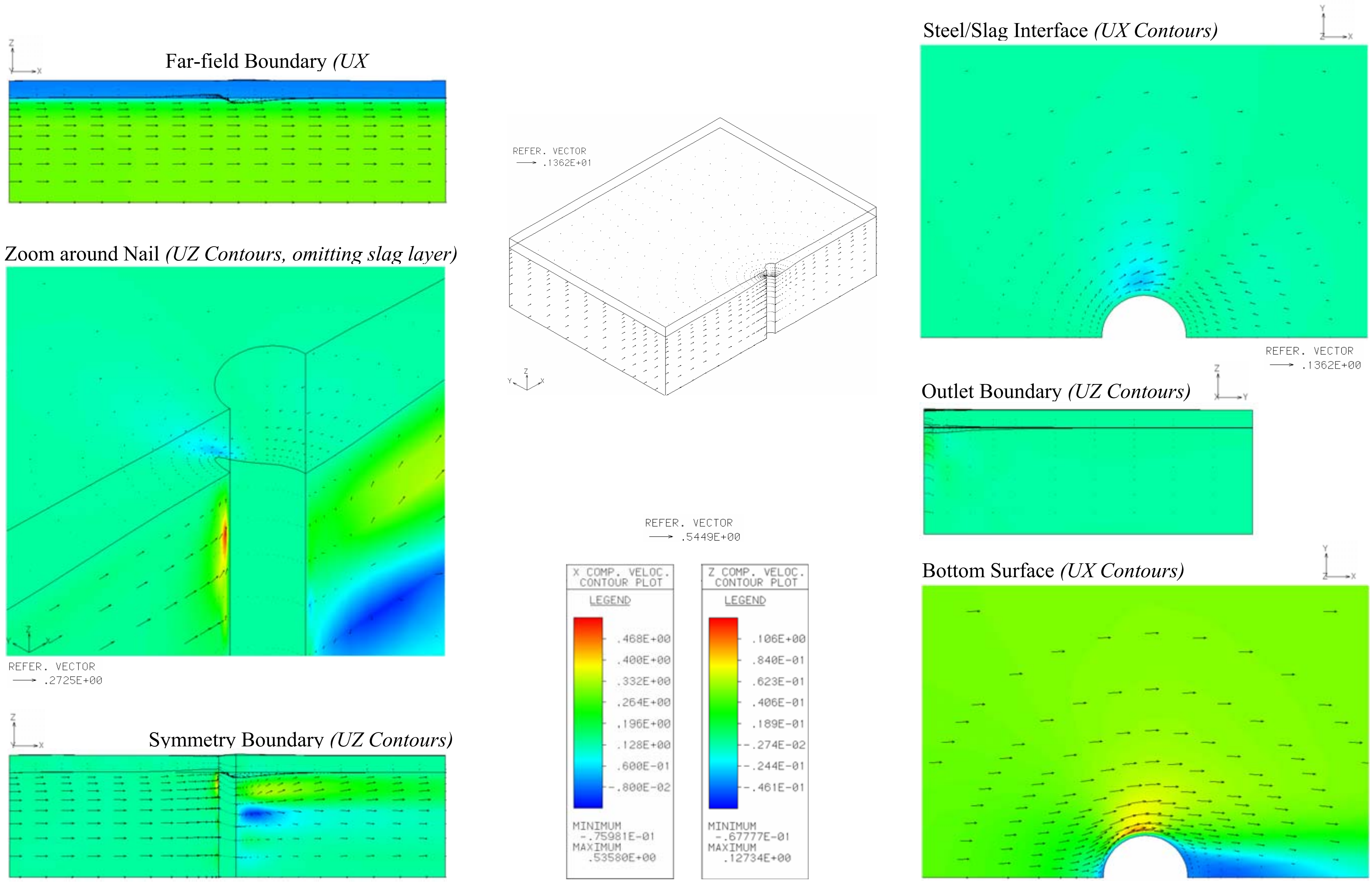

Figure 3.25: Velocity solution for the second, transient simulation in the Slag Model (0.010 m diameter, 0.3 m/s inlet velocity case). Reference vector and contour legends apply to all figures unless otherwise labeled

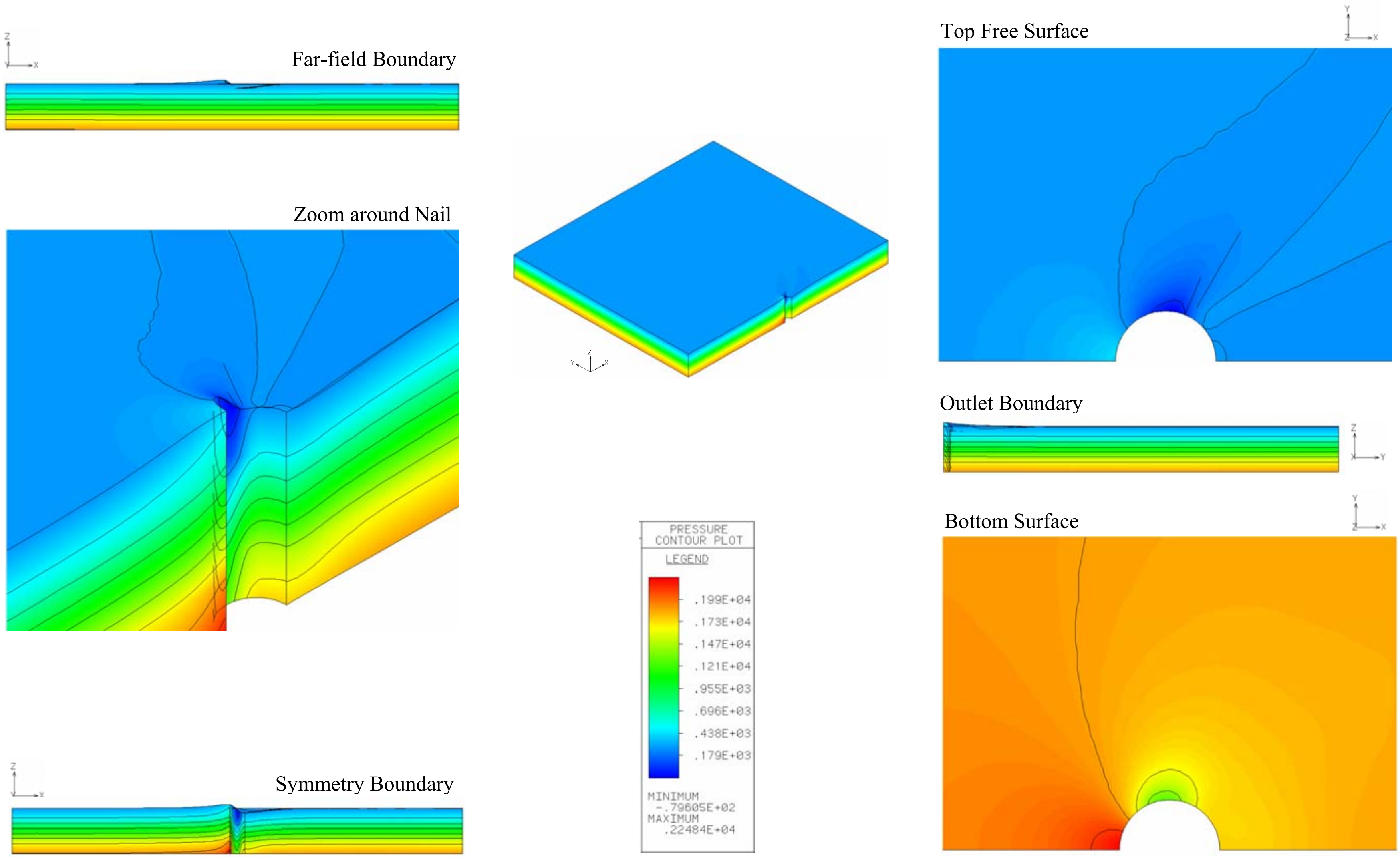

Figure 3.26 Pressure solution for the second, transient simulation in the No-Slag Model (0.010 m diameter, 0.3 m/s inlet velocity case)

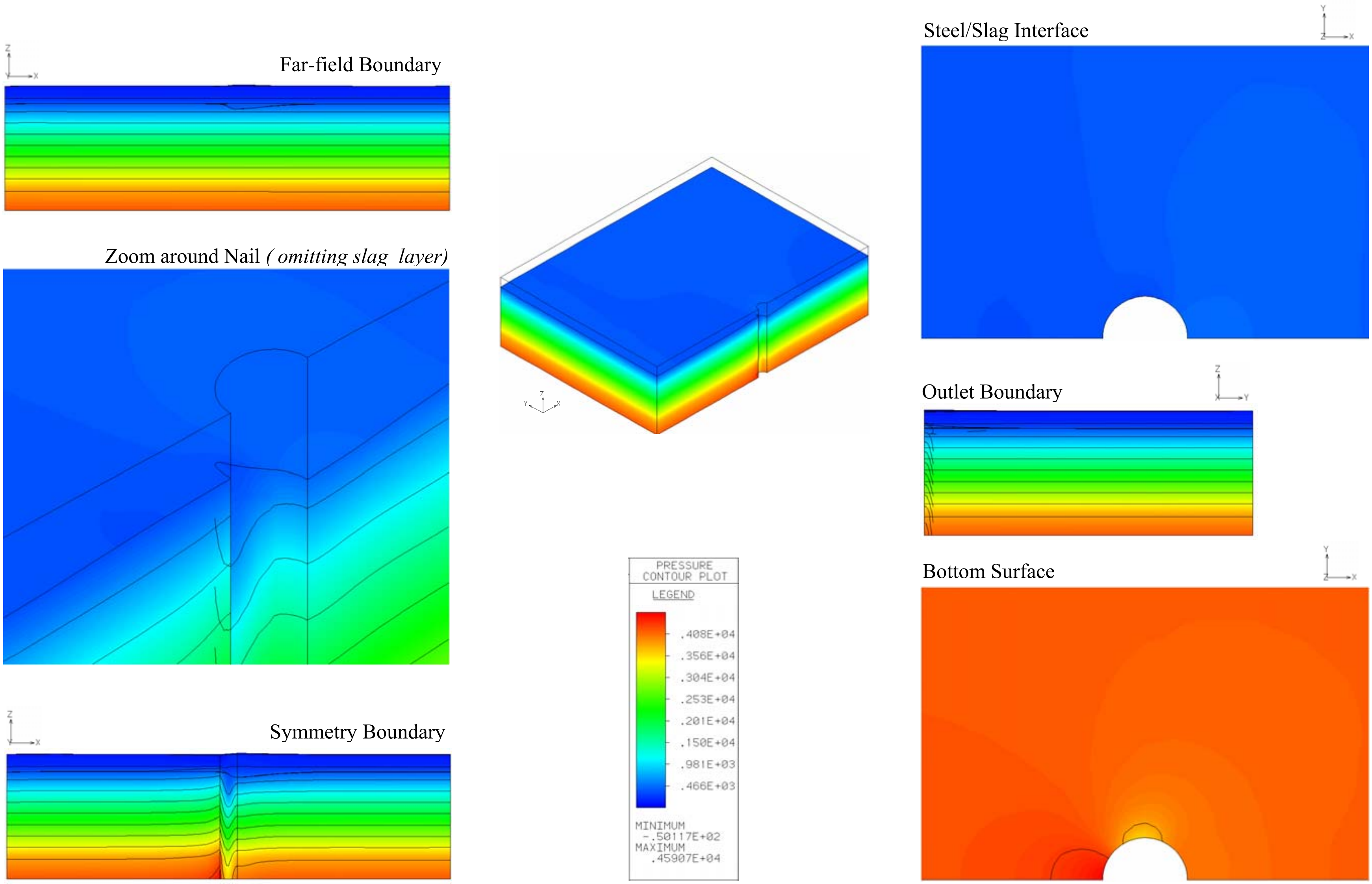

Figure 3.27: Pressure solution for the second, transient simulation in the Slag Model (0.010 m diameter, 0.3 m/s inlet velocity case)

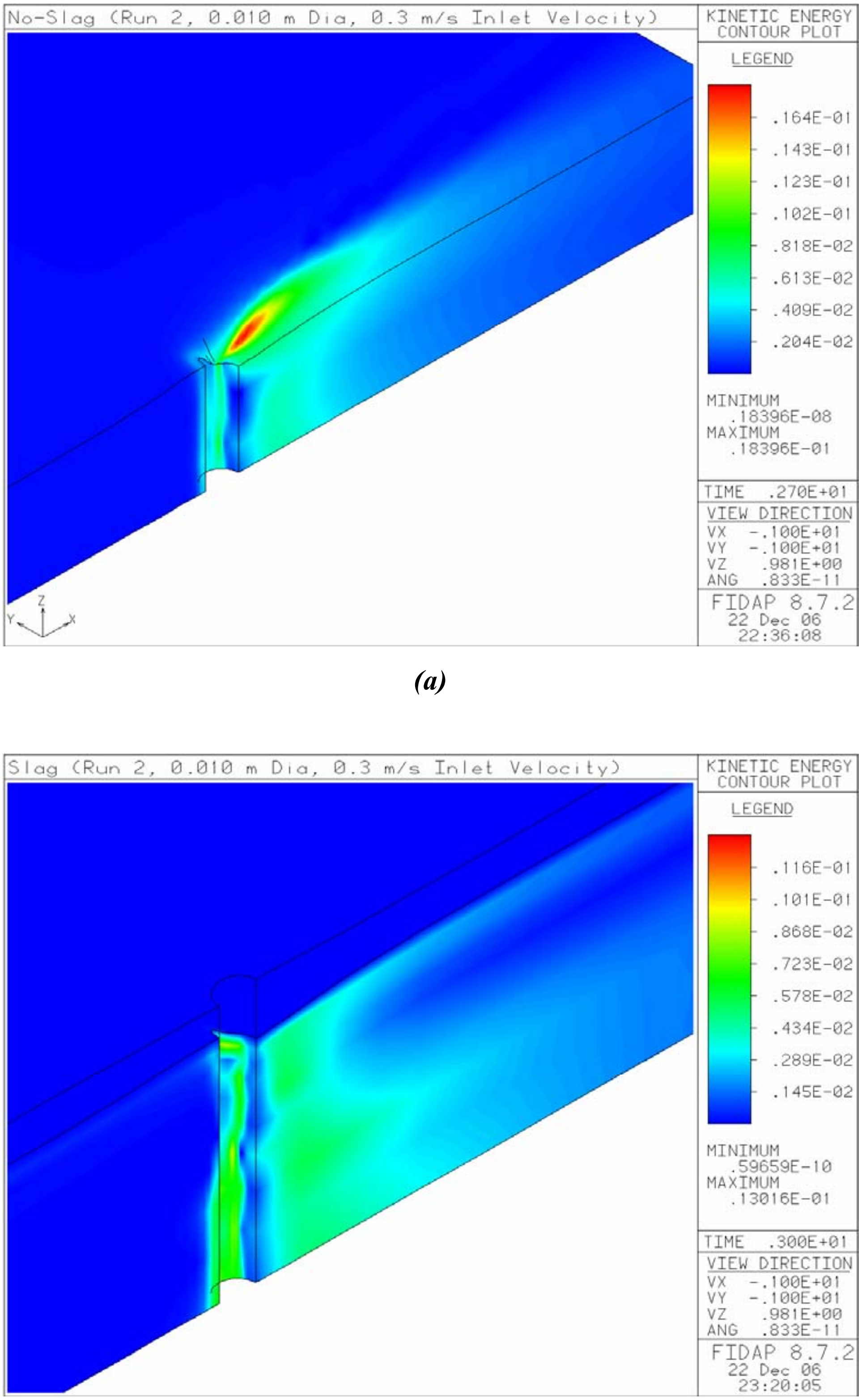

(a)

(b)

Figure 3.28: Kinetic energy contour plot for second, transient simulation: **(a)** No-Slag, **(b)** Slag Models (0.005 m diameter, 0.3 m/s inlet velocity)

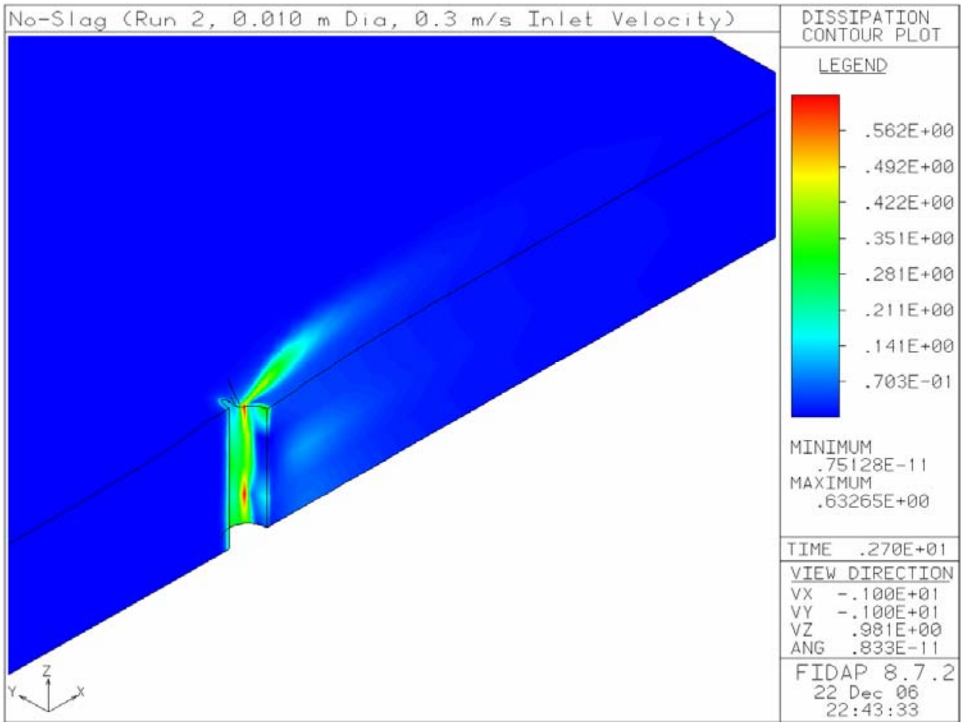

(a)

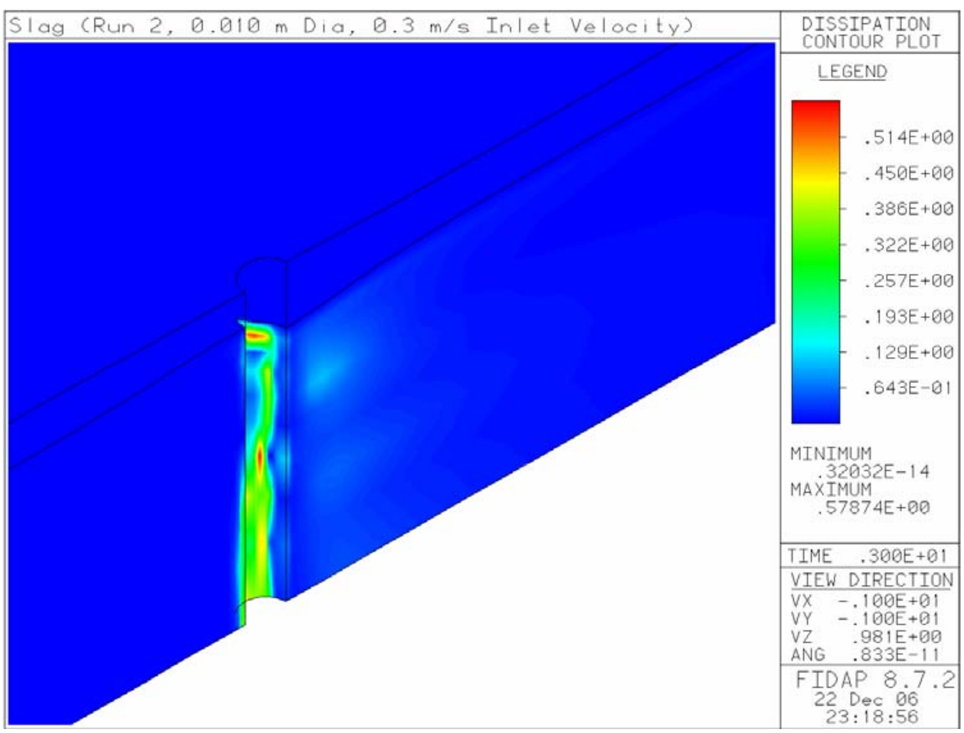

(b)

Figure 3.29: Dissipation energy contour plot for second, transient simulation: **(a)** No-Slag, **(b)** Slag Models (0.005 m diameter, 0.3 m/s inlet velocity)

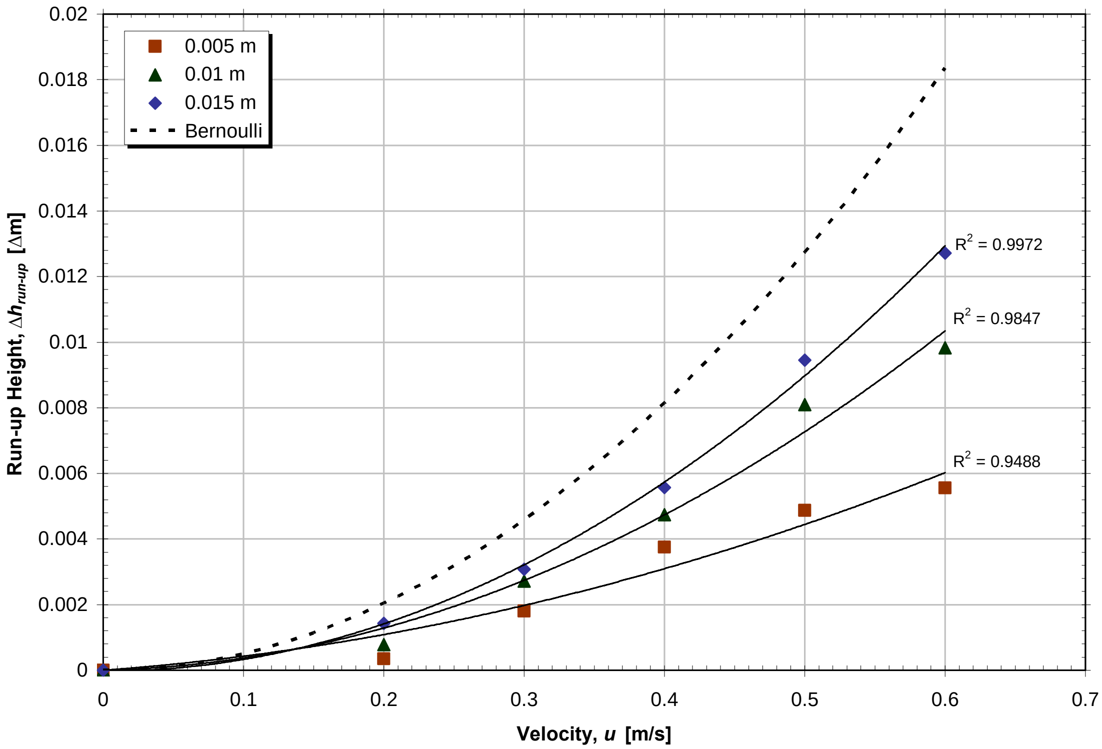

(a)

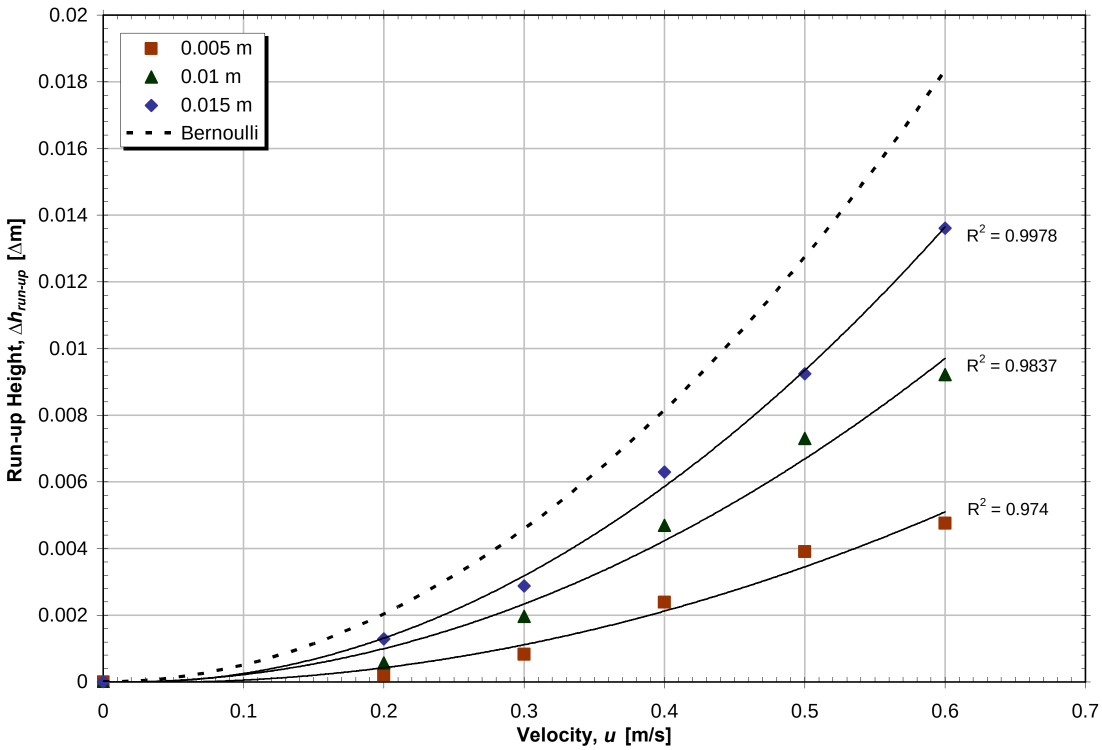

(b)

Figure 3.30: Leading edge run-up for **(a)** No-Slag and **(b)** Slag Models

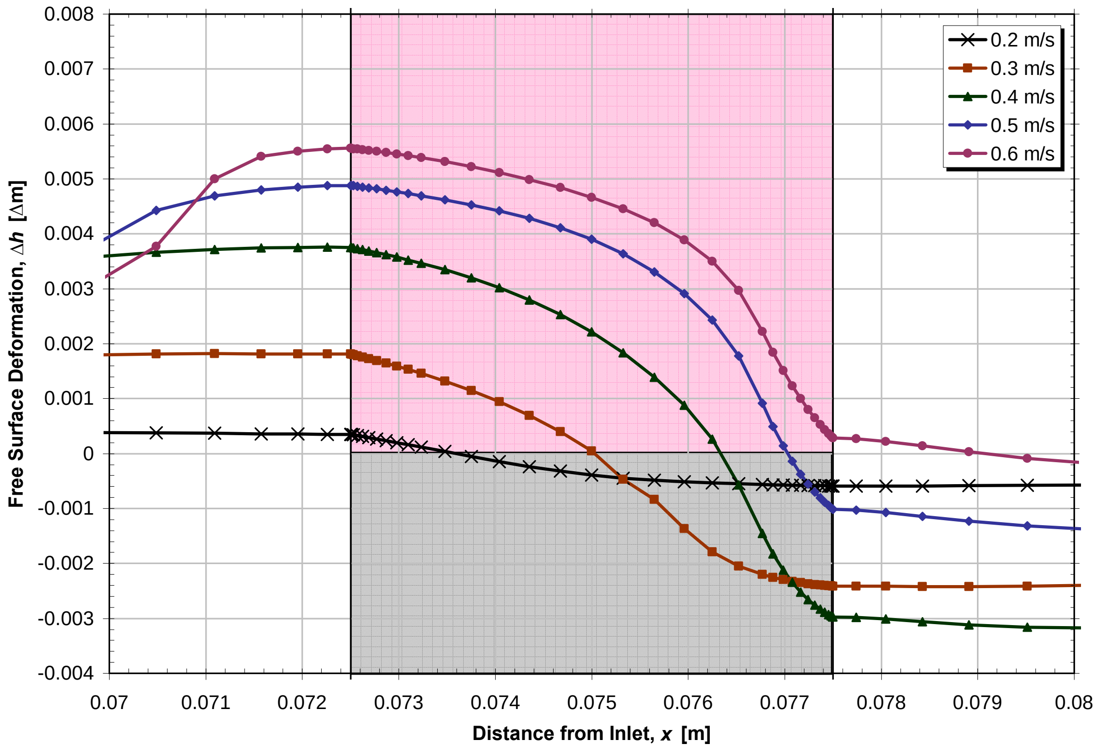

(a)

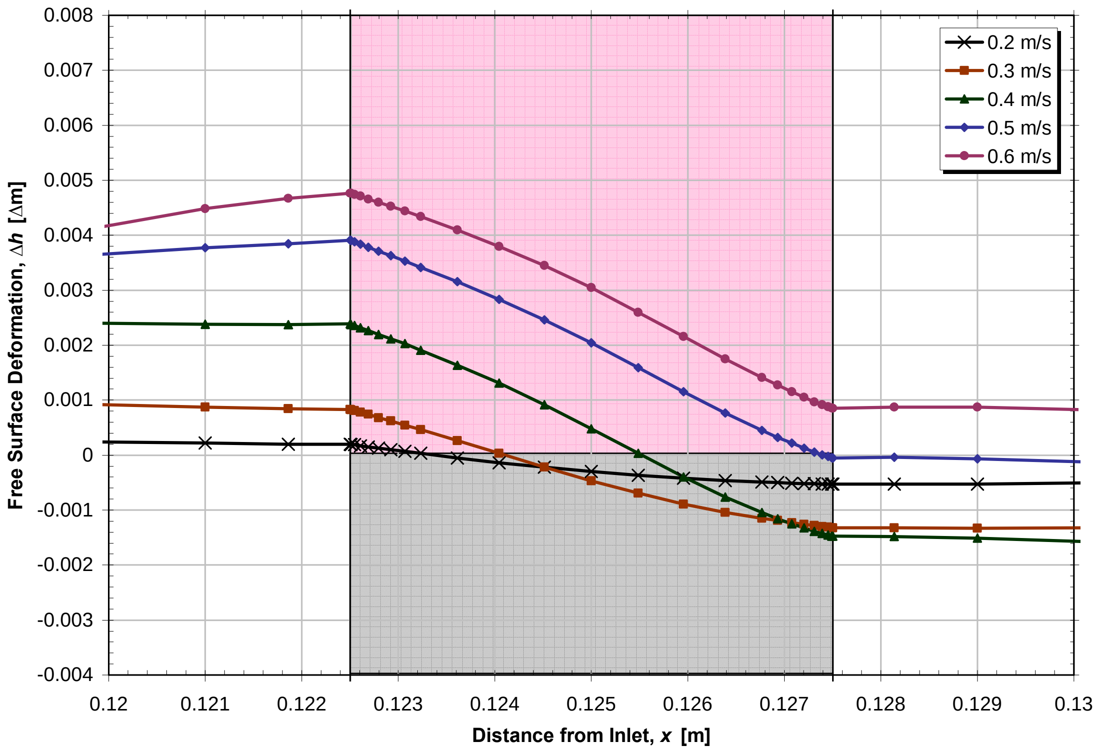

(b)

Figure 3.31: Knob profile data (0.005 m diameter) for **(a)** No-Slag and **(b)** Slag Models

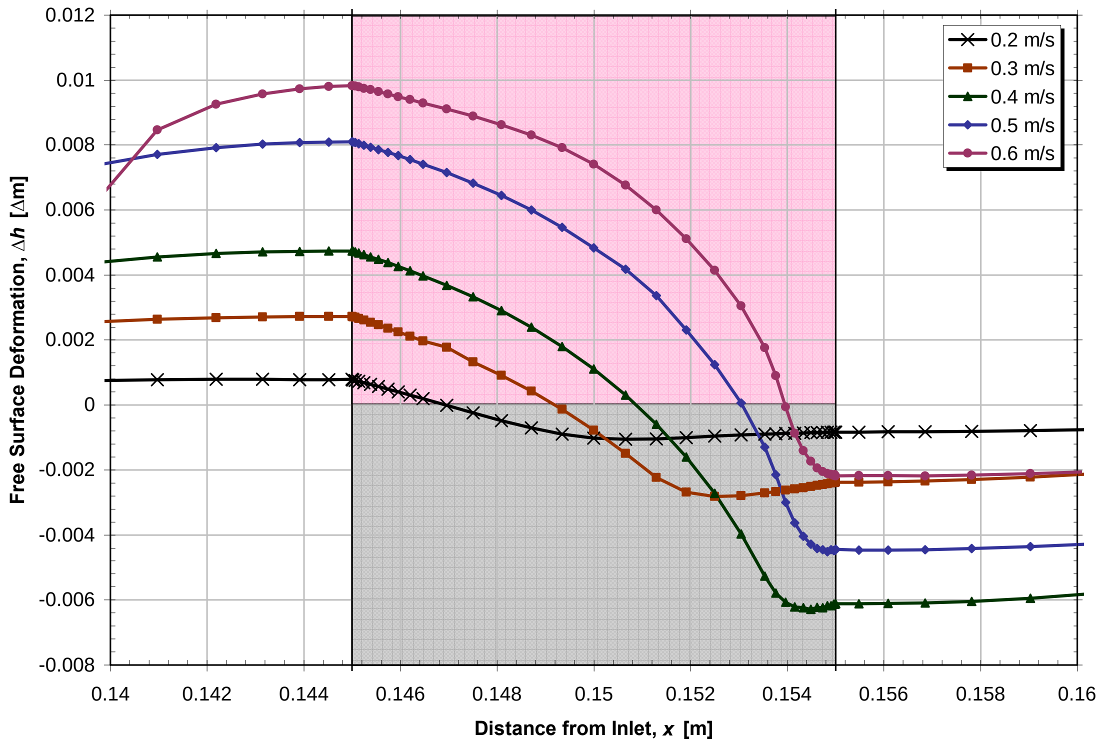

(a)

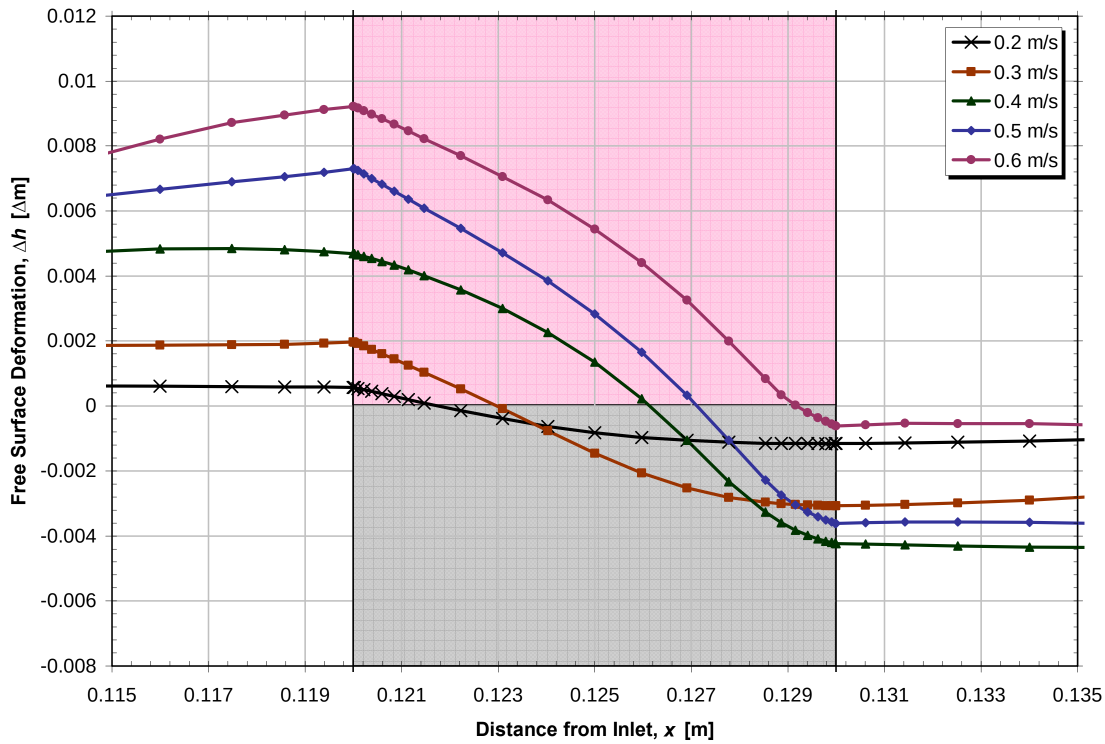

(b)

Figure 3.32: Knob profile data (0.010 m diameter) for **(a)** No-Slag and **(b)** Slag Models

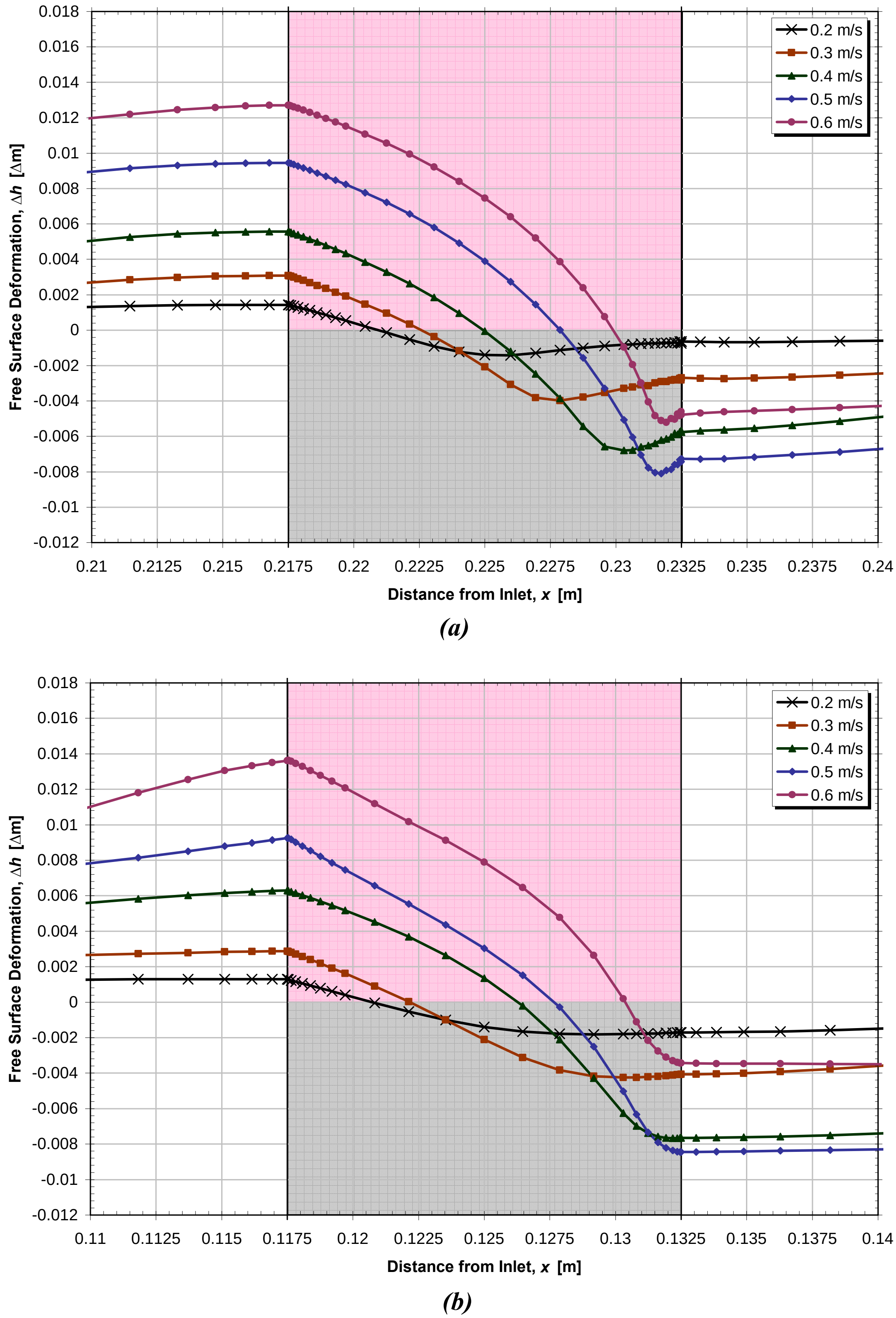

Figure 3.33: Knob profile data (0.015 m diameter) for **(a)** No-Slag and **(b)** Slag Models

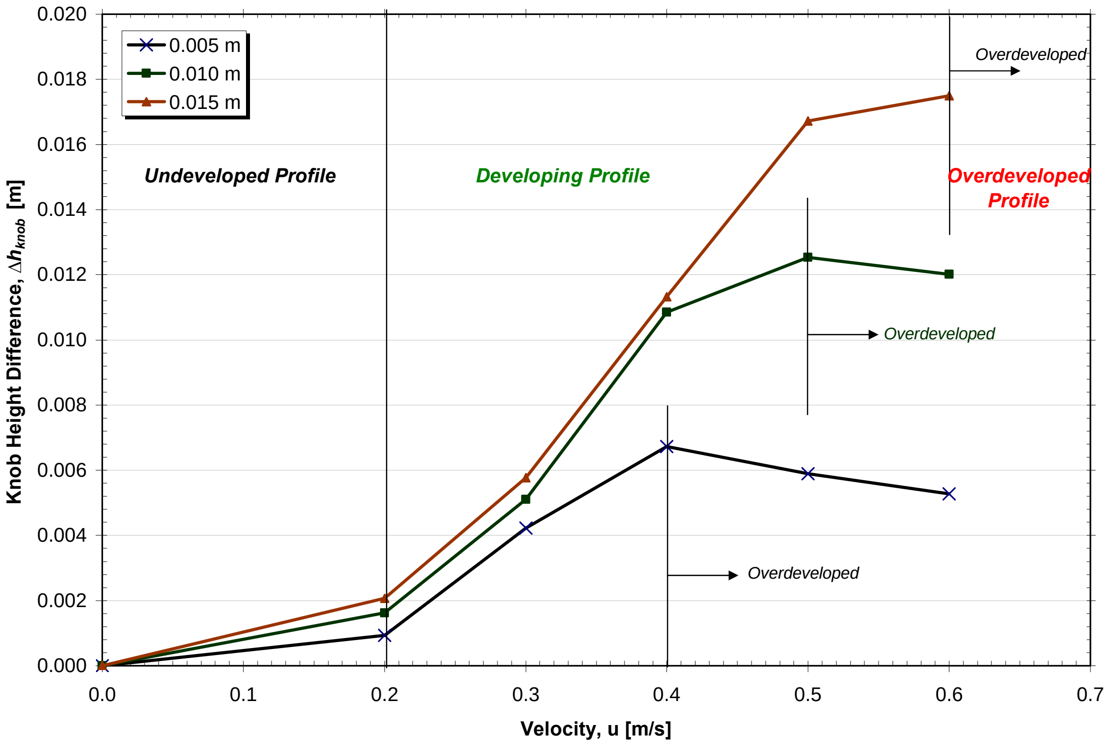

(a)

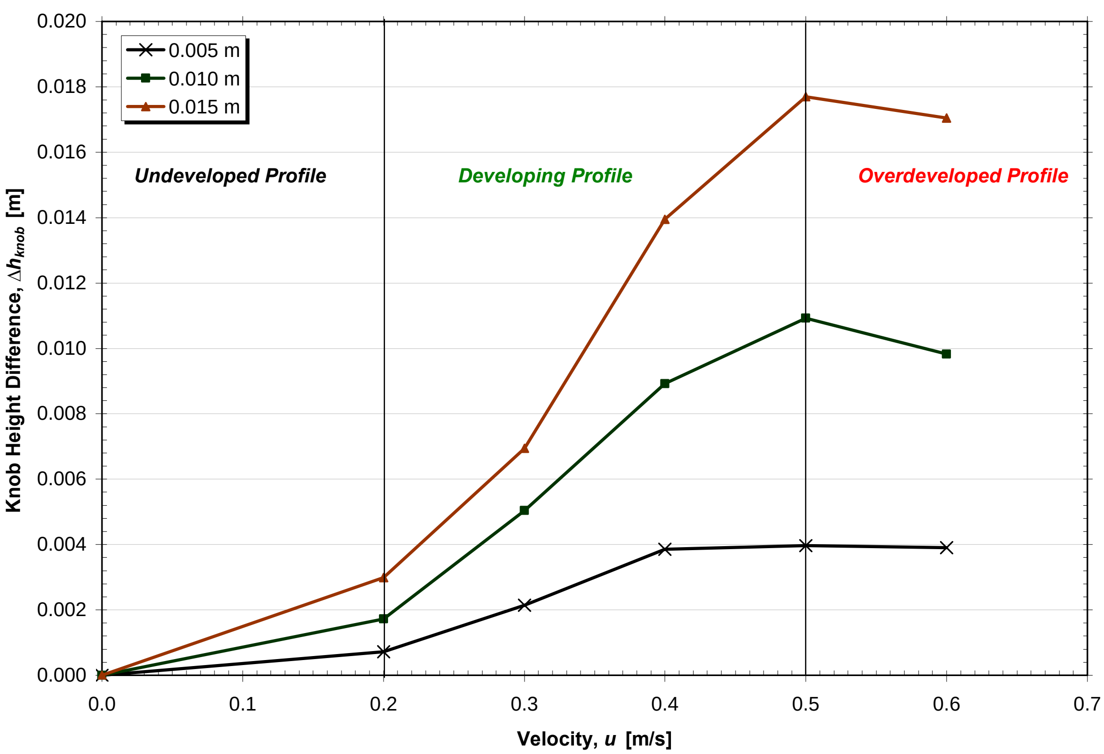

(b)

Figure 3.34: Knob height difference for **(a)** No-Slag and **(b)** Slag Models

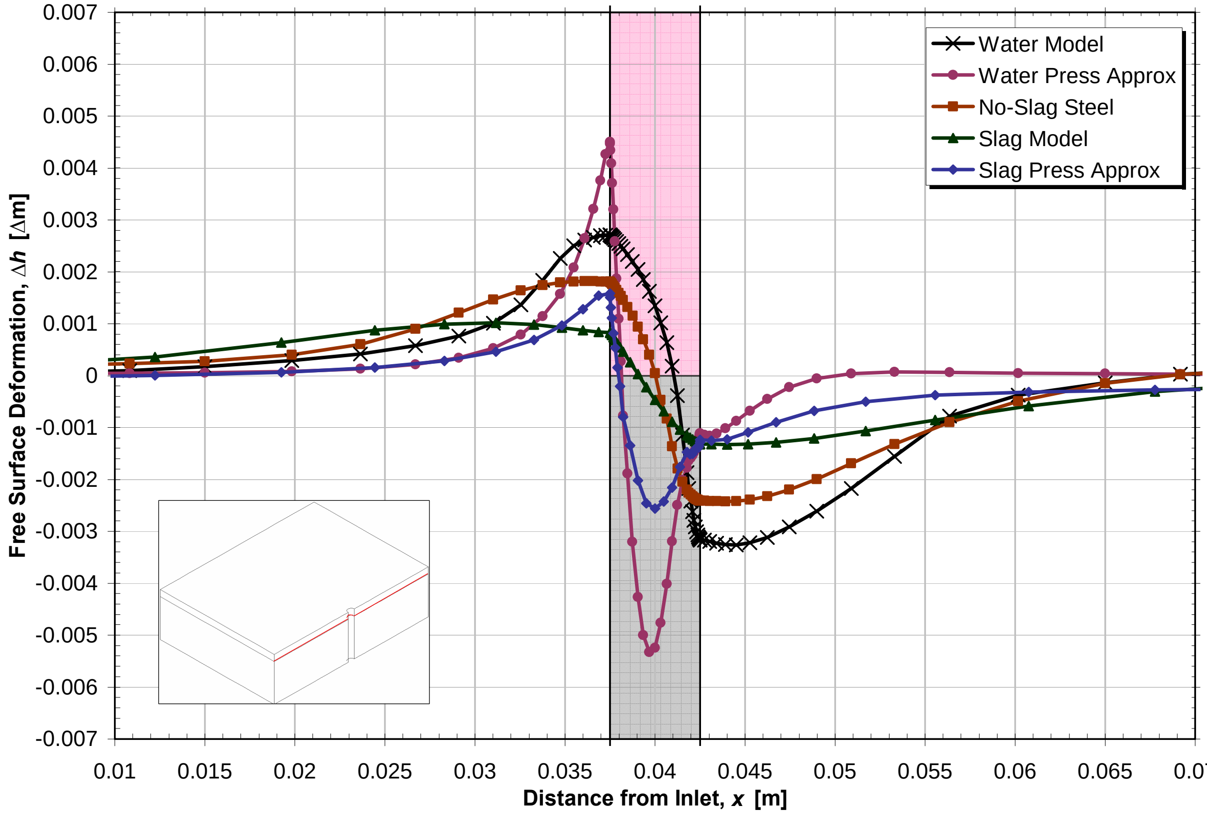

Figure 3.35: Water/steel model comparison including pressure approximations (No-Slag Model, 0.005 m diameter, 0.3 m/s inlet velocity)

CHAPTER 4. INGOT CLEANLINESS INVESTIGATION

4.1 Introduction

Inclusion entrapment is one of the main defects caused by surface velocity problems of concern in the previous two chapters. Inclusions are difficult to quantify in continuous cast steel, owing to their low incidence and cost of analysis. Static ingot casting is also affected by inclusions and is easier to study, so was the subject of an experimental investigation which is included as part of this thesis. Conducted by Zhang, Rietow, Thomas, Eakin and Baird, the work presented in this chapter is the basis of the publication "Large Inclusions in Plain-Carbon Steel Ingots Cast by Bottom Teeming"; journal submissions include Ingot Metallurgy Forum transcripts and ISIJ International[63, 64)].

Even though the fraction of steel produced by this method has decreased to approximately 11% in 2003, ingot casting remains an integral part of the steel industry[65)]. Many grades of steel which cannot be produced via continuous casting are cast using ingot formation methods (namely low-alloy steel grades). Furthermore, it is much more economical for short-run production lots to be ingot-cast rather than continuously cast. Case in point, ingot casting is the primary production method of high carbon chromium bearing steel, thick plate seamless tubes, and specialty forgings[66)]. While continuous casters have a relatively limited range of slab dimensions, the dimensions of ingot-cast slabs have more flexibility. For these reasons, ingot formation remains an attractive alternative in the casting of steel.

A schematic of the entire ingot casting process is shown in Figure 4.1. The method for producing a bottom-teemed ingot is outlined in the following steps.

Step 1: Metal contained within clamshell buckets is melted within an ultra-high powered eccentric bottom-tapping furnace (UHP EBT). Refining using an oxidizing slag in the furnace removes most of the carbon and phosphorus within the steel.

Step 2: Through tapping of the EBT, the steel is transferred into the ladle. Alloy additions are charged and added to the ladle (i.e. aluminum, which reduces oxygen content). A reducing top layer is also added in this step.

Step 3: The ladle enters a treatment station for re-heating. Further refining and alloy addition occurs. Induction stirring ensures proper alloy mixing and allows for impurities to be captured by the slag layer.

Step 4: While in the ladle, vacuum degassing reduces the hydrogen level to under 1 ppm. Induction stirring coupled with argon injection continues circulation of the steel, increasing the interaction of the steel with slag and promoting alloy homogeneity.

Step 5: The ladle enters a secondary treatment station, where the steel is calcium treated through wire feeding. Reheating may occur to maintain acceptable level of superheat, and alloy concentrations are finalized.

Step 6: Once the grade and superheat are proper, the steel is bottom-teemed into the ingots at controlled rates. In some ingot-casting processes, argon shrouding may be used prior to teeming (which minimizes reoxidation and hydrogen/nitrogen contamination of the steel). The ingot examined in this study did *not* include argon shrouding.

Exogenous, non-metallic inclusions in the cast metal can cause major defects in the final product. These unwanted particles come from a variety of sources, however most are a result of either[67)]:

- Deoxidation (Al clusters, TiO, etc…)
- Reoxidation (Fe_2O_3, etc…)
- Exogenous sources (slag globules, dirt, etc…)
- Undesired chemical reactions

Inclusions greatly reduce the physical properties of the steel grade, lowering toughness, minimum strength, surface appearance, and fatigue life among others. If the inclusions are detected prior to delivery of the steel, the unacceptable areas of steel must be removed, thereby reducing the yield. If the inclusions go undetected, the steel may not meet cleanliness standards and can result in detrimental failure of the final product in service.

Steelmakers are becoming more cognizant as to the importance of producing cleaner steel. By examining the location and the composition of exogenous inclusions, stricter casting procedures will result in cleaner steel. Controlling the size distribution, quantity, and morphology of non-metallic inclusions maintains regular, predictive material properties in the final steel product.

This study attempts to characterize inclusion distribution and properties in a cast steel ingot. Recommendations as to their origin will allow for tighter casting parameters to be used, in effect minimizing the likelihood of entrapping detrimental impurities.

4.2 Literature Review

4.2.1 Inclusion Formation

The formation of macro-scale inclusions (> 20 microns in diameter) is typically characterized by four mechanisms (reoxidation, slag-steel interaction, erosion/corrosion during steel pouring, and agglomeration due to clogging while pouring). The following presents a summery of inclusion formation methods provided by work from Cramb[68)].

Reoxidation

Due to the extremely high temperatures necessary to facilitate the melting of liquid steel, chemical reactions occur at much quicker rates than at lower temperatures. Liquid iron, for example, reacts quite spontaneously in the presence of oxygen to form iron oxides. Deoxidizers are added to the steel pool to remove as much free oxygen as possible by converting it into stable oxides (such as aluminum, magnesium, and calcium oxides). Ideally, the deoxidants are removed from the steel when they get trapped in the slag layer. However, this is not always the case; the oxides can remain in the steel slab as inclusions. Furthermore, while the deoxidants are very stable, a small amount can undergo reaction with the iron to produce iron oxides. Reoxidation is typically considered the main cause of macro-scale casting inclusions[69-71)].

Contact with ambient air accounts the majority of reoxidation inclusions. Extreme temperature in regions surrounding the superheated liquid draws oxygen towards the steel via natural convection. With liquid iron and oxygen reacting so spontaneously, any air that is allowed to contact the liquid pool nearly immediately results in oxide production. Cramb explains that the mass flux of oxygen during reoxidation can be quite high[68)], yielding high amounts of oxides submerged in the liquid steel pool.

By using slag high in FeO, MnO, and Silica content, oxygen can be further introduced into the liquid pool, causing serious reoxidation problems[67]. High turbulence near the steel-slag interface enhances this interaction. Even though the reaction between slag and steel is much slower than the air-steel reaction, turbulence-inducing activities such as stirring and pouring produce a considerable amount of oxides through this reaction.

Reaction with refractories is the final main source of reoxidation inclusions. Oxygen present in high moisture refractories and mold walls typically get drawn into the liquid steel pool, forming oxide inclusions. While this is not especially prevalent in typical casting environments, it may account for a significant amount of unwanted inclusions when producing ultra-clean steels.

Steel-Slag Interaction

Emulsification of liquid slag at the slag-steel interface poses additional problems during casting. Given sufficient energy at this interface, slag globules are sheared off and become entrained in the liquid steel pool. Various sources during the ingot casting process provide enough energy to promote slag emulsion, which include:

- <u>Filling ladle/mold at excessive rates</u> (generating high steel velocities past the slag layer). With sufficiently high shear levels at the slag/steel interface, emulsification occurs in which liquid slag globules get drawn into the liquid pool. Macro-scale inclusions are deposited within the final product should these globules reach the solidification front.
- <u>Pouring through the liquid slag layer</u>. Bottom-teemed ingots require the liquid steel inlet to be located at the lower part of the mold. While some casting methods involve suspending bags of slag above the mold floor, others simply rest the slag at the bottom surface prior to filling. In the latter case, steel initially flows *through* the slag, entraining excessive amounts of slag particles. By reducing the rate of filling (and thus slowing the inlet steel velocity), slag entrainment is lessened but not totally eliminated. Tapping from the furnace into the vessel provides another means of steel contamination. It is common for slag from the furnace to flow into the ladle or mold prior to the steel, thereby resulting in high levels of inclusion concentration in the steel pool.
- <u>Vortexing of liquid steel through outlet ports</u>. Sufficiently high pour rates coupled with low steel levels are a recipe for vortex formation in both the tundish and ladle. Should a

vortex generate enough energy, slag may be entrained at the upper steel surface, pulled downward along the vortex, and exit through the tundish/ladle outlet. By slowing or stopping pouring once a vortex reaches fruition, the amount of slag entrainment is minimized.

- Excessive ladle stirring rates. High levels of gas stirring generate turbulence at the slag-steel interface sufficient enough to break off liquid steel globules and emulsify them into the steel pool. By reducing the voracity of the stir rate, slag entrainment due to stirring is minimized at the expense of lessened steel mixing (and a less homogenous pool).

Erosion/Corrosion during Steel Pouring

Most of the extremely large entrapped particles originate as eroded refractory material. Some grades of cast steels (including high manganese grades and steels with high soluble oxygen content) are corrosive to the refractory material. Reoxidation of steel compounds the problem, as FeO-based inclusions wet the refractory material and amplify erosion rates in areas of high turbulence. Other factors which loosen refractory material include thermal expansion of the bricks (and the resulting stress of bricks pushing against each other) or mold binders decomposing at high temperatures.

Agglomeration Due to Clogging While Pouring

Clog formation and subsequent release into the steel pool can result in large inclusion defects in the cast product. While many different theories have been proposed, most suggest that clogging is initiated with the formation of an alumina layer (via chemical reaction) along the surface of the refractory[72-74)]. The high contact angle of alumina in steel (~140 degrees) encourages the sticking of inclusions to the wall to minimize its contact angle with the steel. Due to the slow velocities near the wall (explained through boundary layer theory), the flow past the inclusion may not be sufficient enough to release the inclusion from the wall. Further inclusions collide with the affixed inclusion from both the streamwise and back side directions (as small eddies draw inclusions backwards once past the inclusion), encouraging its growth. The clog is released into the flow when the force of the flow into the large agglomeration exceeds the attachment force. Regions of slow flow facilitate the growth of large clogs, as the flow past the clog typically is not high enough to release the agglomeration from the wall.

Dawson showed that inclusion formation initiated at characteristic locations in the nozzle, typically in regions where flow separation is prevalent[75)]. Flow eddies due to turbulence in these regions facilitate the transport of inclusions to the wall surface. Once formed, the "dead zone" of the flow separation does not contain enough energy to release the clog from the wall. As nozzle roughness increases, the probability of inclusions being captured by the wall and forming clogs also increases[80-84)].

Various methods have been developed to prevent clogs from forming. From a very basic standpoint, if the amount of deoxidation products and formation of reoxidation inclusions in the steel are minimized, the likelihood of clogs forming from these superfluous inclusions is greatly decreased[79-84)].

Faulring discovered the addition of calcium in the liquid steel can prevent nozzle blockage[85)]. Raw calcium forms the deoxidation product CaO, which in turn combines with existing Al_2O_3 inclusions. While the alumina inclusions typically have jagged edges and are easily captured along nozzle walls (thus initiating clog formation), the CaO-2Al_2O_3 inclusions take on a spherical shape, reducing the probability of sticking to the nozzle wall.

Argon injection through the nozzle wall has proven to be effective in clogging reduction. It has been suggested that argon gas develops a film lining the nozzle wall, preventing the alumina layer (and deoxidation products) from contacting the wall[86-88)]. Furthermore, the argon bubbles remove already affixed inclusions from the wall and "floats" the deoxidation products away from clog-prone areas[88,89)].

Nozzle design also plays a large factor in reducing clog formation. By choosing a nozzle material which includes calcia additions, alumina inclusions remain liquified[80,90-92)] and do not propagate the formation of clogs[31)]. Boron nitride nozzles have been shown to reduce clog formation, however its mechanism is not fully understood[78,93,94)]. The surface roughness of boron nitride is very small, and perhaps a boron oxide film forms along the nozzle wall, both of which reduces the probability of clogging[77,93)]. Boron nitride also has a very low coefficient of thermal conduction, thereby reducing the amount of steel freezing along the inner nozzle[95-97)].

Nozzle shape/geometry also plays a large roll reducing clogging. Improving the sealant between joints reduces the amount of air aspiration into the steel (thereby reducing clogging)[98]. Smoothing areas of high turbulence (including rounding the nozzle entrance, eliminating lower nozzle wells, and increasing the nozzle internal diameter below the nozzle entry) reduce the formation of turbulence and flow separation, thus minimizing clogging[77,81,99,100]. Insulation around the nozzle retains steel heat and reduces clog formation due to steel freezing near nozzle walls[81].

4.2.2 Inclusion Detection Methods

Zhang and Thomas have published a comprehensive analysis of inclusion detection methods, which will be the basis of this review[101]. Each technique discussed will be classified as either a direct or an indirect method.

4.2.2.1 Direct Methods

Direct inclusion detection methods are aptly termed due to their direct examination of entrapped inclusions. Such methods may not be appropriate for the continuous monitoring of cast product, as sample preparation typically requires sectioning or modification of the steel prior to analysis. Results generated via direct detection methods are very accurate, albeit at a high cost (whether it be time expenditure or analytical equipment price). Various techniques are briefly outlined in the following sections.

Inclusion Detection for Sectioned Samples

- Metallographic Microscope Observation (MMO) and Image Analysis allow for quantification of inclusion density (with 2-D precision) on the machined surfaces of sectioned steel samples[102].
- Scanning Electron Microscopy (SEM) yields near 3-D images of exogenous inclusions, however a great deal of sample preparation is required to obtain high quality images[103].
- Optical Emission Spectrometry with Pulse Discrimination Analysis (OES-PDA) uses visible wavelengths of high-temperature materials to discern inclusions from the steel via high-intensity spark peaks[104-108]. A similar PDA index approach can be used as an

indirect method by observing the presence/frequency of spark peaks associated with inclusions flowing near the liquid steel surface during casting[108].

Composition Analysis for Sectioned Samples

- Electron Dispersive Spectroscopy (EDS) generates inclusion compositions at discrete locations along SEM-prepared samples. The EDS process begins by directing electron beams towards the sample region. Elemental atoms at the beam impingement location become excited and emit electrons at characteristic frequencies/energies. Observing the properties of emitted electrons allows for the general composition at the beam focus to be determined.
- Auger Electron Spectroscopy (AES) employs similar methodology to EDS by using electron beams to determine composition near flat surfaces of steel samples[109], however the electron penetration depth is limited to about one third as deep as EDS[110].
- X-Ray Photoelectron Spectroscopy is useful in plotting the chemical state of atoms on the specimen surface, however its resolution is limited to test areas larger than 10 nanometers[109].

Inclusion Detection via Specimen Destruction

- Slime Electrolysis uses the dissolving characteristics of strong acids (typically HCl) coupled with electric current to liquefy solid steel samples[108,111]. Steel portions of the sample are dissolved while exogenous inclusions (including FeO) remain solidified. Once completely dissolved, the solid inclusions can be collected and analyzed. Unfortunately, the original inclusion location within the specimen cannot be determined.
- The difference in density of inclusions and steel can be exploited through melting of the specimen. Inclusions (which are typically less dense than steel) “float” to the top of the liquid pool and can be segregated from the steel post-cooling. Examples of processes involving specimen melting include Electron Beam (EB) melting, Cold Crucible (CC) melting, and Fractional Thermal Decomposition (FTD) methods[105,108,112].

4.2.2.2 Indirect Methods

Unlike direct methods, indirect detection methods are typically quick and inexpensive to perform. Most indirect analysis methods involve no modification of the slab/ingot. This non-intrusive nature indicates they are well suited for real-time quality control of cast product. In fact, techniques involving indirect detection methods are frequently used to monitor steel cleanliness in industry[113)].

Pre-Solidification Indirect Methods

- Confocal Scanning Laser Microscopes observe the behavior of individual inclusions at the molten steel surface[114)]. While on-line, this method can be used to actively monitor inclusion size and concentration, however only at exposed liquid surfaces.
- Ultrasonic Techniques for Liquid Systems measures ultrasound pulses and reflections due to inclusions near the liquid surface.

Post-Casting Indirect Methods

- Conventional Ultrasonic Scanning (CUS) involves projecting ultrasonic frequencies through solid 3-D samples. The number of inclusions and other defects (including porosity) larger than 20 nanometers are quantified by measuring disturbances in the projected waves[105)]. However, work covered later in this chapter suggests that ultrasonic methods may only be accurate in discovering inclusions larger than 1 mm in size.
- The Mannesmann Inclusion Detection by Analysis Surfboard method requires rolling the sample into sheets prior to testing[115)]. By effectively removing all porosity from the sample, ultrasonic methods more accurately detect sample inclusions. In cases where continuously cast steel is flattened to produce thin rolls, this methodology requires no any additional sample modification prior to analysis (hence it is considered an indirect method).
- Scanning Acoustic Microscope (SAM) technology also uses ultrasonic frequencies to detect impurities, however its use of a spiraling detector allows uninterrupted inclusion analysis of continuous cast products[116)].

4.2 Experimental Methods

4.3.1 Sample Preparation

Steel Samples

Beginning with the cast ingot and solidified runner sections, rough machining discretized the specimen into manageable sizes (cubic samples with sides approximately 25.4 mm). The samples were first rough-sanded to remove the machining grooves, then underwent a series of preparations using incrementally finer abrasiveness. The progression of sanding is outlined (with grit numbers corresponding to the U.S. Industrial Mesh scale) as:

1. *80 Grit (200 μm) SiC Disc with water*
2. *120 Grit (125 μm) SiC Disc with water*
3. *240 Grit (52 μm) SiC Disc with water*
4. *400 Grit (22 μm) SiC Disc with water*
5. *800 Grit (10 μm) SiC Disc with water*
6. *Gold Label Cloth with 6 μm Polycrystalline Glycol Based Diamond Suspension*
7. *Vel-Cloth Cloth with 1 μm Polycrystalline Glycol Based Diamond Suspension*
8. *Chem-Pol Cloth with 0.2 μm Blue Colloidal Silica Suspension*

All steel samples were hand polished on standard 8" polishing machine. Each step required approximately 5 minutes of polishing time per sample. The samples were subsequently sonicated in an ethyl alcohol solution for approximately 10 minutes in effort to remove all dirt and polishing residue from the examination surface. Once sample preparation was concluded, each sample was left with a mirror finish suitable for SEM analysis.

Refractory preparation

Samples of the brick refractory lining the casting runners (Figure 4.2b) were also examined. Due to the brittleness of the refractory, the machining process performed on the steel samples could not be used. Rather, a 4" diamond wafering blade sectioned the refractory into 3 mm thick slices. Because the blade has abrasives on the flat surface as well as the leading edge, the blade polished the sample surface as it cut. Glycol-based cutting fluid assisted in washing away matter from the blade during operation. A standard 4-6" trim saw was employed for refractory preparation.

4.3.2 Examination Procedure

Steel Samples

With the steel samples fully polished, the first step to macro-inclusion observation was visual examination of the surface. Inclusions of interest (> 20 μm) were easily visible to the naked eye. Once identified, optical microscope photos were taken of the inclusion to document its shape, relative size, and location in the samples. Then, the detailed morphology and composition of each inclusion was analyzed by Scanning Electron Microscope (SEM) using Energy Dispersive X-Ray Analysis (EDX). 3-D SEM photos of the inclusions were taken, which aided in the characterization of each. The composition analysis gave rise to the origin of the inclusions, and also gave insight to whether inclusion agglomeration (or other methods of inclusion growth) netted the macro-scale size observed for each inclusion.

Refractory Samples

The main purpose of examining the refractory samples was to determine its composition near the steel front. Because there were no "inclusions" to study in the refractory, no visual examination or SEM analysis was performed. Had they been generated for the refractory, SEM images would have produced useless results; the lining is composed almost entirely of non-conducting material, which builds up charge under the electron gun rather than reflecting energized photons (yielding very bright, indiscernible regions within the images). Instead, the polished refractory was solely examined through EDX composition methodology. Chemical reactions between the steel and the refractory were studied via observation of composition change extending away from steel front into the refractory.

4.2 Casting Parameters

Ingot Casting Process

The following investigation is a case study of a bottom-teemed ingot cast at Ellwood Quality Steels Co. Steel flows from the ladle into the trumpet via slide gate with a free-open percentage of only about 50%. With such a low maximum open percentage, reoxidation becomes a large concern; high pressure differences near the gate encourage outside oxygen to be drawn into the steel. Historically, it was shown that similar lance-opening processes increased the total oxygen content in the tundish by 10 ppm (compared to free-opening)[117]. Slag from the ladle is prevented from entering the trumpet, as an operator provides visual observation to close the slide gate prior to slag entrainment.

Once through the slide gate, the steel enters a trumpet where it gets distributed to 7-8 channels via a "spider". Refractory bricks line the channels (with inner diameters of 50.8 mm), and each flow to independent ingot molds. 5 kg bags of slag are placed in the bottom of the ingots to provide a steady slag layer for the duration of the filling. Other casting procedures require suspending bags of slag slightly above the lower surface of the ingot, which limits the initial amount of slag entrainment during the first stages of filling[118]. However, suspending the bags also may expose the incoming steel to large amounts of reoxidation prior to the slag shrouding the upper steel surface.

The ingots in this study were round with 0.33 m diameter, 4.7 m height, and weighed 2.91 metric tons. Average filling rate cumulative for all ingots was approximately 1.4 ton/min (23 kg/s), thus each ingot received 0.2 ton/min (3.3 kg/s). The steel level of the ingots rose at approximately 4.87 mm/s, and the total filling time was 16 minutes. Once fully solidified, the ingot was sectioned to produce a total of 54 cubic (1 in^3) samples. The locations of the samples within the cast ingot can be identified in Figure 4.3. The runner leading to the examined ingot was also sectioned and prepared for analysis.

Casting Material Compositions

The ladle slag was mainly composed of CaO. Table 4.1 and Figure 4.4 describe the compositions of the mold flux and refractory bricks. Note that portions of the refractory contain high levels of SiO_2. As previously discussed, the presence of silica introduces oxygen into the liquid steel and is predicted to be a major source of reoxidation. The composition of the cast steel is displayed in Table 4.2.

4.3 Inclusion Analysis

During sample preparation, some inclusions may have been removed in the polishing process, leaving holes on the surface. Voids larger than 20 μm in size were therefore recorded and subsequently classified as either air-related (interdendritic porosity or entrapped bubbles) or likely locations for dislodged inclusions. In addition, a few common sulfide inclusions were documented (although the primary focus of this study is exogenous inclusions).

Prior to direct analysis, a Submerged Ultra Sonic Scanning routine was utilized in effort to discover large inclusions[119)]. This non-intrusive method detected only two non-metallic inclusions in forged bars produced from the cast ingot. One of these inclusions (which exceeded 20 mm in length even after forging) was uncovered and can be seen in Figure 4.5. Its molecular composition was consistent with that of the mold flux, giving rise to its origination. Because only two inclusions were discovered via ultrasonic scanning, it is apparent that only extremely large inclusions can be detected by this method (> 1 mm). Knowing that the cleanliness of steel is not characterized solely by the concentration of 1 mm (or larger) inclusions, a more rigorous method to classify inclusions was desired. For this, the ingot was sectioned, the samples polished, inclusion were viewed through optical microscope and SEM.

Figures 4.9a, 4.11a, 4.16a, and 4.17a compare optical microscope and SEM images of typical inclusions and holes. Notice the increase in detail between the two views; microscopic images give a basic view and location for areas of interest whereas SEM images reveal their true morphologies. In fact, while some microscope photos give the appearance of large inclusions, SEM images prove that they are rather holes on the examination surface, as in defects D34 (hole likely formed when an inclusion was polished away) and D35 (interdendritic porosity). Some inclusions appear to be a single large inclusion under microscope, however SEM detail proves it is an agglomeration of smaller inclusions (D1). Inclusion D26 resembles a large round inclusion under microscopic analysis, but in reality is it merely a hole left from an entrained bubble (with sulfide inclusions following the bubble's trajectory). While microscopic images are beneficial for *detecting* surface imperfections, they typically lack the detail necessary to *classify* the specific of defect. SEM imaging (coupled with EDS analysis) proved invaluable for characterizing the defects examined in this report.

4.3.1 Inclusion Distribution

Of the nearly 35,000 mm^2 surface area examine, 78 non-sulfide inclusions with a minimum size of 20 µm were examined. Information regarding inclusion distribution within the ingot is contained in Figures 4.6 and 4.7 (for visualization of sampling planes, refer to Figure 4.3).

An obvious trend was discovered regarding inclusion concentration versus height within the ingot (as seen in Figure 4.6). Most of the inclusions (47/78) were found of the lowest plane, with the remaining inclusions found on the center plane. Surprisingly, no inclusions 20 µm or larger were found on the upper plane. Note how the inclusion concentration is highest at the bottom and decreases as the distance from the bottom increases. This suggests that many of the inclusions entered the ingot near the completion of filling.

There is no overwhelming trend of inclusion distribution relative to trumpet direction (Figure 4.7), however the small number of inclusions sampled may not constitute a statistically significant population. Along the bottom plane, inclusions are most concentrated at a distances of 40 mm and 115 mm from the ingot center (Figure 4.7a). There may be a higher inclusion concentration along the ingot edge of the center plane, although the inclusions are more scattered (Figure 4.7b).

Inclusion size distributions for 2-D microscopic observations and the associated 3-D approximation are shown in Figure 4.8. Equation 4.1 was used to convert the 2-D data into 3-D estimations.

$$n_{3D} = \frac{n_{2D}}{d} \tag{4.1}$$

The main assumption of this conversion is that the observed 2-D diameter is the actual diameter of a complete *spherical* inclusion. In reality, the exposed diameter is likely much less than the complete inclusion diameter, resulting in the Equation 4.1 being quite underpredictive in estimating total inclusion percentage within the steel.

Not surprisingly, the exogenous inclusion count decreased exponentially for larger diameters. In total, the ingot is estimated to contain ~2.8 x 10^7 macro-scale inclusions per m^3 of steel, corresponding to 76.5 mg/10 kg_{steel} (assuming densities of 3000 kg/m^3 and 7800 m^3 for the inclusions and steel, respectively). Should every inclusions be composed of alumina (Al_2O_3), the inclusion mass fraction would be 7.64 ppm with the steel having an oxygen mass fraction of 3.67 ppm. These numbers only conservatively account for the actual inclusions distribution as inclusions and sulfide deposits smaller than 20 μm were not considered. In previous continuous casting investigations, it was found that about 85% of all inclusions were smaller than 20 μm in diameter[120]. Using this relation to predict the total inclusion concentration, inclusion mass fraction is predicted to be at least 51 ppm while the total oxygen mass fraction is conservatively estimated to be 24 ppm.

4.3.2 Observed Inclusion Types

4.3.2.1 Alumina Inclusions

Clusters of pure alumina (characteristically represented in Figure 4.9 and 4.10) and large lumps of pure alumina (Figure 4.11) accounted for the majority of the observed macro-scale inclusions. In fact, 46 of the 78 examined defects are this type (25 clusters, 21 lumps), and most were larger than 50 μm.

Pure Alumina Clusters

The alumina clusters were found to be composed of individual alumina inclusions with diameter of 1-5 μm. Due to the random cutting planes of the sample surfaces along with the polishing process, the defects were observed in a variety of states. Some observed inclusions included a central alumina nucleus mostly surrounded by steel (D1, D2, D5) and some clusters had steel trapped between individual inclusions (D3, D4, D6). In one case (D7), numerous alumina clusters were located in close proximity of each other; a large dendrite front likely trapped the inclusions as the steel solidified.

The probable mechanism yielding alumina cluster formation was either deoxidation product reaction or reoxidation from air absorption. It is highly unlikely that the *pure* alumina clusters arose solely from the erosion of the refractory material; the refractory composition included *many* elements (not just alumina). It also is unlikely that deoxidation products agglomerated and remained pure alumina clusters in the solidified steel, as the steel was refined under strict cleanliness regulation. During the teeming process, air shrouding was not used during ladle/trumpet transfer thereby introducing a large degree of oxygen absorption into the steel. Because the clusters of alumina did not exhibit dendritic structure, it is predicted that a considerable amount of time passed between the formation of dendritic alumina in the high oxygen environment until they were trapped by the solidifying steel front. This suggests teeming early in the casting process likely resulted in the formation of alumina clusters.

Alumina Clusters with Exogenous Inclusions

Many alumina inclusions were found to have combined with exogenous inclusions prior to solidification (Figure 4.10). It appears that motion of alumina clusters through the steel caused exogenous particles (ladle slag, mold flux, runner refractory, etc…) to agglomerate onto the defect. Nucleation of supersaturated steel compounds may also have facilitated cluster growth. A characteristic defect is seen in D8. Due to its large size (250 μm), composition analysis was performed at two locations. The composition at Location 1 is consistent with mold flux composition (indicative by the presence of K_2O and Na_2O), while pure alumina comprises the 50 μm offshoot at Location 2. High levels of Al_2O_3 and MgO (consistent with refractory composition) were found along the edges of inclusions D9 and D10, indicative that dislodged pieces of lining combined with these alumina clusters prior to ingot solidification.

Lump Alumina

21 lump-shaped alumina inclusions were observed on the samples (Figure 4.11). Some were simply raw lumps with characteristically smooth, rounded shapes (D11, D12, D13, and D14), while some were aggregations of needle-shaped alumina particles (D15 and D16). The large lump inclusions may have been caused by incomplete deoxidation product melting, although this explanation seems unlikely (due to the strong refining practice utilized). The needle-shaped alumina clusters indicates that slivers of alumina dendrites were formed very near to steel solidification, however the mechanism by which alumina inclusions form so close to ingot solidification is unknown. With such peculiar shapes, no explanation for lump alumina formation has been proposed at the time of this report.

4.3.2.2 Al_2O_3 – MgO Inclusions

A large percentage of the observed inclusions (17/78 or 21.8%) were composed primarily of Al_2O_3 and MgO. Characteristic inclusions are shown in Figure 4.12 (D17 and D18). Small Al_2O_3–MgO inclusions were also found agglomerated to the alumina inclusions of D9 and D10. Inclusion sizes range from 20 to 30 μm, with most having an irregular, lumpy shape. Note that the composition of the ladle well block refractory includes both compounds, although at different concentrations. Erosion of the ladle well block or clogs dislodging from the refractory surface typically releases inclusions into the ingot, while subsequent chemical transformation likely converted the released refractory into the observed compositions. Fujii, *et. al.* proposed a mechanism regarding Al_2O_3–MgO inclusion formation, which is summarized by the following chemical reactions[121)]. Note the content of MgO is higher than Al_2O_3 in this mechanism, consistent with the inclusion compositions (whereas the refractory composition was higher in Al_2O_3).

$$(MgO)_{lining} + C_{steel/lining} \Rightarrow [Mg] + CO \tag{4.2}$$

$$3[Mg] + (Al_2O_3)_{lining/inclusion} \Rightarrow 2[Al] + 3(MgO)_{inclusion} \tag{4.3}$$

$$4(Al_2O_3)_{inclusion/lining} + 3[Mg] \Rightarrow 3(MgO\text{-}Al_2O_3)_{inclusion} + 2[Al] \tag{4.4}$$

$$(Al_2O_3)_{inclusion/lining} + [Mg] + [O] \Rightarrow (MgO\text{-}Al_2O_3)_{inclusion} \tag{4.5}$$

$$(MgO)_{lining} + (Al_2O_3)_{inclusion} \Rightarrow (MgO\text{-}Al_2O_3)_{inclusion} \tag{4.6}$$

4.3.2.3 Exogenous Inclusions (propagating from ladle inner nozzle)

7 of the 78 observed inclusions had compositions (94-98% Al_2O_3 + 2-6% ZrO_2) nearly identical to that of the ladle inner nozzle (94% Al_2O_3 + 2.5% ZrO_2 + 1% SiO_2 + 2.5% other). With the only source of zirconium oxide in the entire casting process being at this location, it is reasonable to assume that these inclusions originated at the ladle inner nozzle. Figure 4.13 contains images of these defects. Note the large inclusion size observed for inclusions D21 and D22 (<100 μm). Predictions as to why these inclusions eroded from the nozzle include:

- Excessive fluid velocity through the nozzle
- High levels of steel superheat
- Long exposure time
- Chemical reactions at the interface between the steel and nozzle material

4.3.2.4 Potassium/Sodium Oxide Inclusions

6 of the 78 inclusions observed contained significant levels of potassium and sodium oxides (K_2O or Na_2O), two of which are shown in Figure 4.14. Note the large size of the shown inclusions (<< 100 μm). The most likely sources of these inclusions are the runner bricks or the mold flux, both of which contain the said oxides. Excessive fluid velocities typically cause runner lining erosion and mold flux entrainment.

4.3.2.6 Inclusion Rings (formed by Bubbles)

Air injection is typically employed to float out inclusions within the liquid steel pool. Buoyancy forces carry the bubble to the steel surface, thereby carrying the inclusions to the slag layer. Bubbles can also be inadvertently introduced to the liquid environment while pouring through air entrainment. In some cases (as seen on many samples), the bubbles fail to reach the slag surface; rather they become entrapped in the solidifying steel. The gas portion escapes either through reaction or absorption into the steel, leaving the inclusion shell. Molten steel fills the void inside the bubble left by the escaping gas and solidification around this shell preserves the inclusions in the ingot. In certain cases, inclusions were also found in the wake of the bubble's trajectory. The images of Figure 4.15 show examples of bubble-shaped inclusions. The ring inclusions observed were all larger than 50 μm, and all had MnS inclusions (most likely precipitated during solidification). Most of the smaller inclusions comprising the shell were either Al_2O_3 or MgO in composition (refer to Section 4.3.2.2 for methods regarding their formation).

4.3.2.6 Cavity and Hole Defects

Many of the samples observed contained cavities or holes on the examination surface. It is predicted that the majority these cavities formed as a result of inclusion dislodging during the polishing process. Because mechanical sanding was performed during sample preparation, the probability of the inclusions to being "pulled" out of the sample during polishing is relatively high, especially in the case where a large part of the inclusion is exposed. The existence of smaller non-ferrous fragments near the hole further suggests that inclusions once occupied the hole. An example of such defect can be seen in D34 of Figure 4.16a.

With their irregular shaped boundaries, the remaining holes examined are likely interdendritic cavities formed during the final stages of solidification. Called micro-porosity, gas precipitates due to supercritical concentrations and liquid feeding problems between the steel dendrites just prior to solidification (as a result of steel shrinkage). Numerous examples can be seen in Figure 4.16. Micro-porosity was more prevalent along the ingot center due to a higher concentration of solidification dendrites (with its enlarged mushy zone) and a reduced liquid feeding level. The greater severity of micro-porosity near the center of the ingot can be observed by comparing Figures D36 with D39 and D40. The mild micro-porosity of D36, with smaller size cavities, is located away from the center of the ingot near the outer wall. In contrast, defects D39 and D40 display severe interdendritic porosity near the ingot centerline, detrimentally affecting ingot properties due to their large size (>> 1000 μm).

A similar mechanism which promotes the formation of interdendritic gaseous cavities is also predicted to facilitates micro-segregation of S and Mn to form sulfides between the dendrites. Often, sulfides were observed near interdendritic micro-porosity. Defects D37, D38, and D42 contained MnS precipitation along the dendritic edges.

4.3.2.7 Silica-based Inclusions

Figure 4.17 displays one of the 2 silica-based inclusions examined. Both were of a typical spherical shape with diameters approximately 30 μm. The inclusion shown has a composition of 61.2% Al_2O_3 + 35.9% CaO + 2.8% SiO_2. It is known that the mold flux contained K_2O and Na_2O, and because these compounds were not found in the inclusions, it is unlikely that they originated from the mold flux. Rather, they likely originated from entrained ladle slag.

4.3.2.8 Sulfide Inclusions

Defects composed of Mn and S were not limited to areas around interdendritic micro-porosity cavities. Rather, sulfide defects were found throughout *many* samples. Examples can be seen in Defects D2, D4, D9-11, D14, D26-29, D32-33 D37-38, D42, and Figure 4.18. Sulfides usually precipitate near bubbles and interdendritic porosity, which may be due to supersaturation of Mn and S in the liquid steel around these gaseous regions. While the size of the individual sulfide regions is usually small (<10 μm), they typically form large clusters which can span areas larger than 100 μm).

4.3.3 Ingot Inclusion Conclusions

In total, 78 non-sulfide inclusions greater than 20 μm in diameter were examined and characterized. 59% of the macro-scale inclusions are composed solely of alumina, FeO, or a combination of the two. It is predicted that reoxidation facilitated the growth/formation of these inclusions. The most likely sources by which oxygen is introduced to the liquid steel are:

- Air exposure during teeming from the ladle to the trumpet
- Air exposure at the liquid steel top surface during filling

Inert gas shielding is highly recommended in these regions to prevent formation of reoxidation inclusions.

Predictions as to the origin of the remaining inclusions are: 22% from the ladle well block refractory, 9% from the ladle inner nozzle, 8% from the mold flux, and 2% from other slag inclusions. These results are outlined in Table 4.3. Note that these results omit inclusions polished away during sample preparation (as their compositions remain undefined). Erosion of the runner/trumpet bricks is unlikely to have produced any of the observed defects, as their composition did not match any of the inclusion compositions. In addition to the macro-scale inclusions observed, a large amount of smaller, pure sulfide (among other composition) inclusions were observed. Typically, these smaller inclusions were located near larger defects, or in some cases agglomerated to form the larger defects.

4.4 Runner Analysis

In addition to the ingot, sections of the solidified runner and the runner lining brick were prepared for investigation. The top of the solidified runner section had a flattened shape, most likely caused by steel shrinkage and gravity pulling down on the steel. In this region, a rather thick (~3 mm) black slag region was found (Figure 4.19). A small thickness of this reaction layer was also found on nearly all exposed refractory surfaces (~0.3 mm). This excess slag had a high degree of gas porosity, which may be indicative of gas entrapment within the runner.

Molten steel was found to have broken through the cracks of the refractory bricks, evident by elongated flat steel sections attached to the solidified runner (Figure 4.2a). The poor sealing characteristics of the lining construction is not expected to propagate into ingot defects, however; steel most likely sealed the cracks between bricks prior to any air reoxidation of the liquid pool.

4.4.1 Steel Runner Analysis

Samples of the steel runner sample were taken from three locations: near the upgate (sample R1), midway between the trumpet and the upgate (R2), and near the trumpet (R3, Figure 4.20). The round sections were cut into pie-shaped quadrants, and an analysis consistent with the ingot samples was performed to examine inclusions larger than 20 μm.

4.4.1.1 Inclusion Distribution

Each examination surface slice through the runner sample was assigned a quadrant. The total number of inclusions observed in each of these quadrants can be seen in Figure 4.20. For the most part, a random distribution of inclusions was observed near the runner ends, characteristic of complicated flow patterns in these areas. A more consistent trend was observed in the midway runner sample; a higher concentration of inclusions were found in the upper quadrants. Entrained inclusions will tend to migrate to the upper surface due to their lessened density. Fully-developed flow at the midway runner sample allows the buoyancy forces overcome inertial particle motion, thereby diverting the inclusions upward.

4.4.1.2 Extremely Large Defects

Two very large (> 7 mm) inclusions were discovered in the runner samples, one near the upgate (R1) and another near the runner midpoint (R2; both visible in Figure 4.20). The morphology of the R1 inclusion is outlined in Figure 4.21. Consistent with an inclusion of this size, the composition at different locations is quite different. Many needle-like protrusions of pure Al_2O_3 were found near the edges of the inclusion, surrounded by entrained runner slag (with a surface average composition of ~18% Al_2O_3, ~40% MnO, ~40% SiO_2, and other trace elements). It is predicted that the alumina oxide crystals agglomerated onto the inclusion while still liquid, and subsequently the entrained slag globules formed around these needle structures.

A much higher quantity of MnO-containing inclusions were found in the runner samples than the ingot samples; solidification occurs too quickly for MnO to form in the ingot steel (other than the center portion). Because the runner steel is the last to solidify, a sufficient amount of time is allowed for MnO to precipitate. Remember that the only source of Mn in the casting system is the mold flux.

A higher density of slag-related inclusions was seen in the center of the runner samples. Possessing a lower solidus temperature than steel, the slag remains in liquid globules while the surrounding steel solidifies. Heat transfer near the runner walls cause dendritic fronts to extend into the runner, “pushing” the slag globules to the center. It was observed that liquid slag deviated from their spherical shape and was forced into whatever space was remaining, whether it be interdendritic porosity or internal voids. This behavior can be observed at the inclusion boundaries of Figure 4.21. Notice how the entrained slag globules formed around the alumina needles. MnO was also found along many of the interdendritic porosity boundaries throughout the runner sample (Figure 4.22).

Finally, a large void (> 10 mm) was found at the center of the runner near the trumpet (R3; Figure 4.20). Most likely, solidification shrinkage is to blame as its formation mechanism. This hole is not a cause for concern, as shrinkage is readily anticipated in the runner and is not indicative of improper ingot solidification.

4.4.1.3 Deoxidation/Reoxidation Inclusions (including Al, Si, and Mn)

As with the ingot, many of the inclusions on the runner samples were found to be pure alumina clusters. It is predicted that the mechanism for the formation of Al_2O_3 inclusions must be either residual Al deoxidation products or reoxidation by air absorption. However, because the deoxidation process happens so early in the ingot-forming process (Step 2; Figure 4.1), it is unlikely that alumina particulate would remain entrained after reaching the runner section. As previously noted, the lack of argon shrouding during transfer from the ladle to the trumpet is predicted to introduce a high degree of air absorption into the steel pool. It is *much* more probable that reoxidation during the teeming process caused the formation of these alumina clusters. Al is the most easily reoxidized element of steel alloying elements, thus Al_2O_3 is predicted to form prior to the formation of silica oxide and manganese oxide. Only when the initial Al is depleted from the steel pool does FeO, MnO, and SiO_2 form[122]. Still, their formation is reduced by additional Al diffusing from the surrounding environment (refractory, mold slag, etc…). By this, alumina should have the highest inclusion concentration of all deoxidation products (which was observed in the samples).

Deoxidation inclusions were not limited to alumina; in fact, many MnO-based inclusions were also observed. MnO inclusions were never found in a pure state; a single compound (sulfide, for example) or a combination of deoxidation products (i.e. SiO_2) were also present in the inclusions. Example of inclusions with high MnO content located along the runner boundary can be seen in Figure 4.23. Higher amounts of SiO_2 were found in these such inclusion than the extremely large inclusion of Figure 4.21. In general, MnO-based inclusions did not seem to be manipulated to the center of the runner by the advancing dendrite front. Rather, they were more evenly distributed throughout the runner sample, indicating that either the inclusions were entrained late (due to a much slower formation mechanism) or they were captured by steel solidification already in the solid state.

4.4.2 Runner Lining Observations

Thin slices were made through the brick lining. Under visual analysis and EDX, three distinct regions were observed (from brick/steel interface inward):

1. Reaction Layer (runner slag) (0.3 – 3 mm)
2. Intermediate Layer (3 – 25 mm)
3. Original Brick

The compositions of each layer can be found in Table 4.4. Note the higher levels of Al_2O_3, MnO and lower concentrations of SiO_2 present in the reaction layer compared to the undisturbed brick (with easily identifiable concentration gradients through the intermediate layer). Both inclusion deposition and chemical reaction at the reaction layer are predicted to yield the observed gradient formation.

Inclusion Deposition Along the Runner Brick Surface

Air absorption upstream of the runner (especially during the teeming process) caused the formation of many reoxidation products. With inclusions found deposited throughout the runners and ingot, it is quite possible that many alumina and manganese oxide inclusions became trapped along the runner surface.

Chemical Reaction within the Reaction Layer

The fact that gradients extended into the intermediate layer (where inclusions could not possibly reach) indicates chemical transformation likely occurred within the reaction layer. Two reactions would produce such results, the first of which is:

$$SiO_2 + Al \rightarrow Al_2O_3 + Si \qquad (4.7)$$

The initially high SiO_2 composition of the undisturbed brick would be lessened through combination with free Al in the steel. With the Si atom being released into the steel, the reaction layer would contain increasing amounts of alumina while the SiO_2 concentration would dwindle (which was observed).

The second reaction would occur with free Mn in the steel reacting to exposed refractory silica according to:

$$SiO_2 + Mn \rightarrow MnO + Si \qquad (4.8)$$

This reaction is predicted to be the main source of MnO in the runner slag, however (as with the alumina inclusions) prior reoxidation may have generated the defects which subsequently became lodged in the runner. Because alumina forms prior to manganese oxide, Reaction 4.8 is predicted to occur only after the free Al is sufficiently depleted near the runner surface.

Gas Porosity within the Reaction Layer

As previously noted, a high degree of gas porosity was found in the black runner slag region of the refractory surface. While unconfirmed, it is predicted that CO bubbles were a product of the following reaction at this surface:

$$SiO_2 + C \rightarrow CO + Si \tag{4.9}$$

CO may also be produced in cases where MnO builds up within the reaction layer.

$$MnO + C \rightarrow CO + Mn \tag{4.10}$$

Because the refractory does not contain MnO as a primary ingredient, Reaction 4.10 is not as likely to occur as Reaction 4.9; however it is still allowable given the casting circumstances:

It was observed that the thickness of the slag layer was much higher at the top rather than the sides or bottom of the runner. At the end of casting, the pressure of the incoming steel was not sufficient to promote complete filling within the runner; gravitational forces drew the liquid steel to the bottom of the cylindrical region. A "flattened" top was observed in the solidified runner (as visualized in Sample R3 of Figure 4.20). With a gap at the top of the runner, the less-dense slag particles fill the void to form the reaction layer. Additionally, CO bubble production pulls attached particles to the top of the runner regardless if it is completely full of steel or not (thereby further increasing reaction layer thickness).

Erosion of the Runner Refractory Bricks

Due to chemical reactions at the refractory surface, the internal structure of the bricks may be compromised. It is very probable that pieces of refractory became dislodged and eroded into the liquid pool, depositing as inclusions in the steel ingot. Furthermore, products formed within the reaction layer may become liquefied due to the high temperature of the steel pool. In this case, they can easily be drawn into the steel pool and deposit as exogenous defects.

Recommendations

By examining the mechanisms by which inclusions are produced in the runner samples, a few general recommendations can be made. At the root of many undesirable reactions is silica (SiO_2).

The main source of this compound is the refractory bricks. By creating runner walls out of refractory composed primarily of Al_2O_3 or ZrO_2, the exogenous inclusion density in the steel is predicted to be substantially lower. More attention should be spent on selecting refractory bricks with acceptable compositions, porosity, bulk density, and adhesion strength in effort to produce highly clean ingots.

4.5 Summary

Macro-scale inclusions (> 20 μm) can be detrimental to cast ingot quality. In this report, a comprehensive investigation of such inclusions was performed on a bottom-teemed ingot and its associated runner. Plain carbon steel was being cast in this particular ingot. Ultrasonic detection methods were employed prior to this analysis, and resulted in the discovery of two rare, large inclusions (> 1 mm). Because exogenous inclusions *under* 1 mm can also detrimentally affect ingot quality, alternative methods are required to detect smaller inclusions. Using sectioned and polished samples, optical microscope observation and SEM analysis (including EDX composition analysis) were performed to quantify and characterize exposed inclusions. The composition, size distribution, entrapment locations, and sources of observed inclusions were collected and the data processed.

- The largest inclusion observed was greater than 20 mm and is predicted to originate from the ingot mold flux. This inclusion was found prior to this analysis via indirect inclusion detection methods (ultrasonic scanning).
- Two extremely large inclusions (> 7 mm) were found in the runner sample. Reoxidation with air, coupled with high-Mn steel and runner bricks high in silica content caused the agglomeration of these compound inclusions. Their primary composition included segregated regions of SiO_2, MnO, and Al_2O_3.
- From the 34,839 mm^2 of ingot surface examined, 78 macro-scale inclusions were observed. Extrapolation of this quantity to 3-D suggests ~2.8 x 10^7 macro-scale inclusions are located per mm^3 of ingot steel. As expected, the bigger the inclusion size, the lower their concentration is within the ingot.

- Inclusion population decreased with height up the ingot. 47 of the 78 inclusions were found on the lowest plane (280 mm from the ingot bottom), with inclusion population highest at 40 mm and 115 mm from the ingot center. The rest of the inclusions (31/78) were found scattered randomly along the ingot half-height plane.
- While the data set may not represent a statistically significant population, the distribution of inclusions within the ingot were found to be mostly random with respect to the trumpet side and height.
- 59% of the inclusions are predicted to originate via reoxidation with air. The most likely location for this reoxidation is where the ladle pours into the trumpet. No shrouding was utilized, resulting in the relative high amount of macro-scale alumina clusters and lumps among other reoxidation products.
- 31% of the inclusions observed are predicted to have originated at the refractory lining (runner bricks and ladle well block). Erosion is most likely responsible for releasing these inclusions into the steel pool.
- Ingot cleanliness can be greatly improved by two specific changes:
  - Shroud the teeming process with inert gas, thereby preventing unwanted reoxidation via air absorption of the steel.
  - Utilize high quality lining refractory lining bricks, void of silica.

Table 4.1: Composition of the slag and linings used throughout the ingot casting process

	Ladle Lining						**Nozzle Sand**	**Trumpet/Runner**		**Mold Slag**
	Wall	***Bottom***	***Well Block***	***Inner Nozzle***	***Slide Gates***	***Collector Nozzle***		***Brick***	***Filler***	
SiO_2	0-5	0.8	0.1	1	0.5	10-13	27.6	50.8	0.9	29-36
Al_2O_3	0-5	0.5	91.22	94		83-87	11.8	44.5	0.8	15-21
MgO	80-100	40.1	6.01	Trace	97		7.1	0.1	37.7	<2.0
CaO		57.6	2.51	Trace	1.8		0	0.1	55.6	1-5
Fe_2O_3	0.5	0.9	0.03		0.2	1-2	18.6	1	4.2	5-11
Na_2O			<0.02	0.2		<1		0.47		4-6
K_2O			<0.02	0.2		<1		0.47		<2.0
TiO_2			0.02			1-3		2.1		<1.5
ZrO_2				2.5			0			
Cr_2O_3							32.9			
MnO										<1.0
F										<0.5
C_{tot}	5-15						0.6			23-26

Table 4.2: Composition of the cast ingot steel

0.220 % C	0.260 % Si	0.020 % Mo	0.000 % N
1.010 % Mn	0.110 % Cr	0.000 % Ti	0.000 % Nb
0.014 % S	0.090 % Ni	0.029 % Al	0.000 % Sn
0.011 % P	0.170 % Cu	0.000 % V	0.000 % Co

Table 4.3: Predicted of macro-scale inclusion origins

Origin	Count	Percentage
Air Reoxidation (Alumina)	46	58.97%
Ladle Well Block Refractory	17	21.79%
Ladle Inner Nozzle Refractory	7	8.97%
Mold Flux	6	7.69%
Ladle Slag Inclusions	2	2.56%
Trumpet/Runner Refractory	0	0.00%

Table 4.4: EDX composition within each layer of the runner lining/slag

	Reaction Layer (runner slag)	Intermediate Layer	Original Brick	
			Location 1	*Location 2*
SiO_2	17.99%	27.11%	59.15%	52.49%
AL_2O_3	52.56%	68.63%	34.79%	45.04%
MnO	20.01%	1.15%	1.00%	0.00%
Na_2O	1.73%	1.46%	14.00%	0.66%
K_2O	1.22%	1.20%	1.69%	1.30%
TiO_2	1.72%	0.25%	2.25%	0.20%
Fe_2O_3	4.77%	0.20%	1.97%	0.31%

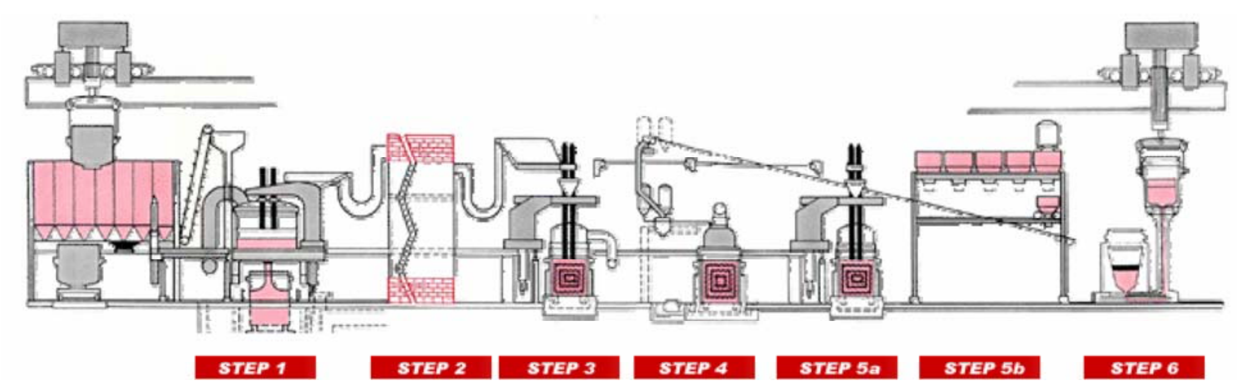

Figure 4.1: Schematic of the entire ingot casting process

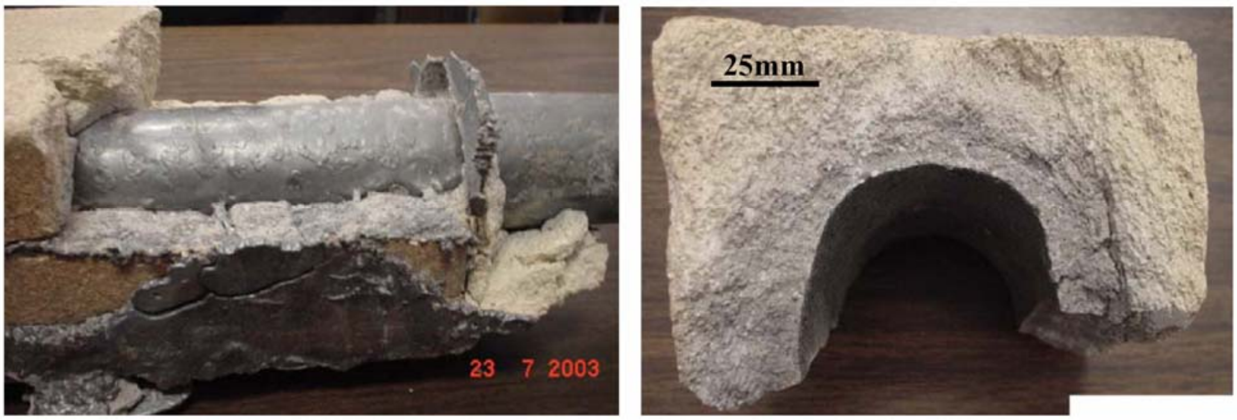

(a) **(b)**

Figure 4.2: Example of **(a)** casting runner and **(b)** brick refractory lining it

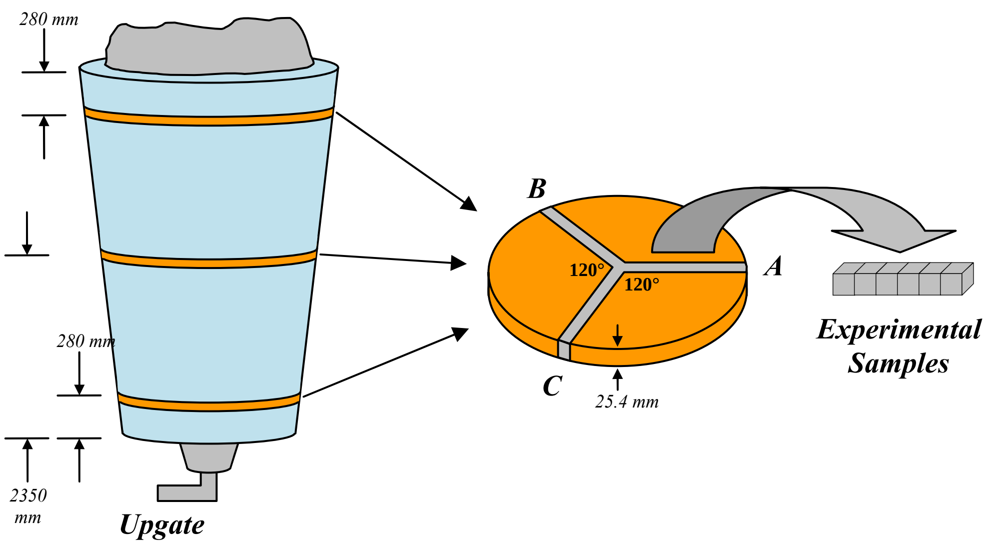

Figure 4.3: Cast ingot sampling locations (with "A" pointing away from the trumpet)

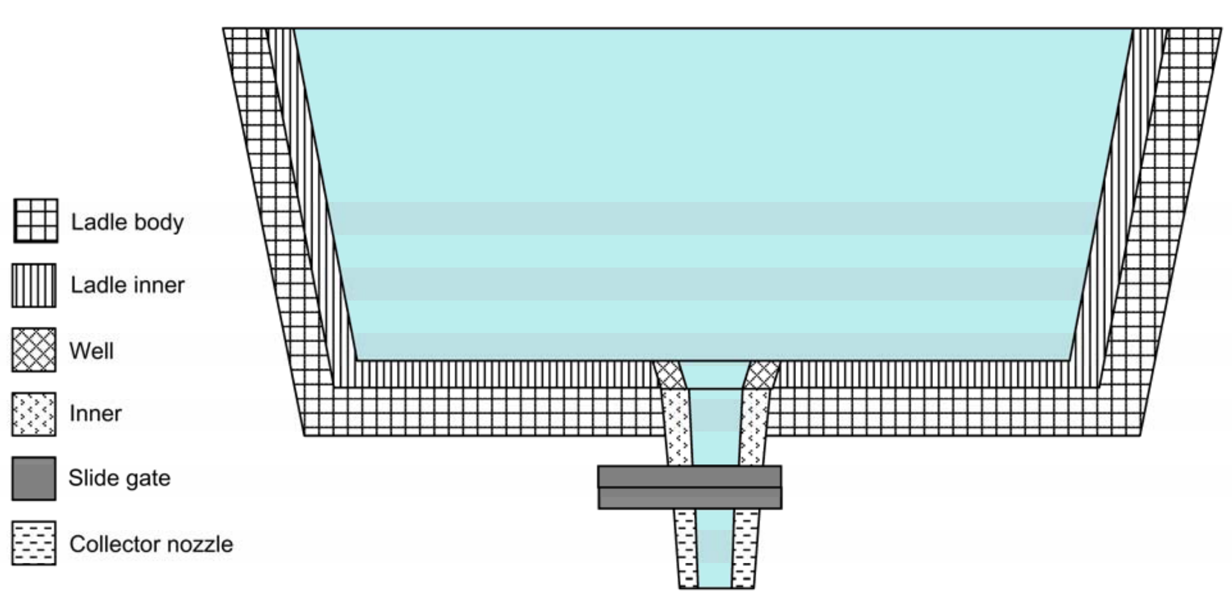

(a)

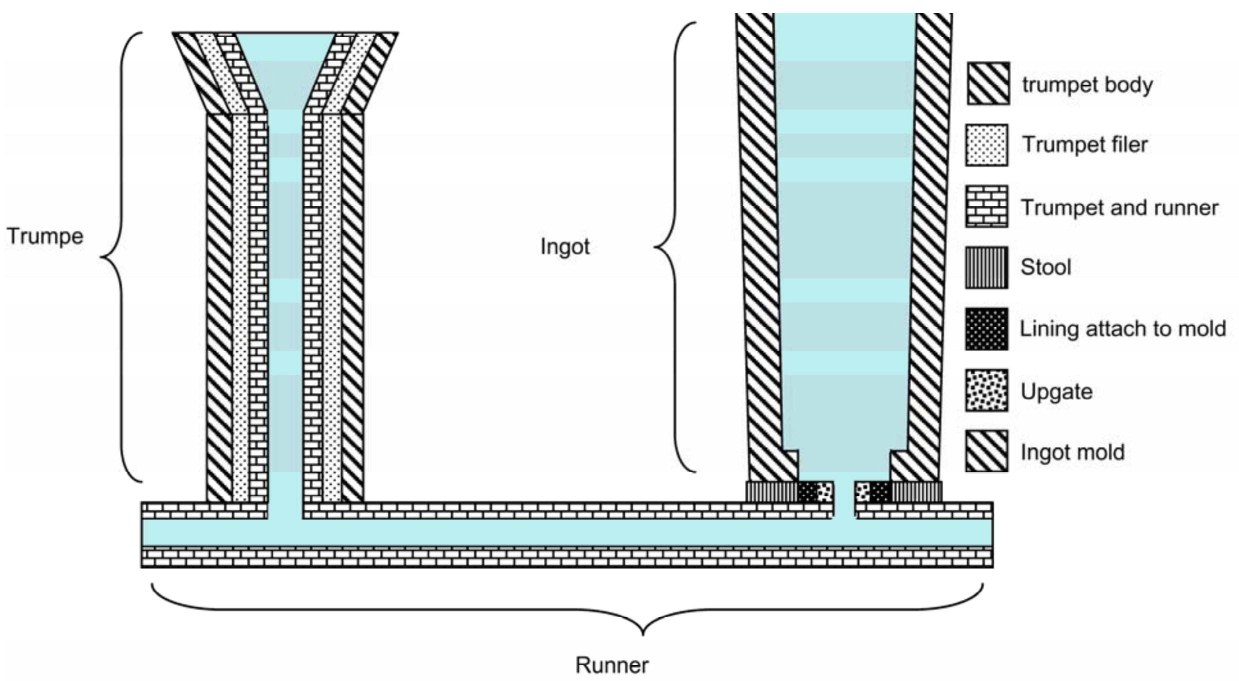

(b)

Figure 4.4: Schematic outlining the bottom teeming process, including both **(a)** the ladle lining materials and **(b)** trumpet, runner, and ingot mold materials

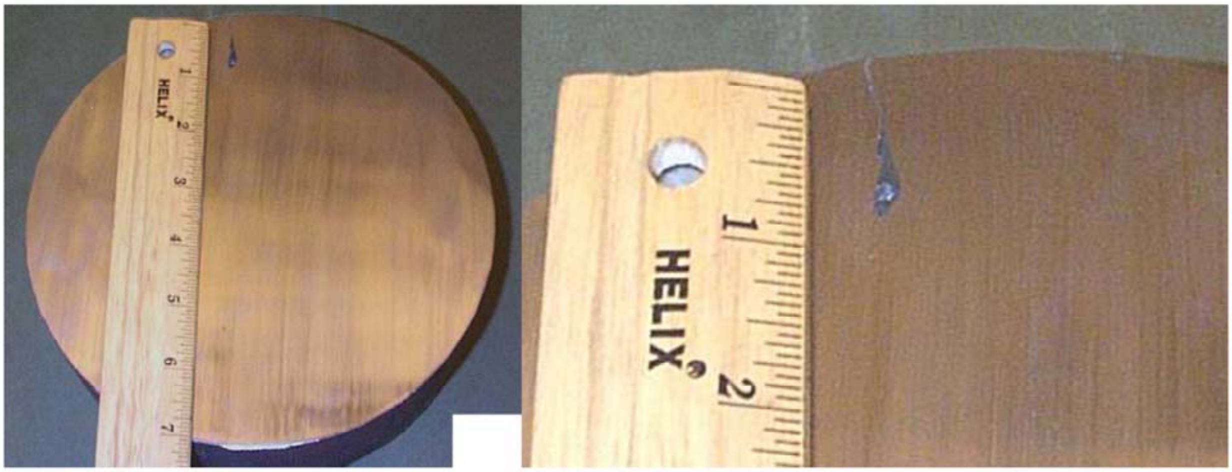

Figure 4.5: Large non-metallic inclusion entrapped in the forged ingot

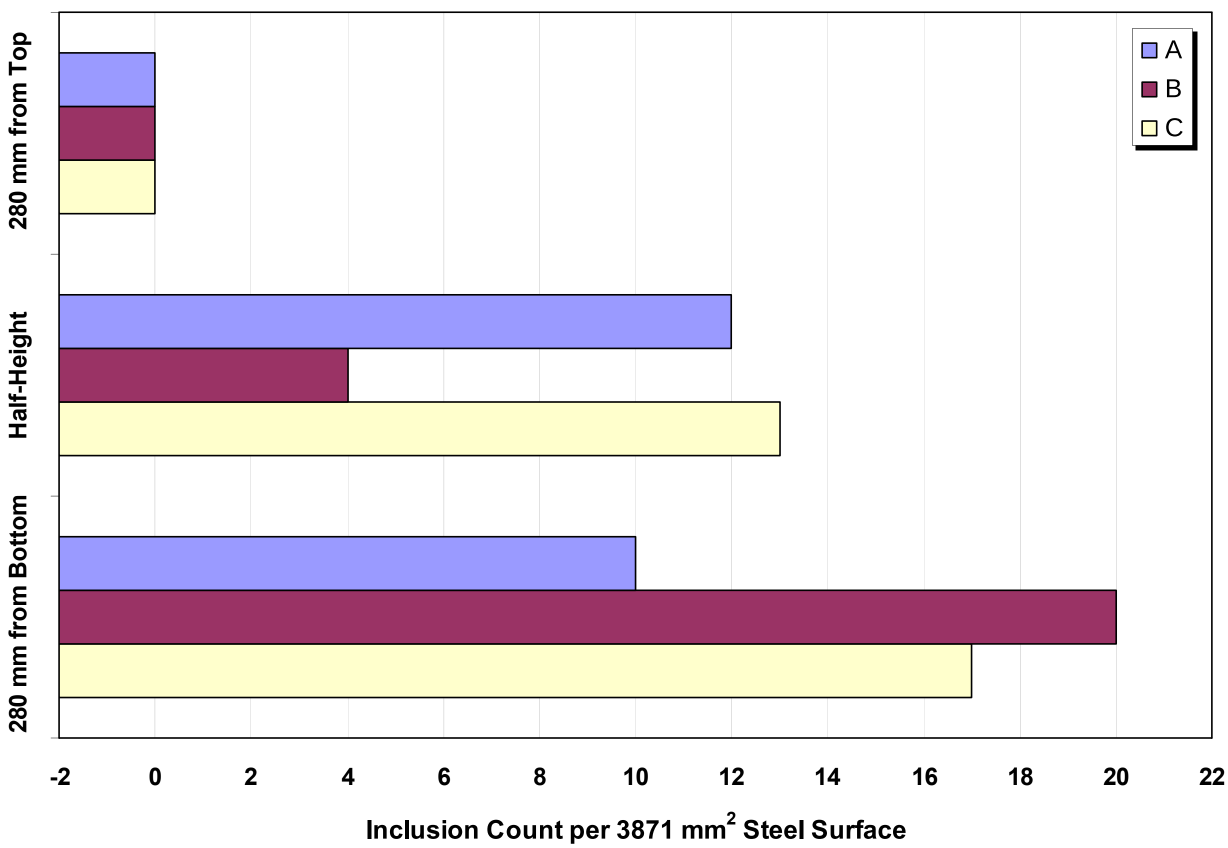

Figure 4.6: Macro-scale inclusions (> 20 μm) count throughout the ingot. "A" represents the ingot side opposite of the trumpet, while "B" and "C" are the two sides close to the trumpet

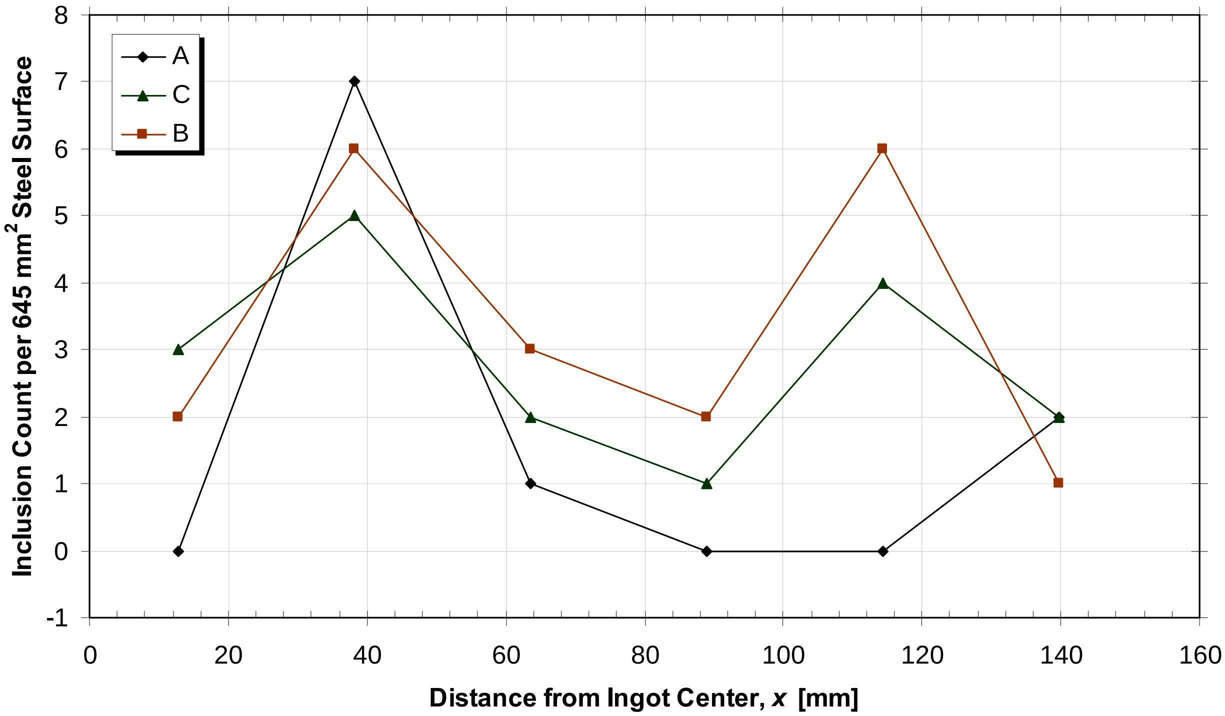

(a)

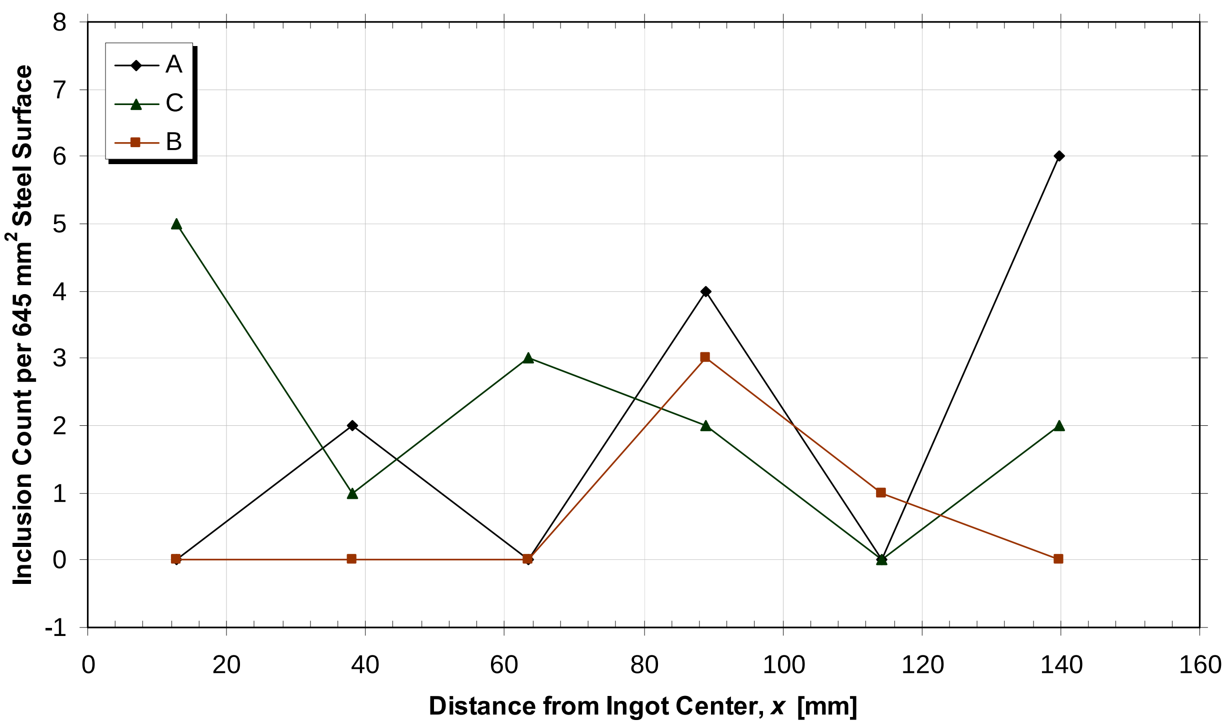

(b)

Figure 4.7: Macro-scale inclusions (> 20 µm) observed at **(a)** 280 mm from bottom and **(b)** 2350 mm from the bottom of the ingot (the ingot half-height)

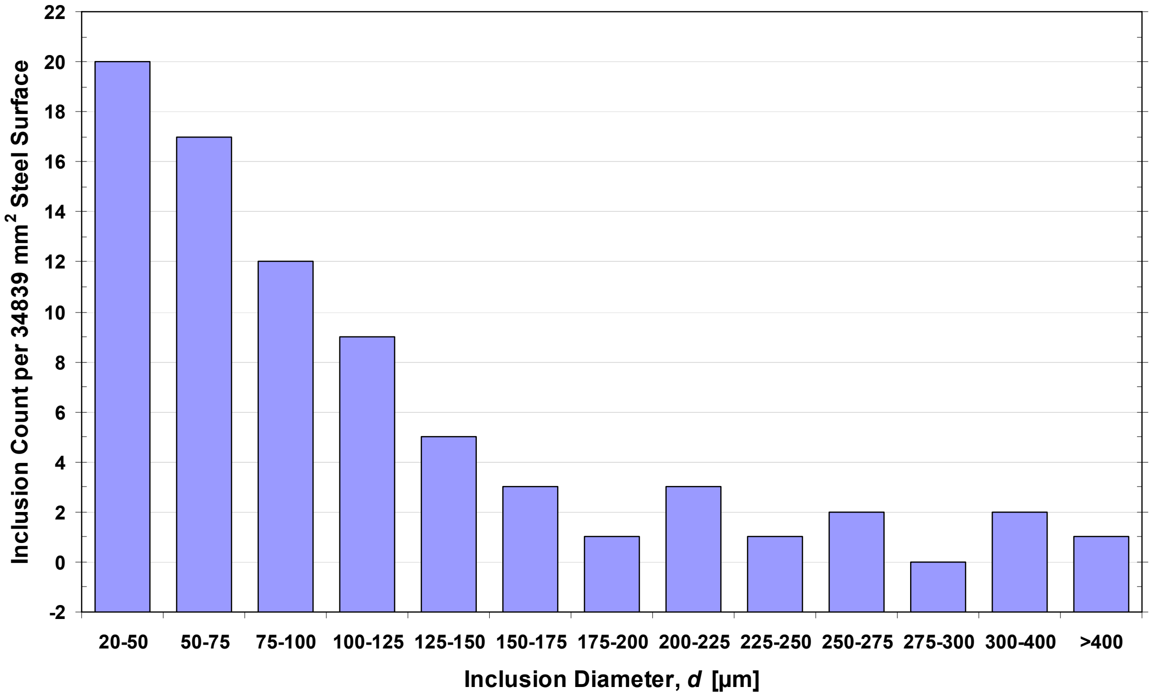

(a)

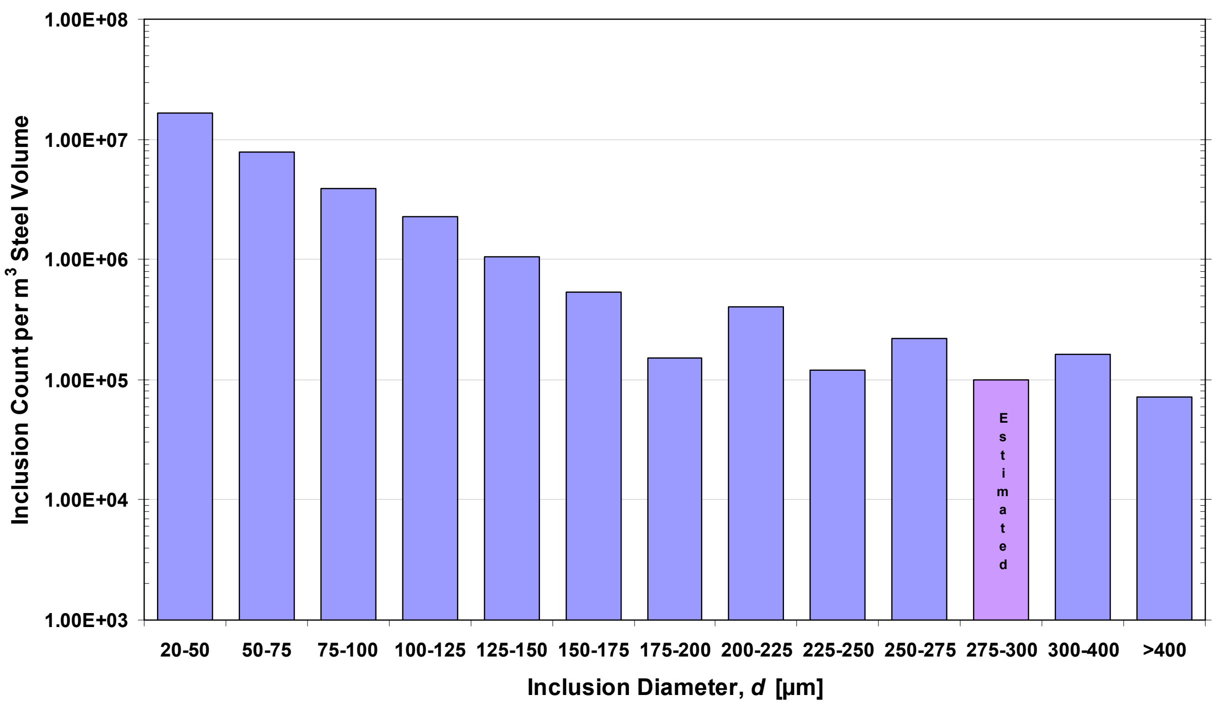

(b)

Figure 4.8: Inclusion size distribution for **(a)** microscopically observed 2-D surface and **(b)** estimated 3-D volume

2-D Microscopic Image ***3-D SEM Image*** ***Description***

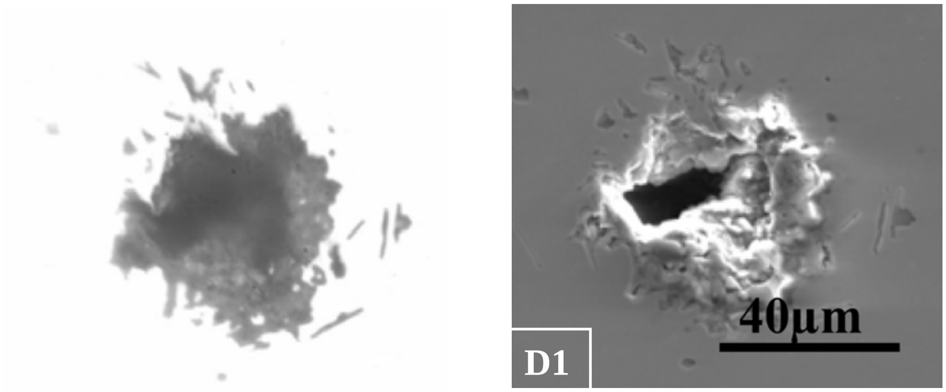

Pure Alumina Cluster; partially dislodged during polishing process; 50 µm Diameter

(a)

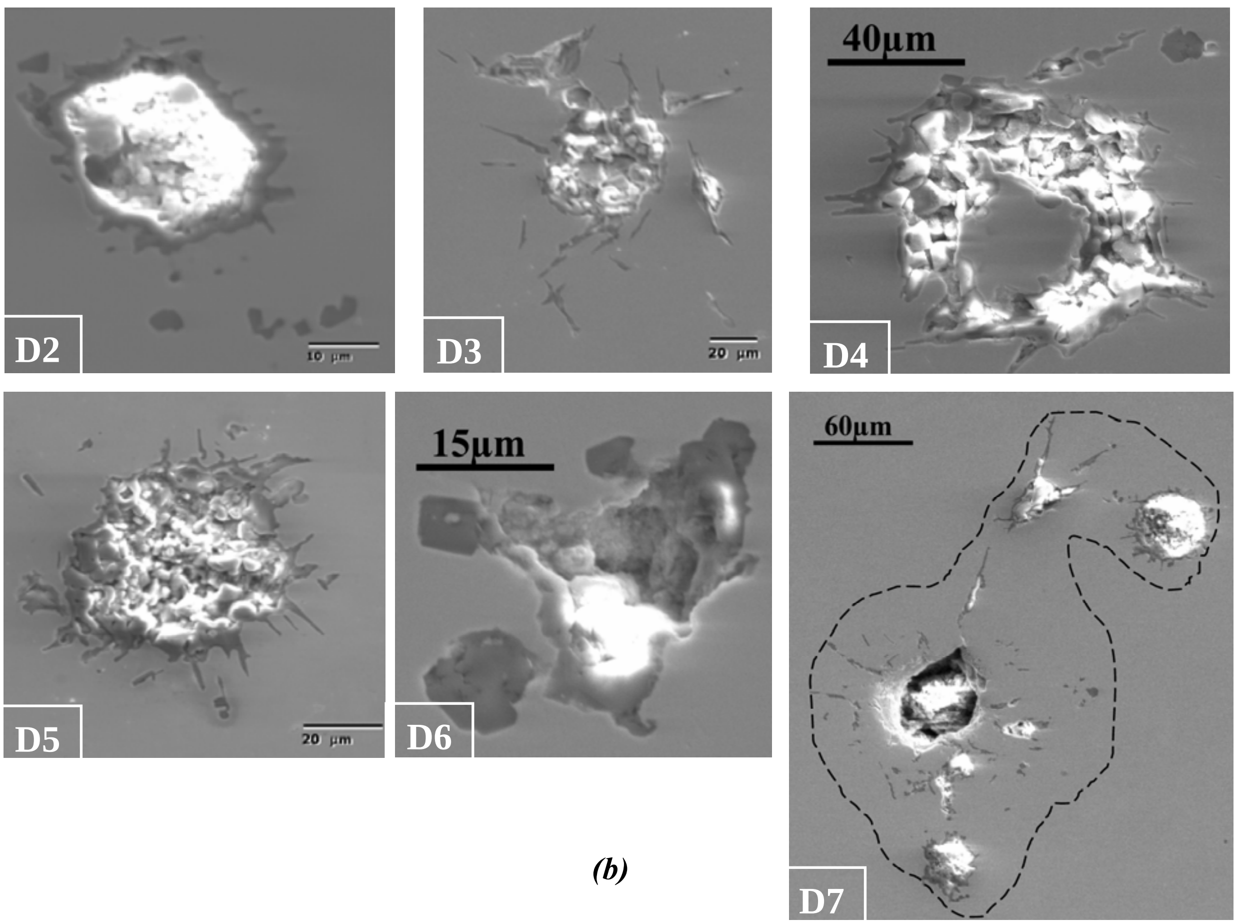

(b)

Figure 4.9: Morphology of observed Pure Alumina Clusters. Represented are **(a)** microscope/SEM comparison and **(b)** SEM images of characteristic inclusions

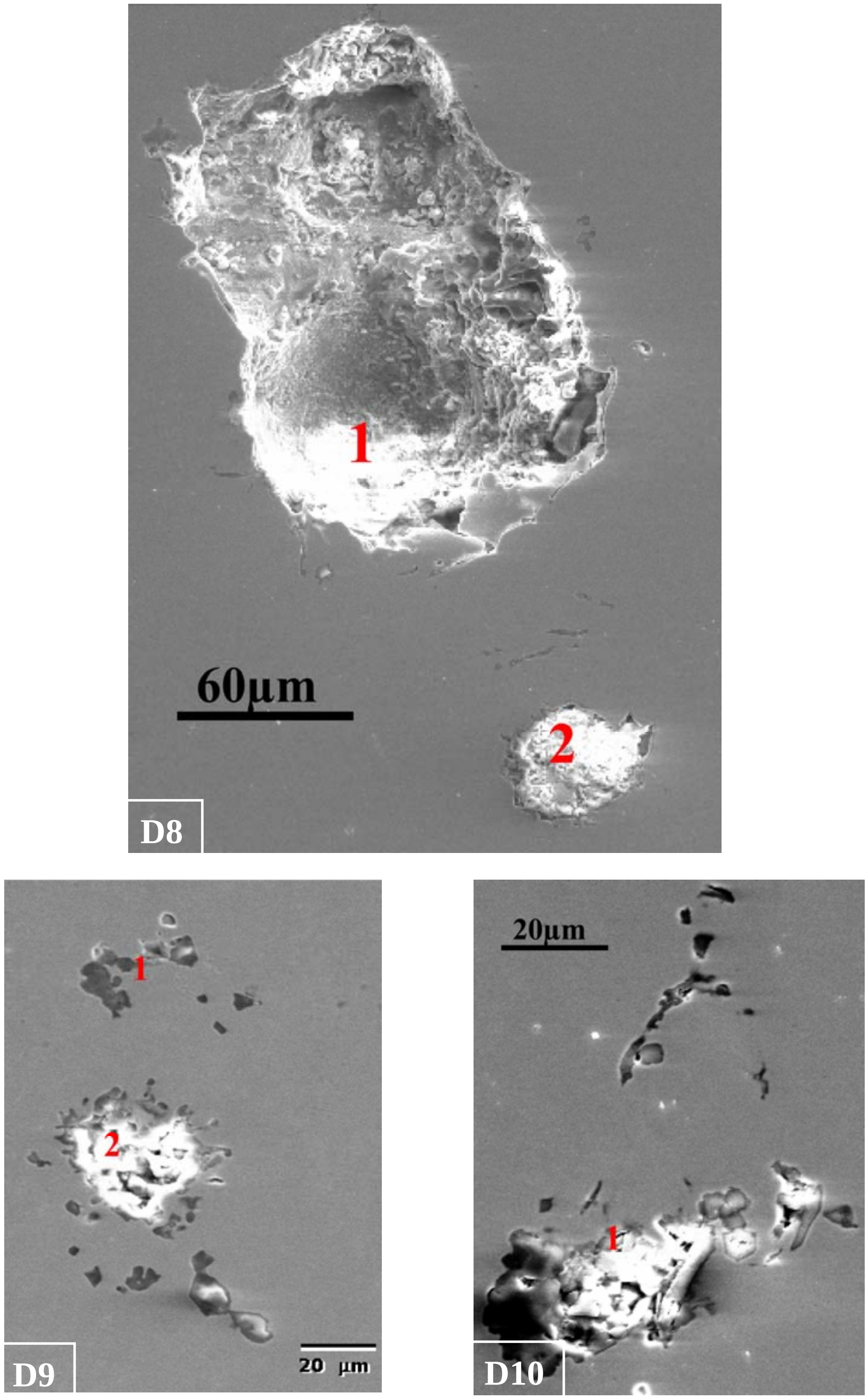

Figure 4.10: SEM morphology images of observed Pure Alumina Clusters affixed with exogenous inclusions

2-D Microscopic Image | ***3-D SEM Image*** | ***Description***

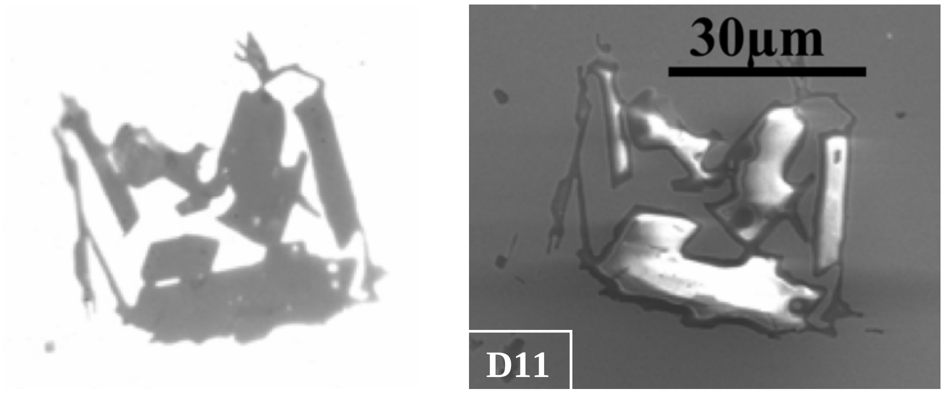

Pure Alumina Lump; 40 µm Diameter

(a)

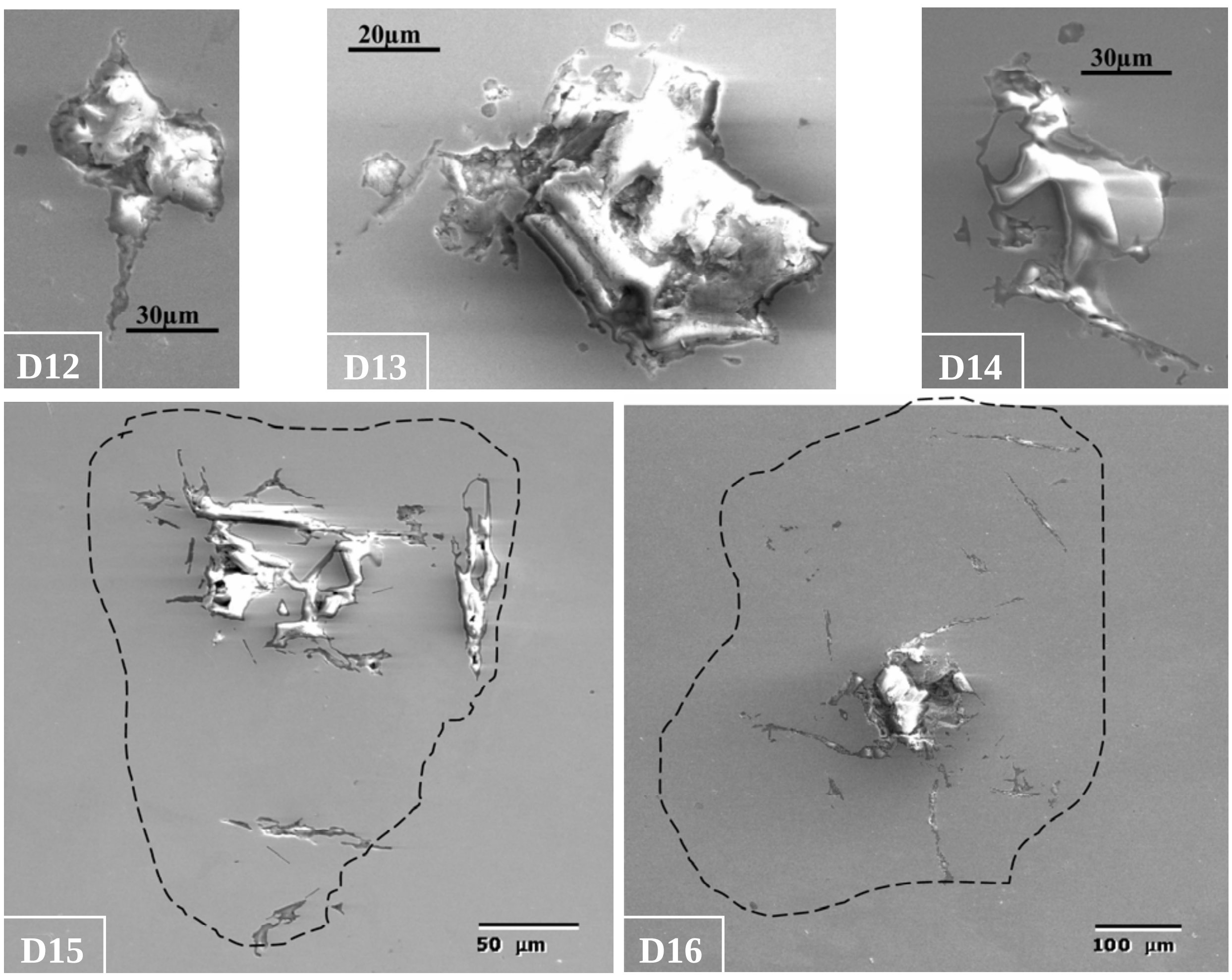

(b)

Figure 4.11: Morphology of observed Lump Alumina. Represented are **(a)** Microscope/SEM comparison and **(b)** SEM images of characteristic inclusions

3-D SEM Image | **Composition**

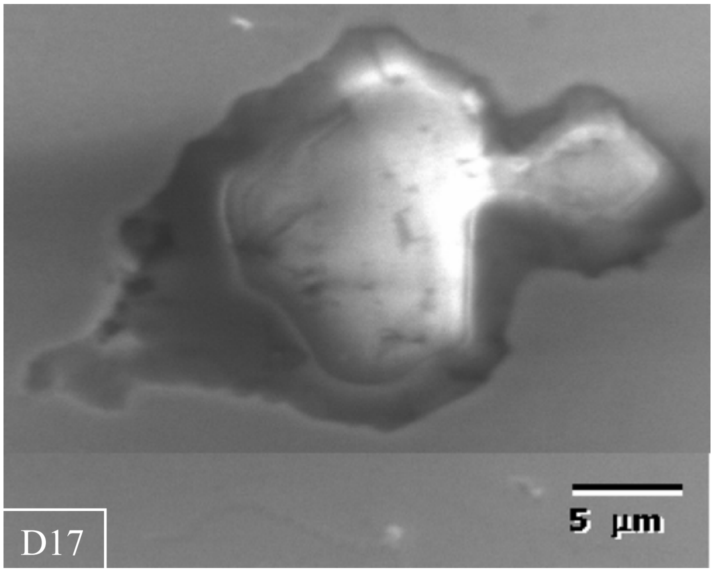

AL_2O_3 71.72%
MgO 23.56%
FeO 1.82%
MnO 2.90%

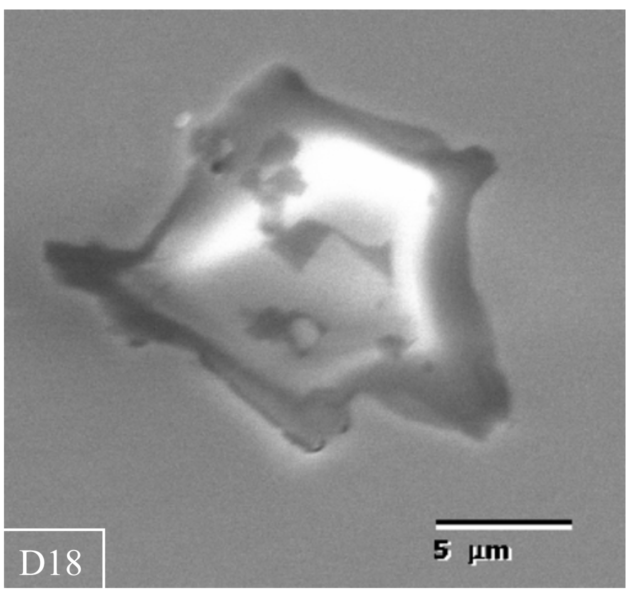

AL_2O_3 89.26%
MgO 10.74%
FeO 0.00%
MnO 0.00%

Figure 4.12: SEM morphology images of observed Al_2O_3 and MgO inclusions

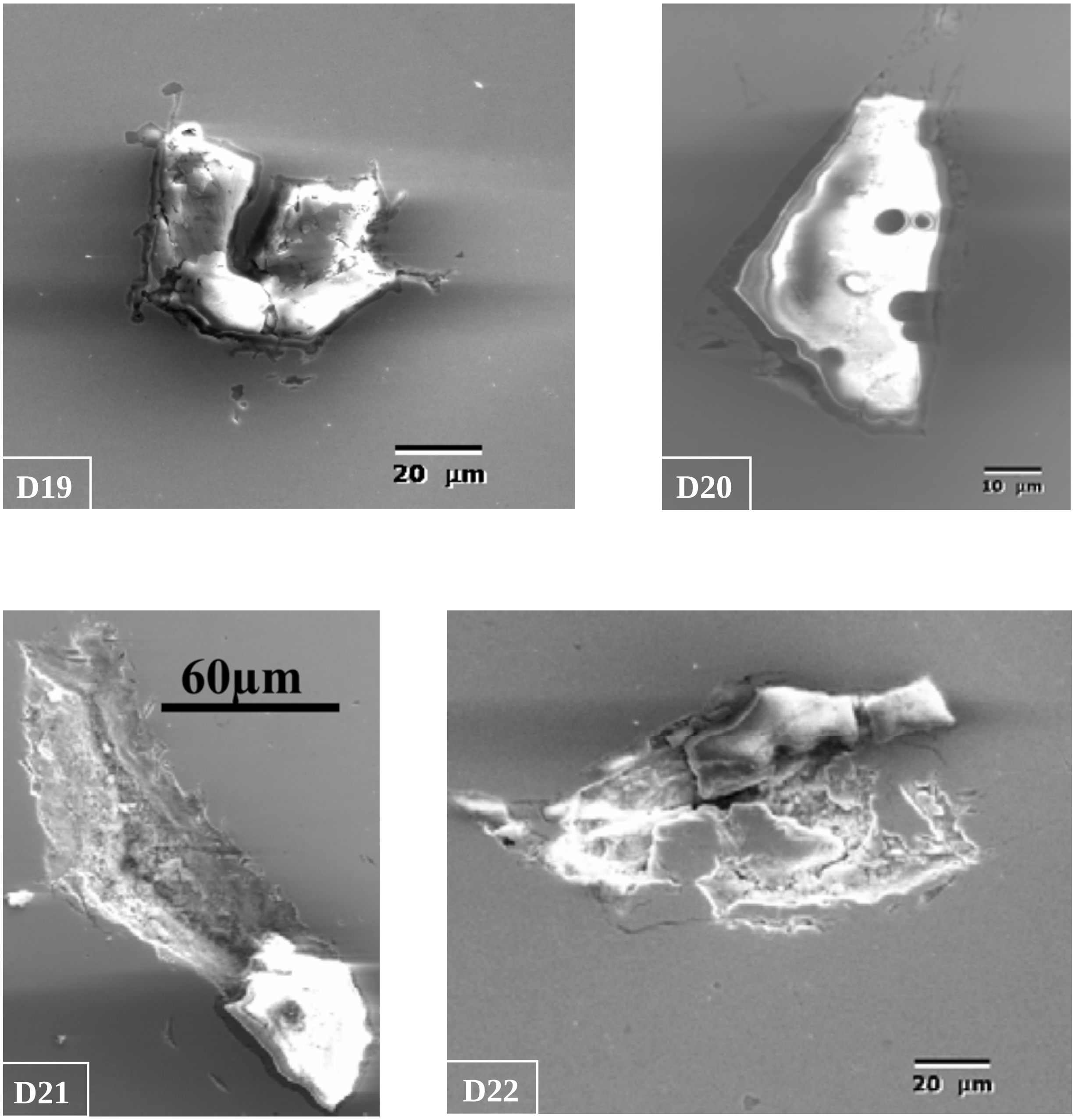

Figure 4.13: SEM morphology images of observed exogenous inclusions propagating from the ladle inner nozzle

3-D SEM Image ***Composition***

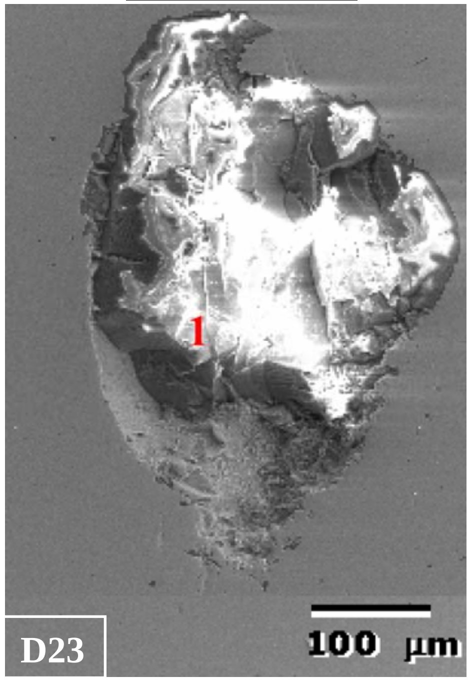

1	
SiO_2	47.02%
AL_2O_3	22.05%
MnO	11.95%
FeO	8.51%
Na_2O	5.07%
CaO	3.15%
MgO	1.88%
K_2O	1.52%

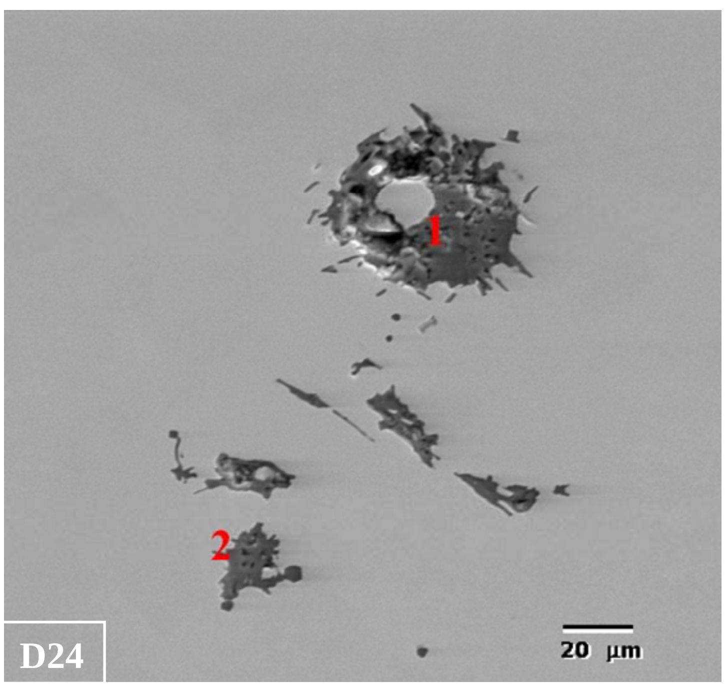

1	
AL_2O_3	83.22%
K_2O	10.26%
MgO	4.36%
CaO	2.16%
FeO	0.00%

2	
AL_2O_3	81.05%
K_2O	10.27%
FeO	4.03%
MgO	3.62%
CaO	1.04%

Figure 4.14: SEM morphology images of observed inclusions containing significant levels of K_2O or Na_2O

2-D Microscopic Image	3-D SEM Image	Description
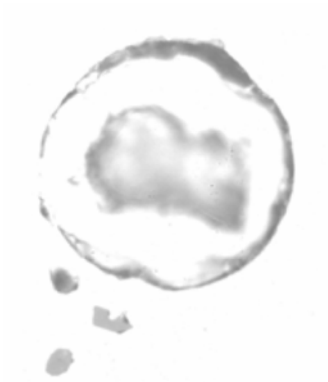	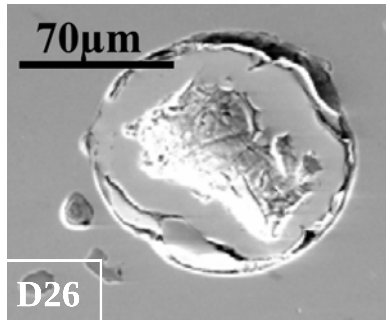	Inclusion Ring formed through bubble entrainment. Sulfide inclusions are found in the bubble wake (lower left of image)

(a)

3-D SEM Image	Composition	Description
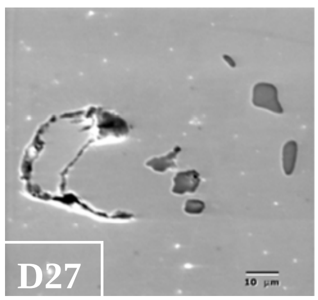	MnS 100%	Sulfide deposits; likely formed during solidification
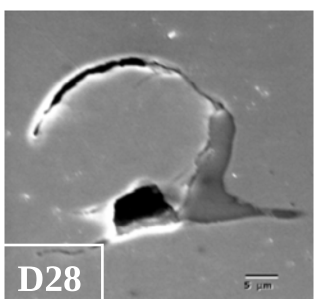	MnS 100%	Sulfide deposits; likely formed during solidification
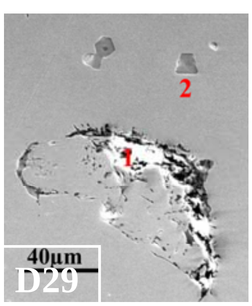	***1*** Al_2O_3 90.76% FeO 9.24% ***2*** MnS 100%	Reoxidation alumina cluster trapped by the bubble cap; sulfide precipitation during solidification

(b)

Figure 4.15: Morphology of observed inclusion rings (formed by bubbles). Represented are **(a)** Microscope/SEM comparison and **(b)** SEM images of characteristic inclusions

3-D SEM Image | ***Composition*** | ***Description***

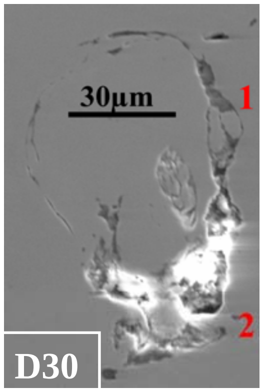

1	Al_2O_3	78.17%
	MgO	11.61%
	FeO	10.22%
2	Al_2O_3	76.23%
	MgO	15.61%
	FeO	8.16%

Alumina and ladle well refractory inclusion cluster along bubble boundary

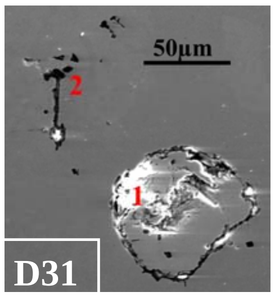

1	Al_2O_3	83.32%
	MgO	16.68%
2	Al_2O_3	83.88%
	CaO	7.29%
	MgO	5.97%
	FeO	2.85%

Alumina, ladle well refractory, and ladle flux inclusion cluster along bubble boundary

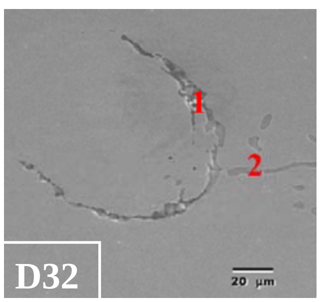

1	Al_2O_3	84.05%
	MgO	15.95%
2	MnS	100.00%

Alumina and ladle well refractory inclusion cluster along bobble boundary; sulfide precipitation during solidification

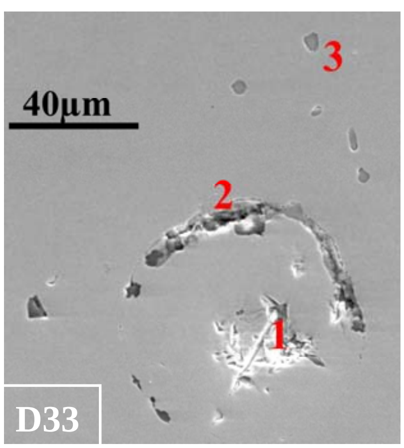

1	FeO	77.16%
	SiO_2	21.84%
	MnO	1.00%
2	FeO	48.20%
	MnO	18.75%
	MgO	15.52%
	MnS	15.42%
	CaO	1.51%
	SiO_2	0.60%
3	MnS	100.00%

Mold Flux and reoxidation inclusions along bubble surface; sulfide precipitation during solidification

(b)

Figure 4.15: (cont'd) Morphology of observed inclusion rings (formed by bubbles). Represented is **(b)** SEM images of characteristic inclusions

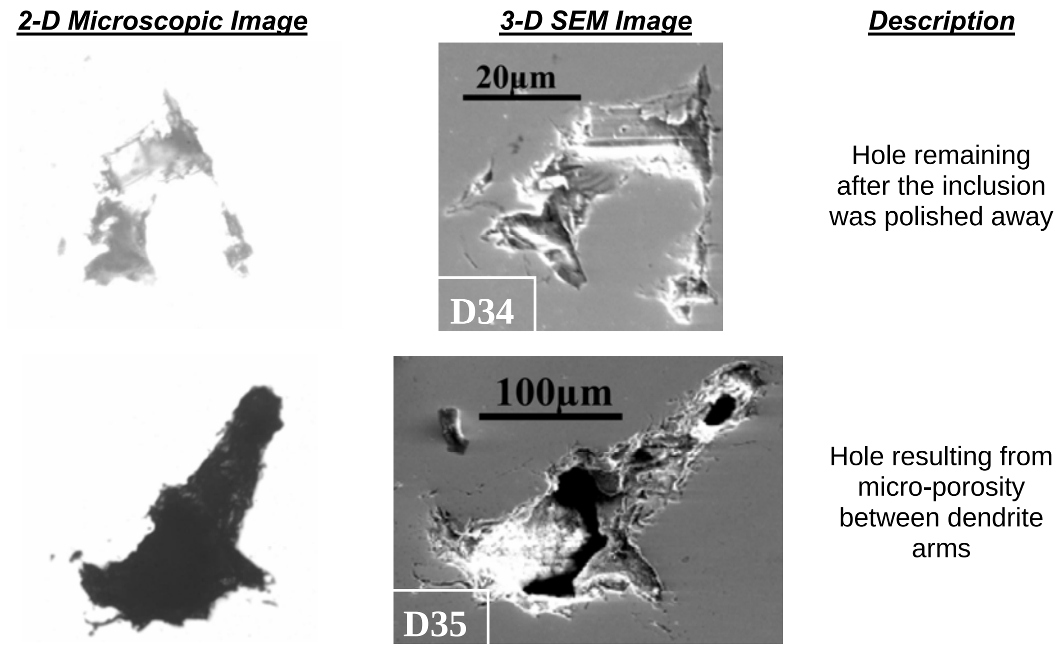

(a)

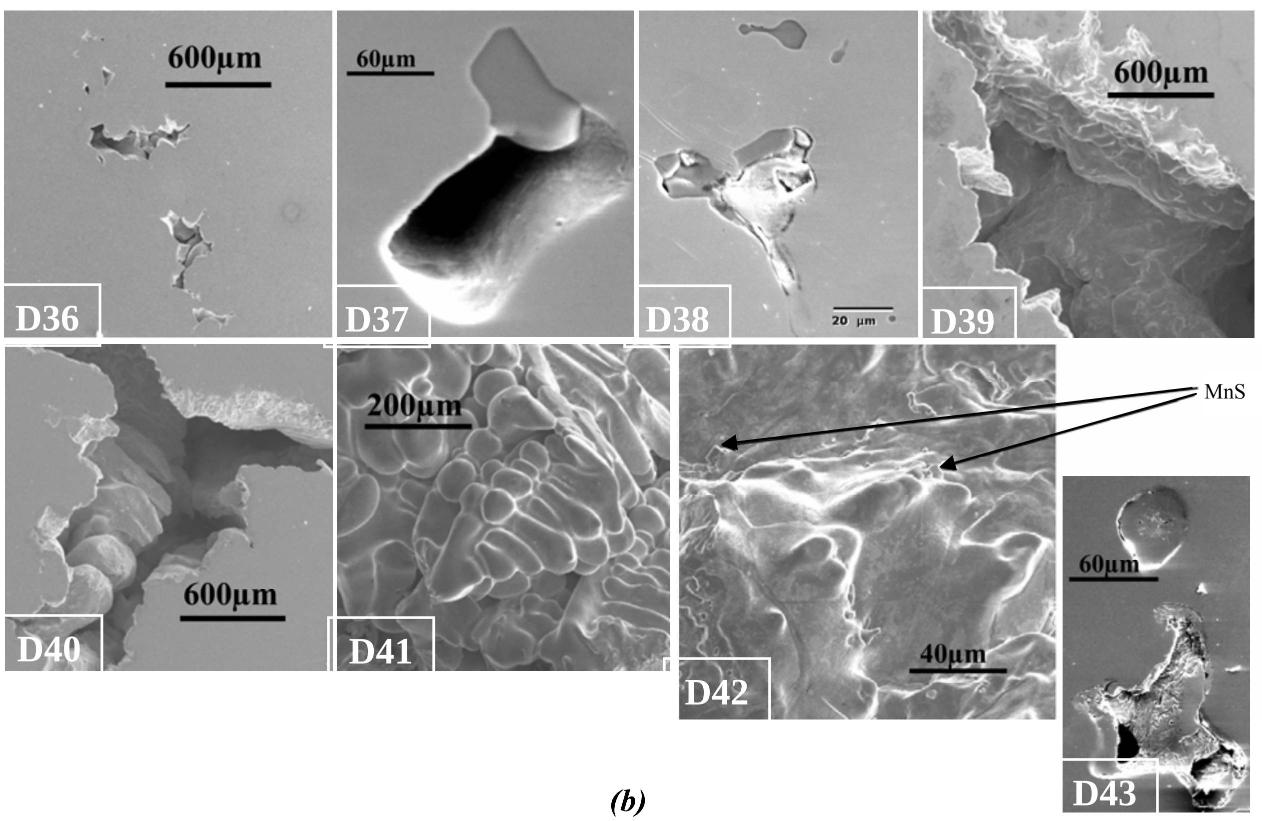

(b)

Figure 4.16: Morphology of cavities and holes found on the examination surfaces. Represented are **(a)** Microscope/SEM comparison and **(b)** SEM images of characteristic defects

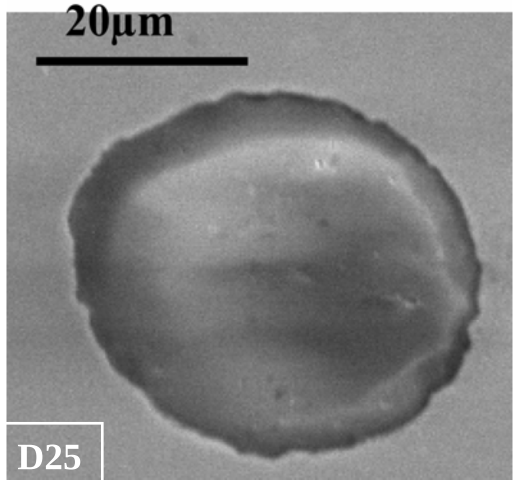

Figure 4.17: SEM morphology image of an observed silica-based inclusion

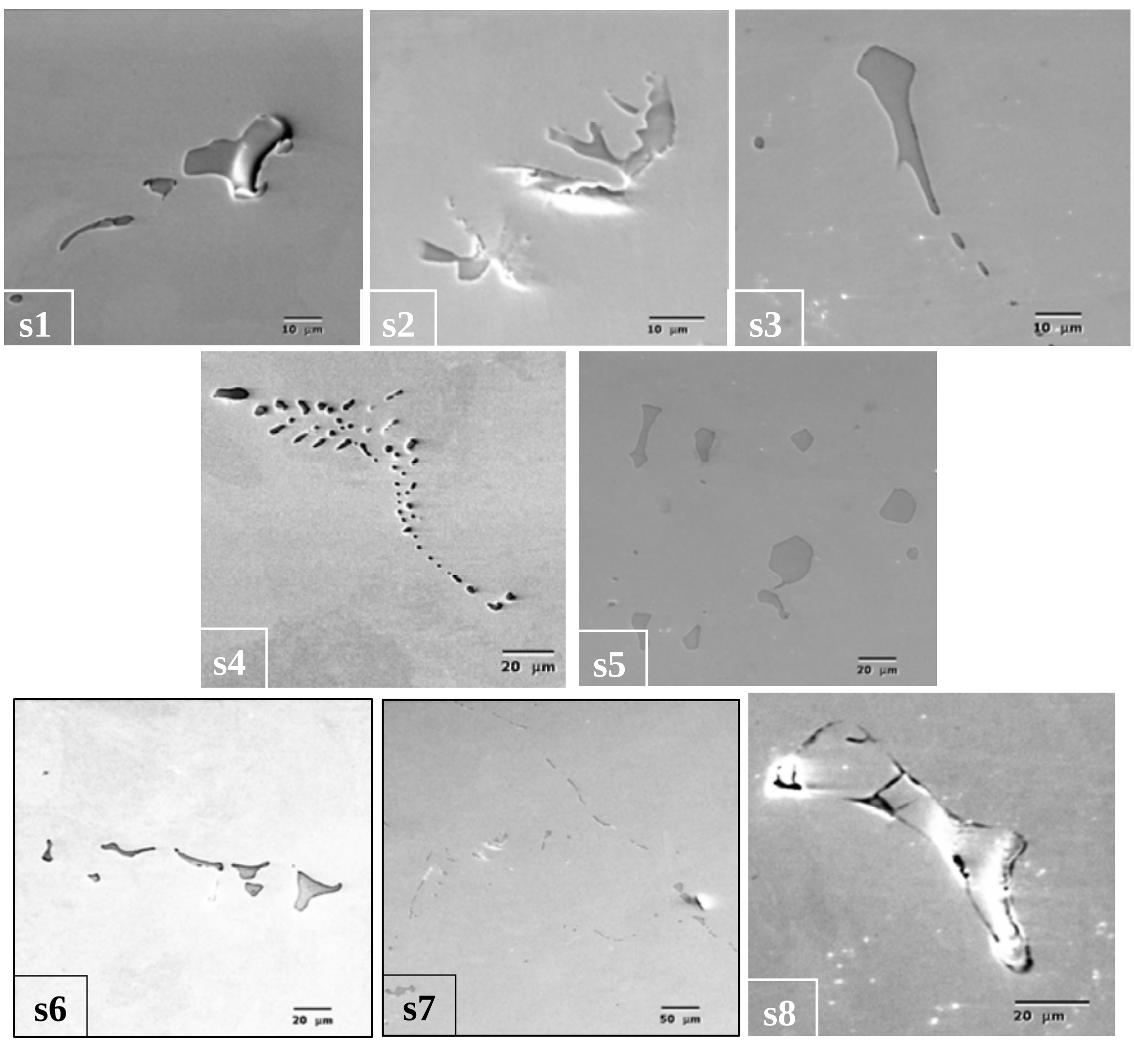

Figure 4.18: SEM morphology images of observed inclusions containing only sulfide

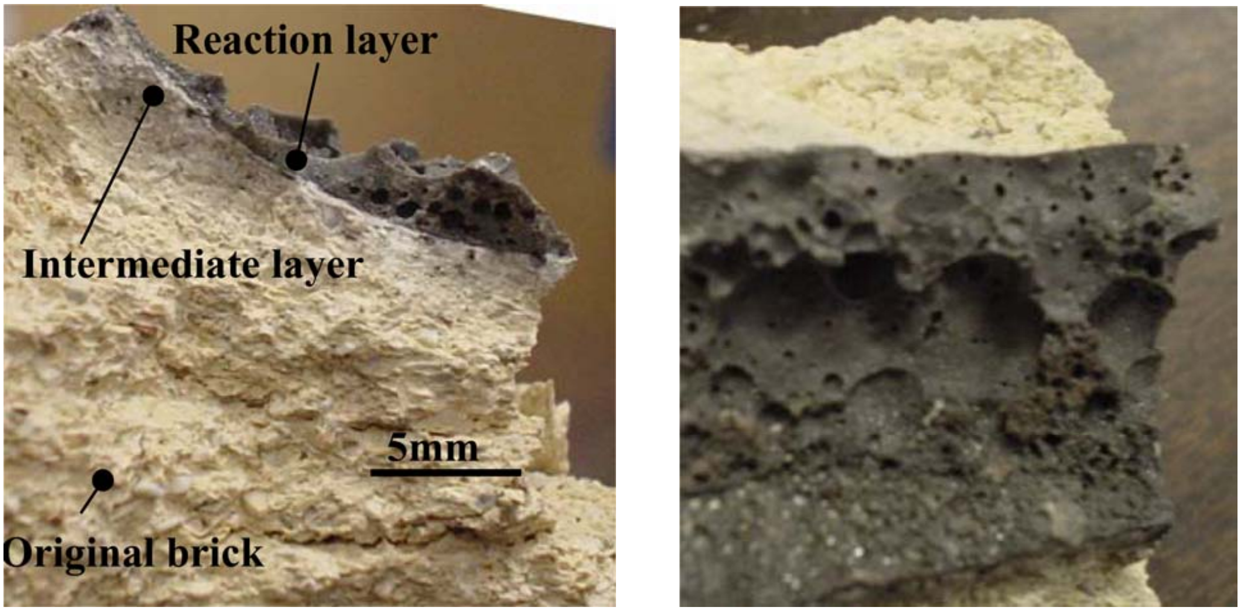

(a) *(b)*

Figure 4.19: Sample refractory lining the runner. Shown are **(a)** top view including three distinct brick zones and **(b)** enhanced side view showing the runner slag (along the steel-brick contact face)

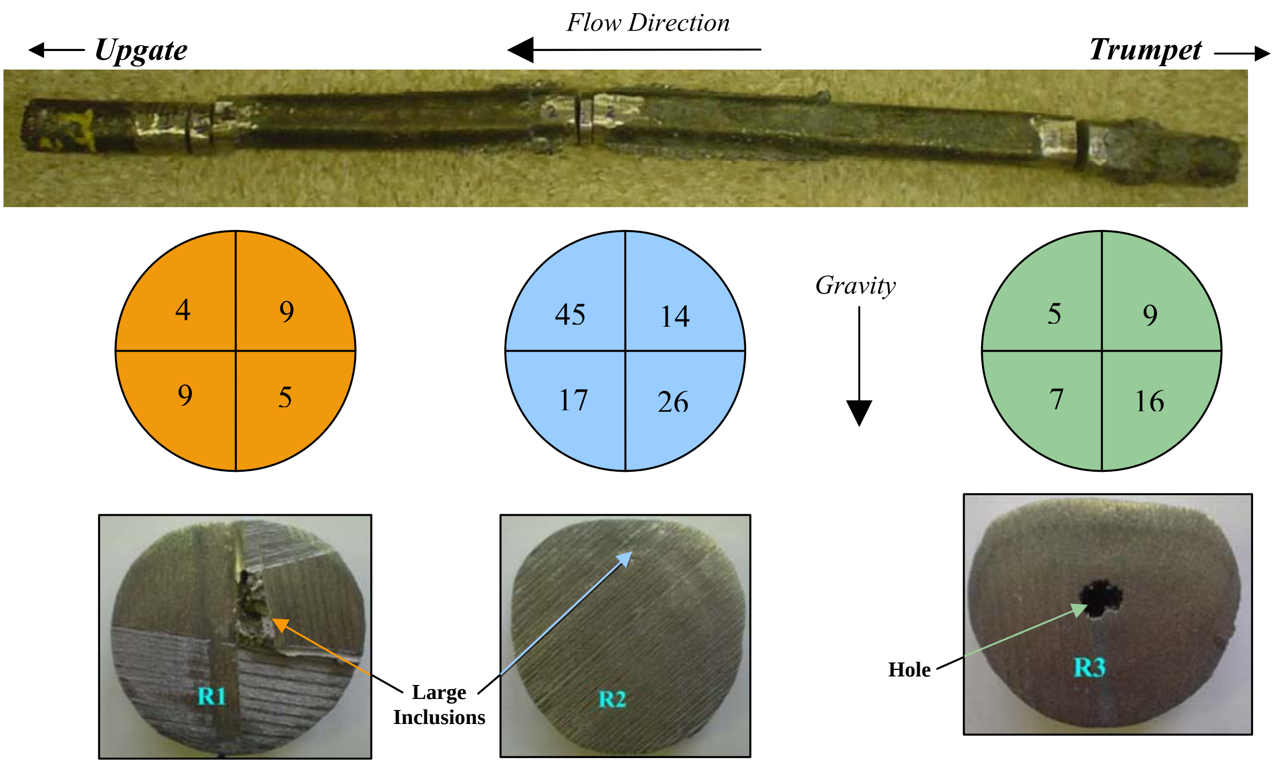

Figure 4.20: Inclusion count distribution within the runner sample

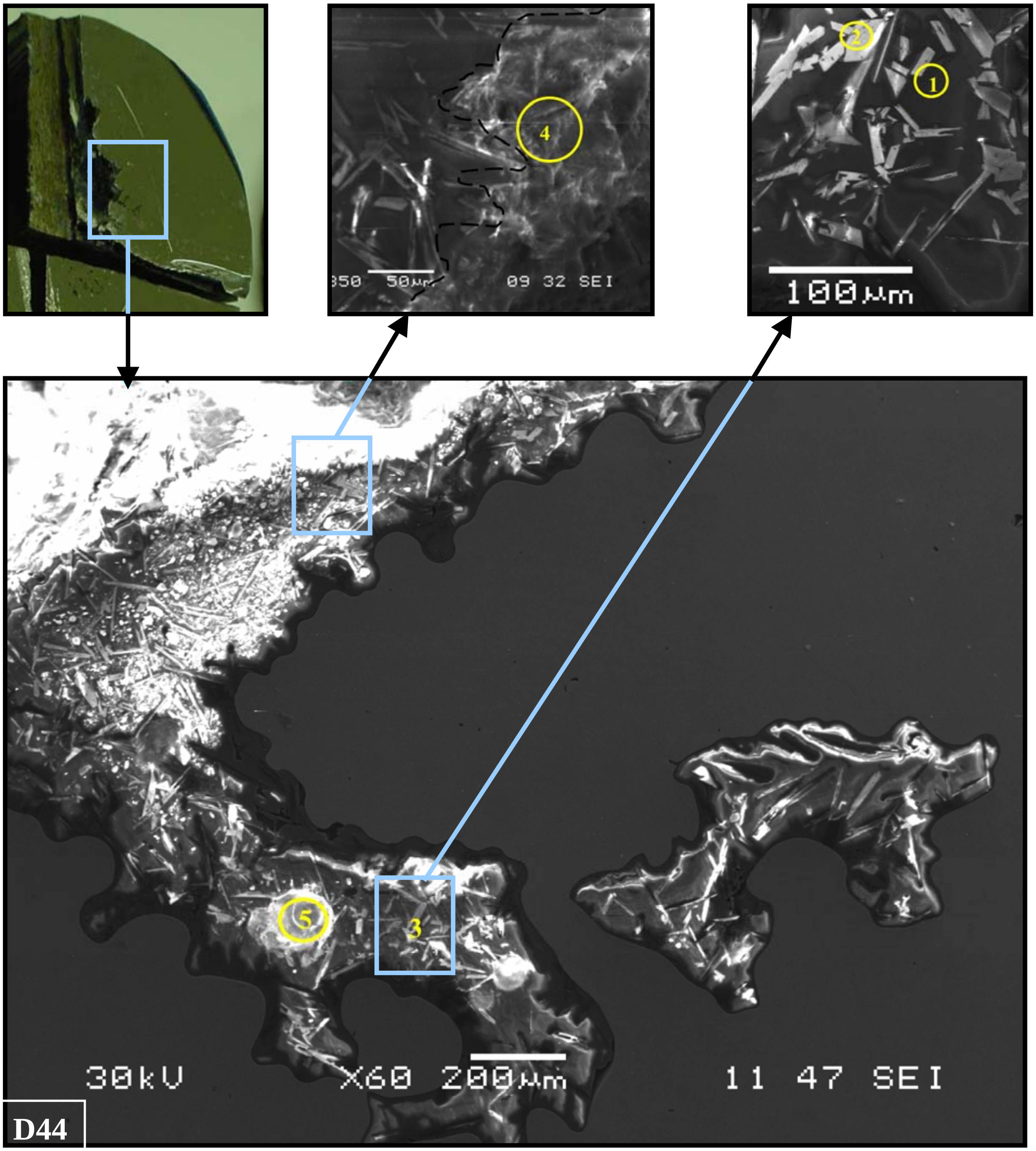

	1	2	3	4	5
SiO_2	40.02%		32.75%	78.39%	82.40%
AL_2O_3	19.93%	100.00%	47.16%	7.13%	3.88%
MnO	36.23%		20.09%	11.21%	10.20%
Na_2O				1.94%	1.39%
K_2O	1.23%				1.94%
TiO_2	2.57%				

Figure 4.21: Morphology and composition of the extremely large inclusion at the center of runner slice R1

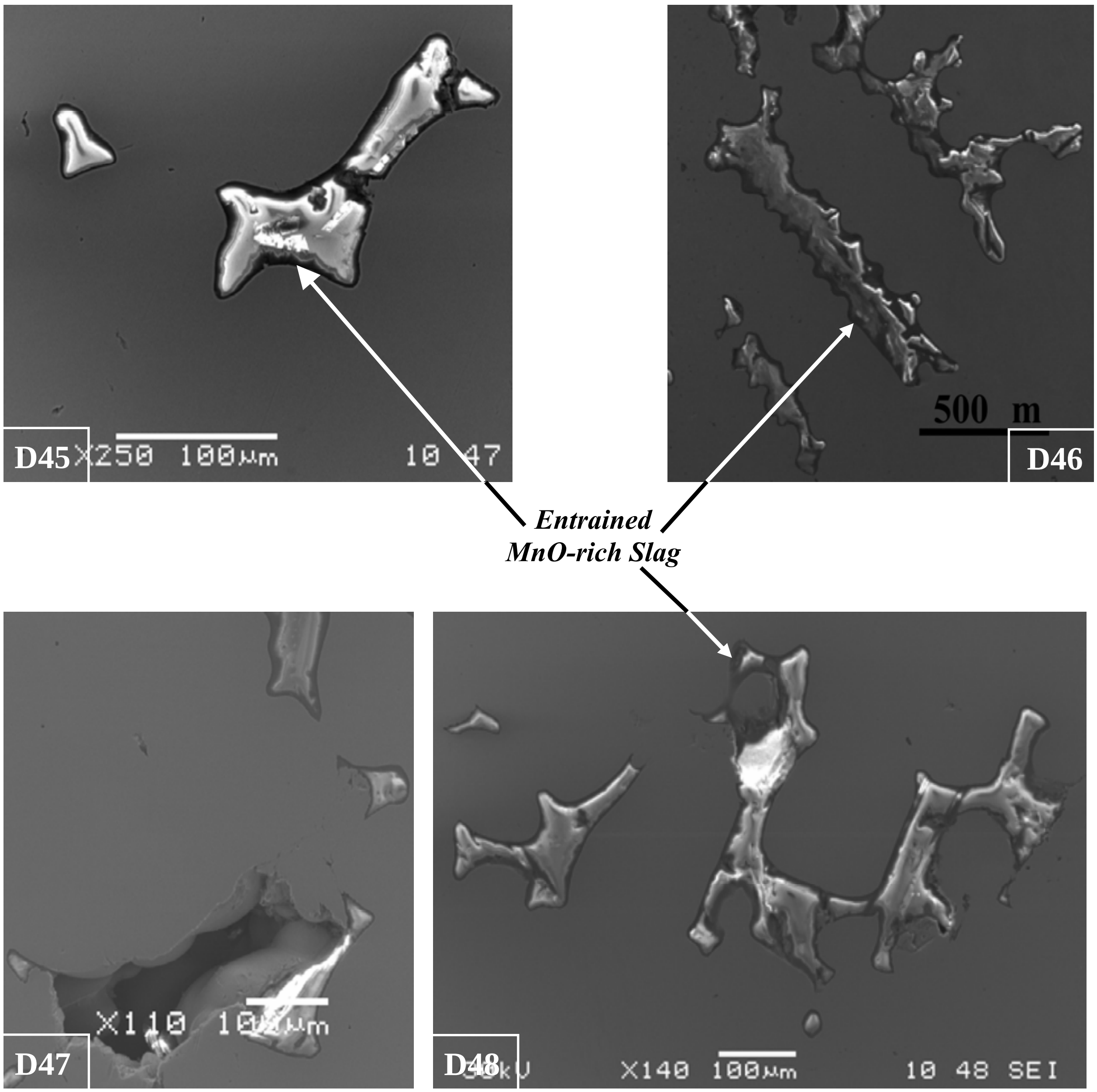

Figure 4.22: MnO inclusions (from mold flux) lining interdendritic porosity boundaries within the runner samples

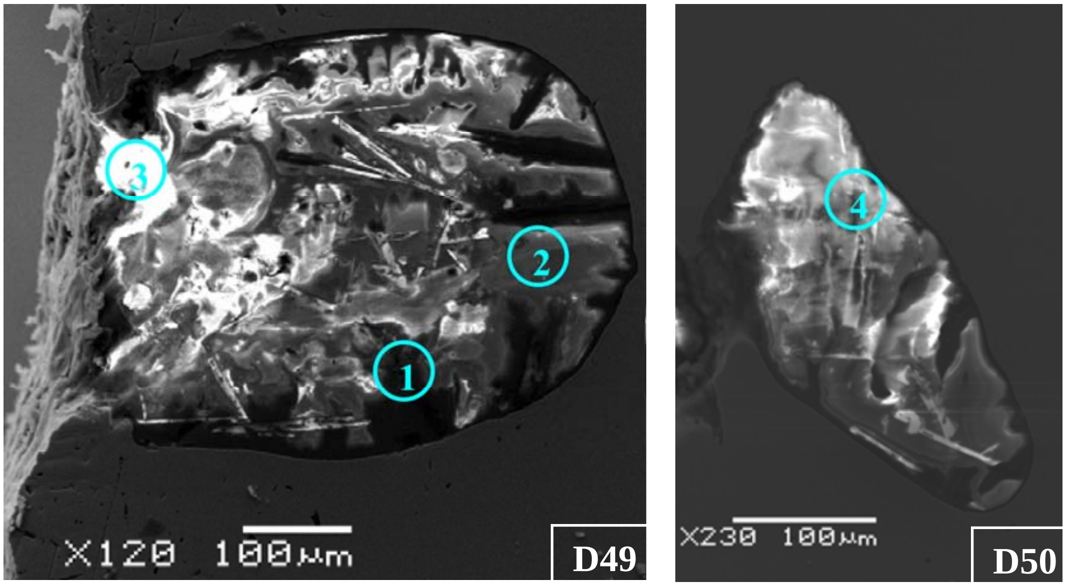

	1	*2*	*3*	*4*
SiO_2	32.60%	48.86%	66.80%	85.58%
AL_2O_3	22.65%	34.10%	3.11%	3.14%
MnO	40.76%	17.04%	28.28%	10.17%
Na_2O				1.11%
K_2O	1.52%		1.31%	
TiO_2	2.47%			

Figure 4.23: MnO-rich inclusions lining the edges of the runner samples

CHAPTER 5: CONCLUSIONS, RECOMMENDATIONS, AND FUTURE WORK

With the overall theme of improving cast steel quality, this thesis utilized numerous models and experimental measurement approaches to draw important findings. A mathematical model simulating turbulent flow was developed to analyze phenomena related to steel quality in a complex funnel mold and associated nozzle via Fluent. The novelty of the model involves the intricate geometry of the mold and strand coupled with realistic simulation of solidification at the boundaries (including proper shell dimensions and the placement of mass/momentum "sink" elements lining the liquid pool). Model validation was performed on a previous thin-slab caster by Yuan. Water models were shown to be quite inaccurate in predicting actual steel flow, and a parametric study conducted using the steel model yielded interesting flow results regarding varying casting speed.

A new technique to estimate mold top surface steel velocities (termed the Nailboard Method) was analyzed using a mathematical model in the finite element code Fidap. Using 3-D, multi-layer, free-surface, turbulent methods, two models were created to simulate the knob formation on a nail after it is dipped into liquid steel. The simplified No-Slag Model validated the approach by agreeing well with experimental run-up simulations performed by Chaplin. A second, more complete Slag Model proved that the solidified knob characteristics (including the top surface profile and diameter) may be used in practice to estimate steel velocity during casting. Using models created to simulate the Nailboard experiment, water models were again shown to be inaccurate in matching steel flow patterns.

Experimental testing on a dissected cast ingot and associated runner allowed for characterization of macro-scale (> 20 μm) exogenous inclusions. Trends involving deposit location and inclusion concentration were developed. Electron-dispersive spectroscopy analysis on each inclusion gave indications of their origination, allowing for recommendations to be made which would theoretically improve ingot quality. The results from all models in this thesis have led to the following conclusions.

5.1 Funnel Mold Flow Study

1. The water model generates a qualitatively accurate double roll flow pattern, but the velocities throughout the upper recirculation zone within the mold are much lower than the steel case. Without the shell to restrict downward flow, the water has a higher tendency to travel downward rather than being "pushed" into the upper recirculation zone. Water model velocity at the top surface is 32% less than in the steel caster and the jet impingement location is 0.12 m lower in the water model; both of which suggest a reduced likelihood of casting defects over the actual steel caster.
2. The solidifying shell produces a calming effect on the flow profiles compared with the water model. The fluid being drawn toward the solidification front smoothes out small eddies, especially in areas of high solidification rate and low velocity (i.e. at the meniscus). The reduction in cross-section area coupled with the mass loss through the solidification front encourages uniform downward flow to develop early in the strand; the lower recirculation zone of the water model extends much deeper. Boundary layer thickness is reduced for the solidification model, encouraging the formation of shell-front defects compared with that predicted in the water model.
3. In the isothermal steel model, all velocity cases generated qualitatively similar double roll flow patterns. The lower recirculation zone extended further into the strand for high casting speeds, increasing the probability of inclusion entrapment once inside the liquid pool. Shell thickness at the jet impingement location was 9.7% and 17.8% thinner than the 3.6 m/min case (8.44 mm, 7.66 mm versus 9.35 mm) and the maximum velocity at 10 mm below the slag/steel interface was 6.9% and 19.0% higher than 3.6 m/min case (0.511 m/s, 0.569 m/s versus 0.478 m/s) for the 4.2 m/min and 4.8 m/min cases (respectively). Using a pressure-height approximation, top surface elevation change increased *exponentially* with increasing casting speed. All these results jointly suggest that funnel mold steel quality is *significantly* reduced with increasing casting speed, unless actions such as electromagnetic flow control are implemented.

5.2 Model of Nailboard Measurement of Surface Velocity

1. Significant evidence shows that the Nailboard method is useful in determining top surface steel velocity. An exponentially (power = 2) increasing run-up height on the leading edge of the solidified knob yields characteristic results for each steel velocity / nail diameter combination. With increasing velocity, increasing diameter simulations approach the limit predicted by the Bernoulli Equation. The knob height difference (knob leading edge run-up minus trailing edge run-down) can be used in conjunction with the knob diameter to estimate surface velocity with relative accuracy (within the 0.2 to 0.5 m/s inlet velocity range). With no slag layer, the shape of the knob profile becomes more distinctive for high velocity, large diameter cases (> 0.3 m/s, > 0.010 m).
2. Height approximations using fixed surface pressures proved to be inaccurate in predicting free surface deformations because the relation neglects surface tension (which was shown to be important from estimation). While the pressure approximation correctly predicts areas of increased free surface level (i.e. directly upstream the nail), it overestimates free surface deformations from the actual case, at times by an order of magnitude.
3. Flow-altering devices, such as electromagnetic brakes (EMBRs), must be turned off during testing with steel nails. The external EMBRs suppress the natural flow pattern, producing slow, irregular surface flow, and yielding indistinct knobs. Optimum submergence time is a function of nail diameter and steel properties, with larger diameter nails requiring slightly longer dip times to form distinct knobs (~ 5 seconds total submersion time for a 8 mm diameter nail). Excessive submersion times promote "mushrooming" at the knob top surface while the lower knob remelts, rendering the knob unusable.

5.3 Ingot Cleanliness Investigation

1. From the 35000 mm^2 of ingot examination surface, 78 macro-scale inclusions (> 20 μm) were examined. Inclusion count was found to decrease exponentially with diameter. Per m^3 of ingot steel, ~2.8×10^7 macro scale inclusions are estimated to be entrapped, translating to a mass fraction of 51 ppm and a oxygen concentration of 24 ppm (conservatively assuming all inclusions are 100% alumina). Inclusion concentration also

decreased from the bottom of the ingot upward, with no distribution trend readily apparent with regard to trumpet side and height in the ingot.

2. Two extremely large inclusions (> 7 mm in width) were found in the runner, formed when high Mn steel and silica from runner bricks agglomerated with reoxidation products. They were primarily composed of segregated SiO_2, MnO, and Al_2O_3 regions.
3. Reoxidation with air produced 59% of the inclusions. Lack of inert-gas shrouding where the ladle pours into the trumpet is predicted to be the main source of these inclusions. It is recommended that the casting process be changed to limit or eliminate steel exposure to non-inert air.
4. 31% of the inclusions are predicted to become entrapped when erosion at the refractory bricks released silica-based inclusions into the steel. High quality lining bricks (void of silica) is predicted to eliminate many of these inclusions.

5.4 Recommendations for Future Work

This work presents three important ways to predict, regulate, and improve steel cleanliness. However, the topics covered merely represent a small part of the complex subject of quality in steel casting. Using the results of this thesis as a groundwork, additional criteria for particle removal and improved caster regulation deserve added validation. Whether it be through supplementary mathematical simulations or data collection via experimentation, important results have yet to be discovered. Additional studies to better understand flow behavior, measurement, and regulation of the casting process are recommended:

- Add particle tracking to the funnel-mold model. Determine areas with high inclusions density, and quantify the effects of flow on inclusion removal. By varying the nozzle and mold geometry and adding complexity of bubble injection, flow patterns can be manipulated to facilitate the maximum degree of inclusion removal.
- Quantify the effects (via parametric study) of changes to the funnel mold simulation to steel quality. Varying other parameters (nozzle depth, steel grade with sulfur content, multiphase flow via gas injection, mold width, nozzle design) allow for optimum nozzle/mold combinations to be developed prior to implementation.

- Collect experimental data using the Nailboard method. The mathematical model proves the feasibility of the technique in estimating flow top surface flow velocity, but fine-tuning of the sampling procedure and examination of physical test results should further validate the method's effectiveness.
- Once implementing the recommended ingot caster changes (Section 4.5), an identical sectioning and inclusion characterization study as outlined in Chapter 4 should be performed. The effect of the changes can be quantified and predictions as to the source of additional macro-scale inclusions can be developed.

APPENDIX A: Mass/Momentum Sink Derivation

One novel aspect of the funnel mold simulation is the implementation of mass and momentum sink elements along the shell front boundaries. Actual solidification is approximated using this methodology, reducing the overall complexity of the simulation. The following formulation describes the derivation and implementation of these elements into the model.

The schematic of the shell and sink elements is shown in Figure A.1. The amount of mass and momentum to be removed at the wall will be calculated using the physical dimensions of the shell element, while the loss will occur within the attached sink element. By making the sink element very thin (1 mm), its effect on altering the fluid flow within the liquid pool will be minimal. A no-slip wall boundary condition will be implemented on face A_s, with the z-velocity set to the casting speed. The x and y-velocities equal zero at face A_s to prevent fluid from passing through the solid wall. Note that all faces in the model are approximated by flat surfaces. Assuming there are many fine elements approximating the curved surfaces, the flat surface approximation is reasonable. Using the approach outlined here, accurate mass and momentum sink amounts can be calculated in any location of the domain knowing only the physical steel properties, the casting speed, and the slopes of the element walls.

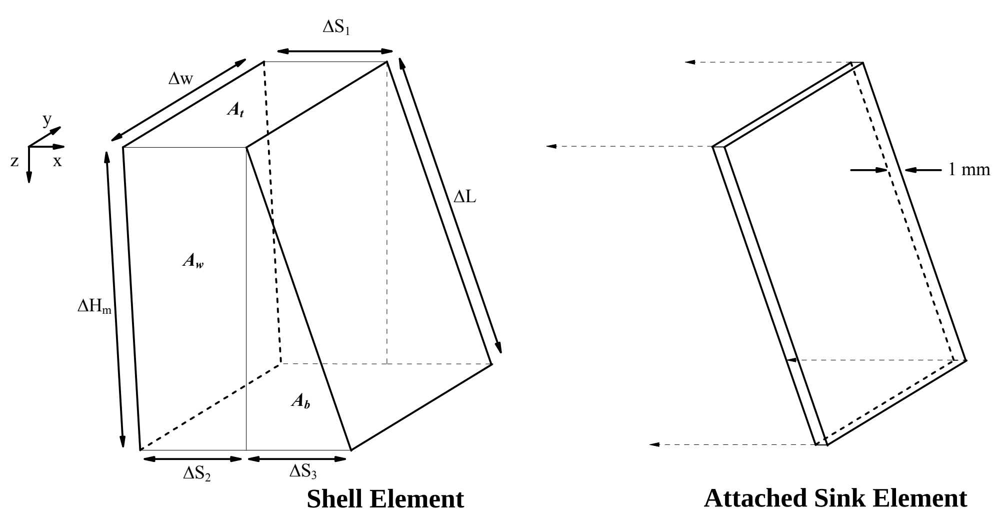

Figure A.1: Schematics for the shell and sink elements

A mass balance through the element will be the source of the mass sink derivation. Using this logic, the mass flowing into the domain must equal the mass out of the domain.

$$\dot{m}_i - \dot{m}_o = \dot{S}_{mass} \tag{A.1}$$

$$[A_t V_c] - [A_b V_c] = \dot{S}_{mass} \tag{A.2}$$

$$[\Delta S_1 \Delta w V_c \rho_{steel,solid}] - [\Delta S_2 \Delta w V_c \rho_{steel,solid} + \Delta S_3 \Delta w V_c \rho_{steel,solid}] = \dot{S}_{mass} \tag{A.3}$$

where $\dot{S}_{mass}$ represents the mass flowing through surface $A_{s.}$ The lengths ΔS_2 and ΔS_3 can be reduced into the following components:

$$\Delta S_2 = \Delta S_1 - \Delta H_m \sin(90 - \theta_2) \tag{A.4}$$

$$\Delta S_3 = \Delta L \sin(\theta_1) \tag{A.5}$$

Inputting Equations A.4 and A.5 into Equation A.3, the simplified equation becomes:

$$\Delta H_m \Delta w \sin(90 - \theta_2) V_c \rho_{steel,solid} - \Delta L \Delta w \sin(\theta_1) V_c \rho_{steel,solid} = \dot{S}_{mass} \tag{A.6}$$

$$V_c \rho_{steel,solid} (\Delta H_m \Delta w \sin(90 - \theta_2) - \Delta L \Delta w \sin(\theta_1)) = \dot{S}_{mass} \tag{A.7}$$

In effort to relate Equation A.7 to the surface projections in the *z*-direction, the following equations are used:

$$N_{A_s \to z} = A_s \sin\theta_1 = \Delta L \Delta w \sin(\theta_1) \tag{A.8}$$

$$N_{A_w \to z} = A_w \sin(90 - \theta_2) = \Delta H_m \Delta w \sin(90 - \theta_2) \tag{A.9}$$

Substituting in Equations A.8 and A.9 and simplifying, Equation A.7 becomes:

$$\dot{S}_{mass} = V_c \rho_{steel,solid} \left(N_{A_w \to z} - N_{A_s \to z}\right) \tag{A.10}$$

The momentum sink amount is a simple extension of the mass sink amount, as momentum equals mass times velocity. Using an iterative process, the mass sink amount determines the steel velocity through the element surface. This velocity is subsequently coupled with the mass source term (which determines the mass flow rate through the surface) to calculate the momentum loss:

$$\dot{S}_{momentum} = V_N \dot{S}_{mass} = V_N V_c \rho_{steel,solid} \left(N_{A_w \to z} - N_{A_s \to z} \right) \tag{A.11}$$

Note that the normal projection in the z-direction for the shell surface (A_s) will always be larger than that for the mold wall (A_w). With all other factors in the equation being positive, the source terms will be negative, indicating that they are "sinks" rather than "sources". By this, fluid and momentum will be removed from the liquid pool at *all* locations along the domain boundary. Refer to Appendix C.1.2 for the complete Fluent subroutine.

APPENDIX B: Fidap Difficulties

Numerous problems arose throughout the course of the project, mainly due to an incomplete understanding of the program Fidap. Should any reader use this CFD program in the future to model fluid flow, there are a few areas of concern which are important to discuss.

The guided user interface is not very easy to use as is in other codes (i.e. Fluent). Text input files are greatly preferred over typing in GUI commands due to their efficiency and the ease of changing parameters.

Fidap unfortunately lacks a resourceful technical support team to assist in problems. Because these simulations were run on an educational Fidap license, verbal contact with technical support representatives was not permitted; emails were required to discuss simulation problems. Emails proved to be quite a difficult method in conversing complicated details about simulations, and it was obvious that the technical support representative did not have a full understanding of the problem. After the frustration of increasingly unhelpful conversation with Fidap "experts" set in, the only logical step was to figure out problems using intuition and the somewhat helpful Fidap help directory.

Much of the time spent on this project was altering the domain and simulation constraints to achieve convergence. Fidap is not very robust, in that small changes in input parameters have a large impact on whether or not convergence for each time step (for transient runs) is achieved. A few of these parameters which must be considered are mesh refinement, time step size, and most importantly relaxation factors. A rigorous routine for achieving convergence was not developed; the preferred method was simply trial and error. If the program had trouble converging during any timestep of a transient run, attempts to discover the cause of the non-convergence were made. Typical course of action involved reducing the time step size and/or increasing the relaxation factors. Refining the mesh in areas of high gradients also proved to allow for better convergence. Maintaining a structured mesh of rectangular elements with reasonable aspect ratios is also essential.

The nature of the Slag problem resulted in formation of velocity gradients extending throughout the domain height. With complicated flow through the domain, assigning flow inlet boundary conditions was not a trivial problem. Numerous attempts were made at using polynomial fits to estimate flow velocity, all with no success. Even slightly improper velocity conditions at the inlet boundaries yield non-physical steel-slag interface deformations near the inlet. To remedy this problem, the 2-D inlet velocity test simulation was used to solve for converged flow parameters at each discreet node along the inlet boundary. These values were subsequently assigned to each respective height-specific node in the full 3-D simulation. Despite the effort, the assigned velocities/turbulence at the inlet were still not perfect; there remained a small degree of surface deformation that could only be attributed to erroneous inlet boundary parameters (the surface deformed in regions far away from the nail-influenced area). Because of this, a control edge was used to quantify deformation caused by the non-perfect inlet boundary conditions. These values were subsequently subtracted from the free surface profile around the nail, essentially filtering out the data to only include deformation due to the nail presence.

With the slag layer barely moving, consideration was taken to ensure that the steel velocity profile past the nearly stationary steel-slag interface was proper. Using the full turbulent regime in both regions caused improper, nearly linear velocity profiles to develop. Intuitively, the flow in the steel layer should have a similar profile to fluid traveling past a stationary wall. Thus wall laws were applied at the interface. This took a bit of finessing to achieve proper convergence, as applying wall laws at a free surface was also not a trivial problem. The free surface and the wall law normals MUST be pointed in opposite directions, otherwise instabilities emerge and cause rapid divergence of the flow solution (this was a problem remedied by trial and error).

APPENDIX C: Sample Input Command Files

C.1: Fluent-Related Files

C.1.1: Pipe-Flow Nozzle Inlet Velocity Specification

(As used to define nozzle inlet velocity in the 3.6 m/min Casting Case)

```
#include "udf.h"
#include "math.h"
DEFINE_PROFILE(inlet_z_velocity, thread, position)
{
  real coord[3];                    /* this will hold the position vector */
  face_t f;
  real x,y;

  begin_f_loop(f, thread)
    {
     F_CENTROID(coord,f,thread);
     x = coord[0];
     y = coord[1];
     F_PROFILE(f, thread, position) = -2.0886831*pow((1-(pow((x*x+y*y),0.5))/.04),(1/7.6967333));
              /*Message("%d \t %d \t %d\n", x,y,f);*/
    }
  end_f_loop(f, thread)
}
```

C.1.2: Mass/Momentum Sink Definition

```
#include "udf.h"
#include "math.h"
#include "sg.h"
#define density 7800 //solid steel density [kg/m3]
#define castingspeed .07    //[m/s]
#define nx_s 35
#define ny_s 37
#define py_s 36
#define nx_i 51
#define ny_i 50
#define py_i 49
#define nx_w 23
#define ny_w 25
#define py_w 24
DEFINE_SOURCE(xmom_source_ny,c,t,dS,eqn)
{ real A1[ND_ND],A2[ND_ND],X[ND_ND],xx,yy,zz;
  real source;
  real x_s,y_s,z_s,x_w,y_w,z_w,ds,es[ND_ND],A_by_es,dr0[ND_ND],dr1[ND_ND];
  int n,nn;
  face_t f, ff;
  cell_t c0, c1, cn;
  Thread *tf, *t0, *t1, *tn, *tff;
  C_CENTROID(X,c,t);
  xx=X[0];
  yy=X[1];
  zz=X[2];
  c_face_loop(c,t,n){
                f = C_FACE(c,t,n);
                tf = C_FACE_THREAD(c,t,n);
  if(THREAD_ID(C_FACE_THREAD(c,t,n)) == ny_s){
                                F_AREA(A1,f,tf);
                                x_s = A1[0]/NV_MAG(A1);
                                y_s = A1[1]/NV_MAG(A1);
                                z_s = A1[2]/NV_MAG(A1);}
                else if (THREAD_ID(C_FACE_THREAD(c,t,n)) == ny_i){
                                c0 = F_C0(f,tf);
                                c1 = F_C1(f,tf);
                                t0 = THREAD_T0(tf);
                                t1 = THREAD_T1(tf);
                                                if (c0 == c){
                                                                cn = c1;
                                                                tn = t1;}
                                                else {
                                                                cn = c0;
                                                                tn = t0;}
                                c_face_loop(cn,tn,nn){
                                f = C_FACE(cn,tn,nn);
                                tf = C_FACE_THREAD(cn,tn,nn);
                                                if(THREAD_ID(C_FACE_THREAD(cn,tn,nn)) == ny_w){
                                                                //Message("%i\t\n",THREAD_ID(C_FACE_THREAD(cn,tn,nn)));
                                                                F_AREA(A2,f,tf);
                                                                x_w = A2[0]/NV_MAG(A2);
                                                                y_w = A2[1]/NV_MAG(A2);
                                                                z_w = A2[2]/NV_MAG(A2);

                                (Mass Sink File):       source = -density*castingspeed*(fabs(z_s)-fabs(z_w))*NV_MAG(A1)/C_VOLUME(c,t);
                                (Mass Sink File):       dS[eqn]=0;
                                (Mom Sink File):        source                          =                                   -density*castingspeed*(fabs(z_s)-
fabs(z_w))*NV_MAG(A1)/C_VOLUME(c,t)*fabs(C_U(c,t));
                                (Mom Sink File):        dS[eqn]=-density*castingspeed*(fabs(z_s)-fabs(z_w))*NV_MAG(A1)/C_VOLUME(c,t);
                                                }
                                }
                }
  }
  return source;
  return dS[eqn];
```

C.2: Fidap-Related Files

C.2.1: Analytical Solution Input File

```
TITLE
ANALYTICAL SOLUTION- SLOSHING IN A TANK
FIMESH(2-D,IMAX=3,JMAX=3)
EXPI
1 0 29
EXPJ
1 0 29
$d=1
$l=2*$d
$dimx=.04
$dimy=.02
POINT
1 1 1 1 0 0
2 3 1 1 ($l) 0
3 3 3 1 ($l) ($d+$d/50)
4 1 3 1 0 ($d-$d/50)

LINE
2 1
2 3
3 4
1 4
SURFACE
1 3
AREA
1 3

ELEMENTS(BOUNDARY,NODES=2,ENTITY="free")
3 4
ELEMENTS(BOUNDARY,NODES=2,ENTITY="sidewalls")
1 4
2 3
ELEMENTS(BOUNDARY,NODES=2,ENTITY="bottomwall")
1 2
ELEMENTS(ALL,QUADRILATERAL,NODES=4,ENTITY="fluid")
END

FIPREP
EXECUTION(NEWJOB)
PROBLEM (2-D,TRANSIENT,nonlinear,FREE)
SOLU(N.R.=10,schange=0,velc=0.0001,surfconv=.0001)

ENTITY(FLUID,NAME="fluid")
ENTITY(SURFACE,NAME="free",SPINES,DEPTH=0,STRAIGHT,ANG1=0,ANG2=180)
ENTITY(PLOT,NAME="sidewalls")
ENTITY(PLOT,NAME="bottomwall")

DENSITY(CONSTANT=1000)
VISCOSITY(CONSTANT=.01)
BODYFORCE(CONSTANT,FX=0,FY=-9.81,FZ=0,ENTITY="fluid")
TIMEINTEGRATION(NSTEPS=10001,TSTART=0,DT=.001,FIXED)
BCNODE(UX,ZERO,ENTITY="sidewalls")
BCNODE(UY,ZERO,ENTITY="bottomwall")
SURFACETENSION(CONSTANT=0)
POSTPROCESS(NBLOCKS=1)
1 10001 100

END
CREATE(FISOLV)
RUN(FISOLV)
```

C.2.2: No-Slag Model Initial, Steady-State Run Input File

(Sample file is for the 0.010 m nail diameter, 0.3 m/s inlet velocity case)

```
//Nail Diameter
$dnail = 0.010
//Inlet Velocity
$invel = 0.3

TITLE
No-Slag (Run 1, 0.010 m Dia, 0.3 m/s Inlet Velocity)
FIMESH(3-D,IMAX=13,JMAX=7,KMAX=3)
EXPI
1 0 6 0 11 0 17 0 23 0 29 0 35
EXPJ
1 0 15 0 27 0 33
EXPK
1 0 5
//Constants
$steelvisc = 0.006
$steeldensity = 7400
$steelst = 1.6
$kine=(0.005*$invel*$invel)
$DISS=(7400*0.09*$kine*$kine/(10.*0.0074))
$dup=10*$dnail
$Widthtwo=10*$dnail
$downstream=10*$dnail
$upstream=10*$dnail
$sin=0.707106781187
$cose=0.923879532511
$tane=0.414213562373
$tanang=1.91997174485
$height=.03

POINT
/# I J K X Y Z
/TOP
1 1 5 3 0 0 ($height)
2 1 3 3 ($upstream) 0 ($height)
3 1 1 3 ($upstream+($dup-$dnail)/2) 0 ($height)
4 5 1 3 ($upstream+($dup)/2-$sin*$dnail/2) ($sin*$dnail/2) ($height)
5 9 1 3 ($upstream+($dup)/2+$sin*$dnail/2) ($sin*$dnail/2) ($height)
6 13 1 3 ($upstream+$dup/2+$dnail/2) 0 ($height)
7 13 3 3 ($dup/2+$upstream+$dup/2) 0 ($height)
8 13 5 3 ($dup/2+$upstream+$dup/2+$downstream) 0 ($height)
9 11 5 3 ($dup+$upstream+$downstream) ($tane*($dup/2+$upstream)) ($height)
10 9 3 3 ($upstream+$dup/2+$sin*$dup/2) ($sin*$dup/2) ($height)
11 5 3 3 ($upstream+$dup/2-$sin*$dup/2) ($sin*$dup/2) ($height)
12 3 5 3 0 ($tane*($dup/2+$upstream)) ($height)
13 5 5 3 (0.25*($dup+$upstream+$downstream)) ((0.25*($dup+$upstream+$downstream))*$tanang) ($height)
14 3 7 3 0 (($upstream+$dup/2)/$cose+$widthtwo) ($height)
15 11 7 3 ($dup+$upstream+$downstream) (($upstream+$dup/2)/$cose+$widthtwo) ($height)
16 0 0 0 ($upstream+$dup/2) 0 ($height)
37 9 5 3 (0.75*($dup+$upstream+$downstream)) ((0.25*($dup+$upstream+$downstream))*$tanang) ($height)
39 7 5 3 (0.5*($dup+$upstream+$downstream)) (($upstream+$dup/2)/$cose) ($height)
/BOTTOM
19 1 5 1 0 0 0
20 1 3 1 ($upstream) 0 0
21 1 1 1 ($upstream+($dup-$dnail)/2) 0 0
22 5 1 1 ($upstream+($dup)/2-$sin*$dnail/2) ($sin*$dnail/2) 0
23 9 1 1 ($upstream+($dup)/2+$sin*$dnail/2) ($sin*$dnail/2) 0
24 13 1 1 ($upstream+$dup/2+$dnail/2) 0 0
25 13 3 1 ($dup/2+$upstream+$dup/2) 0 0
26 13 5 1 ($dup/2+$upstream+$dup/2+$downstream) 0 0
27 11 5 1 ($dup+$upstream+$downstream) ($tane*($dup/2+$upstream)) 0
28 9 3 1 ($upstream+$dup/2+$sin*$dup/2) ($sin*$dup/2) 0
29 5 3 1 ($upstream+$dup/2-$sin*$dup/2) ($sin*$dup/2) 0
30 3 5 1 0 ($tane*($dup/2+$upstream)) 0
```

```
31 5 5 1 (0.25*($dup+$upstream+$downstream)) ((0.25*($dup+$upstream+$downstream))*$tanang) 0
32 3 7 1 0 (($upstream+$dup/2)/$cose+$widthtwo) 0
33 11 7 1 ($dup+$upstream+$downstream) (($upstream+$dup/2)/$cose+$widthtwo) 0
34 0 0 0 ($upstream+$dup/2) 0 0
38 9 5 1 (0.75*($dup+$upstream+$downstream)) ((0.25*($dup+$upstream+$downstream))*$tanang) 0
40 7 5 1 (0.5*($dup+$upstream+$downstream)) (($upstream+$dup/2)/$cose) 0

LINE
/P1 P2
/TOP
1 2
3 2 .05 4
4 11 .05 4
5 10 .05 4
6 7 .05 4
7 8
8 9
10 37
11 13
1 12
12 13
13 39
39 37
37 9
12 14
14 15
9 15
/BOTTOM
19 30
19 20
21 20 .05 4
22 29 .05 4
23 28 .05 4
24 25 .05 4
25 26
26 27
30 31
31 40
40 38
38 27
27 33
32 33
30 32
29 31
28 38
/SIDES
1 19
2 20
3 21
4 22
5 23
6 24
7 25
8 26
9 27
10 28
11 29
12 30
13 31
14 32
15 33
37 38

ARC
/P1 P2 CENTER
/TOP
2  11 16
3  4  16
11 10 16
4  5  16
```

5 6 16
10 7 16
/BOTTOM
20 29 34
21 22 34
29 28 34
22 23 34
23 24 34
28 25 34

SURFACE
/P1 P2
/TOP
2 13
3 11
4 10
11 37
10 8
5 7
12 15
/BOTTOM
20 31
21 29
22 28
29 38
28 26
23 25
30 33
/SIDES
1 20
2 21
3 22
4 23
5 24
6 25
7 26
27 8
9 33
15 32
14 30
12 19
12 31
13 38
38 9
11 31
11 22
11 20
11 28
37 28
10 23
10 25

AREA
/P1 P2
/TOP
2 13
3 11
4 10
11 37
10 8
5 7
12 15
/BOTTOM
20 31
21 29
22 28
29 38
28 26
23 25
30 33

```
/SIDES
1 20
2 21
3 22
4 23
5 24
6 25
7 26
27 8
9 33
15 32
14 30
12 19
12 31
13 38
38 9
11 31
11 22
11 20
11 28
37 28
10 23
10 25

VOLUME
2  31
3  29
11 38
4  28
5  25
10 26
12 33

3-D
2  31
3  29
11 38
4  28
5  25
10 26
12 33

ELEMENTS(BRICK,NODES=8,ALL,ENTITY="fluid")
ELEMENTS(BOUNDARY,ENTITY="outflow")
8 27
9 33
ELEMENTS(BOUNDARY,ENTITY="inflow")
1 30
12 32
ELEMENTS(BOUNDARY,ENTITY="free")
3 11
4 10
5 7
2 13
11 37
7 37
12 15
ELEMENTS(BOUNDARY,ENTITY="symmetry")
1 20
2 21
6 25
7 26
ELEMENTS(BOUNDARY,EDGE,ENTITY="edge")
3 4
4 5
5 6
6 7
7 8
8 9
9 15
```

```
14 15
ELEMENTS(BOUNDARY,EDGE,ENTITY="boundary")
1 12
12 14
ELEMENTS(BOUNDARY,ENTITY="bottom")
21 29
20 31
30 33
29 38
22 28
23 25
28 26
ELEMENTS(BOUNDARY,ENTITY="nail")
22 3
4 23
5 24
ELEMENTS(BOUNDARY,ENTITY="farfield")
32 15

BCNODE( COOR )
  1
 19
  8
 26
 14
 32
 15
 33
END

FIPREP
PROBLEM(3-D,TURBULENT,NONLINEAR)
PRESSURE(MIXED,DISCONTINUOUS)
EXECUTION(NEWJOB)
SOLUTION(SEGREGATED=1000,VELC=0.0001)

ENTITY(OUTFLOW,NAME="outflow")
ENTITY(FLUID,NAME="fluid",MDENS=1,MVISC=1)
ENTITY(WALL,NAME="nail")
ENTITY(PLOT,NAME="symmetry")
ENTITY(PLOT,NAME="bottom")
ENTITY(PLOT,NAME="farfield")
ENTITY(PLOT,NAME="edge")
ENTITY(PLOT,NAME="boundary")
ENTITY(OUTFLOW,NAME="inflow")
ENTITY(SURFACE,NAME="free",DEPTH=0,SPINE,STRAIGHT,MSURF=1)

DENSITY(SET="1",CONSTANT=$steeldensity)
VISCOSITY(SET="1",CONSTANT=$steelvisc,TWO-EQUATION)
SURFACETENSION(SET="1",CONST=$steelst)
BODYFORCE(CONSTANT,FX=0.,FY=0,FZ=-9.81)
OPTION(SIDES)

BCNODE(UX,ENTITY="inflow",CONSTANT=$invel)
BCNODE(UY,ZERO,ENTITY="inflow")
BCNODE(UZ,ZERO,ENTITY="inflow")
BCNODE(KINETIC,ENTITY="inflow",CONSTANT=$kine)
BCNODE(DISSIPATION,ENTITY="inflow",CONSTANT=$DISS)
BCNODE(UZ,ZERO,ENTITY="bottom")
BCNODE(UY,ZERO,ENTITY="farfield")
BCNODE(VELOCITY,ENTITY="nail",ZERO)
BCNODE(UY,ENTITY="symmetry",ZERO)

ICNODE(UX,ENTITY="fluid",CONSTANT=$invel)
ICNODE(KINETIC,ENTITY="fluid",CONSTANT=$kine)
ICNODE(DISSIPATION,ENTITY="fluid",CONSTANT=$DISS)
END

CREATE(FISOLV)
RUN(FISOLV)
```

C.2.3: No-Slag Model Second, Transient Run Input File

(Sample file is for the 0.010 m nail diameter, 0.3 m/s inlet velocity case)

```
FIPREP
EXECUTION(NEWJOB)
FILES(RENAME,FROM="NS(0.010,0.3)..FDPOST",TO=" NS(0.010,0.3)..FDREST")
SOLU(ENTRY=1,REPLACE,SEGRE=1000,CR=2000,CGS=2000,VELC=0.001,NCGC=1e-6,SCGC=1e-6,SCHANGE=0)
PROBLEM(ENTRY=1,REPLACE,3-D,TURBULENT,TRANSIENT,NONLINEAR,FREE)

ICNODE(ENTRY=1,REPLACE,ENTITY="fluid",VELOCITY,READ)
ICNODE(ENTRY=2,REPLACE,ENTITY="fluid",KINETIC,READ)
ICNODE(ENTRY=3,REPLACE,ENTITY="fluid",DISSIPATION,READ)

TIMEINTEGRATION(DT=0.0003,TSTART=0,NSTEPS=15001,FIXED)
POSTPROCESS(NBLOCKS=1)
1 15001 100
PRINTOUT(NBLOCKS=1)
1 15001 15000

BCNODE(CONTACTANGLE,ENTITY="free",CONSTANT=90)
BCNODE(COORDINATE,ENTITY="boundary",CONSTANT=1)
BCNODE(COORDINATE,ENTITY="edge",CONSTANT=1)
BCSYSTEM( SET = 1, NORM )
0 0 1 0 0 0 0 0 0

BCNODE(SURFACE,ZERO,ENTITY="boundary")
BCNODE(UZ,FREE,ENTITY="edge")

RELAXATION(HYBRID)
/u  v  w  p  t  s   k  e
//0.3 0.3 0.3 0.6  0  0.25 0.8 0.8 0.3
END

CREATE(FISOLV)
RUN(FISOLV)
```

C.2.4: Slag Model Inlet Velocity Simulation Input File

(Sample file is for the 0.010 m nail diameter, 0.3 m/s inlet velocity case)

```
//Inlet Velocities
$invel=0.3


TITLE
INLET VELOCITY SIMULATION (0.3 m/s)
FIMESH(2-D,IMAX=3,JMAX=5)
EXPI
1 0 25
EXPJ
1 0 10 0 13

//Constants
$slaginvel=.0375*$invel/0.3
$kine=(0.005*$invel*$invel)
$DISS=(7400*0.09*$kine*$kine/(10.*0.0074))
$slagkine=(0.005*$invel*$invel)
$SLAGDISS=(7400*0.09*$kine*$kine/(10.*0.0074))

POINT
1 1 1 1 0 0
2 3 1 1 .3 0
3 1 3 1 0 .06
4 3 3 1 .3 .06
5 1 5 1 0  .07
6 3 5 1 .3 .07

LINE
1 2
3 4
5 6
3 5
4 6
3 1 .07 4
4 2 .07 4

SURFACE
1 4
3 6

AREA
1 4
3 6

ELEMENTS(QUADRILATERAL,NODES=4,ENTITY="steel")
1 4
ELEMENTS(QUADRILATERAL,NODES=4,ENTITY="slag")
3 6
ELEMENTS(BOUNDARY,EDGE,ENTITY="interface")
3 4
ELEMENTS(BOUNDARY,EDGE,ENTITY="bottom")
1 2
ELEMENTS(BOUNDARY,EDGE,ENTITY="top")
5 6
ELEMENTS(BOUNDARY,EDGE,ENTITY="steelinflow")
1 3
ELEMENTS(BOUNDARY,EDGE,ENTITY="slaginflow")
3 5
ELEMENTS(BOUNDARY,EDGE,ENTITY="steeloutflow")
2 4
ELEMENTS(BOUNDARY,EDGE,ENTITY="slagoutflow")
4 6
ELEMENTS(BOUNDARY,EDGE,ENTITY="interface_wall")
3 4
```

```
END
FIPREP
EXECUTION( NEWJ )
SOLUTION (SEGREGATED = 1000, KINEMATIC = 25, VELC = 0.0001,SURFCONV = 0.01)
PROB (NONLINEAR,TURBULENT)
PRESSURE(MIXE=1.e-14,DISCONTINUOUS)

ENTITY(fluid,NAME="steel",MDENS=2,MVISC=2)
ENTITY(fluid,NAME="slag",MDENS=1,MVISC=1)
ENTITY(SURFACE,NAME="top",SPINES,STRAIGHT,DEPTH=0,CONTINUE,MSURF=1)
ENTITY(wall,NAME="interface_wall",ATTACH="steel",NATTACH="slag")
ENTITY(SURFACE,NAME="interface",DEPTH=-
1,SPINE,STRAIGHT,ANG1=0,ANG2=180,ATTACH="steel",NATTACH="slag",MSURF=2)
ENTITY(PLOT,NAME="bottom")
ENTITY(outflow,NAME="slaginflow")
ENTITY(outflow,NAME="steelinflow")
ENTITY(outflow,NAME="slagoutflow")
ENTITY(outflow,NAME="steeloutflow")

DENSITY(SET="1",CONSTANT=3000)
VISCOSITY(SET="1",CONSTANT=1,TWO-EQUATION)
SURFACETENSION(SET="1",CONSTANT=0)
DENSITY(SET="2",CONSTANT=7400)
VISCOSITY(SET="2",CONSTANT=0.006,TWO-EQUATION)
SURFACETENSION(SET="2",CONST=0)
BODYFORCE(ENTITY="slag",CONSTANT,FX=0.,FY=-9.81,FZ=0)
BODYFORCE(ENTITY="steel",CONSTANT,FX=0.,FY=-9.81,FZ=0)

BCNODE(UX,ENTITY="steelinflow",CONSTANT=$invel)
BCNODE(UX,ENTITY="slaginflow",CONSTANT=$slaginvel)
BCNODE(UY,ENTITY="steelinflow",CONSTANT=0)
BCNODE(UY,ENTITY="slaginflow",CONSTANT=0)
BCNODE(UY,ZERO,ENTITY="bottom")
BCNODE(UX,ZERO,ENTITY="top")

ICNODE(UX,ENTITY="steel",CONSTANT=$invel)
ICNODE(KINETIC,ENTITY="steel",CONSTANT=$kine)
ICNODE(DISSIPATION,ENTITY="steel",CONSTANT=$DISS)
ICNODE(UX,ENTITY="slag",CONSTANT=$slaginvel)
ICNODE(KINETIC,ENTITY="slag",CONSTANT=$slagkine)
ICNODE(DISSIPATION,ENTITY="slag",CONSTANT=$SLAGDISS)

RELAXATION
/u  v  w  p  t  s   k  e
0.5,  0.5,  0.00,  0.0, 0.0,  0.75,  0.5,  0.5
END

CREATE(FISOLV)
RUN(FISOLV)



FIPREP(  )
EXECUTION( NEWJ )
FILES( RENA, FROM = "VT0.4.FDPOST", TO = "VT0.4.FDREST" )
SOLUTION( ENTR = 1, REPL, SEGR = 1000, CR = 2000, CGS = 2000, VELC = 0.001,
NCGC = 1e-06, SCGC = 1e-06, SCHA = 0 )
PROBLEM( ENTR = 1, REPL, 2-D, TURB, TRANS, FREE, NONL)
TIMEINTEGRATION( DT = 0.001, TSTA = 0, NSTE = 690, FIXE )

ICNODE( ENTR = 1, REPL, ENTI = "steel", VELOCITY, READ )
ICNODE( ENTR = 2, REPL, ENTI = "steel", KINE, READ )
ICNODE( ENTR = 3, REPL, ENTI = "steel", DISS, READ )
ICNODE( ENTR = 4, REPL, ENTI = "slag", VELOCITY, READ )
ICNODE( ENTR = 5, REPL, ENTI = "slag", KINE, READ )
ICNODE( ENTR = 6, REPL, ENTI = "slag", DISS, READ )

BCNODE( ENTR = 1, DELE )
BCNODE( ENTR = 2, DELE )
BCNODE( CONT, ENTI = "top", CONS = 90 )
```

```
BCNODE( CONT, ENTI = "interface", CONS = 90 )
BCNODE( SURF, ZERO, NODE=226 )
BCNODE( SURF, ZERO, NODE=301 )
BCNODE( COORDINATE, NODE=226 )
BCNODE( COORDINATE, NODE=250 )
BCNODE( COORDINATE, NODE=301 )
BCNODE( COORDINATE, NODE=325 )

POSTPROCESS (NBLOCK=2)
1 664 25
665 690 25
PRINTOUT( NBLO = 1 )
1 690 690

RELAXATION(hybrid)
0, 0, 0.00, 0.0, 0.0, 0, 0, 0, 0, 0, 0, 0, 0
END(  )

CREATE( FISO )
RUN( FISOLV )
```

C.2.5: Slag Model Initial, Steady-State Simulation Input File

(Sample file is for the 0.010 m nail diameter, 0.3 m/s inlet velocity case)

```
//Nail Diameter
$dnail = 0.010
//Inlet Velocities
$invel = 0.3
$slaginvel = 0.0375*$invel/0.3

TITLE
Slag (Run 1, 0.010 m Dia, 0.3 m/s Inlet Velocity)
FIMESH(3-D,IMAX=13,JMAX=7,KMAX=5)
EXPI
1 0 5 0 9 0 13 0 17 0 21 0 25
EXPJ
1 0 12 0 17 0 23
EXPK
1 0 10 0 13

//Constants
$slagvisc = 1
$steelvisc = 0.006
$slagdensity = 3000
$steeldensity = 7400
$slagst = 0.65
$steelst = 1.6
$kine=(0.005*$invel*$invel)
$DISS=($steeldensity*0.09*$kine*$kine/(10.*$steelvisc))
$slagkine=(0.005*$slaginvel*$slaginvel)
$SLAGDISS=($slagdensity*0.09*$slagkine*$slagkine/(10.*$slagvisc))
$dref=0.005
$dup=20*$dref
$Widthtwo=10*$dref
$downstream=15*$dref
$upstream=15*$dref
$sin=0.707106781187
$cose=0.923879532511
$tane=0.414213562373
$tanang=1.91997174485
$height=0.06
$height2=0.01
$fone=0.2
$ftwo=0.5
$fthree=0.8
$fwidth=.2

//Explicit Inlet Boundary Constants
//X-Velocity
$one=           0.299968
$two=           0.299474
$three=         0.299487
$four=          0.299566
$five=          0.299169
$six=           0.301614
$seven=         0.276950
$eight=         0.243561
$nine=          0.204200
$ten=           0.0186406
$eleven=        0.0124494
$twelve=        0.00628692
$thirteen=      0.00000000

//Kinetic Energy
$oneK=          0.27750775e-4
$twoK=          0.59658623e-10
$threeK=        0.23642246e-4
```

```
$fourK=         0.59658623e-10
$fiveK=         0.51757264e-5
$sixK=          0.59658623e-10
$sevenK=        0.29695159e-3
$eightK=        0.56991840e-3
$nineK=         0.59277825e-3
$tenK=          0.59277825e-3
$elevenK=       0.50449332e-4
$twelveK=       0.50468371e-4
$thirteenK=     0.50484494e-4

//Dissipation
$oneD=          0.10615146e-6
$twoD=          0.32032361e-14
$threeD=        0.89134396e-6
$fourD=         0.32032361e-14
$fiveD=         0.18803432e-4
$sixD=          0.32032361e-14
$sevenD=        0.81002501e-3
$eightD=        0.25668868e-2
$nineD=         0.46237263e-2
$tenD=          0.46237263e-2
$elevenD=       0.43120889e-4
$twelveD=       0.42099948e-4
$thirteenD=     0.41789382e-4

POINT
/TOP
41  1 5 5 0 0 ($height+$height2)
42  1 3 5 ($upstream) 0 ($height+$height2)
43  1 1 5 ($upstream+($dup-$dnail)/2) 0 ($height+$height2)
44  5 1 5 ($upstream+($dup)/2-$sin*$dnail/2) ($sin*$dnail/2) ($height+$height2)
45  9 1 5 ($upstream+($dup)/2+$sin*$dnail/2) ($sin*$dnail/2) ($height+$height2)
46  13 1 5 ($upstream+$dup/2+$dnail/2) 0 ($height+$height2)
47  13 3 5 ($dup/2+$upstream+$dup/2) 0 ($height+$height2)
48  13 5 5 ($dup/2+$upstream+$dup/2+$downstream) 0 ($height+$height2)
49  11 5 5 ($dup+$upstream+$downstream) ($tane*($dup/2+$upstream)) ($height+$height2)
50 9 3 5 ($upstream+$dup/2+$sin*$dup/2) ($sin*$dup/2) ($height+$height2)
51 5 3 5 ($upstream+$dup/2-$sin*$dup/2) ($sin*$dup/2) ($height+$height2)
52 3 5 5 0 ($tane*($dup/2+$upstream)) ($height+$height2)
53 5 5 5 ($fone*($dup+$upstream+$downstream)) (($fwidth*($dup+$upstream+$downstream))*$tanang) ($height+$height2)
54 3 7 5 0 (($upstream+$dup/2)/$cose+$widthtwo) ($height+$height2)
55 11 7 5 ($dup+$upstream+$downstream) (($upstream+$dup/2)/$cose+$widthtwo) ($height+$height2)
56 0 0 0 ($upstream+$dup/2) 0 ($height+$height2)
57 9 5 5 ($fthree*($dup+$upstream+$downstream)) (($fwidth*($dup+$upstream+$downstream))*$tanang) ($height+$height2)
58 7 5 5 ($ftwo*($dup+$upstream+$downstream)) (($upstream+$dup/2)/$cose) ($height+$height2)
60 7 7 5 (($dup+$upstream+$downstream)/2) (($upstream+$dup/2)/$cose+$widthtwo) ($height+$height2)

/MIDDLE
1  1 5 3 0 0 ($height)
2  1 3 3 ($upstream) 0 ($height)
3  1 1 3 ($upstream+($dup-$dnail)/2) 0 ($height)
4  5 1 3 ($upstream+($dup)/2-$sin*$dnail/2) ($sin*$dnail/2) ($height)
5  9 1 3 ($upstream+($dup)/2+$sin*$dnail/2) ($sin*$dnail/2) ($height)
6  13 1 3 ($upstream+$dup/2+$dnail/2) 0 ($height)
7  13 3 3 ($dup/2+$upstream+$dup/2) 0 ($height)
8  13 5 3 ($dup/2+$upstream+$dup/2+$downstream) 0 ($height)
9  11 5 3 ($dup+$upstream+$downstream) ($tane*($dup/2+$upstream)) ($height)
10 9 3 3 ($upstream+$dup/2+$sin*$dup/2) ($sin*$dup/2) ($height)
11 5 3 3 ($upstream+$dup/2-$sin*$dup/2) ($sin*$dup/2) ($height)
12 3 5 3 0 ($tane*($dup/2+$upstream)) ($height)
13 5 5 3 ($fone*($dup+$upstream+$downstream)) (($fwidth*($dup+$upstream+$downstream))*$tanang) ($height)
14 3 7 3 0 (($upstream+$dup/2)/$cose+$widthtwo) ($height)
15 11 7 3 ($dup+$upstream+$downstream) (($upstream+$dup/2)/$cose+$widthtwo) ($height)
16 0 0 0 ($upstream+$dup/2) 0 ($height)
37 9 5 3 ($fthree*($dup+$upstream+$downstream)) (($fwidth*($dup+$upstream+$downstream))*$tanang) ($height)
39 7 5 3 ($ftwo*($dup+$upstream+$downstream)) (($upstream+$dup/2)/$cose) ($height)
59 7 7 3 (($dup+$upstream+$downstream)/2) (($upstream+$dup/2)/$cose+$widthtwo) ($height)

/BOTTOM
```

```
19 1 5 1 0 0 0
20 1 3 1 ($upstream) 0 0
21 1 1 1 ($upstream+($dup-$dnail)/2) 0 0
22 5 1 1 ($upstream+($dup)/2-$sin*$dnail/2) ($sin*$dnail/2) 0
23 9 1 1 ($upstream+($dup)/2+$sin*$dnail/2) ($sin*$dnail/2) 0
24 13 1 1 ($upstream+$dup/2+$dnail/2) 0 0
25 13 3 1 ($dup/2+$upstream+$dup/2) 0 0
26 13 5 1 ($dup/2+$upstream+$dup/2+$downstream) 0 0
27 11 5 1 ($dup+$upstream+$downstream) ($tane*($dup/2+$upstream)) 0
28 9 3 1 ($upstream+$dup/2+$sin*$dup/2) ($sin*$dup/2) 0
29 5 3 1 ($upstream+$dup/2-$sin*$dup/2) ($sin*$dup/2) 0
30 3 5 1 0 ($tane*($dup/2+$upstream)) 0
31 5 5 1 ($fone*($dup+$upstream+$downstream)) (($fwidth*($dup+$upstream+$downstream))*$tanang) 0
32 3 7 1 0 (($upstream+$dup/2)/$cose+$widthtwo) 0
33 11 7 1 ($dup+$upstream+$downstream) (($upstream+$dup/2)/$cose+$widthtwo) 0
34 0 0 0 ($upstream+$dup/2) 0 0
38 9 5 1 ($fthree*($dup+$upstream+$downstream)) (($fwidth*($dup+$upstream+$downstream))*$tanang) 0
40 7 5 1 ($ftwo*($dup+$upstream+$downstream)) (($upstream+$dup/2)/$cose) 0
61 7 7 1 (($dup+$upstream+$downstream)/2) (($upstream+$dup/2)/$cose+$widthtwo) (0)

LINE
/P1 P2
/TOP
41 42
43 42 .05 4
44 51 .05 4
45 50 .05 4
46 47 .05 4
48 47
48 49
50 57
51 53
41 52
52 54
54 60
55 60
49 55
/MIDDLE
1 2
3 2 .05 4
4 11 .05 4
5 10 .05 4
6 7 .05 4
8 7
8 9
10 37
11 13
1 12
12 14
14 59
15 59
9 15
/BOTTOM
19 30
19 20
21 20 .05 4
22 29 .05 4
23 28 .05 4
24 25 .05 4
26 25
27 26
27 33
32 61
33 61
30 32
29 31
28 38
/SIDES
1 19  .25 4
2 20  .25 4
```

```
3 21  .25 4
4 22  .25 4
5 23  .25 4
6 24  .25 4
7 25  .25 4
8 26  .25 4
9 27  .25 4
10 28  .25 4
11 29  .25 4
12 30  .25 4
13 31  .25 4
14 32  .25 4
15 33  .25 4
37 38  .25 4
59 61  .25 4
1 41 .33 4
2 42 .33 4
3 43 .33 4
4 44 .33 4
5 45 .33 4
6 46 .33 4
7 47 .33 4
8 48 .33 4
9 49 .33 4
10 50 .33 4
11 51 .33 4
12 52 .33 4
13 53 .33 4
39 58 .33 4
37 57 .33 4
14 54 .33 4
15 55 .33 4
59 60 .33 4

ARC
/P1 P2 CENTER
/TOP
43 44 56
44 45 56
45 46 56
42 51 56
51 50 56
50 47 56
52 53 56
53 58 56
58 57 56
57 49 56
/MIDDLE
2  11 16
3  4  16
11 10 16
4  5  16
5  6  16
10 7  16
12 13 16
13 39 16
39 37 16
37 9 16
/BOTTOM
20 29 34
21 22 34
29 28 34
22 23 34
23 24 34
28 25 34
30 31 34
31 40 34
40 38 34
38 27 34
```

```
SURFACE
/P1 P2
/TOP
42 53
43 51
44 50
45 47
51 57
50 48
52 55
/MIDDLE
2 13
3 11
4 10
11 37
10 8
5 7
12 15
/BOTTOM
20 31
21 29
22 28
29 38
28 26
23 25
30 33
/SIDES
1 20
2 21
3 22
4 23
5 24
6 25
7 26
27 8
9 33
15 32
14 30
12 19
12 31
13 38
38 9
11 31
11 22
11 20
11 28
37 28
10 23
10 25
1 42
2 43
2 51
3 44
4 45
5 46
6 47
7 48
8 49
9 57
37 50
45 10
10 47
44 11
50 11
41 12
51 13
52 13
53 39
58 37
49 15
```

52 14
54 15

AREA
/P1 P2
/P1 P2
/TOP
42 53
43 51
44 50
45 47
51 57
50 48
52 55
/MIDDLE
2 13
3 11
4 10
11 37
10 8
5 7
12 15
/BOTTOM
20 31
21 29
22 28
29 38
28 26
23 25
30 33
/SIDES
1 20
2 21
3 22
4 23
5 24
6 25
7 26
27 8
9 33
15 32
14 30
12 19
12 31
13 38
38 9
11 31
11 22
11 20
11 28
37 28
10 23
10 25
1 42
2 43
2 51
3 44
4 45
5 46
6 47
7 48
8 49
9 57
37 50
45 10
10 47
44 11
50 11
41 12
51 13

```
52 13
53 39
58 37
49 15
52 14
54 15

VOLUME
2  31
3  29
11 38
4  28
5  25
10 26
12 33
2 53
3 51
44 10
45 7
10 48
51 37
12 55

3-D
2  31
3  29
11 38
4  28
5  25
10 26
12 33
2 53
3 51
44 10
45 7
10 48
51 37
12 55

ELEMENTS(BRICK,NODES=8,ENTITY="fluid")
3 26
12 33
ELEMENTS(BRICK,NODES=8,ENTITY="slag")
43 8
54 9
ELEMENTS(BOUNDARY,ENTITY="slagoutflow")
9 55
8 49
ELEMENTS(BOUNDARY,ENTITY="outflow")
8 27
9 33
ELEMENTS(BOUNDARY,ENTITY="slaginflow")
1 52
12 54
ELEMENTS(BOUNDARY,ENTITY="inflow")
1 30
12 32
ELEMENTS(BOUNDARY,NODES=4,ENTITY="slagfree")
43 47
50 48
42 57
52 55
ELEMENTS(BOUNDARY,NODES=4,ENTITY="interface")
3 7
10 8
2 37
12 15
ELEMENTS(BOUNDARY,NODES=4,ENTITY="interface_wall")
3 7
10 8
```

```
2 37
12 15
ELEMENTS(BOUNDARY,ENTITY="symmetry")
1 20
2 21
6 25
7 26
ELEMENTS(BOUNDARY,ENTITY="slagsymmetry")
1 42
2 43
6 47
7 48
ELEMENTS(BOUNDARY,EDGE,ENTITY="edge1")
1 12
12 14
ELEMENTS(BOUNDARY,EDGE,ENTITY="edge2")
41 52
52 54
ELEMENTS(BOUNDARY,EDGE,ENTITY="interface edge")
1  2
2  3
3  4
4  5
5  6
6  7
7  8
8  9
9  15
14 15
ELEMENTS(BOUNDARY,EDGE,ENTITY="slagfree edge")
41 42
42 43
43 44
44 45
45 46
46 47
47 48
48 49
49 55
54 55
ELEMENTS(BOUNDARY,ENTITY="bottom")
21 29
20 31
30 33
29 38
22 28
23 25
28 26
ELEMENTS(BOUNDARY,ENTITY="nail")
22 3
4 23
5 24
3 44
4 45
5 46
ELEMENTS(BOUNDARY,ENTITY="farfield")
32 15
ELEMENTS(BOUNDARY,ENTITY="slagfarfield")
14 55
BCNODE(COORDINATE)
1
19
41
8
26
48
14
32
54
15
```

```
33
55
3
21
43
6
24
46
12
30
52
9
27
49
END

FIPREP
PROBLEM(3-D,TURBULENT,NONLINEAR)
PRESSURE(MIXED,DISCONTINUOUS)
EXECUTION(NEWJOB)
SOLUTION(SEGREGATED=5000,VELC=0.001,RESCONV=0.001,schange=0)

ENTITY(outflow,NAME="outflow")
ENTITY(outflow,NAME="slagoutflow")
ENTITY(FLUID,NAME="slag",MDENS=1,MVISC=1)
ENTITY(FLUID,NAME="fluid",MDENS=2,MVISC=2)
ENTITY(WALL,NAME="nail")
ENTITY(PLOT,NAME="symmetry")
ENTITY(PLOT,NAME="slagsymmetry")
ENTITY(PLOT,NAME="bottom")
ENTITY(PLOT,NAME="slagfarfield")
ENTITY(PLOT,NAME="farfield")
ENTITY(outflow,NAME="slaginflow")
ENTITY(outflow,NAME="inflow")
ENTITY(SURFACE,NAME="slagfree",SPINES,STRAIGHT,DEPTH=0,CONTINUE,MSURF=1)
ENTITY(WALL,NAME="interface_wall",ATTACH="fluid",NATTACH="slag")
ENTITY(SURFACE,NAME="interface",DEPTH=-1,NATTACH="fluid",ATTACH="slag",SPINES,STRAIGHT,MSURF=2)
ENTITY(PLOT,NAME="edge1")
ENTITY(PLOT,NAME="edge2")
ENTITY(PLOT,NAME="interface edge")
ENTITY(PLOT,NAME="slagfree edge")

DENSITY(SET="1",CONSTANT=$slagdensity)
VISCOSITY(SET="1",CONSTANT=$slagvisc,TWO-EQUATION)
SURFACETENSION(SET="1",CONSTANT=$slagst)
DENSITY(SET="2",CONSTANT=$steeldensity)
VISCOSITY(SET="2",CONSTANT=$steelvisc,TWO-EQUATION)
SURFACETENSION(SET="2",CONST=$steelst)
OPTION(SIDES)
BODYFORCE(ENTITY="slag",CONSTANT,FX=0.,FY=0,FZ=-9.81)
BODYFORCE(ENTITY="fluid",CONSTANT,FX=0.,FY=0,FZ=-9.81)

//Boundary Conditions
BCNODE(UZ,ZERO,ENTITY="slagfree")
BCNODE(UZ,ZERO,ENTITY="interface")
BCNODE(VELOCITY,ZERO,ENTITY="nail")
BCNODE(UZ,ZERO,ENTITY="bottom")
BCNODE(UY,ZERO,ENTITY="farfield")
BCNODE(UY,ZERO,ENTITY="slagfarfield")
BCNODE(UY,ZERO,ENTITY="symmetry")
BCNODE(UY,ZERO,ENTITY="slagsymmetry")
BCNODE(UX,NODE=401,CONSTANT=$one)
BCNODE(UX,NODE=402,CONSTANT=$one)
BCNODE(UX,NODE=403,CONSTANT=$one)
BCNODE(UX,NODE=404,CONSTANT=$one)
BCNODE(UX,NODE=405,CONSTANT=$one)
BCNODE(UX,NODE=426,CONSTANT=$one)
BCNODE(UX,NODE=443,CONSTANT=$one)
BCNODE(UX,NODE=460,CONSTANT=$one)
BCNODE(UX,NODE=477,CONSTANT=$one)
```

```
BCNODE(UX,NODE=494,CONSTANT=$one)
BCNODE(UX,NODE=511,CONSTANT=$one)
BCNODE(UX,NODE=928,CONSTANT=$two)
BCNODE(UX,NODE=929,CONSTANT=$two)
BCNODE(UX,NODE=930,CONSTANT=$two)
BCNODE(UX,NODE=931,CONSTANT=$two)
BCNODE(UX,NODE=932,CONSTANT=$two)
BCNODE(UX,NODE=953,CONSTANT=$two)
BCNODE(UX,NODE=970,CONSTANT=$two)
BCNODE(UX,NODE=987,CONSTANT=$two)
BCNODE(UX,NODE=1004,CONSTANT=$two)
BCNODE(UX,NODE=1021,CONSTANT=$two)
BCNODE(UX,NODE=1038,CONSTANT=$two)
BCNODE(UX,NODE=1455,CONSTANT=$three)
BCNODE(UX,NODE=1456,CONSTANT=$three)
BCNODE(UX,NODE=1457,CONSTANT=$three)
BCNODE(UX,NODE=1458,CONSTANT=$three)
BCNODE(UX,NODE=1459,CONSTANT=$three)
BCNODE(UX,NODE=1480,CONSTANT=$three)
BCNODE(UX,NODE=1497,CONSTANT=$three)
BCNODE(UX,NODE=1514,CONSTANT=$three)
BCNODE(UX,NODE=1531,CONSTANT=$three)
BCNODE(UX,NODE=1548,CONSTANT=$three)
BCNODE(UX,NODE=1565,CONSTANT=$three)
BCNODE(UX,NODE=1982,CONSTANT=$four)
BCNODE(UX,NODE=1983,CONSTANT=$four)
BCNODE(UX,NODE=1984,CONSTANT=$four)
BCNODE(UX,NODE=1985,CONSTANT=$four)
BCNODE(UX,NODE=1986,CONSTANT=$four)
BCNODE(UX,NODE=2007,CONSTANT=$four)
BCNODE(UX,NODE=2024,CONSTANT=$four)
BCNODE(UX,NODE=2041,CONSTANT=$four)
BCNODE(UX,NODE=2058,CONSTANT=$four)
BCNODE(UX,NODE=2075,CONSTANT=$four)
BCNODE(UX,NODE=2092,CONSTANT=$four)
BCNODE(UX,NODE=2509,CONSTANT=$five)
BCNODE(UX,NODE=2510,CONSTANT=$five)
BCNODE(UX,NODE=2511,CONSTANT=$five)
BCNODE(UX,NODE=2512,CONSTANT=$five)
BCNODE(UX,NODE=2513,CONSTANT=$five)
BCNODE(UX,NODE=2534,CONSTANT=$five)
BCNODE(UX,NODE=2551,CONSTANT=$five)
BCNODE(UX,NODE=2568,CONSTANT=$five)
BCNODE(UX,NODE=2585,CONSTANT=$five)
BCNODE(UX,NODE=2602,CONSTANT=$five)
BCNODE(UX,NODE=2619,CONSTANT=$five)
BCNODE(UX,NODE=3036,CONSTANT=$six)
BCNODE(UX,NODE=3037,CONSTANT=$six)
BCNODE(UX,NODE=3038,CONSTANT=$six)
BCNODE(UX,NODE=3039,CONSTANT=$six)
BCNODE(UX,NODE=3040,CONSTANT=$six)
BCNODE(UX,NODE=3061,CONSTANT=$six)
BCNODE(UX,NODE=3078,CONSTANT=$six)
BCNODE(UX,NODE=3095,CONSTANT=$six)
BCNODE(UX,NODE=3112,CONSTANT=$six)
BCNODE(UX,NODE=3129,CONSTANT=$six)
BCNODE(UX,NODE=3146,CONSTANT=$six)
BCNODE(UX,NODE=3563,CONSTANT=$seven)
BCNODE(UX,NODE=3564,CONSTANT=$seven)
BCNODE(UX,NODE=3565,CONSTANT=$seven)
BCNODE(UX,NODE=3566,CONSTANT=$seven)
BCNODE(UX,NODE=3567,CONSTANT=$seven)
BCNODE(UX,NODE=3588,CONSTANT=$seven)
BCNODE(UX,NODE=3605,CONSTANT=$seven)
BCNODE(UX,NODE=3622,CONSTANT=$seven)
BCNODE(UX,NODE=3639,CONSTANT=$seven)
BCNODE(UX,NODE=3656,CONSTANT=$seven)
BCNODE(UX,NODE=3673,CONSTANT=$seven)
BCNODE(UX,NODE=4090,CONSTANT=$eight)
BCNODE(UX,NODE=4091,CONSTANT=$eight)
```

```
BCNODE(UX,NODE=4092,CONSTANT=$eight)
BCNODE(UX,NODE=4093,CONSTANT=$eight)
BCNODE(UX,NODE=4094,CONSTANT=$eight)
BCNODE(UX,NODE=4115,CONSTANT=$eight)
BCNODE(UX,NODE=4132,CONSTANT=$eight)
BCNODE(UX,NODE=4149,CONSTANT=$eight)
BCNODE(UX,NODE=4166,CONSTANT=$eight)
BCNODE(UX,NODE=4183,CONSTANT=$eight)
BCNODE(UX,NODE=4200,CONSTANT=$eight)
BCNODE(UX,NODE=4617,CONSTANT=$nine)
BCNODE(UX,NODE=4618,CONSTANT=$nine)
BCNODE(UX,NODE=4619,CONSTANT=$nine)
BCNODE(UX,NODE=4620,CONSTANT=$nine)
BCNODE(UX,NODE=4621,CONSTANT=$nine)
BCNODE(UX,NODE=4642,CONSTANT=$nine)
BCNODE(UX,NODE=4659,CONSTANT=$nine)
BCNODE(UX,NODE=4676,CONSTANT=$nine)
BCNODE(UX,NODE=4693,CONSTANT=$nine)
BCNODE(UX,NODE=4710,CONSTANT=$nine)
BCNODE(UX,NODE=4727,CONSTANT=$nine)
BCNODE(UX,NODE=5144,CONSTANT=$ten)
BCNODE(UX,NODE=5145,CONSTANT=$ten)
BCNODE(UX,NODE=5146,CONSTANT=$ten)
BCNODE(UX,NODE=5147,CONSTANT=$ten)
BCNODE(UX,NODE=5148,CONSTANT=$ten)
BCNODE(UX,NODE=5169,CONSTANT=$ten)
BCNODE(UX,NODE=5186,CONSTANT=$ten)
BCNODE(UX,NODE=5203,CONSTANT=$ten)
BCNODE(UX,NODE=5220,CONSTANT=$ten)
BCNODE(UX,NODE=5237,CONSTANT=$ten)
BCNODE(UX,NODE=5254,CONSTANT=$ten)
BCNODE(UX,NODE=5671,CONSTANT=$eleven)
BCNODE(UX,NODE=5672,CONSTANT=$eleven)
BCNODE(UX,NODE=5673,CONSTANT=$eleven)
BCNODE(UX,NODE=5674,CONSTANT=$eleven)
BCNODE(UX,NODE=5675,CONSTANT=$eleven)
BCNODE(UX,NODE=5696,CONSTANT=$eleven)
BCNODE(UX,NODE=5713,CONSTANT=$eleven)
BCNODE(UX,NODE=5730,CONSTANT=$eleven)
BCNODE(UX,NODE=5747,CONSTANT=$eleven)
BCNODE(UX,NODE=5764,CONSTANT=$eleven)
BCNODE(UX,NODE=5781,CONSTANT=$eleven)
BCNODE(UX,NODE=6198,CONSTANT=$twelve)
BCNODE(UX,NODE=6199,CONSTANT=$twelve)
BCNODE(UX,NODE=6200,CONSTANT=$twelve)
BCNODE(UX,NODE=6201,CONSTANT=$twelve)
BCNODE(UX,NODE=6202,CONSTANT=$twelve)
BCNODE(UX,NODE=6223,CONSTANT=$twelve)
BCNODE(UX,NODE=6240,CONSTANT=$twelve)
BCNODE(UX,NODE=6257,CONSTANT=$twelve)
BCNODE(UX,NODE=6274,CONSTANT=$twelve)
BCNODE(UX,NODE=6291,CONSTANT=$twelve)
BCNODE(UX,NODE=6308,CONSTANT=$twelve)
BCNODE(UX,NODE=6725,CONSTANT=$thirteen)
BCNODE(UX,NODE=6726,CONSTANT=$thirteen)
BCNODE(UX,NODE=6727,CONSTANT=$thirteen)
BCNODE(UX,NODE=6728,CONSTANT=$thirteen)
BCNODE(UX,NODE=6729,CONSTANT=$thirteen)
BCNODE(UX,NODE=6750,CONSTANT=$thirteen)
BCNODE(UX,NODE=6767,CONSTANT=$thirteen)
BCNODE(UX,NODE=6784,CONSTANT=$thirteen)
BCNODE(UX,NODE=6801,CONSTANT=$thirteen)
BCNODE(UX,NODE=6818,CONSTANT=$thirteen)
BCNODE(UX,NODE=6835,CONSTANT=$thirteen)

BCNODE(KINETIC,NODE=401,CONSTANT=$oneK)
BCNODE(KINETIC,NODE=402,CONSTANT=$oneK)
BCNODE(KINETIC,NODE=403,CONSTANT=$oneK)
BCNODE(KINETIC,NODE=404,CONSTANT=$oneK)
BCNODE(KINETIC,NODE=405,CONSTANT=$oneK)
```

```
BCNODE(KINETIC,NODE=426,CONSTANT=$oneK)
BCNODE(KINETIC,NODE=443,CONSTANT=$oneK)
BCNODE(KINETIC,NODE=460,CONSTANT=$oneK)
BCNODE(KINETIC,NODE=477,CONSTANT=$oneK)
BCNODE(KINETIC,NODE=494,CONSTANT=$oneK)
BCNODE(KINETIC,NODE=511,CONSTANT=$oneK)
BCNODE(KINETIC,NODE=928,CONSTANT=$twoK)
BCNODE(KINETIC,NODE=929,CONSTANT=$twoK)
BCNODE(KINETIC,NODE=930,CONSTANT=$twoK)
BCNODE(KINETIC,NODE=931,CONSTANT=$twoK)
BCNODE(KINETIC,NODE=932,CONSTANT=$twoK)
BCNODE(KINETIC,NODE=953,CONSTANT=$twoK)
BCNODE(KINETIC,NODE=970,CONSTANT=$twoK)
BCNODE(KINETIC,NODE=987,CONSTANT=$twoK)
BCNODE(KINETIC,NODE=1004,CONSTANT=$twoK)
BCNODE(KINETIC,NODE=1021,CONSTANT=$twoK)
BCNODE(KINETIC,NODE=1038,CONSTANT=$twoK)
BCNODE(KINETIC,NODE=1455,CONSTANT=$threeK)
BCNODE(KINETIC,NODE=1456,CONSTANT=$threeK)
BCNODE(KINETIC,NODE=1457,CONSTANT=$threeK)
BCNODE(KINETIC,NODE=1458,CONSTANT=$threeK)
BCNODE(KINETIC,NODE=1459,CONSTANT=$threeK)
BCNODE(KINETIC,NODE=1480,CONSTANT=$threeK)
BCNODE(KINETIC,NODE=1497,CONSTANT=$threeK)
BCNODE(KINETIC,NODE=1514,CONSTANT=$threeK)
BCNODE(KINETIC,NODE=1531,CONSTANT=$threeK)
BCNODE(KINETIC,NODE=1548,CONSTANT=$threeK)
BCNODE(KINETIC,NODE=1565,CONSTANT=$threeK)
BCNODE(KINETIC,NODE=1982,CONSTANT=$fourK)
BCNODE(KINETIC,NODE=1983,CONSTANT=$fourK)
BCNODE(KINETIC,NODE=1984,CONSTANT=$fourK)
BCNODE(KINETIC,NODE=1985,CONSTANT=$fourK)
BCNODE(KINETIC,NODE=1986,CONSTANT=$fourK)
BCNODE(KINETIC,NODE=2007,CONSTANT=$fourK)
BCNODE(KINETIC,NODE=2024,CONSTANT=$fourK)
BCNODE(KINETIC,NODE=2041,CONSTANT=$fourK)
BCNODE(KINETIC,NODE=2058,CONSTANT=$fourK)
BCNODE(KINETIC,NODE=2075,CONSTANT=$fourK)
BCNODE(KINETIC,NODE=2092,CONSTANT=$fourK)
BCNODE(KINETIC,NODE=2509,CONSTANT=$fiveK)
BCNODE(KINETIC,NODE=2510,CONSTANT=$fiveK)
BCNODE(KINETIC,NODE=2511,CONSTANT=$fiveK)
BCNODE(KINETIC,NODE=2512,CONSTANT=$fiveK)
BCNODE(KINETIC,NODE=2513,CONSTANT=$fiveK)
BCNODE(KINETIC,NODE=2534,CONSTANT=$fiveK)
BCNODE(KINETIC,NODE=2551,CONSTANT=$fiveK)
BCNODE(KINETIC,NODE=2568,CONSTANT=$fiveK)
BCNODE(KINETIC,NODE=2585,CONSTANT=$fiveK)
BCNODE(KINETIC,NODE=2602,CONSTANT=$fiveK)
BCNODE(KINETIC,NODE=2619,CONSTANT=$fiveK)
BCNODE(KINETIC,NODE=3036,CONSTANT=$sixK)
BCNODE(KINETIC,NODE=3037,CONSTANT=$sixK)
BCNODE(KINETIC,NODE=3038,CONSTANT=$sixK)
BCNODE(KINETIC,NODE=3039,CONSTANT=$sixK)
BCNODE(KINETIC,NODE=3040,CONSTANT=$sixK)
BCNODE(KINETIC,NODE=3061,CONSTANT=$sixK)
BCNODE(KINETIC,NODE=3078,CONSTANT=$sixK)
BCNODE(KINETIC,NODE=3095,CONSTANT=$sixK)
BCNODE(KINETIC,NODE=3112,CONSTANT=$sixK)
BCNODE(KINETIC,NODE=3129,CONSTANT=$sixK)
BCNODE(KINETIC,NODE=3146,CONSTANT=$sixK)
BCNODE(KINETIC,NODE=3563,CONSTANT=$sevenK)
BCNODE(KINETIC,NODE=3564,CONSTANT=$sevenK)
BCNODE(KINETIC,NODE=3565,CONSTANT=$sevenK)
BCNODE(KINETIC,NODE=3566,CONSTANT=$sevenK)
BCNODE(KINETIC,NODE=3567,CONSTANT=$sevenK)
BCNODE(KINETIC,NODE=3588,CONSTANT=$sevenK)
BCNODE(KINETIC,NODE=3605,CONSTANT=$sevenK)
BCNODE(KINETIC,NODE=3622,CONSTANT=$sevenK)
BCNODE(KINETIC,NODE=3639,CONSTANT=$sevenK)
```

```
BCNODE(KINETIC,NODE=3656,CONSTANT=$sevenK)
BCNODE(KINETIC,NODE=3673,CONSTANT=$sevenK)
BCNODE(KINETIC,NODE=4090,CONSTANT=$eightK)
BCNODE(KINETIC,NODE=4091,CONSTANT=$eightK)
BCNODE(KINETIC,NODE=4092,CONSTANT=$eightK)
BCNODE(KINETIC,NODE=4093,CONSTANT=$eightK)
BCNODE(KINETIC,NODE=4094,CONSTANT=$eightK)
BCNODE(KINETIC,NODE=4115,CONSTANT=$eightK)
BCNODE(KINETIC,NODE=4132,CONSTANT=$eightK)
BCNODE(KINETIC,NODE=4149,CONSTANT=$eightK)
BCNODE(KINETIC,NODE=4166,CONSTANT=$eightK)
BCNODE(KINETIC,NODE=4183,CONSTANT=$eightK)
BCNODE(KINETIC,NODE=4200,CONSTANT=$eightK)
BCNODE(KINETIC,NODE=4617,CONSTANT=$nineK)
BCNODE(KINETIC,NODE=4618,CONSTANT=$nineK)
BCNODE(KINETIC,NODE=4619,CONSTANT=$nineK)
BCNODE(KINETIC,NODE=4620,CONSTANT=$nineK)
BCNODE(KINETIC,NODE=4621,CONSTANT=$nineK)
BCNODE(KINETIC,NODE=4642,CONSTANT=$nineK)
BCNODE(KINETIC,NODE=4659,CONSTANT=$nineK)
BCNODE(KINETIC,NODE=4676,CONSTANT=$nineK)
BCNODE(KINETIC,NODE=4693,CONSTANT=$nineK)
BCNODE(KINETIC,NODE=4710,CONSTANT=$nineK)
BCNODE(KINETIC,NODE=4727,CONSTANT=$nineK)
BCNODE(KINETIC,NODE=5144,CONSTANT=$tenK)
BCNODE(KINETIC,NODE=5145,CONSTANT=$tenK)
BCNODE(KINETIC,NODE=5146,CONSTANT=$tenK)
BCNODE(KINETIC,NODE=5147,CONSTANT=$tenK)
BCNODE(KINETIC,NODE=5148,CONSTANT=$tenK)
BCNODE(KINETIC,NODE=5169,CONSTANT=$tenK)
BCNODE(KINETIC,NODE=5186,CONSTANT=$tenK)
BCNODE(KINETIC,NODE=5203,CONSTANT=$tenK)
BCNODE(KINETIC,NODE=5220,CONSTANT=$tenK)
BCNODE(KINETIC,NODE=5237,CONSTANT=$tenK)
BCNODE(KINETIC,NODE=5254,CONSTANT=$tenK)
BCNODE(KINETIC,NODE=5671,CONSTANT=$elevenK)
BCNODE(KINETIC,NODE=5672,CONSTANT=$elevenK)
BCNODE(KINETIC,NODE=5673,CONSTANT=$elevenK)
BCNODE(KINETIC,NODE=5674,CONSTANT=$elevenK)
BCNODE(KINETIC,NODE=5675,CONSTANT=$elevenK)
BCNODE(KINETIC,NODE=5696,CONSTANT=$elevenK)
BCNODE(KINETIC,NODE=5713,CONSTANT=$elevenK)
BCNODE(KINETIC,NODE=5730,CONSTANT=$elevenK)
BCNODE(KINETIC,NODE=5747,CONSTANT=$elevenK)
BCNODE(KINETIC,NODE=5764,CONSTANT=$elevenK)
BCNODE(KINETIC,NODE=5781,CONSTANT=$elevenK)
BCNODE(KINETIC,NODE=6198,CONSTANT=$twelveK)
BCNODE(KINETIC,NODE=6199,CONSTANT=$twelveK)
BCNODE(KINETIC,NODE=6200,CONSTANT=$twelveK)
BCNODE(KINETIC,NODE=6201,CONSTANT=$twelveK)
BCNODE(KINETIC,NODE=6202,CONSTANT=$twelveK)
BCNODE(KINETIC,NODE=6223,CONSTANT=$twelveK)
BCNODE(KINETIC,NODE=6240,CONSTANT=$twelveK)
BCNODE(KINETIC,NODE=6257,CONSTANT=$twelveK)
BCNODE(KINETIC,NODE=6274,CONSTANT=$twelveK)
BCNODE(KINETIC,NODE=6291,CONSTANT=$twelveK)
BCNODE(KINETIC,NODE=6308,CONSTANT=$twelveK)
BCNODE(KINETIC,NODE=6725,CONSTANT=$thirteenK)
BCNODE(KINETIC,NODE=6726,CONSTANT=$thirteenK)
BCNODE(KINETIC,NODE=6727,CONSTANT=$thirteenK)
BCNODE(KINETIC,NODE=6728,CONSTANT=$thirteenK)
BCNODE(KINETIC,NODE=6729,CONSTANT=$thirteenK)
BCNODE(KINETIC,NODE=6750,CONSTANT=$thirteenK)
BCNODE(KINETIC,NODE=6767,CONSTANT=$thirteenK)
BCNODE(KINETIC,NODE=6784,CONSTANT=$thirteenK)
BCNODE(KINETIC,NODE=6801,CONSTANT=$thirteenK)
BCNODE(KINETIC,NODE=6818,CONSTANT=$thirteenK)
BCNODE(KINETIC,NODE=6835,CONSTANT=$thirteenK)

BCNODE(DISSIPATION,NODE=401,CONSTANT=$oneD)
```

```
BCNODE(DISSIPATION,NODE=402,CONSTANT=$oneD)
BCNODE(DISSIPATION,NODE=403,CONSTANT=$oneD)
BCNODE(DISSIPATION,NODE=404,CONSTANT=$oneD)
BCNODE(DISSIPATION,NODE=405,CONSTANT=$oneD)
BCNODE(DISSIPATION,NODE=426,CONSTANT=$oneD)
BCNODE(DISSIPATION,NODE=443,CONSTANT=$oneD)
BCNODE(DISSIPATION,NODE=460,CONSTANT=$oneD)
BCNODE(DISSIPATION,NODE=477,CONSTANT=$oneD)
BCNODE(DISSIPATION,NODE=494,CONSTANT=$oneD)
BCNODE(DISSIPATION,NODE=511,CONSTANT=$oneD)
BCNODE(DISSIPATION,NODE=928,CONSTANT=$twoD)
BCNODE(DISSIPATION,NODE=929,CONSTANT=$twoD)
BCNODE(DISSIPATION,NODE=930,CONSTANT=$twoD)
BCNODE(DISSIPATION,NODE=931,CONSTANT=$twoD)
BCNODE(DISSIPATION,NODE=932,CONSTANT=$twoD)
BCNODE(DISSIPATION,NODE=953,CONSTANT=$twoD)
BCNODE(DISSIPATION,NODE=970,CONSTANT=$twoD)
BCNODE(DISSIPATION,NODE=987,CONSTANT=$twoD)
BCNODE(DISSIPATION,NODE=1004,CONSTANT=$twoD)
BCNODE(DISSIPATION,NODE=1021,CONSTANT=$twoD)
BCNODE(DISSIPATION,NODE=1038,CONSTANT=$twoD)
BCNODE(DISSIPATION,NODE=1455,CONSTANT=$threeD)
BCNODE(DISSIPATION,NODE=1456,CONSTANT=$threeD)
BCNODE(DISSIPATION,NODE=1457,CONSTANT=$threeD)
BCNODE(DISSIPATION,NODE=1458,CONSTANT=$threeD)
BCNODE(DISSIPATION,NODE=1459,CONSTANT=$threeD)
BCNODE(DISSIPATION,NODE=1480,CONSTANT=$threeD)
BCNODE(DISSIPATION,NODE=1497,CONSTANT=$threeD)
BCNODE(DISSIPATION,NODE=1514,CONSTANT=$threeD)
BCNODE(DISSIPATION,NODE=1531,CONSTANT=$threeD)
BCNODE(DISSIPATION,NODE=1548,CONSTANT=$threeD)
BCNODE(DISSIPATION,NODE=1565,CONSTANT=$threeD)
BCNODE(DISSIPATION,NODE=1982,CONSTANT=$fourD)
BCNODE(DISSIPATION,NODE=1983,CONSTANT=$fourD)
BCNODE(DISSIPATION,NODE=1984,CONSTANT=$fourD)
BCNODE(DISSIPATION,NODE=1985,CONSTANT=$fourD)
BCNODE(DISSIPATION,NODE=1986,CONSTANT=$fourD)
BCNODE(DISSIPATION,NODE=2007,CONSTANT=$fourD)
BCNODE(DISSIPATION,NODE=2024,CONSTANT=$fourD)
BCNODE(DISSIPATION,NODE=2041,CONSTANT=$fourD)
BCNODE(DISSIPATION,NODE=2058,CONSTANT=$fourD)
BCNODE(DISSIPATION,NODE=2075,CONSTANT=$fourD)
BCNODE(DISSIPATION,NODE=2092,CONSTANT=$fourD)
BCNODE(DISSIPATION,NODE=2509,CONSTANT=$fiveD)
BCNODE(DISSIPATION,NODE=2510,CONSTANT=$fiveD)
BCNODE(DISSIPATION,NODE=2511,CONSTANT=$fiveD)
BCNODE(DISSIPATION,NODE=2512,CONSTANT=$fiveD)
BCNODE(DISSIPATION,NODE=2513,CONSTANT=$fiveD)
BCNODE(DISSIPATION,NODE=2534,CONSTANT=$fiveD)
BCNODE(DISSIPATION,NODE=2551,CONSTANT=$fiveD)
BCNODE(DISSIPATION,NODE=2568,CONSTANT=$fiveD)
BCNODE(DISSIPATION,NODE=2585,CONSTANT=$fiveD)
BCNODE(DISSIPATION,NODE=2602,CONSTANT=$fiveD)
BCNODE(DISSIPATION,NODE=2619,CONSTANT=$fiveD)
BCNODE(DISSIPATION,NODE=3036,CONSTANT=$sixD)
BCNODE(DISSIPATION,NODE=3037,CONSTANT=$sixD)
BCNODE(DISSIPATION,NODE=3038,CONSTANT=$sixD)
BCNODE(DISSIPATION,NODE=3039,CONSTANT=$sixD)
BCNODE(DISSIPATION,NODE=3040,CONSTANT=$sixD)
BCNODE(DISSIPATION,NODE=3061,CONSTANT=$sixD)
BCNODE(DISSIPATION,NODE=3078,CONSTANT=$sixD)
BCNODE(DISSIPATION,NODE=3095,CONSTANT=$sixD)
BCNODE(DISSIPATION,NODE=3112,CONSTANT=$sixD)
BCNODE(DISSIPATION,NODE=3129,CONSTANT=$sixD)
BCNODE(DISSIPATION,NODE=3146,CONSTANT=$sixD)
BCNODE(DISSIPATION,NODE=3563,CONSTANT=$sevenD)
BCNODE(DISSIPATION,NODE=3564,CONSTANT=$sevenD)
BCNODE(DISSIPATION,NODE=3565,CONSTANT=$sevenD)
BCNODE(DISSIPATION,NODE=3566,CONSTANT=$sevenD)
BCNODE(DISSIPATION,NODE=3567,CONSTANT=$sevenD)
```

```
BCNODE(DISSIPATION,NODE=3588,CONSTANT=$sevenD)
BCNODE(DISSIPATION,NODE=3605,CONSTANT=$sevenD)
BCNODE(DISSIPATION,NODE=3622,CONSTANT=$sevenD)
BCNODE(DISSIPATION,NODE=3639,CONSTANT=$sevenD)
BCNODE(DISSIPATION,NODE=3656,CONSTANT=$sevenD)
BCNODE(DISSIPATION,NODE=3673,CONSTANT=$sevenD)
BCNODE(DISSIPATION,NODE=4090,CONSTANT=$eightD)
BCNODE(DISSIPATION,NODE=4091,CONSTANT=$eightD)
BCNODE(DISSIPATION,NODE=4092,CONSTANT=$eightD)
BCNODE(DISSIPATION,NODE=4093,CONSTANT=$eightD)
BCNODE(DISSIPATION,NODE=4094,CONSTANT=$eightD)
BCNODE(DISSIPATION,NODE=4115,CONSTANT=$eightD)
BCNODE(DISSIPATION,NODE=4132,CONSTANT=$eightD)
BCNODE(DISSIPATION,NODE=4149,CONSTANT=$eightD)
BCNODE(DISSIPATION,NODE=4166,CONSTANT=$eightD)
BCNODE(DISSIPATION,NODE=4183,CONSTANT=$eightD)
BCNODE(DISSIPATION,NODE=4200,CONSTANT=$eightD)
BCNODE(DISSIPATION,NODE=4617,CONSTANT=$nineD)
BCNODE(DISSIPATION,NODE=4618,CONSTANT=$nineD)
BCNODE(DISSIPATION,NODE=4619,CONSTANT=$nineD)
BCNODE(DISSIPATION,NODE=4620,CONSTANT=$nineD)
BCNODE(DISSIPATION,NODE=4621,CONSTANT=$nineD)
BCNODE(DISSIPATION,NODE=4642,CONSTANT=$nineD)
BCNODE(DISSIPATION,NODE=4659,CONSTANT=$nineD)
BCNODE(DISSIPATION,NODE=4676,CONSTANT=$nineD)
BCNODE(DISSIPATION,NODE=4693,CONSTANT=$nineD)
BCNODE(DISSIPATION,NODE=4710,CONSTANT=$nineD)
BCNODE(DISSIPATION,NODE=4727,CONSTANT=$nineD)
BCNODE(DISSIPATION,NODE=5144,CONSTANT=$tenD)
BCNODE(DISSIPATION,NODE=5145,CONSTANT=$tenD)
BCNODE(DISSIPATION,NODE=5146,CONSTANT=$tenD)
BCNODE(DISSIPATION,NODE=5147,CONSTANT=$tenD)
BCNODE(DISSIPATION,NODE=5148,CONSTANT=$tenD)
BCNODE(DISSIPATION,NODE=5169,CONSTANT=$tenD)
BCNODE(DISSIPATION,NODE=5186,CONSTANT=$tenD)
BCNODE(DISSIPATION,NODE=5203,CONSTANT=$tenD)
BCNODE(DISSIPATION,NODE=5220,CONSTANT=$tenD)
BCNODE(DISSIPATION,NODE=5237,CONSTANT=$tenD)
BCNODE(DISSIPATION,NODE=5254,CONSTANT=$tenD)
BCNODE(DISSIPATION,NODE=5671,CONSTANT=$elevenD)
BCNODE(DISSIPATION,NODE=5672,CONSTANT=$elevenD)
BCNODE(DISSIPATION,NODE=5673,CONSTANT=$elevenD)
BCNODE(DISSIPATION,NODE=5674,CONSTANT=$elevenD)
BCNODE(DISSIPATION,NODE=5675,CONSTANT=$elevenD)
BCNODE(DISSIPATION,NODE=5696,CONSTANT=$elevenD)
BCNODE(DISSIPATION,NODE=5713,CONSTANT=$elevenD)
BCNODE(DISSIPATION,NODE=5730,CONSTANT=$elevenD)
BCNODE(DISSIPATION,NODE=5747,CONSTANT=$elevenD)
BCNODE(DISSIPATION,NODE=5764,CONSTANT=$elevenD)
BCNODE(DISSIPATION,NODE=5781,CONSTANT=$elevenD)
BCNODE(DISSIPATION,NODE=6198,CONSTANT=$twelveD)
BCNODE(DISSIPATION,NODE=6199,CONSTANT=$twelveD)
BCNODE(DISSIPATION,NODE=6200,CONSTANT=$twelveD)
BCNODE(DISSIPATION,NODE=6201,CONSTANT=$twelveD)
BCNODE(DISSIPATION,NODE=6202,CONSTANT=$twelveD)
BCNODE(DISSIPATION,NODE=6223,CONSTANT=$twelveD)
BCNODE(DISSIPATION,NODE=6240,CONSTANT=$twelveD)
BCNODE(DISSIPATION,NODE=6257,CONSTANT=$twelveD)
BCNODE(DISSIPATION,NODE=6274,CONSTANT=$twelveD)
BCNODE(DISSIPATION,NODE=6291,CONSTANT=$twelveD)
BCNODE(DISSIPATION,NODE=6308,CONSTANT=$twelveD)
BCNODE(DISSIPATION,NODE=6725,CONSTANT=$thirteenD)
BCNODE(DISSIPATION,NODE=6726,CONSTANT=$thirteenD)
BCNODE(DISSIPATION,NODE=6727,CONSTANT=$thirteenD)
BCNODE(DISSIPATION,NODE=6728,CONSTANT=$thirteenD)
BCNODE(DISSIPATION,NODE=6729,CONSTANT=$thirteenD)
BCNODE(DISSIPATION,NODE=6750,CONSTANT=$thirteenD)
BCNODE(DISSIPATION,NODE=6767,CONSTANT=$thirteenD)
BCNODE(DISSIPATION,NODE=6784,CONSTANT=$thirteenD)
BCNODE(DISSIPATION,NODE=6801,CONSTANT=$thirteenD)
```

```
BCNODE(DISSIPATION,NODE=6818,CONSTANT=$thirteenD)
BCNODE(DISSIPATION,NODE=6835,CONSTANT=$thirteenD)

BCNODE(UY,ZERO,ENTITY="inflow")
BCNODE(UZ,ZERO,ENTITY="inflow")
BCNODE(UY,ZERO,ENTITY="slaginflow")
BCNODE(UZ,ZERO,ENTITY="slaginflow")
BCNODE(UX,ZERO,ENTITY="slagfree")
BCNODE(UY,ZERO,ENTITY="slagfree")
BCNODE(COORDINATE,ENTITY="edge1",CONSTANT=1)
BCNODE(COORDINATE,ENTITY="edge2",CONSTANT=1)
BCNODE(COORDINATE,ENTITY="slagfree edge",CONSTANT=1)
BCNODE(COORDINATE,ENTITY="interface edge",CONSTANT=1)
BCSYSTEM(SET=1,EDGE)

ICNODE(UX,ENTITY="fluid",CONSTANT=$invel)
ICNODE(KINETIC,ENTITY="fluid",CONSTANT=$kine)
ICNODE(DISSIPATION,ENTITY="fluid",CONSTANT=$DISS)
ICNODE(UX,ENTITY="slag",CONSTANT=$slaginvel)
ICNODE(KINETIC,ENTITY="slag",CONSTANT=$slagkine)
ICNODE(DISSIPATION,ENTITY="slag",CONSTANT=$SLAGDISS)

RELAXATION(HYBRID)
0.6 0.6 0.6 0.9 0.3 0.75 0.75 0.75 0.75
END

CREATE(FISOLV)
RUN(FISOLV)
```

C.2.6: Slag Model Second, Transient Simulation Input File

(Sample file is for the 0.010 m nail diameter, 0.3 m/s inlet velocity case)

```
FIPREP
EXECUTION(NEWJOB)
FILES(RENAME,FROM="10-3.FDPOST",TO="10-3.FDREST")
SOLU(ENTRY=1,REPLACE,SEGRE=1000,CR=2000,CGS=2000,VELC=0.001,NCGC=1e-6,SCGC=1e-6,SCHANGE=0)
PROBLEM(ENTRY=1,REPLACE,3-D,TURBULENT,transient,NONLINEAR,FREE)

TIMEINTEGRATION(DT=0.0003,TSTART=0,NSTEPS=10001,FIXED)
POSTPROCESS(NBLOCKS=2)
1 500 5
501 10001 100
PRINTOUT(NBLOCKS=1)
1 10001 10000

BCNODE(CONTACTANGLE,ENTITY="slagfree",CONSTANT=90)
BCNODE(CONTACTANGLE,ENTITY="interface",CONSTANT=90)
BCNODE(UZ,FREE,ENTITY="slagfree edge")
BCNODE(UZ,FREE,ENTITY="interface edge")

BCNODE(ENTRY=1,DELETE)
BCNODE(ENTRY=2,DELETE)
BCNODE(SURFACE,ZERO,ENTITY="edge1")
BCNODE(SURFACE,ZERO,ENTITY="edge2")

ICNODE(ENTRY=1,REPLACE,ENTITY="slag",VELOCITY,READ)
ICNODE(ENTRY=2,REPLACE,ENTITY="slag",KINETIC,READ)
ICNODE(ENTRY=3,REPLACE,ENTITY="slag",DISSIPATION,READ)
ICNODE(ENTRY=4,REPLACE,ENTITY="fluid",VELOCITY,READ)
ICNODE(ENTRY=5,REPLACE,ENTITY="fluid",KINETIC,READ)
ICNODE(ENTRY=6,REPLACE,ENTITY="fluid",DISSIPATION,READ)

RELAXATION(HYBRID)
/u  v  w  p  t  s  k  e
0.9 0.9 0.9 0.9  0  0.75 0.8 0.8 0.3
END

CREATE(FISOLV)
RUN(FISOLV)
```

REFERENCES

1. B.G. Thomas. "Overview of the Continuous Casting Process" http://ccc.me.uiuc.edu/introduction/overview.html

2. W.H. Emling, T.A. Waugaman, S.L. Feldbauer, and A.W. Cramb. "Subsurface Mold Slag Entrainment in Ultra-Low Carbon Steels", *Steelmaking Conference Proceedings*, ISS, Warrendale, PA, Vol. 77, 1994, pp. 371-379.

3. J. Herbertson, Q.L. He, P.J.Flint, and R.B. Mahapatra. "Modeling of Metal Delivery to Continuous Casting Molds", *Steelmaking Conference Proceedings*, ISS, Warrendale, PA, Vol. 74, 1991, pp 171-185.

4. R. McDavid and B.G. Thomas. "Flow and Thermal Behavior of the Top Surface Flux Powder Layers in Continuous Casting Molds", *Metallurgical Transactions B*, Vol. 27B, No. 4, 1996, pp 672-685.

5. D.T. Creech and B.G. Thomas. "3-D Turbulent Multiphase Modeling of Molten Steel Flow and Heat Transfer in a Continuous Slab Caster", *CFX User's Conference*, Wilmington, DE, Oct 1, 1998.

6. Y. Sahai, J.E. Battles, R.S. Carbonara and C.E. Mobley. *Proceedings of an International Symposium on Casting of Near Net Shape Products*, Honolulu, HI, 1988.

7. J.K. Yoon and J.E. Lee. *Proceedings of the International Conference on Modeling and Simulation in Metallurgical Engineering and Materials Science*, Beijing, China, 1996, pp 341.

8. I.V. Samarasekera and J.K. Brimacombe. *Iron Steelmaker*, Vol. 21, 1994, 29.

9. A.W. Cramb and E.S. Szekeres. "Mold Operations for Quality and Productivity", *The Iron and Steel Society of AIME*, Warrendale, 1992, pp. 37.

10. H. Nam, H.S. Park, and J.K. Yoon. "Numerical Analysis of Fluid Flow and Heat Transfer in the Funnel Type Mold of a Thin Slab Caster", *ISIJ International*, Vol. 40, No. 9, 2000, pp. 886–892.

11. T. Honeyands and J. Herbertson. "Flow Dynamics in Thin Slab Caster Moulds", *Steel Research,* Vol. 66, No. 7, 1995, pp. 287-293.

12. H. Nam, H.S. Park and J.K. Yoon. "Numerical Analysis of Fluid Flow and Heat Transfer in the Funnel Type Mold of a Thin Slab Caster", *ISIJ International*, Vol. 40, No. 9, 2000, pp. 886–892.

13. Q. Yuan. "Transient Study of Turbulent Flow and Particle Transport During Continuous Casting of Steel Slabs", PhD Thesis, University of Illinois at Urbana-Champaign, Urbana, 2004.

14. D. Creech. "Computational Modeling of Multiphase Turbulent Fluid Flow and Heat Transfer in the Continuous Slab Casting Mold", M.S. Thesis, University of Illinois at Urbana-Champaign, Urbana, 1999.

15. M.B. Assar, P.H. Dauby, and G.D. Lawson. "Opening the Black Box: Piv and Mfc Measurements in a Continuous Caster Mold", *Steelmaking Conference Proceedings*, Vol. 83, 2000, ISS, Warrendale, PA, pp. 397-411.

16. B.G. Thomas, and L. Zhang. "Mathematical Modeling of Fluid Flow in Continuous Casting", *ISIJ International*, Vol. 41, No. 10, 2001, pp. 1181-1193.

17. D. Gupta, and A.K. Lahiri. "Water Modeling Study of the Jet Characteristics in a Continuous Casting Mold", *Steel Research*, Vol. 63, No. 5, 1992, pp. 201-204.

18. R. Sobolewski, and D.J. Hurtuk. "Water Modeling of Slab Caster Flow Conditions", *2nd Process Technology Conference Proceedings*, Iron and Steel Society, Warrendale, PA, 1982, pp. 160-165.

19. B.G. Thomas, R. O'Malley, T. Shi, Y. Meng, D. Creech, and D. Stone. "Validation of Fluid Flow and Solidification of a Continuous Thin-Slab Caster", *MCWASP IX*, Aachen, Germany, 2000, pp. 769-776.

20. D. Gupta, S. Chakraborty, and A.K. Lahiri. "Asymmetry and Oscillation of the Fluid Flow Pattern in a Continuous Casting Mould: A Water Model Study", *ISIJ International*, Vol. 37, No. 7, 1997, pp. 654-658.

21. B.E. Launder and D.B. Spalding. "The Numerical Computation of Turbulent Flows", *Computer Methods in Applied Mechanics and Engineering*, Vol. 3, 1974, pp. 269-289.

22. Fluent Inc. "10.4.1 The Standard k-ε Model", *Fluent 6.1 Documentation*, 2003.

23. R. McDavid. "Fluid Flow and Heat Transfer Behavior of Top-Surface Flux Layers in Steel Continuous Casting", M.S. Thesis, University of Illinois at Urbana-Champaign, Urbana, 1994.

24. H. Bai and B.G. Thomas. "Two-Phase Fluid Flow in Continuous Casting Nozzles", *Continuous Casting Consortium Report*, 1998.

25. L. Zhang, Private communication, 2004

26. B.G. Thomas, B. Ho, and G. Li. "CON1D User's Manual", Report, University of Illinois, 1994.

27. Fluent Inc. "24.1 Overview of Numerical Schemes", *Fluent 6.1 Documentation*, 2003.

28. D.E. Hershey and B.G. Thomas. "Turbulent Flow of Steel Through Continuous Casting Nozzles using 3D Finite Element Models", *10th Process Technology Conference*, The Iron and Steel Society, Warrendale, PA, 1992.

29. B.G. Thomas, R.J. O'Malley, and D.T. Stone. "Measurement of Temperature, Solidification, and Microstructure in a Continuous Cast Thin Slab", *Modeling of Casting, Welding, and Advanced Solidification Processes*, San Diego, CA, and TMS, Warrendale, PA, 1998, pp. 1185-1199.

30. Algoma Steel, Private communication, 2002

31. K. Rackers and B.G. Thomas. 78th Steelmaking Conference Proceedings, Nashville, TN, April 2, 995, *Iron and Steel Society*, Warrendale, PA, Vol. 78, 1995, pp. 723-734.

32. G.A. Panaras, A. Theodorakakos, and G. Bergeies. "Numerical Investigation of the Free Surface in a Continuous Steel Casting Mold Model", *Metallurgical and Materials Transactions*, Vol. 29B, No. 5, 1998, pp. 1112-1126.

33. Fluent Inc. "24.1.1 Segregated Solution Method", *Fluent 6.1 Documentation*, 2003.

34. M. Hanao, M. Kawamoto, H. Mizukami, K. Hanazaki. "Influence of Velocity of Molten Steel Flow near the Meniscus in a Continuous Casting Mold on Surface Quality of Slabs." *Iron and Steelmaker*. Vol. 27, n.11, Nov. 2000, pp 55-59.

35. A.C. Mikrovas and S.A. Argyropoulos. "A Novel Technique to Estimate Velocity in Liquid Steel and in Other High Temperature Liquid Metals." *Iron and Steelmaker*, October, 1993, pp. 85-94.

36. B.G. Thomas. "Proposal Presentation Comments." February, 2004.

37. F.H. Harlow and J.E. Welch. “The MAC Method: A Computing Technique for Solving Viscous, Incompressible, Transient Fluid Flow Problems Involving Free Surfaces.” *Phys. Fluids*, Vol. 8, 1965, pp. 2182.

38. C.W. Hirt and B.D. Nichols. “Volume of Fluid (VOF) Method for the Dynamics of Free Boundaries”, *Journal of Computational Physics*, Vol. 39, 1981, pp. 201-225.

39. Q. Yuan, S.P. Vanka, and B.G. Thomas. “Large Eddy Simulations of Turbulent Flow and Inclusion Transport in Continuous Casting of Steel”, *Int. Symp. on Turbulent and Shear Flow Phenomena Proc.*, Stockholm, Sweden: Inst. Of Technology (KTH), Vol. 2, 2001, pp. 519-522.

40. B.G. Thomas. Personal Communication, February 19th, 2003.

41. C.W. Hirt, A.A. Amsden, and J.L. Cook. “An Arbitrary Lagrangian-Eulerian Computing Method for all Flow Speeds.” *Journal of Computational Physics*, Vol. 14, 1974, pp. 227-253.

42. A. Huerta, W.K. Liu. “Viscous Flow with Large Free Surface Motion”, *Computational Methods and Applied Mechanical Engineering*, Vol. 69, 1988, pp. 227-324.

43. M. Souli and J.P. Zolesio. “Arbitrary Lagrangian-Eulerian and Free Surface Methods in Fluid Mechanics.” *Computational Methods and Applied Mechanical Engineering*, Vol. 191, 2001, pp. 451-466.

44. J. Donea, S. Giuliani, and J.P. Halleux. “An Arbitrary Lagrangian-Eulerian Finite Element Method for Transient Dynamic Fluid-Structure Interactions.” *Computational Methods and Applied Mechanical Engineering*, Vol. 33, 1982, pp. 689-723.

45. T.E. Tezduyar, M. Behr, and J. Liou. “A new Strategy for Finite Element Computations Involving Moving Boundaries and Interfaces- the Deforming-Spatial-Domain/Space-Time Procedure: I. The Concept and the Preliminary Numerical Tests.” *Computational Methods and Applied Mechanical Engineering*, Vol. 94, 1992, pp. 339-351.

46 F. Harlow and A. Amsden. Fluid Dynamics, and Introductory Text, Los Alamos Scientific Laboratory, LA-4700, 1980.

47 S. Rabier and M. Medale. “Computation of Free Surface Flows with a Projection FEM in a Moving Mesh Framework”, *Computer Methods in Applied Mechanics and Engineering*, Vol. 192, 2003, pp. 4703-4721.

48. B. Perot and R. Nallapati. “A Moving Unstructured Staggered Mesh Method for the Simulation of Incompressible Free-Surface Flows”, *Journal of Computational Physics*, Vol. 184, 2003, pp. 192-214.

49. FIDAP Tutorial Manual. Fluent, Inc., 2001.

50. L.K. Forbes. “Critical Free-Surface Flow over a Semi-Circular Obstruction.” *Journal of Engineering Mathematics*, Vol. 22, 1988, pp.3-13.

51. J.R. Chaplin and P. Teigen. “Steady Flow Past a Vertical Surface-Piercing Cylinder.” *Journal of Fluids and Structures*, Vol. 18, 2003, pp. 271-285.

52. J. Samedov. “A Lagrangian-Eulerian Approach to Two-Dimensional Numerical Modeling.”, MS Thesis, Turkmenistan, 1998.

53. J.A. Dantzig and C.L. Tucker. Modeling in Materials, Cambridge University Press, New York, 2001.

54. J.A. Schetz. Boundary Layer Analysis, Prentice Hall, Englewood Cliffs, 1993.

55. G.E. Raynor. "The Annals of Mathematics", 2nd Series, Vol. 32, No. 1, Jan 1931, pp 17-22.

56. J.W. Shaver. "The Behavior of the Molten Steel Flux Interface and Related Defects in Thin-Slab Casting", MS Thesis, University of British Columbia, 2002.

57. Sorenson. Basic Coastal Engineering, 1978, pp. 32.

58. R. Sumer and Fredsøe. Hydrodynamics Around Cylindrical Structures, 1997, pp. 163-168.

59. G.X. Wu, R. Eatock Taylor, and D.M. Greaves. "The Effect of Viscosity on the Transient Free-Surface Waves in a Two-Dimensional Tank." *Journal of Engineering Mathematics*, Vol. 40, 2001, pp. 77-90.

60. X. Huang and B. G. Thomas. "Modeling Transient Flow Phenomena in Continuous Casting of Steel", *35th Conference of Metallurgists*, 23B, C. Twigge-Molecey, Montreal, Canada, CIM, 1996, pp. 339-356.

61. J. Anagnostopoulos and G. Bergeles. "Three-Dimensional Modeling of the Flow and the Interface Surface in a Continuous Casting Mold Model", *Metallurgical and Materials Transactions B*, Vol. 30B, No.6, 1999, pp. 1095-1105.

62. B.J. Keene. "Review of Data for the Surface Tension of Iron and its Binary Alloys." *International Materials Reviews*, Vol. 33, No. 1, 1988, pp. 1-37.

63. L. Zhang, B. Rietow, B.G. Thomas and K. Eakin. "Large Inclusions in Plain-Carbon Steel Ingots Cast by Bottom Teeming", *ISIJ International*, Vol. 46, No. 5, 2006, pp. 670-679.

64. L. Zhang, B. Rietow, B.G. Thomas, K. Eakin, and D.Q. Baird. "Investigation of Steel Cleanliness during Ingot Teeming, Final Report to Ingot Metallurgy Forum", Ingot Metallurgy Forum Fall Meeting, IMF, Canton, OH, Nov. 2, 2005.

65. *Steel Statistical Yearbook 2002*, ed., eds., International Iron and Steel Institute, Brussels, 2002.

66. E. Fuchs and P. Jonsson. *High Temperature Materials and Processes*,19(2000, pp. 333.

67 L. Zhang and B.G. Thomas. "State of the Art in Evaluation and Control of Steel Cleanliness", *ISIJ International*, Vol. 43, No. 3, 2003, pp. 271-291.

68. A.W. Cramb. "Inclusion Formation During Foundry Processing", Carnegie Mellon University, 1998, http://neon.mems.cmu.edu/afs/afs2/window2.html .

69. J.A. Horwath and G.M. Goodrich. "Micro-inclusion Classification in Steel Casting", *AFS Transactions*, 1995, pp. 495- 510.

70 J.M. Svoboda, R.W. Monroe, C.E. Bates and J. Griffin. "Appearance and Composition of Macro-inclusions in Steel Castings", *AFS Transactions*, 1987, pp 187- 202.

71. C.R. Wanstall, J. Griffin and C.E. Bates. "Clean Steel Cast Technology", *Steel Founders Society of America*, Research Report No. 106.

72. S.N. Singh. *Met. Trans*, Vol. 5, 1974, pp. 2165-2178.

73. S.K. Friendlander and H.F. Johnstone. *Industrial and Engineering Chemistry*, Vol. 49, No. 7, 1957, pp. 1152.

74. A.C. Wells and A.C. Chamberlin. *Brit. J. Appl. Phys.*, Vol. 18, 1967, pp. 1793-1799.

75. S. Dawson. *Steelmaking Conference Proceedings*, Vol. 73, 1990, pp. 15-31.

76. W. Fix, H. Jacobi, and K. Wünnenberg. "Collision-controlled Growth of Composites in Casting Nozzles", *Steel Research*, Vol. 64, No. 1, 1993, pp. 71-76.

77. S. Dawson. "Tundish Nozzle Blockage During the Continuous Casting of Aluminum-Killed Steel", *Iron and Steelmaker*, April, 1990, pp. 33-42.

78. N.A. McPherson and A. McLean. Continuous Casting - Volume Six - Tundish to Mold Transfer Operations, *Iron and Steel Society*, Warrendale, PA, 1992, pp. 11-15.

79. G.C. Duderstadt, R.K. Iyengar, and J.M. Matesa. "Tundish Nozzle Blockage in Continuous Casting", *Journal of Metals*, April 1968, pp. 89-94.

80. S. Ogibayashi et. al. "Mechanism and Countermeasure of Alumina Buildup on Submerged Nozzle in Continuous Casting", *75th ISS Steelmaking Conference*, Toronto, Canada, April 1992.

81 E.S. Szekeres. "Review of Strand Casting Factors Affecting Steel Product Cleanliness", *Fourth International Conference on Clean Steel*, Balatonszéplak, Hungary, June 1992.

82. G.A. Demasi and R.F. Hartmann. "Development of the Ladle Shroud Mechanism and its Metallurgical Benefits", The Shrouding of Steel Flow for Casting and Teeming, *Iron and Steel Society*, Warrendale, PA, 1986, pp. 3-11.

83. C.H. Bode, J.D. Duke, and F.J. Dewez. "Design of Slab-Casting Facilities to Maximize Machine Availability", *Continuous Casting of Steel*, Biarritz, France, May 1976.

84. A.W. Cramb and I. Jimbo. "Interfacial Considerations in Continuous Casting", *ISS Transactions*, Vol. 11, 1990, pp. 67-79.

85. G.M. Faulring, J.W. Farrell, and D.C. Hilty. "Steel Flow Through Nozzles: Influence of Calcium", Continuous Casting, Volume One, Chemical and Physical Interactions During Transfer Operations, *Iron and Steel Society*, Warrendale, PA, 1985, pp. 57-66.

86. T.R. Meadowcroft and R.J. Milbourne. "A New Process for Continuously Casting Aluminum Killed Steel", *Journal of Metals*, June 1971, pp. 11-17.

87. H. Buhr and J. Pirdzun. "Development of Refractories for Continuous Casting", *Continuous Casting of Steel*, Biarritz, France, May 1976.

88. L.J. Heaslip et. al. "Model Study of Fluid Flow and Pressure Distribution During SEN Injection - Potential for Reactive Metal Additions During Continuous Casting", *Iron and Steelmaker*, August 1987, pp. 49-64.

89. M.C. Tai, C.H. Chen, and C.L. Chou. "Development and Benefits of Four-Port Submerged Nozzle for Bloom Continuous Casting", *Continuous Casting '85*, London, England, May 1985.

90. E. Marino. "Use of Calcium Oxide as Refractory Material in Steel Making Processes", *Refractories for the Steel Industry*, Edited by R. Amavis, Elsevier Applied Science, New York, 1990, pp. 59-68.

91. T. Aoki et. al. "Alumina Clogging Resistant Materials for Tundish Shrouds", *74th ISS Steelmaking Conference*, Washington, D.C., April 1991.

92. P.M. Benson, Q.K. Robinson, and H.K. Park, "Evaluation of Lime-Containing Sub-Entry Shroud Liners to Prevent Alumina Clogging", *76th ISS Ironmaking and Steelmaking Conference*, Dallas, Texas, March 1993.

93. E. Lührsen et. al. "Boron Nitride Enrichment of the Submerged Entry Nozzles: A Solution to Avoid Clogging", *1st European Conference on Continuous Casting*, Florence, Italy, September 1991.

94. E. Höffken, H. Lax, and G. Pietzko. "Development of Improved Immersion Nozzles for Continuous Slab Casting", *Fourth International Conference on Continuous Casting*, 1988.

95. L.I. Evich et. al. "Experience in the Use of Chamotte Nozzles in Slide Gates in Teeming of Stainless Steel", *Ogneupory*, Vol. 11, November 1985, pp. 44-46.

96. K.K. Strelov et. al. "Clogging of the Channel of a Fosterite Nozzle in Teeming of Aluminum- Deoxidized Steel", *Ogneupory*, Vol. 8, August 1985, pp. 46-49.

97. R. Szezesny, C. Naturel, and J. Schoennahl. "Tundish Nozzles with a Double Layer Conception Used at Vallourec Saint-Saulve Plant", *Fourth International Conference on Continuous Casting*, 1988.

98. S.R. Cameron. "The Reduction of Tundish Nozzle Clogging During Continuous Casting at Dofasco", *75th ISS Steelmaking Conference*, Toronto, Canada, April 1992.

99. W.T. Lankford et. al. "The Physical Chemistry of Iron and Steelmaking", *The Making, Shaping, and Treating of Steel*, 10th Edition, Herbick & Held, Pittsburgh, PA, 1985, pp. 367-502.

100. N. Tsukamoto et. al. "Improvement of Submerged Nozzle Design Based on Water Model Examination of Tundish Slide Gate", *74th ISS Steelmaking Conference*, Washington, D.C., April 1991.

101. L. Zhang and B.G. Thomas. "State of the Art in Evaluation and Control of Steel Cleanliness", *ISIJ International*, Vol. 43, No. 3, 2003, pp. 271-291.

102. R. Kiessling. *Met. Sci.*, Vol. 15, No. 5, 1980, pp. 161.

103. R. Rastogi and A.W. Cramb. *84th Steelmaking Conf. Proc.*, ISS, Warrendale, PA, Vol. 84, 2001, pp. 789.

104. M. Goransson, F. Reinholdsson and K. Willman. *Iron Steelmaker*, Vol. 26, No. 5, 1999, pp. 53.

105. T. Hansen and P. Jonsson. *2001 Electric Furnace Conf. Proc*., ISS, Warrendale, PA, Vol. 59, 2001, pp. 71.

106. F. Ruby-Meyer and G. Willay. *Rev. Métall. Cah. Inf. Tech.*, Vol. 94, No. 3, 1997, pp. 367.

107. R. Meilland, H. Hocquaux, C. Louis, l. Pollino and F. Hoffert. *Rev. Métall. Cah. Inf. Tech.*, Vol. 96, No. 1, 1999, pp. 88.

108. M. Burty, C. Louis, P. Dunand, P. Osmont. F. Ruby-Meyer, M. Nadif, F. Penet, T. Isono, E. Takeuchi and T. Toh: *Rev. Métall. Cah. Inf. Tech.*, Vol. 97, No. 6, 2000, pp. 775.

109. H. Matsuta, T. Sato and M. Oku. *ISIJ International*, Vol. 36, 1996, Supplement, S125.

110. "SEM/EDS: Scanning Electron Microscopy with X-ray microanalysis: Technique Description", http://www.sdm.buffalo.edu/scic/sem-eds.html .

111. L. Zhang and K. Cai. BaoSteel, Report No., 1997.

112. Y. Nuri and K. Umezawa. *Tetsu-to-Hagané*, Vol. 75, No. 10, 1989, pp. 1897.

113. R.I.L. Guthrie and H.C. Lee. *75th Steelmaking Conf. Proc.*, ISS, Warrendale, PA,1992, pp. 799.

114. H. Yin, H. Shibata, T. Emi and M. Suzuki. *ISIJ International.*, Vol. 37, 1997, No. 10, pp. 936.

115. B. Debiesme, I. Poissonnet, P. Choquet and F. Penet. *Rev. Métall. Cah. Inf. Tech.*, Vol. 90, 1993, No. 3, pp. 387.

116. P.C. Glaws, R.V. Fryan and D.M. Keener. *74th Steelmaking Conf. Proc.*, ISS, Warrendale, PA, 1991, pp. 247.

117. K.P. Hughes, C.T. Schade, and M.A. Shepherd. *Iron & Steel Maker*, Vol. 22, 1995, pp. 35.

118. H.F. Marston. *69th Steelmaking Conference Proceedings*, ISS, Warrendale, PA, 1986, pp. 107.

119. J. Cheng, R. Eriksson, and P. Jonsson. *Ironmaking and Steelmaking*, Vol. 30, 2003, pp. 66.

120. L. Zhang, B.G. Thomas, K. Cai, L. Zhu and J. Cui. ISSTech2003, ISS, Warrandale, PA, 2003, pp. 141.

121. K. Fujii, T. Nagasaka and M. Hino. *ISIJ International*, Vol. 40, 2000, pp. 1059.

122. Y. Habu, H. Kitaoka, Y. Yoshii, T. Emi, Y. Iida, and T. Ueda. *Tetsu-To-Hagane*, Vol. 62, 1976, pp. 1803.